Microstructural and Optical Properties of Self-Assembled Quantum Dots for Optical Devices Grown By Molecular Beam Epitaxy

by

Maria Noemi Perez-Paz

A dissertation submitted to the Graduate Faculty in Chemistry in partial fulfillment of the requirements for the degree of Doctor of Philosophy, the City University of New York

UMI Number: 3187434

UMI Microform 3187434

ProQuest Information and Learning Company
300 North Zeeb Road
P.O. Box 1346
Ann Arbor, MI 48106-1346

This manuscript has been read and accepted for the Graduate Faculty in Chemistry in satisfaction of the dissertation requirement for the degree of Doctor of Philosophy.

09/07/05	**Maria C. Tamargo**
----------	**----------**
Date	**Chair of Examining Committee**
09/07/05	**Prof. Gerald Koeppl**
----------	**----------**
Date	**Executive Officer**

Professor Maria C. Tamargo

Professor Alexander Couzis

Professor Hiroshi Matsui

Professor Louis Brus

Supervisory Committee

THE CITY UNIVERSITY OF NEW YORK

Abstract

Microstructural and Optical Properties of Self-Assembled Quantum Dots for Optical Devices Grown By Molecular Beam Epitaxy

By

Maria Noemi Perez-Paz

Adviser: Professor Maria C. Tamargo

Low-dimensional semiconductor heterostructures have been extensively studied because of their potential applications and the unique physical phenomena they exhibit. Quantum dots (QDs) represent the latest innovation in the development of these structures. Due to the three-dimensional confinement of the carriers, semiconductor QD structures are expected not only to lead to the improvement of the device performance but also to limit the device degradation of the II-VI semiconductor-based devices. On the other hand, ZnCdMgSe material system shows potential in fabricating interband and intersubband devices with applications from the UV-visible to infrared range due to their widely adjustable bandgaps. For the first time, single and multi-QDs (MQDs) of CdSe with ZnCdMgSe barriers were

successfully grown by self-assembling using molecular beam epitaxy and their properties were characterized. Atomic force microscopy (AFM) measurements showed CdSe QDs in uncapped structures. Control and reproducibility of the QD size leading to light emission throughout the entire visible spectrum was obtained by varying the CdSe deposition time. Based on this, stacked QD structures consisting of three QD layers emitting in the red, green and blue regions of the spectrum were grown. Photoluminescence (PL) measurements exhibited bright white emission that was observed by eye, at 77K or at room temperature, because of the mixing of colors. Preliminary light emitting diodes structures designed to obtain white emission were grown and tested.

Size reduction, higher uniformity, higher density and a blue-shifted PL peak of the QD layer, by increasing Mg concentration in the $Zn_{1-x}Cd_xMg_{1-x-y}$ Se barrier were demonstrated. Results pointed to Mg as chemical factor that induced QD formation, either by increasing the atomic steps or/and by changing the surface energy of the $Zn_xCd_yMg_{1-x-y}Se$. Electronic coupling and polarization of the emitted light from the MQD layers were accomplished by changing the spacer thickness and its MgSe composition. Power dependence studies demonstrated the PL peak position associated with coupled QDs depends on the laser excitation power while the one of the uncoupled QDs remains invariable. Polarized studies consistent with AFM images demonstrated the presence of a spontaneous QD organization for the uncoupled MQDs (wire-like structure). No surface organization was obtained for the coupled case.

This thesis is dedicated to Flavio

Acknowledgements

This thesis would have never been completed without the guidance of my advisor Prof. Maria C. Tamargo. Her continuous encouragement, inspiration and protection along with instructive scientific discussions have allowed me to gain knowledge and independence in the semiconductor research field. I would like to thank her for the opportunity and the autonomy to choose and carry out a project that I really love. I would like to thank her not only for her valuable scientific advices but also for her familiarity and friendship that make us to feel so well when everything looks really the opposite.

I am indebted to H. Lu, M. Sohel, and Dr. A. Shen, from whom I have learned many experimental skills and gained more knowledge about the growth and characterization of semiconductor materials. They supported me during my work as well as with their friendship.

I am especially indebted to X. Zhou, my friend and my colleague, without her help at the beginning of my research, my fast advance will not be possible. Thank you, Zhou.

Many thanks to Prof. L. Brus, Prof. A. Couzis and Prof. H. Matsui for kindly serving on my thesis committee. Thanks are also due to, Prof. Lombardi, Prof. Giardi and Mr. R. Livinstong for the surface-enhance Raman measurements; to Prof. Isabel Alonso and her group in Spain for the help with the Raman measurements; Prof. Alfano, Dr. G. Comanescu, Dr. Taposh, Dr. Zhang, Dr. Das and other members of the Prof. Alfano group for their help with the time-resolved, absorbance, reflectance measurements; Prof. D. Akins and Mr. F. Jean-Mary for the assistance with the

atomic force microscopy measurements; Prof M. Muñoz for his assistance with the contactless electroreflectance measurements, and Prof. Zheng in the Hunter College for his interesting discussions about the light-emitting diodes fabrication and performance.

The financial support from the Department of Chemistry, National Science Foundation, Department of defense, the Center for Analysis of Surface and Interface, New York State Center for Advanced Technology on Photonic Materials and Applications are gratefully acknowledged.

On the personal side, I would like to thank, expressly, my father for his encouragement, support and love during all the unbreakable moments that we (my family) passed together.

Finally, “il mio profondo amore" is for Flavio without him next to me during these four years, nothing would have been possible.

Table of Contents

List of Tables

Chapter 1

Chapter 2

Chapter 3

Chapter 5

Chapter 6

List of Illustrations

Chapter 1

Chapter 2

Chapter 3

Chapter 4

Chapter 5

Chapter 6

Chapter 1. Introduction

1.1. Background

The compounds of the II-VI semiconductor family have recently been extensively investigated as materials to fabricate low dimensional structures with new optical and optoelectronic applications due to the higher exciton binding energy and the large energy band gap that these materials offer[1]. The wide band gap quaternary $Zn_xCd_yMg_{1-x-y}Se$ material system can be grown lattice matched to the InP substrate offering the possibility of an ample selection of band gaps, from 2.1 eV to ~3.6 eV[2], overlapping with most of the visible spectrum and even further, up to the near ultraviolet region.

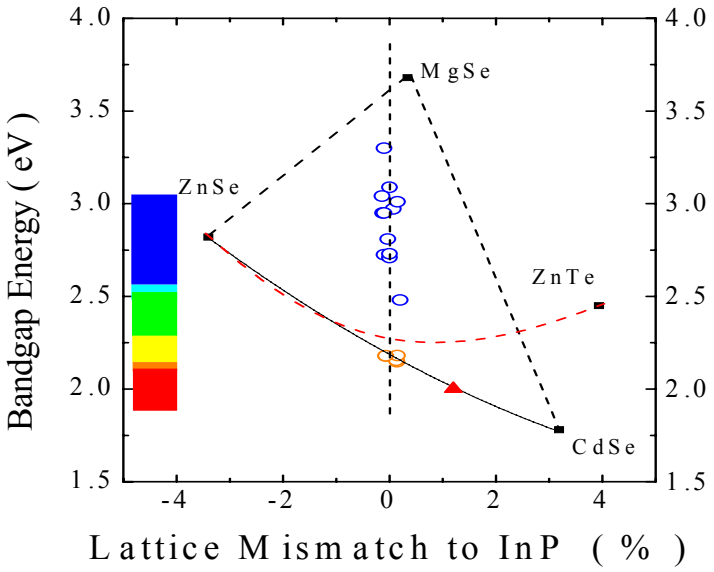

Figure 1.1. Band gap energy versus percent lattice-mismatch to InP for $Zn_xCd_yMg_{1-x-y}Se$ quaternary layers grown on InP substrates.

Figure 1.1 shows the plot of the bandgap versus lattice-constant for this family of materials at 77K. Lattice-mismatch [(Δa/a) x 100] to InP is plotted instead of the actual lattice-constant, since InP is the substrate of interest. The zero-mismatch compositions for the $Zn_xCd_yMg_{1-x-y}Se$ grown on InP are represented as open circles on the vertical dashed-line. The three solid squares represent the position of binary end points: ZnSe, CdSe and MgSe. The solid line represents the empirical fit to the $Zn_xCd_{1-x}Se$ data reported in the literature. The two dashed lines represent linear representations of the $Zn_xMg_{1-x}Se$ and $Cd_xMg_{1-x}Se$ ternaries compositions. The Fig. 1.1 also shows the bandgap versus composition for the $ZnSe_yTe_{1-y}$ alloys. In earlier work we have shown that that lattice-matched $ZnSe_yTe_{1-y}$ layers can be grown highly p-type doped and consequently, serve as p-type ohmic contacts for the device structures based on $Zn_xCd_yMg_{1-x-y}Se$ materials. Table 1.1 summarizes typical material properties for $Zn_xCd_yMg_{1-x-y}Se$ and p-doped $ZnSe_yTe_{1-y}$ alloys.

Previously, our group was the first group to grow high quality $Zn_xCd_yMg_{1-x-y}Se$ material matched to InP substrates, having a low defect density (defect density calculated by etch pit density or EPD was as low as $5x10^4$ cm^{-2}), narrow X-ray linewidths, and efficient luminescence even at room temperature.[3]

Emission energy range	~2.1-3.0 eV
Defect densities	$< 5 \times 10^4/cm^2$
n-type doping	$>1 \times 10^{18}/cm^3$
p-type doping	$\sim 1 \times 10^{16}/cm^3$
ZnSeTe p+ doping	$>1 \times 10^{19}/cm^3$

Table 1.1. Materials parameters for $Zn_xCd_yMg_{1-x-y}Se$ alloys on InP substrates.

Considering all these advantages provided by this new material system, our group tried to incorporate this quaternary system, first, as cladding and waveguides in laser diodes (LDs) and light emitting diodes (LEDs) designs and secondly, as active layer of these structures. Initially, the lattice-matched $Zn_{0.51}Cd_{0.49}Se$ ternary with a band gap of 2.1eV was used as quantum well (QW) layer. Photoluminescence (PL) emission was obtained from the blue to the yellow only by changing the $Zn_xCd_{1-x}Se$ QW thickness. Red emission was achieved by using a strained $Zn_xCd_{1-x}Se$ QW layer with excess of Cd ($\Delta a/a>1.2\%$), whose thickness was kept within the pseudomorphic regime to avoid formation of misfit dislocations.

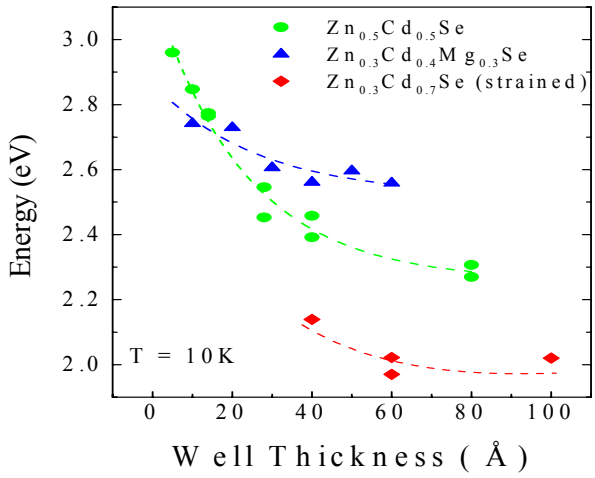

Figure 1.2. Emission energy versus QW thickness for a series of $Zn_xCd_yMg_{1-x-y}Se$-based QW structures.

The Fig. 1.2 shows the emission energy as a function of QW thickness for several QW structures with $Zn_xCd_yMg_{1-x-y}Se$ quaternary barriers, lattice-matched to InP substrates with a bandgap energy of ~ 3 eV. The three curves correspond to different QW compositions of this system. The first two symbolized by circles and diamonds,

represent respectively $Zn_xCd_{1-x}Se$ lattice-matched to InP and the $Zn_xCd_{1-x}Se$ QWs with excess Cd for red emission. These two curves clearly illustrate the potential optical applications of this system since the entire optical spectrum is possible from a single material system. By varying the thickness and/or composition of the QW layer of lattice-matched (or pseudomorphic) structures, it is possible to tune the PL emission of the light. Based on $Zn_xCd_{1-x}Se/Zn_xCd_yMg_{1-x-y}Se$ QWs structures, R-G-B photopumped lasers[4] and LEDs with emission throughout the visible spectrum[5], whose lifetimes were longer than the traditional $Zn_xCd_{1-x}Se/Zn_{1-x}Mg_xS_{1-y}Se_y$[6], were obtained by a number of groups.

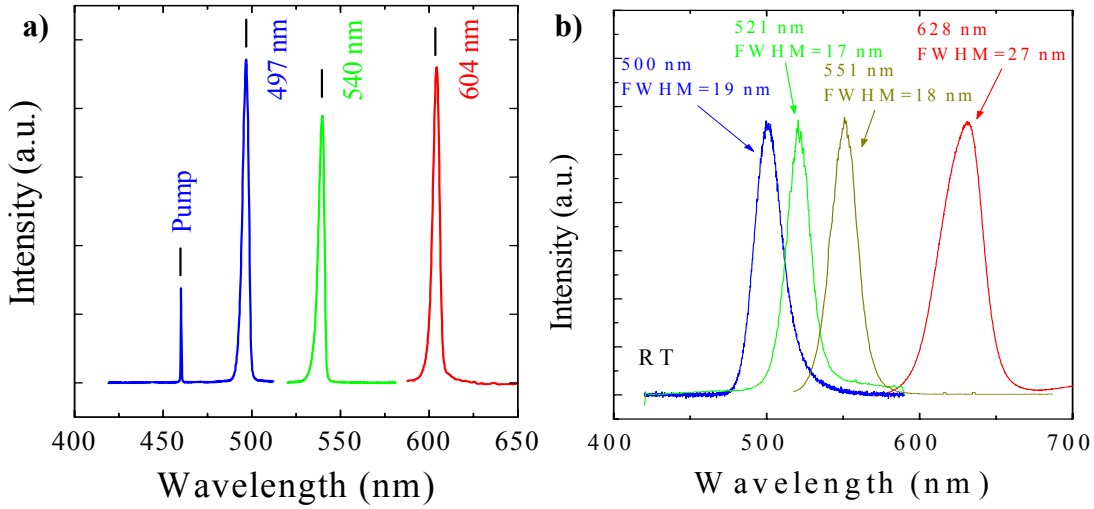

Figure 1.3. a) Optically pumped lasing spectra for three $Zn_xCd_yMg_{1-x-y}Se$ lasers that emit in the red, green and blue and b) Electroluminescence spectra for four $Zn_xCd_yMg_{1-x-y}Se$ -based LEDs that emit throughout the visible range.

Parts a and b in Fig. 1.3 show, respectively, the lasing properties of three optically-pumped laser structures and the electroluminescence spectra of LEDs structures covering the whole visible spectrum. Even though all the Zn_xCd_{1-}

$_x$Se/$Zn_xCd_yMg_{1-x-y}Se$ QWs structures were grown successfully in our lab, some drawbacks derived from a very thin QW, ≤20Å were found for the QW with blue emission. Some of these shortcomings are broad luminescence emission peak, a weak quantum confinement, and great sensitivity to thickness fluctuations during the MBE growth process, which resulted in a difficult to control QW emission energy. To solve these issues, the $Zn_xCd_{1-x}Se$ QW was replaced by a $Zn_xCd_yMg_{1-x-y}Se$ QW, providing the opportunity to obtain blue emission with a thicker well and resulting in an improvement of structural and electronic properties[7]. The curve of triangles presented in Fig 1.2 shows several $Zn_xCd_yMg_{1-x-y}Se$ QW structures with different thicknesses that achieve blue emission.

In spite of all the progress realized in the growth and performance of II-VI semiconductor QW-based devices, these materials have still not reached the levels of performance of III-V semiconductor QW-based devices due mainly to concerns associated with the active layer degradation as a result of the propagation of dark line defects. A QDs active layer instead of a QW is anticipated to decrease the defect-induced degradation effects that actually limit the II-VI devices applications[8] and this expectation along with the general promising performance characteristics of QDs-based devices, suggest that QDs are a good candidate to improve the lifetime of II-VI based-devices.

Our group initiated its work on II-VI self-assembled quantum dots (SAQDs) with the traditional II-VI QDs system, CdSe QDs on ZnSe barriers grown pseudomorphic to GaAs substrates. Afterward, small amounts of beryllium were introduced to attain a matched $Zn_{1-x}Be_xSe$ barrier to the GaAs substrate and to improve the quality of the

barrier (higher bond energies for Be alloys)[9]. Taking into account these early studies realized in CdSe QDs (effects of beryllium on the CdSe QD formation) and the advantages of the $Zn_xCd_yMg_{1-x-y}Se$ family system that were explained previously, we grew CdSe QDs on $Zn_xCd_yMg_{1-x-y}Se$ barriers. In this dissertation, we present morphology and optical properties of this new II-VI QDs system, CdSe QDs with $Zn_xCd_yMg_{1-x-y}Se$ barriers, grown by molecular bema epitaxy (MBE) on InP substrates. Single and multi quantum dot (MQD) structures for visible and white sources applications were grown. In addition, based on all these results some LED structures were grown and their diode behavior tested.

1.2. Aim of Thesis

Extensive research has been carried out in the fabrication and applications of low-dimensional heterostructures such as quantum wires (QWRs)[10], QDs[11] and coupled arrays of MQDs[12] due to their potential advantages[13] (such as excellent lasing characteristics) compared to traditional (thick layer) semiconductor[14, 15] or QW-based devices[16, 17]. Although the advantages of low dimensional semiconductor heterostructures, were predicted about 30 years ago by Dingle and Henry[18], commercial applications of QDs are limited and are still much fewer than those of QWs. Since the morphological properties (shape, size, density and spatial arrangement) determine the electronic properties of the QDs and consequently, their device applications, it is critical to have a deep familiarity with the diverse factors that influence the growth of these low-dimensional heterostructures.

The QDs represent the last innovation in the realization of semiconductor structures with reduced dimensionality. Due to the three-dimensional confinement on the carriers or excitons, semiconductor QD structures are expected to lead to improvement in the performance (lower lasing threshold, wavelength tunability, maximum material gain and lower temperature dependence of the device response) of LEDs and semiconductor LDs[19]. Even though, R-G-B light emitters and semiconductor-based full color displays are currently manufactured, their fabrication still requires complex engineering designs and/or combinations of different materials[20]. Semiconductor systems with flexibility and simplicity in the structure design are required for these photonic applications in the visible range. Light emission and intensity of semiconductor QDs are anticipated to be controllable through the size and density of the dots, offering a new possibility for these aforementioned optical device applications.

Wide bandgap II-VI semiconductors are promising materials for the development of the LEDs and LDs in the visible and the UV range of the spectrum. In 1991, the first ZnSe-blue-green laser of II-VI was obtained using a GaAs substrate.[21] However, due to a lack of II-VI bulk substrates, QW structures were grown pseudomorphically (not matched) to GaAs, which was responsible, in part, of the formation dark line defects that reduced the luminescence and device lifetime. When InP is used as substrate instead of GaAs, an entirely lattice-matched structure, based on ZnCdMgSe, can be grown offering the possibility of a wide selection of band gaps, from 2.1 eV to ~3.6 eV, as mentioned in the last section. This, together with the incorporation of magnesium (a hard material with high bonding energy)

makes this a suitable and promising system to improve the lifetime of the II-VI photonic devices.

Thus, the major goal of this thesis is to develop a new II-VI QD material system based on the high-quality ZnCdMgSe materials and to study its optical and morphological properties, as well as, to pursue its control, improvement and understanding by different approaches. Once we have achieved control of its growth and properties, we propose to incorporate the material into devices structures with the aim of improving the optical quality and the lifetime of the II-VI optical devices, which is the main commercial drawback of this semiconductor family.

1.3. Thesis Structure

The rest of the thesis is organized as follows:

In Chapter 2, the principles of the MBE technique and the main components of the MBE system used at the City College of New York are illustrated. This is followed by a brief description of the characterization techniques, applied either "in situ" (during the growth) or "ex-situ" (after the growth), for the determination of the structural, optical and electronic properties of the epilayers and device structures.

In Chapter 3, a review is given of the state-of-art of SAQDs growth and devices applications, as well as, a quantum physics introduction to the subject and some equilibrium and kinetics models. Then, our experimental studies and results to achieve the control of morphology of the QDs are provided.

In Chapter 4, the growth of staked layers of QDs with different CdSe deposition time is described. Optical studies are shown. Structures were grown and

explored with the goal of achieving white light from current-injection devices. The current-voltage characteristics of p-n junctions are presented.

In Chapter 5, the growth and properties of MQD structures are described. The first part of the chapter described the growth and characterization of initial MQD structures by optical transmission, reflectivity, PL experiments, and time-resolved PL. The second part of the chapter focuses on structures grown to investigate the vertical correlation (ordering in the vertical direction) and the electronic coupling between different stacked QD layers.

Chapter 6 contains the Raman spectroscopy studies of single quantum dot (SQD) layer structures. In the first part of the chapter, a brief introduction to the principles of Raman spectroscopy is offered, which is followed by a section about the Raman studies of capped quantum dot samples with different sizes of QDs. Finally, the last section presents the initial studies of surface enhanced Raman spectroscopy effects in uncapped CdSe SAQDs on ZnCdMgSe barriers.

Finally, Chapter 7 closes the thesis with a brief summary of all the dissertation work, with concluding remarks of the thesis contribution and promising future work. A list of publications and conference presentations is given to highlight the key achievements of this dissertation.

Chapter 2. Experimental Techniques

2.1. Molecular Beam Epitaxy

During the 1940's, evaporated films of lead and tin chalcogenides were grown and extensively investigated but it was not until 1964 that Schoolar and Zemel demonstrated the growth of epitaxial PbS films on NaCl, using molecular beams generated from effusion cells[22]. This achievement probably constitutes the fundaments of a more advance epitaxy and gives the base for the modern MBE.

Epitaxial crystal growth involves a wide range of growth techniques such as Liquid Phase Epitaxy (LPE), Vapor Phase Epitaxy (VPE), Metal Organic Chemical Vapor Deposition (MOCVD) and MBE. The word "epitaxy" comes from the union of two Greek words: "epi" (upon) and "taxis" (ordered), meaning is the ordered continuation of the substrate crystal. Generally speaking, epitaxy, and this MBE, is a growth process of a solid film on crystalline substrate in which the atoms of the growing film mimic the arrangement of the atoms of the substrate.[23]

MBE is an epitaxial crystal growth technique used to tailor artificial crystal structures with defined optical and optoelectronic properties. In contrast to other epitaxial techniques (LPE or VPE), MBE is not governed by conditions near thermodynamic equilibrium but mainly by the kinetics of the surface processes (diffusion processes occurring in the crystallizing phase surrounding the substrate crystal). The surface physics and the surface atom rearrangements result from the relations between the atom arrival rate (beam flux) and the substrate temperature,

which in turn determine the composition of the growing epilayer and even the doping level (if an element dopant is being introduced in the growth).[24]

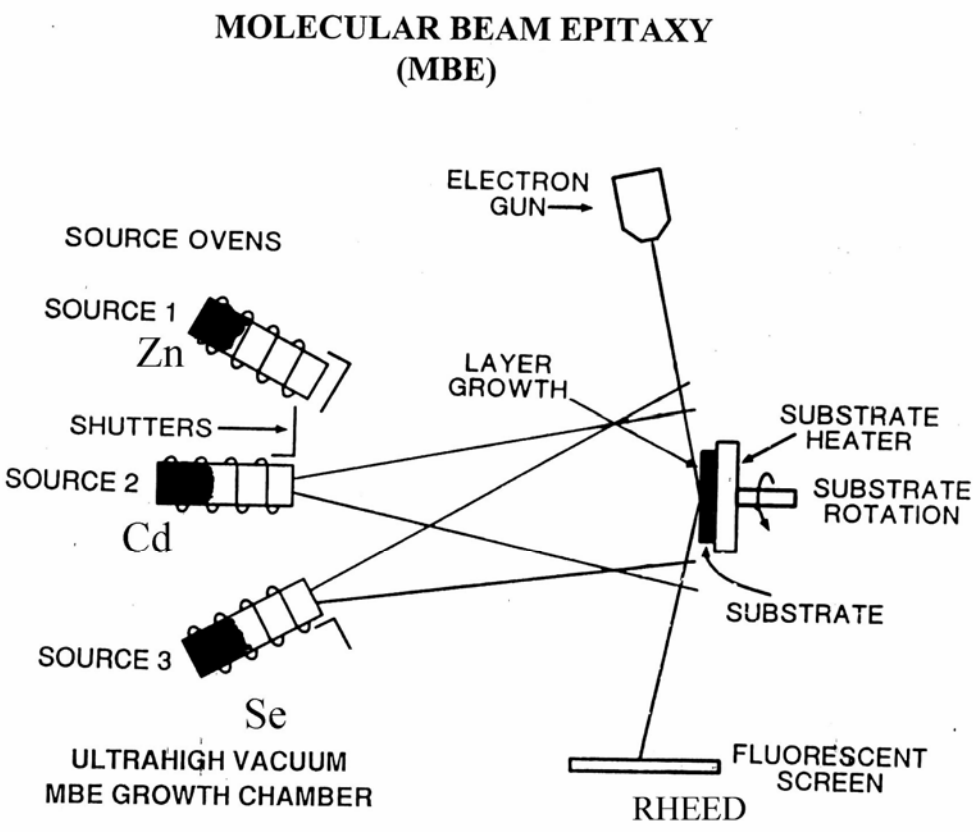

Figure 2.1. Schematic of MBE chamber for a CdSe epitaxial film growth.

The MBE technique is based on the chemical reaction of one or more thermal molecular beams with a crystalline surface of substrate in an ultra-high vacuum (UHV) environment. This environment prevents the collision of the molecular beams with undesired contaminants[25] and permits the in situ monitor of the growth by surface diagnostic methods such as Reflection High-energy Electron Diffraction (RHEED). The MBE process with the essential components for the growth of a CdSe epitaxial film (since the Zn shutter is closed) is illustrated schematically in Fig. 2.1.

Thermal Knudsen effusion cells or source ovens (zinc, cadmium and selenium cells on the drawing) provide the molecular or atomic beams. Each cell contains a crucible with one of chemical elements or compounds of the desired epilayer. Individual thermocouples are embedded in each cell oven, as well as, in the substrate heater. By means of a power-integral-derivative (PID) controller, a feedback loop between each thermocouple and the corresponding heater permits the control of the temperature. The PID values of the cells and the PID of the substrate heater facilitate, respectively, the establishment of a stable temperature for the sources and the substrate, which permit a precise control of the evaporation rates of the elements situated inside the sources, as well as the control of the surface migration of these elements on the substrate material once they reach its surface. The cells are arranged so that the central portion of the beam flux distribution from each cell intersects the substrate. Molecular beam fluxes and geometrical relationship between the configuration of the sources and the substrate will determine the thickness and the composition of the films. The control of the flux is by means of a shutter, located between the cell and the substrate. Operation of these shutters permits abrupt cessation or initiation of any given beam flux to the substrate. The material composition is determined by the flux ratio of elements. These fluxes are determined by measuring the beam equivalent pressures (BEP) obtained by a flux gauge placed at the equivalent position of the substrate. The temperature of the cells is selected according to the vapor pressure of the component in the cell and should be high enough for the generation of thermal energy molecular beams (or atomic) by free evaporation. The composition of the epilayer depends on the relative arrival rates of the constituent elements, which in

turn are determined by the temperatures of the cells. Therefore, cell temperatures are important factors to determine the final composition of the epilayer. Another important factor to control during the growth is the temperature of substrate. The temperature of substrate is selected high enough to allow atom migration but not so high that can cause the re-evaporation of the components of the epilayer.

The extremely high precision in beam flux control allows the growth of very thin layers, even monolayers. This control is essential for the case of nanostructured materials, and in particular QDs. The typical growth rate for MBE growth is 1μm/hr (1 monolayer/s), which allows 2-dimensional growth (layer by layer) and facilitates the achievement of smooth surfaces and high quality materials. The mechanism of this layer-by-layer epitaxial growth is described by the Burton-Cabrera-Frank theory. According to this model, growth proceeds according to the following steps:

(1) Atoms impinge on the sample surface, where they are absorbed

(2) The atoms migrate along the surface towards atomic steps, where the increased number of atomic bonds stabilizes them;

(3) The atoms migrate along the step edges to a kink site, where they are incorporated into the lattice. Deposition involves the lateral motion of the step edges or the growth of two-dimensional islands until an atomic layer is completed.

2.1.1. Molecular Beam Epitaxy System

All the samples described in this dissertation were grown in an MBE system with two Riber 2300P growth chambers in the City College of New York. Fig. 2.2 shows a top-view scheme of this system and Fig. 2.3 is a photograph of the MBE apparatus. The system includes 6 chambers: loading chamber, transfer channel, substrate treatment chamber, metallization chamber and two growth chambers: one for III-V materials and another for II-VI materials. The chambers are connected to each other by the transfer channel, which permits the transport of the sample from one to another, keeping ultra-high vacuum (UHV) conditions. There are several gate valves to separate all the chambers to ensure that unintentional cross contamination between them does not occur. In order to avoid contamination and achieve the UHV, (10^{-9}-10^{-11} Torr), all the chambers are pumped by an ion-pump and a Ti sublimation pump except the loading chamber, which is pumped by a turbo-molecular pump with a mechanical pump as the first stage, and the substrate treatment chamber, which is pumped by a cryo-pump. Besides the ion pump, the II-VI chamber and the metallization chamber are each pumped by an additional cryo-pump. The metallization chamber is equipped with an e-beam evaporator, which can deposit metal layers in situ on the sample, useful to fabricate contacts for device applications.

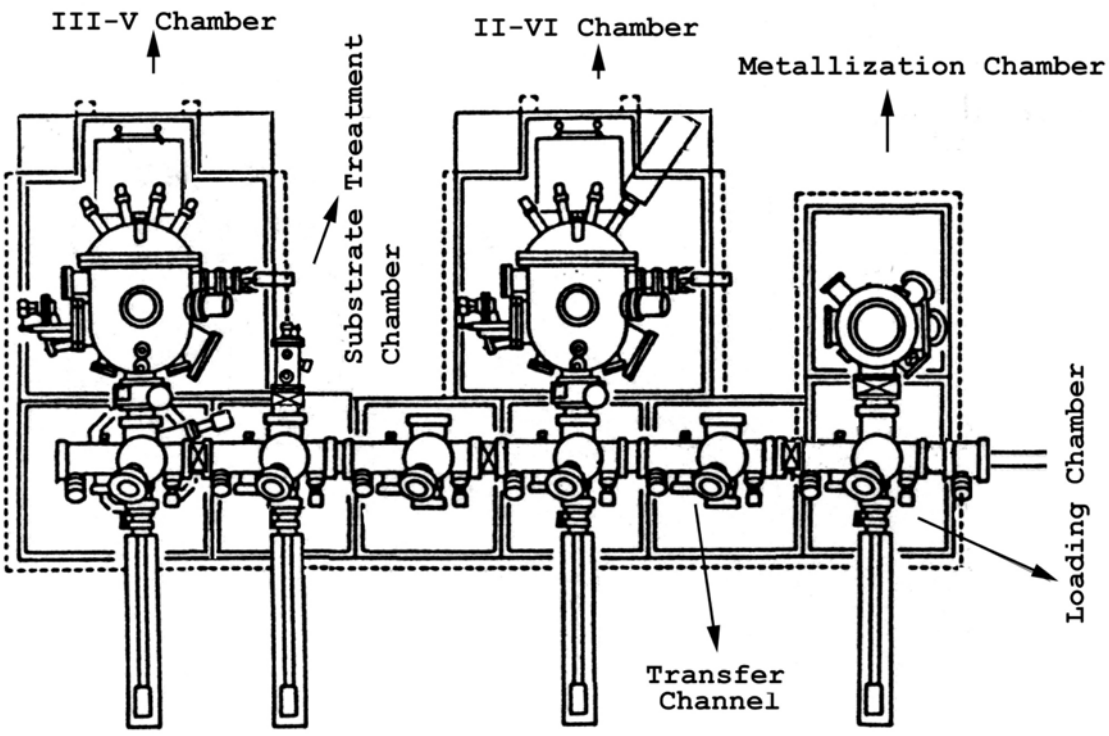

Figure 2.2. MBE system in the City College of New York.

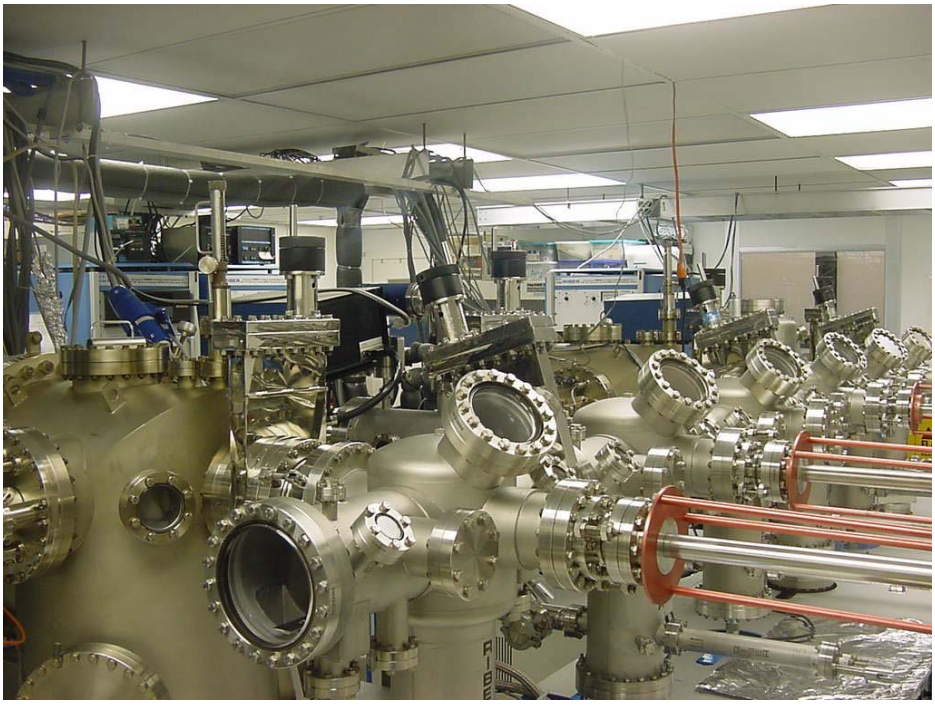

Figure 2.3. Photograph of the MBE system in the City College of New York.

The basic components of each of the growth chambers consist of a substrate manipulator (holder, rotator, heater and temperature sensor or thermocouple of the substrate), RHEED, quadrupole mass spectrometer, and cryo-shrouds around the manipulator and the cells. These cryo-shrouds will have a flow of liquid nitrogen (LN) through them during growth to prevent the thermal interference between the sources and also trap the residual molecules inside the chamber to obtain UHV. There are 8 cell ports in the III-V chamber, 6 are equipped for Ga, In, Al, As, Si (for n-type doping) and Be (for p-type doping), and 8 cells in the II-VI chamber for Zn, Cd, Mg, Se, Te, Be (initially, but afterward, substituted by other cell of Zn), $ZnCl_2$ (for Cl flux used for n-type doping) and a radio frequency (RF) nitrogen cell for p-type doping. Very high purity materials from 6N to 8N have been used as the source materials to ensure high purity films are grown.

2.1.2. General Procedure of MBE Growth

In this section, the general procedure of a MBE growth is illustrated. In Chapters 3, 4 and 5, SQD and multi-QDs growth procedures will be described in more detail.

2.1.2.1 Cleaning of Substrate

The cleaning of substrate is a previous and important step before starting any epitaxial growth. The preparation process can change according to the type of substrate and its properties, such as the hardness. For the case of InP, the substrates are degreased by trichloroethylene (TCE), acetone and methanol and after that, are etched by a solution of H_2SO_4:H_2O_2:H_2O (4:1:1) for 1 minute to remove the residual

polishing damage. To prevent from the contamination of carbon and make the surface relatively stable to laboratory air, the surface is flushed with deionized water to produce an oxide layer, which will later be removed in-situ by a desorption process (or deoxidation process) immediately before the growth of the epilayer. Then the substrates are bonded onto a molybdenum block by using indium (Fig. 2.4), which will facilitate the loading and manipulation of substrates in the chamber.

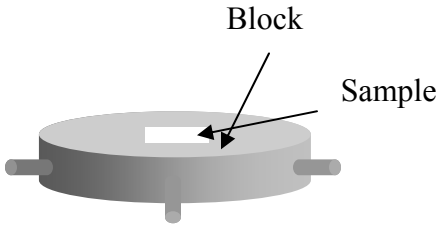

Figure 2.4. Sample bonded to block by Indium.

2.1.2.2. Loading of Substrate

The loading chamber is used to introduce the substrates (attached to the molybdenum block) in the MBE system. Two gate valves between the loading chamber and the transfer channel, and between the loading chamber and the metallization chamber, allow the venting of the loading chamber by using ultra pure nitrogen gas without affecting the vacuum of the other chambers, keeping it in the order of 10^{-9}-10^{-10} Torr. After sample loading, the pressure is high inside the chamber so the samples can not be transferred immediately to the other chambers (still in UHV) to start the growth process. It is necessary to pump down the loading chamber to 10^{-8} Torr, which will be carried out by using several pumping stages: first, a

mechanical pump to pressures of 10^{-1} Torr, followed by two sorption pumps to pressures of about 10^{-3} Torr and finally, with a turbo-pump system to 10^{-8}-10^{-9} Torr. The process takes about 1 hr.

2.1.2.3. Transference to Substrate Treatment Chamber (or TAC)

This step is not always performed but is always desirable to avoid the presence of moisture inside the III-V growth chamber. The substrates are transported from the loading chamber to the substrate treatment chamber by using the transfer cart, which is mechanically moved along the UHV transfer channel. The substrate on the block is introduced into the TAC and placed on the heater, which is situated on the substrate manipulator of the TAC. By heating the substrate using this heater, the out-gassing of substrate is achieved. If the transfer to the TAC is not performed the out-gassing process will be carried out in the III-V chamber before starting the growth. The temperature and time duration depend on the type of material, for the case of an InP substrate it is 20 min at 150ºC. The TAC is also used for the baking of new blocks that have not been previously introduced in the MBE system.

2.1.2.4. Transference to III-V Growth Chamber

After out-gassing process, the sample is transferred to the growth chamber and placed on the manipulator. The cell temperatures have been previously adjusted so that they produce the desired fluxes, measured using the flux gauge placed in the substrate position (an empty block is placed on the sample holder during the flux

measurements). First, the oxide is removed by heating the substrate with an As flux impingent on the substrate surface. This deoxidization process can be monitored by using the Reflection High-Energy Electron Diffraction (RHEED), which first reveals a pattern of an amorphous layer due to the oxide layer, and becomes streaky and bright when the oxide layer is removed (for details about the RHEED transformations see section 2.2.2.1). Once the oxide is removed, the substrate temperature is carefully set to the desired growth temperature and the layer growth is initiated by opening the relevant shutters. If the interest is only the growth of a III-V structure, the growth procedure will end with the deposition of the desired III-V layers. On the other hand, if the goal is the growth of a II-VI structure, a III-V buffer layer matched to the substrate is grown to smooth the substrate surface, and the sample will be transferred to the II-VI growth chamber to perform the growth of II-VI structure. After the III-V buffer growth is finished, the As shutter is kept opened to obtain a III-V surface terminated by As (more details about this process will be explained in the next section). $In_xGa_{1-x}As$ and GaAs layers are grown as buffer layers, respectively, for InP and GaAs substrates. In the case of GaAs, the growth is homoepitaxial (the buffer layer is the same material as the substrate material) so the Ga flux is the only parameter that is adjusted to control the growth. By contrast, the heteroepitaxial growth of $In_xGa_{1-x}As$ on InP substrate requires the careful calibration of In and Ga fluxes (In/Ga~2) to be able to obtain a layer the is lattice matched to InP, which is fundamental to obtain a good crystalline quality buffer without formation of defects (misfit dislocations), originating from the mismatch between the substrate and the buffer layer.

2.1.2.5. Transference to II-VI Growth Chamber

The optimization of the III-V/II-VI heterointerface is crucial for the high quality growth of II-VI epilayers. It has been shown that an improvement of the II-VI/III-V interface is the main reason of the reduction of defect density and increase of lifetime in devices based on II-VI semiconductors[26]. For example, in the case of the traditional II-VI material, ZnSe, grown over III-V GaAs substrate, an increase of device lifetime from a few seconds to more than 100 hours was obtained by a reduction of defect density of three orders of magnitude (from 10^7 to 10^4 cm^{-2}). In order to obtain a defect reduction in the ZnSe-based materials, it has been demonstrated that it is important to avoid an initial interation between the selenium and the III-V surface. This fact results in the formation of isolated islands (possibly, Ga_2Se_3 or/and In_2Se_3 clusters) that will be the origin of a very high density of stacking faults and dislocations[27]. Farrell et al. proposed the precise control of the III-V surface stoichiometry to reduce the interaction of the group VI element with elements of group III[28]. Some initial methods performed to adjust the surface stoichiometry of ZnSe layers on GaAs were (1) suitable preparation of the substrate to form a group-V rich surface, (2) Zn exposure of the III-V surface before the initial growth of II-VI material[29] and (3) use of migration enhanced epitaxy technique[30]. In the case of materials grown InP substrate, there are even more difficulties than in the case of GaAs-based materials. This situation is mainly due to the InP congruent evaporation temperature, which is lower than its deoxidation temperature, so it is harder to obtain a clean and, at the same time, a smooth surface with the correct stoichiometry. Our group demonstrated that the defect density of ZnCdMgSe was

reduced to 10^6 cm^{-2} by the growth of a ZnCdSe buffer layer at low temperature (170 °C) compared with the normal growth temperatures of this family system (270 °C)[31]. This low temperature growth seems to favor initial two-dimensional growth of the II-VI layers, which is difficult for II-VI materials grown InP substrates. After this achievement, further studies demonstrated that a Zn irradiation (exposure of the substrate surface to the Zn flux) at 170 °C, performed just before the ZnCdSe low temperature layer growth, (no interruption between Zn irradiation and ZnCdSe layer growth), helped to obtain a much less defect density of ~5 x 10^4 cm^{-2} (evaluated by EPD).

To summarize, in order to improve the quality of II-VI/ III-V interface of the ZnCdMgSe family system several steps are performed before the growth of the desired structure 1) terminating the surface of the III-V buffer with As (As-rich surface) 2) exposing the III-V surface firstly to Zn only (Zn irradiation) before the initial growth of II-VI material, and 3) starting the growth at low temperature and finally, 4) adjusting the temperature to "normal" growth temperature (growth interruption). Once all these steps have been performed, the desired II-VI layers can be grown by opening the shutters of the epilayer components.

2.1.3. Radio Frequency Discharge Nitrogen Plasma Source

2.1.3.1. Setup Description

Nitrogen doped reference layers of $Zn_xCd_yMg_{1-x-y}Se$ and $ZnSe_yTe_{1-y}$ were used to determine the doping level of the p-doped $Zn_xCd_yMg_{1-x-y}Se$ barrier and the p-type $ZnSe_yTe_{1-y}$ contact layers of the light emitted diode structures fabricated to obtain white light (see Chapter 4). The p-type dopant, atomic nitrogen, is obtained by a RF-discharge N plasma. Nitrogen plasma is generated by inductively coupling 13.56 MHz energy into a small cylindrical pyrolytic boron nitride (PBN) discharge chamber supplied with ultra-pure (99.9999 %) nitrogen gas. Fig. 2.5 shows the schematic diagram of the nitrogen source setup. The discharge system (MPD 21R) was manufactured by Oxford Applied Research (UK). The PBN discharge tube is surrounded by a water-cooled RF coil. The N_2 gas is fed into the tube via a leak valve at one end of the tube while at the other end, a PBN disk with nine fine holes (0.2 mm in diameter) serve as the beam exit plate. The fine holes permit a fraction of the active nitrogen species to diffuse out of the discharge chamber towards the substrate inside the MBE growth chamber. The assembly is mounted on a Conflat flange and fits on the MBE growth chamber in the place of a conventional effusion source. The RF input power supplied to the discharge chamber in the source can be varied up to 400 W (at 13.56 MHz), the reflected power being < 2W as established by an automatic tuning network. For the characterization of the emission from the discharge nitrogen

plasma, two types of optical detectors, including a Si photodiode and a photodiode array (PDA) detector which is connected with an optical fiber, are alternatively mounted on the air side of the discharge chamber.

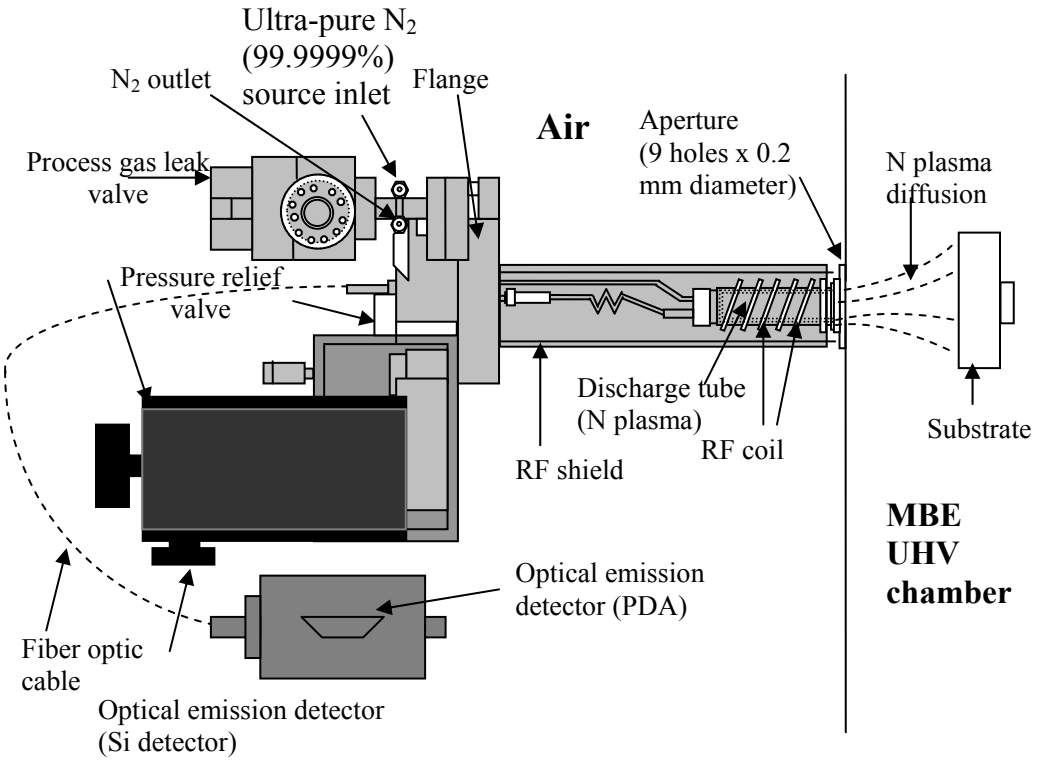

Figure 2.5. Setup diagram of a radio frequency-discharge Nitrogen plasma mounted on the II-VI MBE chamber.

2.1.3.2. General Procedure

The standard operation procedure starts by filling with pure molecular N_2 the discharge PBN chamber. Then the RF discharge power must be turned on and kept at 200 W. By adjusting the N_2 flow rate, a "low brightness" discharge mode will be first turned on at a specific flow rate consistent with a nitrogen background pressure of high 10^{-6} torr. As soon as the "low brightness" mode is achieved, the discharge of a "high brightness" is struck by reducing the N_2 flow rate. The "high brightness" mode

is preferred for better doping efficiency. A higher or lower RF discharge power can be further adjusted depending on the doping level intended. A Si photodiode is used to monitor the overall intensity of the plasma emission. In general, the measured intensity is dependent on both the RF discharge power and the nitrogen flow (or the partial pressure in the growth chamber). The Si photodiode output (the overall plasma emission intensity) is typically maintained at a stable value, which is obtained by establishing an equilibrium nitrogen background pressure in the MBE growth chamber. For an optimum doping condition of $Zn_xCd_yMg_{1-x-y}Se$, the plasma emission intensity typically is kept at about 600mV corresponding to the RF discharge power of 400 W and a nitrogen background pressure of 8 x 10^{-6} Torr. These conditions typically produce a net acceptor concentration of low 10^{16} cm^{-3} in uniformly N doped $Zn_xCd_yMg_{1-x-y}Se$.

2.2. Characterization Techniques

Once the structure is grown (or, sometimes during the growth *in situ*), it is important to characterize the structure to know its properties and its quality. Characterization techniques can be classified according to the time in which they are applied for studying the properties of the material. They can be used *in situ*, within the MBE system, to determine the quality of the epilayer that is being grown (in-growth techniques) or has being grown (post-growth techniques); or *ex-situ*, outside the MBE, (samples were previously taken out from the chamber and removed from the molybdenum block). A wide range of information can be obtained from these techniques, including crystal structure, electronic structure, chemical composition, carrier concentration and quality of epilayer.

2.2.1. *In situ* Characterization

The versatility of experimental arrangement of MBE systems along with the experimental conditions in which the growth is performed (ultrahigh vacuum environment) makes the MBE technique a compatible technique with *in situ* surface diagnostic methods. Besides the Reflection High-Energy Electron Diffraction (RHEED) that is the main technique to control dynamically the growth process (described in the next section), there are other important techniques that can be applied in-growth (during the growth) in the MBE. Some examples of these techniques are: ellipsometry, reflectance anisotropy, laser interferometry and Raman spectroscopy. Other in-situ but post-growth techniques (applied inside the MBE but after the growth) are: Auger Electron Spectroscopy (AES), for the determination of surface chemical composition; Secondary Ion Mass Spectroscopy (SIMS), for the determination of the chemical composition of the outermost atomic layers of the grown epilayer; X-ray Photoelectron spectroscopy (XPS) and Ultraviolet Photoelectron Spectroscopy (UPS), for the study of the electronic structure and energy of the film; Scanning Electron Microscopy (SEM) and Atomic Force Microscopy (AFM), for surface topography of the grown epilayer. In our system only RHEED is utilized to characterized in situ the growth of the epilayers.

2.2.1.1 Reflection High-Energy Electron Diffraction (RHEED)

Reflection High-Energy Electron Diffraction (RHEED)[16, 17] is a highly suitable technique to monitor the surface characteristics during the substrate deoxidation and epilayer growth. In the RHEED, electrons with energies 10-100 keV are generated by an electron gun. They will reach the sample surface with a very small (glancing) angle (~1º). Calculating the de Broglie wavelength of the electrons using a mathematical approximation[32] for these conditions, a range of 0.12-0.037 Å is obtained, which insures that the penetration of the beam into the surface is low and restricted to the outermost few atomic layers[33]. As it is shown, even though the electrons have high energy (~ 10 keV, in normal RHEED operation), the penetration depth is very small (0.12 Å for 10keV), which can be explained because of the only important component that influences the penetration is the normal component to the surface (low energy component, ~150 eV for electrons with an energy of 10 keV). Forward scattering geometry of RHEED, as shown in the Fig. 2.6, is the most appropriate configuration for MBE, since the electron beam can be placed at glancing incidence, whereas the molecular beams impinge almost normally on the substrate. The wavelength of the electrons is similar to the lattice constant of the material, resulting in a diffraction pattern that can be viewed on phosphor screen due to the fluorescence caused by the electrons. The RHEED pattern depends on the atomic arrangement, flatness of the surface and the crystalline orientation of the growth surface. Typical RHEED pattern for a disordered (amorphous) surface (for example before the deoxidization) is a diffuse pattern or rings due to the thin amorphous oxide layer on the surface, for a clean surface after deoxidization it is streaky lines or

ordered spots. RHEED is a technique that is not only sensitive to the cleanliness and smoothness of the surface, but also to the mode of growth that is occurring on the substrate (three dimensional, two dimensional or 0-dimensional) and to some extent, on the chemical nature of the surface. For the case of three dimensional ("rough") growth, as in the growth a strained thick layer or the growth of three-dimensional QDs, ordered spots are expected as the RHEED pattern, while for two dimensional growth ("flat", layer-by-layer growth), it is "rods" or "streaks". The typical surface reconstructions for As-rich (001) GaAs surfaces are dependent on how much excess of As is on the surface (2 X 4) or c(2 X 8) or c(4 X 4) [34,] . In contrast, for a Ga-rich (001) GaAs, the surface reconstructions are (4 X 2) or c(8 X 2). For the case of InGaAs on (001) InP substrate, surfaces reconstructions are, also respectively, (2 X 4) or (4 X 2) in As-rich or Ga-rich surfaces. Finally, for a Se-rich (001) ZnSe the typical pattern is (2 X 1) and for Zn-rich (001) ZnSe the pattern is c(2 X 2).[28]

Fundamentals of electron diffraction: Origin of the RHEED features

Applying the general Bragg law equation of diffraction in crystals (for details about the law, see section 2.2.2.3, "principles of X-ray diffraction") and the conditions for constructive interference of elastically scattered electrons that may be inferred using the Ewald construction in the reciprocal lattice (Fig. 2.6), interplanar distance (d_{hkl}) in the crystal lattice and atom arrangement in the solid can be inferred.

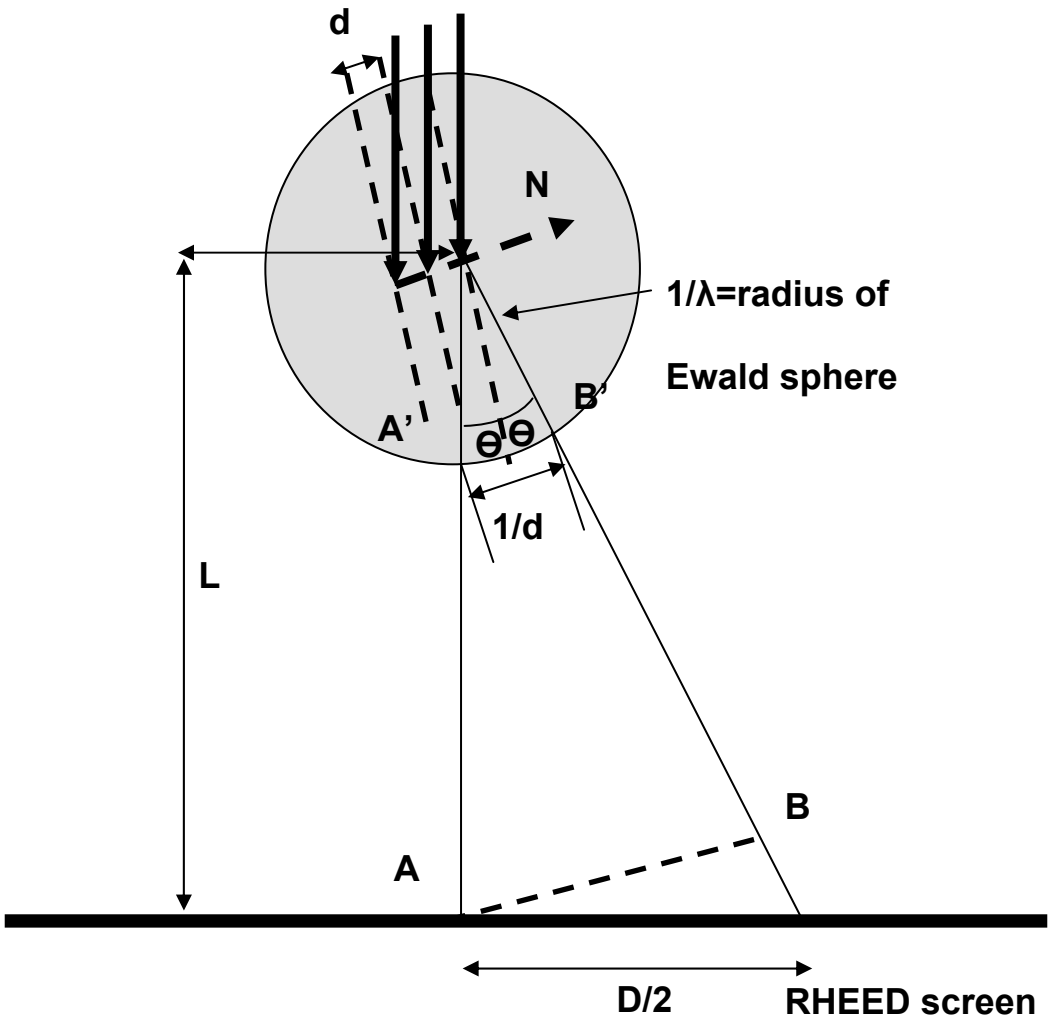

Figure 2.6. Illustration of the relationship between the real interplanar distance (d) of a crystal and its diffraction pattern representation in the RHEED screen (D/2).

Considering equation 2.1 (Bragg law) and geometry relationship of the angles represented in the Fig. 2.6, we can yield equation 2.3, which gives the correlation between the observed diffraction pattern in the RHEED and the interplanar distance (d_{hkl}). Measuring diffraction spot spacings (D/2) in the fluorescent screen of the RHEED, it will be possible to reconstruct the surface crystal structure of the solid.

$$n\lambda = 2d_{hkl}\sin\theta \qquad (2.1)$$

$$\frac{1}{d_{hkl}} = 2\left(\frac{1}{\lambda}\right)\sin\theta \qquad (2.2)$$

$$\frac{\frac{D}{2}}{\frac{1}{d_{hkl}}} = \left(\frac{\frac{L}{1}}{\frac{1}{\lambda}} \right) \text{ or } \quad d_{hkl} = \frac{2\lambda L}{D} \quad (2.3)$$

L= the distance between the sample and the fluorescent screen

D= 2 x distance between the diffraction spots and the center of the screen.

Θ=Bragg angle

d_{hkl}: spacing of lattice planes with Miller indices (hkl).

Considering that the magnitude of the reciprocal lattice vector for a cubic crystal (vector that represents the point (h, k, l) in the reciprocal space, i.e., $G = h\left(\frac{1}{a}\right) + k\left(\frac{1}{b}\right) + l\left(\frac{1}{c}\right)$), the lattice constant *a of* the cubic crystal can be obtained (equation 2.4).

$$d_{hkl} = \sqrt{\left(\frac{h}{a}\right)^2 + \left(\frac{k}{a}\right)^2 + \left(\frac{l}{a}\right)^2} \text{ or } \quad d_{hkl} = a / \sqrt{h^2 + k^2 + l^2} \quad (2.4)$$

where h, k, l are the Miller indices

In the case of a two dimensional growth (layer by layer), the interaction of the electron beam is essentially with a two-dimensional atomic net so the third dimension in real space is missing, and therefore the third dimension in the reciprocal space is not defined. Consequently, the surface is represented in the reciprocal space by rods in a direction normal to the real surface. To explain the observation of streaking lines instead of rods, we should consider that in the case of electron diffraction, the radius of the Ewald sphere is very much larger than the separation of the rods. Using the approximation in the reference 20 for electrons with energy of 10 KeV (normal conditions for the use of the RHEED), the radius of Ewald sphere is $1/\lambda = 8.3$ Å^{-1}. If the surface lattice net has a lattice constant *a* of 5.869 Å (unconstructed InP), then the distance between adjacent rods in the reciprocal space $2\pi/a$ will be 1.07 Å. As a

result, the intersection of the sphere and rods occurs some way along their length, resulting in a streaked rather than a spotty, diffraction pattern for a two dimensional growth. In the case of a three-dimensional ordered growth, the third dimension in the reciprocal space is defined and consequently, spots will be observed in the fluorescent screen of the RHEED.

2.2.2. *Ex situ* Characterization

After the removal of the samples from the MBE system, the quality and properties (structural, electrical and optical) of the epilayer will be determined using different techniques. The thickness of the epilayer and its growth rate were found by determination of the thickness using an optical microscope or based on X-ray measurements. The electronic structure of the material was studied by steady state PL. The crystalline quality and lattice-mismatch were measured by single crystal x-ray diffraction and double crystal x-ray diffraction. Surface topography, height and lateral size and the density of QDs was measured by AFM. Doping level and hall mobility of the doped layers were determined by Hall Effect and electrical capacitance voltage (C-V) measurements. Metal contacts (gold contacts) for doped layers or devices structures were fabricated by a vapor deposition technique. An alpha step profiler is used to determine the thickness of the contact deposited. Current-voltage (I-V) measurements were performed to characterize the electric properties of LEDs structures. We have done studies on QDs samples based on Raman scattering, surface enhanced Raman spectroscopy, elipsometry, reflectance, absorbance and time-resolved PL measurements.

2.2.2.1 Determination of Epilayer Thickness by Using a Radial Sectioning Instrument

A 2015 Radial Sectioning Instrument, which has a spindle to groove the surface of the crystal, was used in our lab to determine the thickness of the samples. To obtain accurate results, the spindle forms a very low angle section permitting the magnification of the layer 100-400 times using an optical microscope. A photograph of the groove is taken under the microscope (see Fig. 2.7 and Fig. 2.8). From the photograph, two different widths: outer (W_1 or W_1') and inner (W_2 or W_2') widths are determined. Figure 2.7 shows a drawing of the cross section of a groove, where R is the radius of the spindle, W_1 is the width of the cylindrical section, W_2 is the width of the section at the level of the layer interface (III-V/II-VI interface in our case) and X_t is the thickness of the epilayer. Mathematically, the layer thickness, X_t, is given by the difference in the heights of two triangles with common radius, R, as the hypotenuse (equation 2.5). This process is repeated twice and the average of these two values is calculated (see Fig. 2.8).

$$X_t = \left[R^2 - \left(\frac{W_2}{2} \right)^2 \right]^{1/2} - \left[R^2 - \left(\frac{W_1}{2} \right)^2 \right]^{1/2} \qquad (2.5)$$

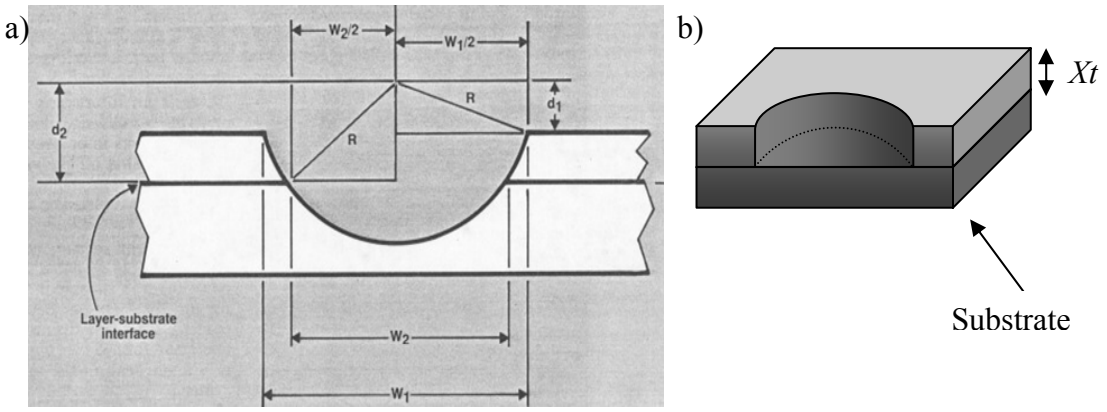

Figure 2.7. a) Schematic of thickness determination. b) Cross section drawing of a "grooved" sample.

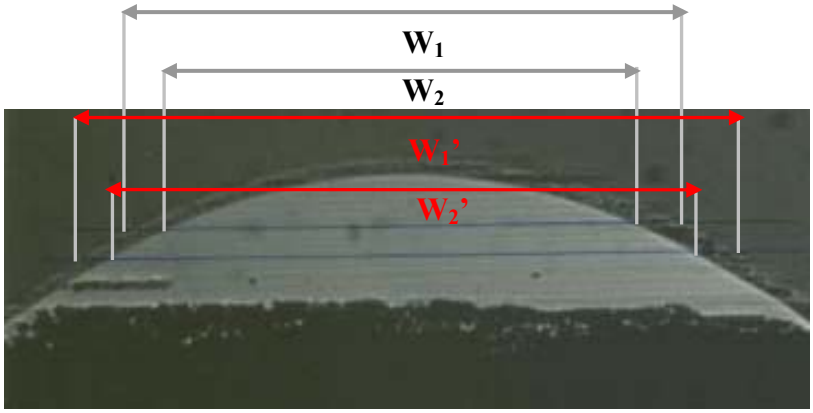

Figure 2.8. Experimental determination of thickness for a sample ZnCdMgSe grown on InP. Top view of a "grooved" sample. The photograph was taken under a 100 times-optical microscope magnification. Average thickness= 0.84 ± 0.01µm.

Bellow, the accuracy of this method is evaluated.

The radius of the spindle is 19 mm, which is much larger than the values of W_1 and W_2 (on the order of a few hundred µm), so X_t can be expressed as:

$$X_t = R\left\{\left[1-\left(\frac{W_2}{2R}\right)^2\right]^{1/2} - \left[1-\left(\frac{W_1}{2R}\right)^2\right]^{1/2}\right\} \approx R\left\{\left[1-\frac{1}{2}\left(\frac{W_2}{2R}\right)^2\right]^2 - \left[1-\frac{1}{2}\left(\frac{W_1}{2R}\right)^2\right]^2\right\} = \left[\frac{1}{8R}\right]\left(W_1^2 - W_2^2\right) \quad (2.6)$$

Then the derivative (or small change) of *Xt* will be:

$$dX_t = \left(\frac{1}{4R}\right)\left(W_1 dW_1 - W_2 dW_2\right) \quad (2.7)$$

where dW_1 and dW_2 are the derivatives or small changes of W_1 and W_2.

When $dW_1 = -dW_2 = dW$, dX_t, will be maximum:

$$\left[dX_t\right]_{\max} = \left(\frac{1}{4R}\right)\left(W_1 - W_2\right)dW \quad (2.8)$$

Divided both sides by *Xt* in the equation 2.8:

$$\left[\frac{dX_t}{X_t}\right]_{\max} = \left(\frac{2}{\left(W_1 - W_2\right)}\right)dW \quad (2.9)$$

From this expression, it can be concluded that in order to reduce $\left[\frac{dX_t}{X_t}\right]_{\max}$, $(W_1 - W_2)$ should be large and dW should be small. Therefore, the time for grooving should be optimal to get maximum $(W_1 - W_2)$. Generally, for a sample with an epilayer of thickness of ~1μm, the $(W_1 - W_2)$ is ~100 μm and the error to measure W_1 and W_2 on the picture amplification of 100 is ~0.05 cm, which means that dW is ~5 μm, and $\left[\frac{dX_t}{X_t}\right]_{\max}$ is about 0.1, meaning that the error is ~10%.

Therefore, the determination of the thickness using this method is approximate, and it was only used to determine thickness in thick (bulk) layers. For

the case of more accurate thickness measurement, a reference superlattice was grown and the superlattice period was obtained from the positions of the satellites peaks in the X-ray spectrum (see more details in section 2.2.2.3).

2.2.2.2. Photoluminescence

In general way, photoluminescence (or light emission process) can be defined as an optical excitation in which photons are absorbed by the semiconductor, creating electron-hole pairs that, afterward, will recombine emitting photons.[35] This technique is commonly used in a MBE lab, not only for the possibility to characterize the most fundamental optical properties of the grown materials, such as band gap, donor and/or acceptor states, deep defect levels, the quality and the band structure of epilayers, but also for the flexibility of its setup geometry. In addition, for the PL excitation it is not necessary to fabricate a contact or a junction (as electroluminescence), making PL an interesting method to characterize materials and devices in early stages of development and growth. Besides these advantages, there are others that made this technique a useful tool in a semiconductor lab. Some of them are:

(i). It is a non-destructive technique where only small quantities of material are needed.

(ii). It provides information mainly on minority carrier properties and, thus, it is complementary to electrical characterization techniques. The lifetime, the diffusion length, the quantum efficiency could be inferred through the study of the recombination paths. When the photogenerated e-h pair density is larger than the free carrier concentration (high excitation conditions), majority carrier properties are also accessible;

(iii). It is an easy technique, because it does not require particular sample handling and preparation. The experimental set-up complexity is proportional to the needs: for fast characterization a very simple and inexpensive apparatus is adequate[19];

(iv). It is sensitive to the chemical species of impurities which can be detected even at very low densities;

(v). It is an optical spectroscopic technique, i.e., it gives energetically resolved information.

Figure 2.9 represents schematically the steps that are involved in a general PL process. There are three different processes represented: 1.The e-h pair excitation, 2. The e-h pair thermalization and diffusion, 3. The e-h recombination. Initially, the e-h pairs are photoexcited to a non-equilibrium state by absorption of light (generally, generated by a laser). Then, they diffuse and relax into a quasiequilibrium distribution to the lowest energy state (non-radiative process) and finally, they recombine, emitting photons, or by other, non-radiative processes.

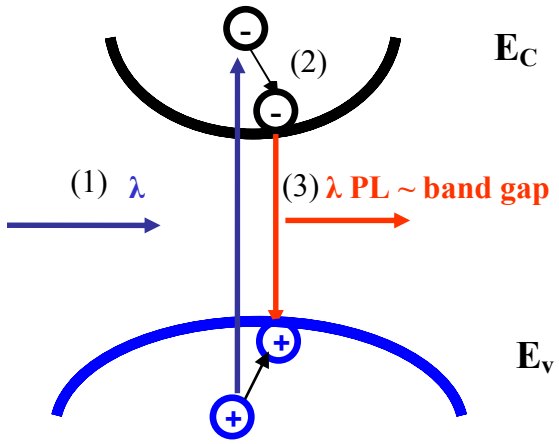

Figure 2.9. General steps involved in a PL experiment.

Therefore, PL intensity depends on the competition between the radiative recombination and the non-radiative recombination processes both affecting in the overall recombination process after photoexcitation. This competition is reflected in the quantum efficiency parameter which is defined as $\eta = \frac{\tau}{\tau_{nr}}$ where $\frac{1}{\tau} = \frac{1}{\tau_r} + \frac{1}{\tau_{nr}}$, where τ is the total lifetime, τ_{nr} is the non-radiative lifetime, and τ_r is the radiative lifetime.

The main non radiative processes are: Auger effect, surface recombination, recombination through defects or inclusions and multiple-photon emission.

Among the radiative transitions involved in luminescence emission, we must emphasize those that occur at or near the band edges: excitonic recombination, conduction band (C) to valence band (V) transitions (or C-V transitions), transition between a band (conduction or valence band) and an impurity level, and donor-acceptor transitions (or D-A transitions). Bellow, a brief summary of the fundamental transitions and their description are given. The Fig. 2.10 shows a schematic diagram of the energy involved in each transition.

1. Excitonic Recombination

An excitonic transition is the result of the recombination of electrons and holes that, previously, were paired off into excitons by a radiation with the laser. This transition usually results in a narrow spectral line in the PL spectrum. There two types of excitonic transitions: free exciton (E), implying a pure excitonic transition, and

bound exciton (BE) in the presence of impurities in the crystal, whose emission is characterized by a narrow spectral width at a lower photon energy than that of the free exciton. The energy involved in these two transitions are shown in the equations 2.10 (free exciton) and 2.11 (bound exciton).

$$h\nu_E = Eg - E_x \qquad (2.10)$$

$$h\nu_{BE} = E_g - E_x - E_p \qquad (2.11)$$

2. Conduction Band to Valence Band Transitions (C—V)

The conduction band to valence band transitions (C-V) are transitions produced by the recombination of free carriers that are localized in different bands (band-to-band). These free carriers are excited electron-hole pairs that remain as free carriers occupying band states instead forming an excitonic entity These transitions dominate at temperatures such as $kT>E_x$, and also in less pure or in imperfect crystals, where local fields tend to break up excitons into free carriers.

$$h\nu_{C-V} = E_g \qquad (2.12)$$

3. Transition Between a Band and an Impurity Level

Within the transitions between a band and an impurity level, we can highlight three categories of transitions based on the levels that are involved: shallow transitions, deep transitions or transitions to deep levels. Shallow transitions occur between the bands and the impurities levels, neutralizing ionized donors or acceptors

when they are taking place. They are expected to be radiative in the far infrared even though their probability of occurrence is not very high. Two types of shallow transitions can be distinguished: from the conduction band to the donor level (C-D) or from the acceptor level to the valence band level (A-V). Equation 2.13 and 2.14 represent the emitted energies of these transitions.

$$h\nu_{C-D} = E_D \qquad (2.13)$$

$$h\nu_{A-V} = E_A \qquad (2.14)$$

A deep transition is either transition between an electron from the conduction band to an acceptor state (C-A) or a transition from a donor state to the valence band (D-V). Equation 2.15 and 2.16 show the corresponding energies for C-A and D-V transitions.

$$h\nu_{C-A} = Eg - E_A \qquad (2.15)$$

$$h\nu_{D-V} = Eg - E_D \qquad (2.16)$$

Transitions to deep levels occur in crystals doped with impurities that have large ionization energies, and therefore form deep levels in the gap. Hence, these transitions can be from a deep donor (DD) to the valence band, symbolized by DD-V, or from the conduction band to a deep acceptor (DA), denoted by C-DA. They are usually characterized by a broad PL peak and an intensity dependent of the impurity concentration. Sometimes, they can be associated with defects, for example the donor-Ga-vacancy complex in GaAs forms a deep level, or band levels, which gives a broad emission at about 1.20 eV. PL energies emitted in DD-V and C-DA transitions are represented by the following equations:

$$h\nu_{DD-V} = Eg - E_{DD} \qquad (2.17)$$

$$h\nu_{C-DA} = Eg - E_{DA} \qquad (2.18)$$

4. Donor-to-Acceptor Transitions (D—A)

Donor-to-acceptor transitions are present in semiconductor that have both donor and acceptor impurities. When this happens, a coulomb interaction $\left(\frac{q^2}{\varepsilon r}\right)$ between the donor and acceptor is involved, which will modify their binding energies compared with the binding energy of an isolated-impurity case. The energy involved is:

$$h\nu_{DA} = E_g - E_A - E_D + \frac{q^2}{\varepsilon r} \qquad (2.19)$$

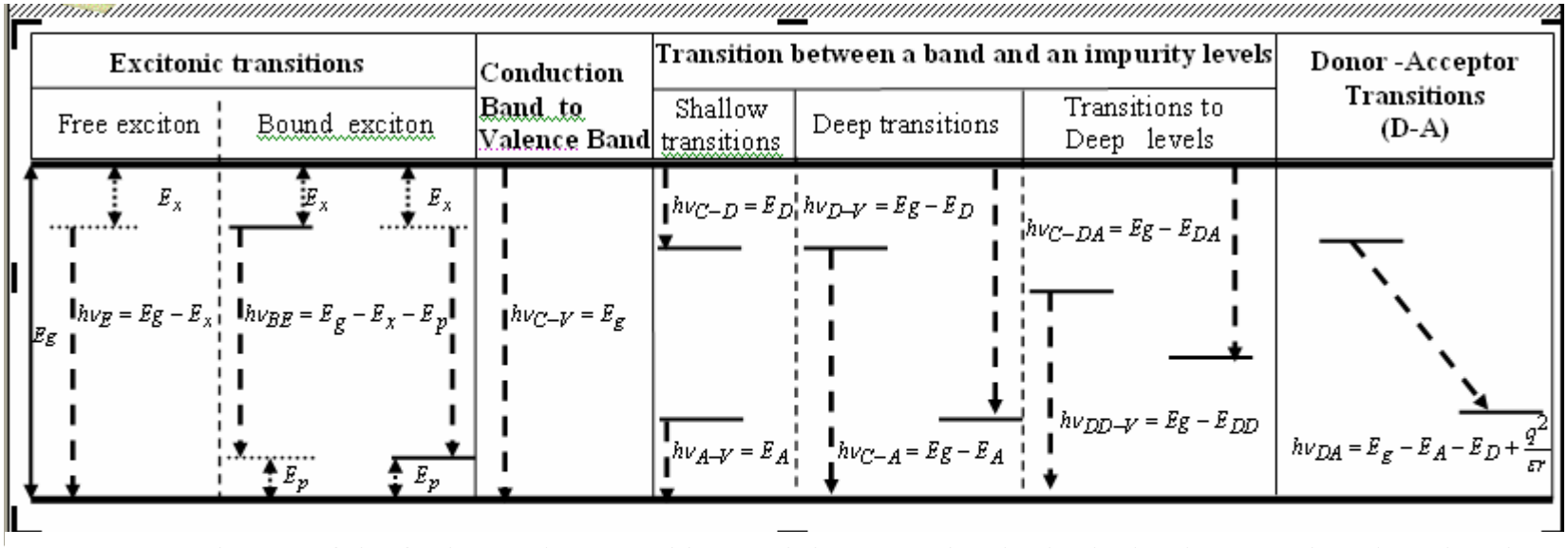

Figure 2.10. Diagram of the fundamental PL transitions and the energy involved. The band gap, exciton, bound exciton, conduction band, valence band, donor level, acceptor level, deep donor and deep acceptor are represented, respectively, by the symbols Eg, E, BE, C, V, D, A, DD and DA.

Through the analysis of the luminescence spectrum as a function of different parameters (temperature, excitation energy, excitation intensity, external fields, polarization etc.), more information can be obtained, such as material quality, type of transitions involved, and structural and electronic information. In the Chapter 5, polarized PL and power dependence PL data will be shown.

Steady State Photoluminescence (PL) Experimental Setup

The schematic of the steady state PL system is shown in Fig. 2.11. The samples are mounted on the cold finger of a Janis cryostat. The system is pumped to 10^{-5} Torr. The measurements are usually made at 77K by cooling down the finger with liquid nitrogen. Cooling to liquid He temperatures (5.8 K) can also be accomplished. The temperature of the cold finger can be controlled from 5.8 K to 300K, using a heater installed on the back of the cold finger. The exciting light of a He-Cd laser (325nm) passes through a chopper, changing the dc laser light to an ac signal, which is necessary because of the type of signal amplifier used in this setup (lock-in amplifier). Then, the light and is focused to a small spot on a sample by using several lenses. The luminescence of the light is collected by a lens and converted to a collimated beam, which is focused on a spot on the front slit of the spectrometer (SPEX 1680-B). The light that passes through the spectrometer is detected by a photomultiplier and converted to an electrical signal that is fed to lock-in amplifier to be amplified. Finally, this amplified signal is inputted into a databox (DataScan) connected to a computer to collect and produce the spectrum. An example of a PL

spectrum for ZnCdSe quantum wells with barriers of ZnCdMgSe grown on InP is given in the Fig. 2.12 for two different temperatures. At 77 K, the figure shows two peaks, one peak is assigned to the electron-hole recombination in the barrier (labeled ”barrier” in the Fig. 2.12) and other, corresponds to the recombination of the carriers in the QW, which is stronger than the barrier (bulk) due to the one dimensional confinement effect. At room temperature, only the quantum well peak is noted. This is expected because the electron kinetic energy is higher at 300 K than at 77 K and electrons will diffuse faster to the QW at this temperature. These transitions are represented schematically in figure 2.13. Figure 2.14 represents the layers structure of the same sample, which was grown by MBE in our lab.

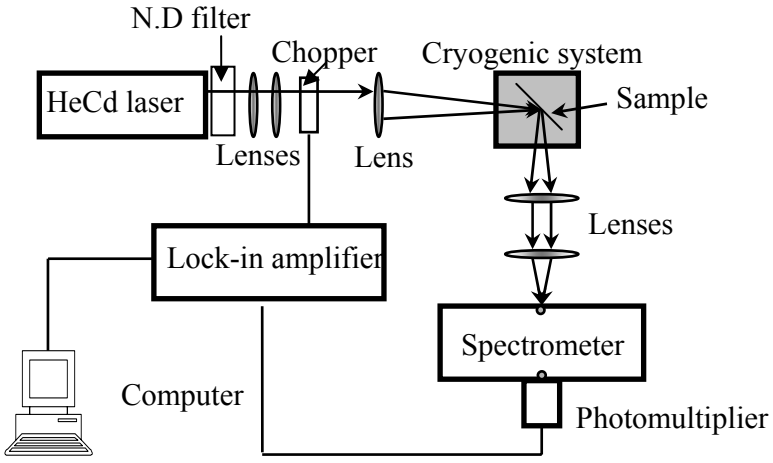

Figure 2.11. Schematic of the steady state PL setup.

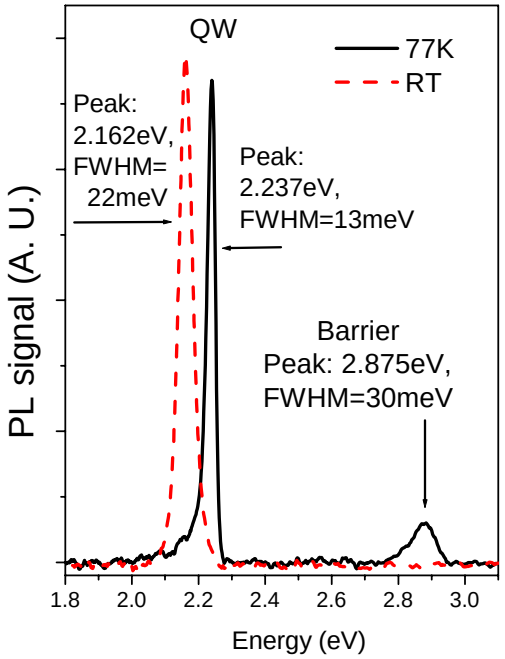

Figure 2.12. Photoluminescence spectrum of ZnCdSe quantum wells with barriers of ZnCdMgSe grown on InP at room temperature and 77 K.

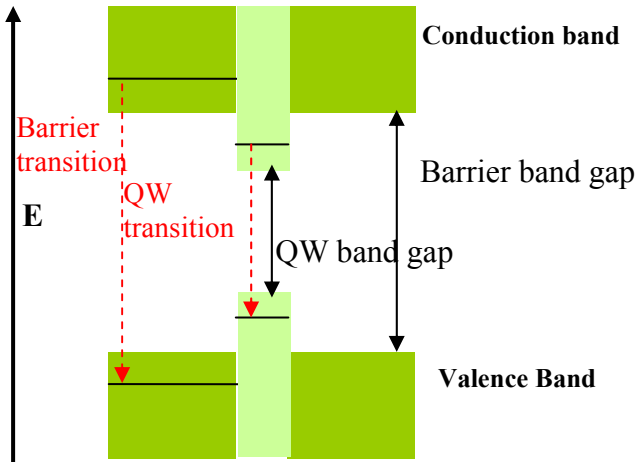

Figure 2.13. Schematic of transitions produced in Fig. 2.14. Barrier and QW peaks are the transitions produced between levels in the barrier and QW respectively.

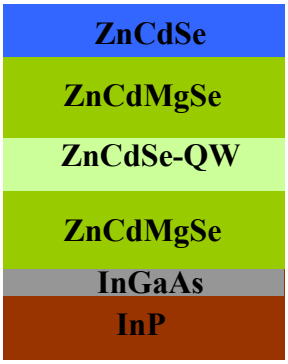

Figure 2.14. Schematic of layer structure of the sample shown in Fig 2.14.

Power dependence PL studies

The excitation density of the He-Cd laser that is focused on the sample during the PL measurements can be changed using different neutral density filters (NDFs) placed between the lenses and the laser (see Fig. 2.11). The rest of the setup parameters in the power dependence studies were kept constant (integration time, sensitivity, filters of lock-in amplifier; sample position, lenses' location and slit apertures of the monochromator).

Linearly polarized photoluminescence

Linearly polarized PL was used to determine the polarization of the light emitted by the QDs. Polarization of the light was obtained using a UV-Glen-Thompson polarizer between the laser and the first lens. Polarization of the light was inverted just by a 90° rotation of the polarizer. Two types of experiments were performed: one in the edge configuration and the other in the surface configuration. By edge configuration we mean that the sample is excited on the edge (Fig. 2.15 a), while in surface configuration (Fig. 2.15 b) the sample was excited on the surface (using the usual angle of sample configuration in the PL setup, i.e. 45° with respect to the laser incident light). Due to the fact that some excitation light is lost in this configuration, (approximately half) the two configuration measurements can not be compared directly to each other in absolute values. Comparison can be established within the same configuration between different polarizations of the light.

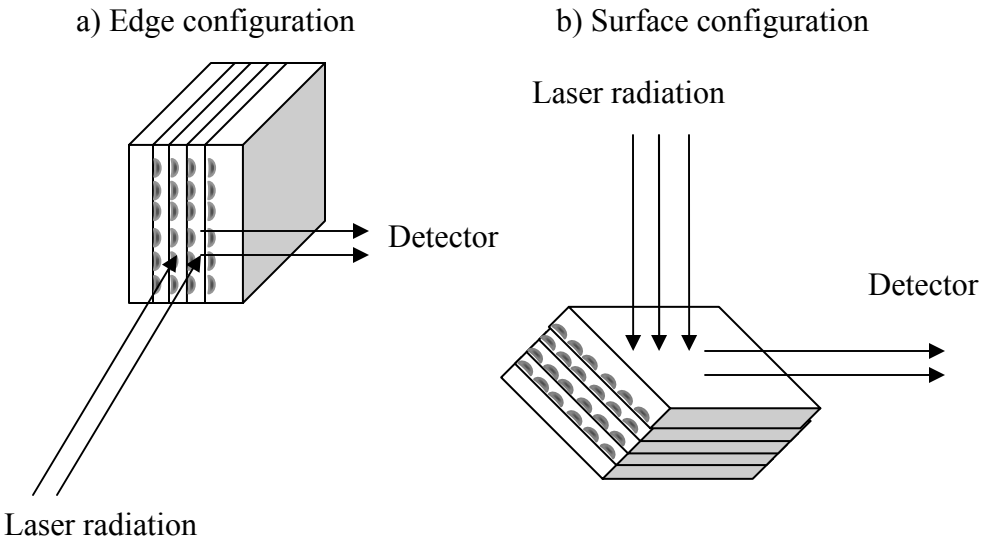

Figure 2.15. Sample configurations for linearly polarized photoluminescence measurements.

Time-Resolved Photoluminescence Experimental Setup

Time-Resolved photoluminescence (TRPL) spectroscopy is a very powerful technique for the investigation of carrier dynamics in low-dimensional semiconductor structures. In TRPL, electron-hole pairs are excited by a short pulse of light, and then the decay of the PL intensity is observed as a function of time. From fitting of the decay curves, value of the lifetime τ can be evaluated. Figure 2.16 is a schematic diagram of TRPL measurement setup. TRPL measurements were carried out using the second harmonic (400 nm) of a Ti: sapphire laser light with a wavelength emission of 800 nm (pulse width=100 fs, repetition rate=60 MHz). The second harmonic of the laser light was generated by passing the laser light through a frequency doubling crystal (KTP crystal). The filter 1 ensured that the light from Ti:

sapphire laser would not reach the sample and that only the light with a wavelenght of 400 nm striked in the sample. After the filter, the light was focused on the sample using a mirror. The luminescence of the light was collected by lenses and converted to a collimated beam. The spectrally integrated emission of the sample was obtained by using a streak camera with a time resolution of 10 fs. The data was recorded into the computer, which is connected to the streak camera. Filter 2 ensured that the excitation light (400 nm) would not arrive at the streak camera.

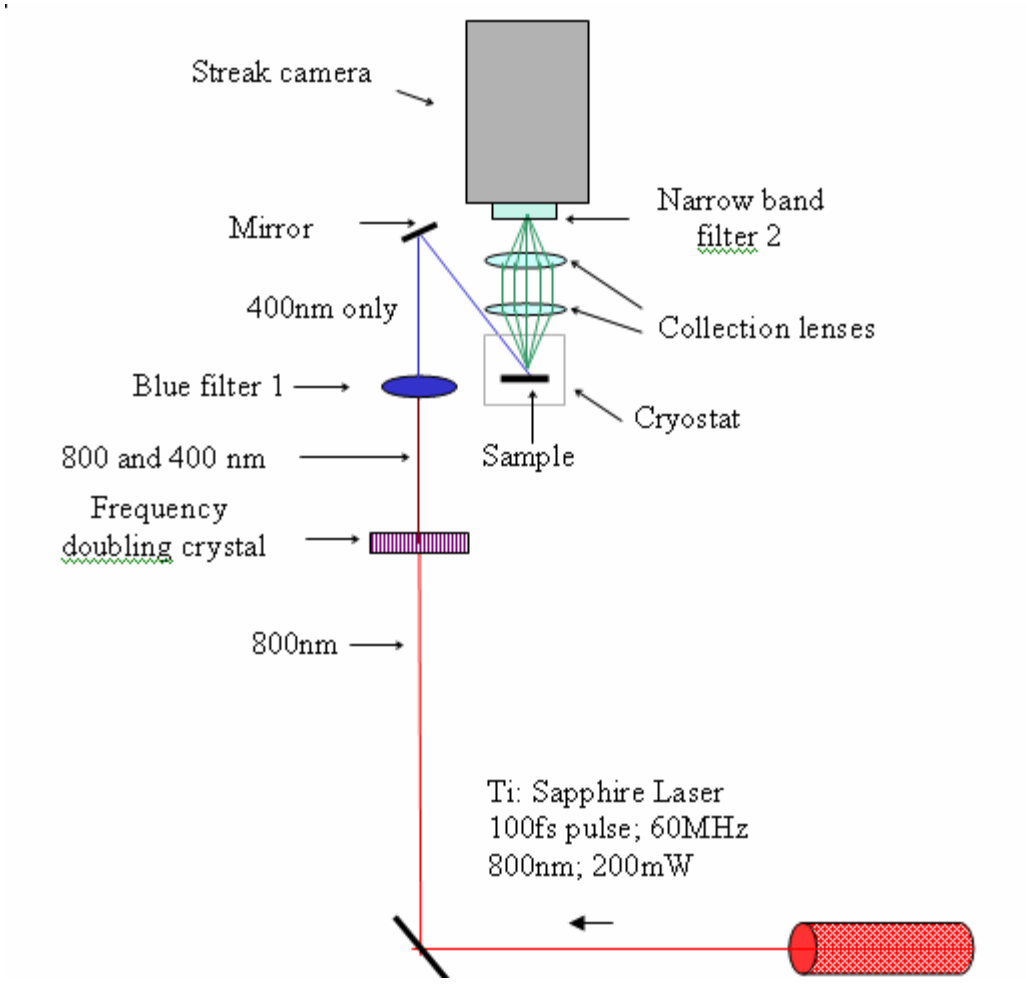

Figure 2.16. Schematic of the time-resolved PL setup.

Temperature dependence measurements can be also carried out if the sample is placed on a cold finger or cryostat. As described in the steady state PL

measurements, the cold finger can be filled with liquid nitrogen (77 K) and its temperature can be controlled using a heater installed on its back.

2.2.2.3. X-ray Diffraction

X-ray diffraction is an important technique[21] used to characterize semiconductor materials. It can give information about the lattice constant, the crystal structure, the quality (dislocation content, inhomogeneities, misorientation, mosaico spread), curvature, thickness and the strain in the layer (relaxation and mismatch).[36] A representation of our x-ray diffraction system is shown in Fig. 2.17. It consists of an x-ray source, a single crystal x-ray diffraction (SCXRD) system shown on the right manufactured by RIGAKU and a double crystal x-ray diffraction (DCXRD) system shown on the left manufactured by Blake Industries, Inc. X-ray radiation is produced in the X-ray vacuum tube when a high energy electrons, generated in a tungsten filament, are bombarded with high speed to an atomic target (copper metal). The SCXRD and DCXRD setups have different goniometers (X-ray detectors) but both use the sais double that of the peak corresponding to Cu $K_{\alpha 2.}$ Two electromagnetic shutters, labeled 1 and 2, permit respectively, the access of the X-ray beam to the double or single crystal setup (both measurements, SCXRD and DCXRD, can be used simultaneously if both shutters are opened). In the Fig. 2.17, the solid arrows represent the path followed by the X-ray beam in the double crystal setup while dashed arrows indicated the path in the single crystal setup. The incident angle (angle formed between the beam and the sample) is "ω". The angle formed between the goniometer and the incident beam is "2Θ". The sample is placed on a holder that is mobile, permitting with its rotation the change of incident angle "ω". Rotation of

goniometer will change the angle "2Θ". In SCXRD measurement, the sample (ω) and the goniometer (2Θ) are rotated simultaneously while in DCXRD measurement only the sample is rotated (ω). This measurement is usually called "rocking curve" since in this type of x-ray diffraction (the goniometer and Ge crystal are fixed). The DCXRD spectrum shows only $K_{\alpha 1}$ since the incident x-ray is "filtered" by a Ge crystal, labeled as "first crystal" in the Fig. 2.17, and then the radiation passes through a slit before the arrival to the sample (second crystal). In this way, the X-ray that reaches to the sample is almost monochromatic.

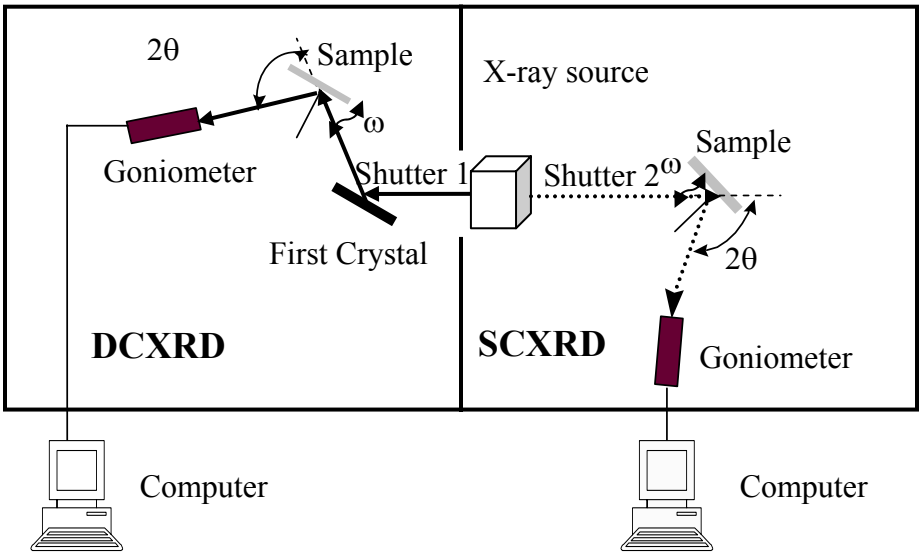

Figure 2.17. X-ray diffraction setup. Double crystal X-ray diffraction (DCXRD) and single crystal X-ray diffraction (SCXRD) are illustrated, respectively, in the left and right sides of the figure. Shutters, labeled 1 and 2, permit, respectively, the control of the path of the X-ray beam to DCXRD (solid arrows) or SCXRD (dashed arrows) setups.

Single crystal X-ray diffraction (SCXRD)

In SCXRD, only one crystal (the sample) is used, so the incident x-ray is not monochromatic. Therefore, the incident x-ray beam contains both Cu $K_{\alpha 1}$ and Cu $K_{\alpha 2}$ lines. In the diffraction, each layer has two peaks corresponding to Cu $K_{\alpha 1}$ and Cu $K_{\alpha 2}$. Because the beam has a broad band of wavelengths, the resultant diffraction peaks of the sample are usually broad. In SCXRD, we usually use "$\theta - 2\theta$ coupled" mode, which means that the ω and 2θ are moving simultaneously and ω is always half of 2θ, i.e. θ. In the practice, the complete removal of the indium from the back of the sample is very difficult. Heating up in the hot plate, indium that bonds sample to the block is melted permitting their separation, but sometimes some indium remains on the back of the sample. Therefore, when an X-ray measurement is performed, it is difficult to mount the sample exactly parallel to the sample holder. Hence, in order to make sure the ω and 2θ are coupled, we first fix the 2θ and rotate the ω using "only θ mode", find the ω value corresponding to the peak of the sample and then, adjust the θ value in the computer to make sure the θ value of the computer corresponds to the peak value found, which means the ω and 2θ are coupled. Afterward, we set the scan mode as the "$\theta - 2\theta$ coupled mode" to measure the diffraction. In general, for a sample, four diffraction peaks are observed, two from the substrate ($K_{\alpha 1,\ substrate}$ and $K_{\alpha 2,\ substrate}$) and two from the epilayer ($K_{\alpha 1,\ epilayer}$ and $K_{\alpha 2,\ epilayer}$). If the sample is matched or nearly matched, the peaks of the epilayer could be very close to the peaks of the substrate and sometimes, it is not possible to distinguish them (two peaks in the spectrum) or one of them (three peaks in the spectrum). In that case, DCXRD must be used to analyze the accurate lattice mismatch of these samples.

The SCXRD gives information about lattice constant, mismatch of semiconductor materials, crystal structure, and a rough indication of crystalline quality.

Double crystal X-ray diffraction (DCXRD)

In DCXRD, a first crystal [(100) Ge in our system] is used to separate the various wavelengths of the incident x-ray beam in order to narrow the x-ray band of wavelengths before the x-ray beam reaches the sample. Hence, the incident beam on the sample is highly monochromatic. The sample is the second crystal. In DCXRD, a "rocking curve" is usually measured, that is, the 2θ is fixed and the ω is varied around θ. The DCXRD is used to obtain more resolution in the measurement of the crystal parameters, in particular it can give a more accurate assessment of the crystalline quality and of the material composition of high quality epilayers.[22] This technique is particularly useful for epitaxial layers grown on a thick substrate. In general, for such cases, two diffraction peaks are observed, one from the substrate and one from the epilayer. From the full width at half maximum (FWHM), we can evaluate the material quality. From the peak separation, we can obtain information about the lattice-mismatch.

Principles of X-ray diffraction

The principle of the X-ray diffraction is the same than the case of electron diffraction (see section 2.2.1.1). The only difference is that the Ewald sphere for X-ray diffraction will be smaller than in the case of electron diffraction. Both measurements, X-ray and RHEED, are based on Bragg's law (equation 2.1). When Bragg's law is satisfied, the scattered X-rays will interfere constructively and the X-

ray diffraction peak will form. The Fig. 2.18 represents two x-rays beams, labeled 1 and 2. If these beams reflect from atomic planes that are a distance d_{hkl} apart, they will be in phase (interfere constructively and therefore not be extinguished) only if the distance traveled by beam 2 is an integral number of wavelengths greater than the distance traveled by beam 1. In the figure, *AB = BC*, *sin Θ = AB/d*, therefore *AB =d sinΘ*. If *n* is an integer and λ is the wavelength of the X-rays, *2d sinΘ (AB + BC)* must be equal nλ for reflection to take place. If a similar plane of atoms is added (dashed plane), just halfway between these two, the extra path length to it will be just half of ABC, the reflected beam will therefore be just out of phase with beam 1 and will cancel it (interfered destructively).

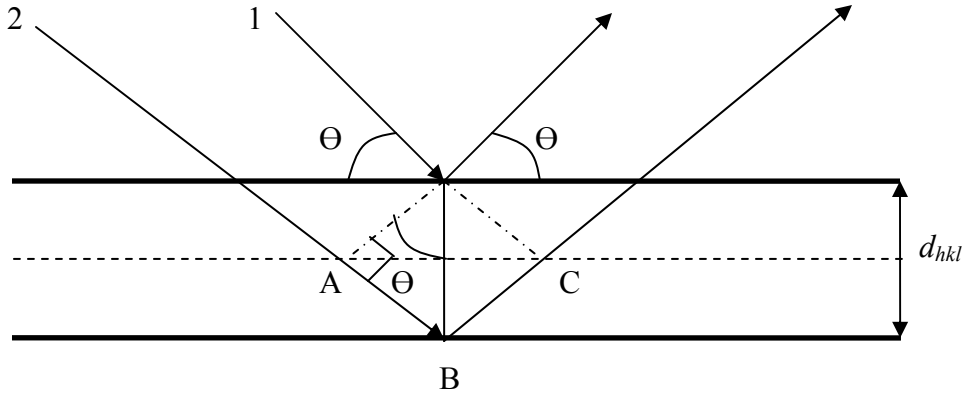

Figure 2.18. Principle of X-ray diffraction: The Bragg's law.

Determination of lattice constant

Lattice constant can be also calculated using equations 2.1 and 2.4 where a, θ, d_{hkl} and h, k, l, Miller indices, have the same meaning as in the section 2.2.1.1 and λ is the wavelength of incident X-ray.

Determination of crystal composition

If there is not a crystallographic phase change with the composition, the lattice constant of the ternary and quaternary alloys can be expressed by Vegard's law[37]. This law states that there is a linear dependence between the alloy composition and the lattice constant.

For the case of a ternary alloy, the relationship is simple:

$$a(A_{1-x}B_xC) = (1-x)\,a_1(AC) + xa_2(BC) \quad (2.20)$$

where a_1 and a_2 are, respectively, the lattice constant of the binaries AC and BC that form the ternary alloy. Therefore, if there is known the Θ of the epilayer by the X-ray diffraction, applying the equation 2.1 and 2.4, we can know the lattice constant and then, the composition of the epilayer using equation 2.20.

For the case of a quaternary alloy (double substituted cation), the situation is more complex since there are two unknown x and y and another equation is needed.

$$a(A_xB_yC_{1-x-y}D) = xa_1(AD) + ya_2(BD) + (1-x-y)a_3(CD) \quad (2.21)$$

where a_1, a_2, a_3 are, respectively, the lattice constants of the binaries AD, BD and CD that form the quaternary $A_xB_yC_{1-x-y}D$

For example, the lattice constant of the $Zn_xCd_yMg_{1-x-y}Se$ quaternary alloy can be expressed using the lattice constants of the binary systems: ZnSe (5.668Å), CdSe (6.050Å) and MgSe (5.890Å) so a for $Zn_xCd_yMg_{1-x-y}Se$ can be expressed as:

$$a(Zn_xCd_yMg_{1-x-y}Se) = 5.668x + 6.050y + 5.890(1-x-y) \quad (2.22)$$

To obtain the composition, it is necessary to have another equation where the composition is also an unknown. Band gap of quaternaries alloys do not follow a linear relationship with the composition (as the cited Vegard's law), but it can be

expressed in terms of composition by means of a quadratic experimental relation. A second degree equation can be used for the case of a ZnCdMgSe, where Eg and b represents, respectively, the band gap and the bowing factor of the material that is indicated on the subscript:

$$Eg^{Zn_xCd_yMg_{1-x-y}Se} = Eg_{MgSe} + \left(Eg_{ZnSe} - Eg_{MgSe} - b_{Zn_xMg_{1-x}Se}\right)x + \left(Eg_{CdSe} - Eg_{MgSe} - b_{Cd_yMg_{1-y}Se}\right)y + \left(b_{Zn_xMg_{1-x}Se} + b_{Cd_yMg_{1-y}Se} - b_{Zn_xCd_ySe}\right)xy + b_{Zn_xMg_{1-x}Se}x^2 + b_{Cd_yMg_{1-y}Se}y^2 \quad (2.23)$$

When x=0, the material is $Cd_yMg_{1-y}Se$ and the equation of its band gap is:

$$Eg^{Cd_yMg_{1-y}Se} = Eg_{MgSe} + \left(Eg_{CdSe} - Eg_{MgSe} - b_{Cd_yMg_{1-y}Se}\right)y + b_{Cd_yMg_{1-y}Se}y^2 \quad (2.24)$$

When y=0, the material is $Zn_xMg_{1-x}Se$ and the equation of its band gap is:

$$Eg^{Zn_xMg_{1-x}Se} = Eg_{MgSe} + \left(Eg_{ZnSe} - Eg_{MgSe} - b_{Zn_xMg_{1-x}Se}\right)x + b_{Zn_xMg_{1-x}Se}x^2 \quad (2.25)$$

Assuming the linear dependence of the band gap (i.e., bowing factors considered zero or negligible compared with the band gap values of the binaries), $b_{Cd_yMg_{1-y}Se} \approx 0$ and $b_{Zn_xMg_{1-x}Se} \approx 0$, we can obtain equation 2.26 for the quaternary and 2.27 and 2.28 for the ternaries:

$$Eg^{Zn_xCd_yMg_{1-x-y}Se} = Eg_{MgSe} + \left(Eg_{ZnSe} - Eg_{MgSe}\right)x + \left(Eg_{CdSe} - Eg_{MgSe}\right)y + \left(b_{Zn_xMg_{1-x}Se} + b_{Cd_yMg_{1-y}Se} - b_{Zn_xCd_ySe}\right)xy \quad (2.26)$$

$$Eg^{Cd_yMg_{1-y}Se} = Eg_{MgSe} + \left(Eg_{CdSe} - Eg_{MgSe}\right)y \quad (2.27)$$

$$Eg^{Zn_xMg_{1-x}Se} = Eg_{MgSe} + \left(Eg_{ZnSe} - Eg_{MgSe}\right)x \quad (2.28)$$

Using the values of the band gap of the binary systems at RT, Eg_{ZnSe}=2.70 eV, Eg_{CdSe}=1.66 eV and Eg_{MgSe}=4.0 eV of the reference, the equations become (the

equations can be also solved for other temperatures using the appropriate values of the band gap at the temperature of interest):

$$Eg^{Zn_xCd_yMg_{1-x-y}Se} = 4.0 - 1.3x - 2.34y + \left(b_{Zn_xMg_{1-x}Se} + b_{Cd_yMg_{1-y}Se} - b_{Zn_xCd_ySe}\right)xy$$

(2.29)

and $\beta = b_{Zn_xMg_{1-x}Se} + b_{Cd_yMg_{1-y}Se} - b_{Zn_xCd_ySe}$

when x+y=1, the material is Zn_xCd_ySe ternary. Considering that the Eg of this ternary is:

$$Eg^{Zn_xCd_{1-x}Se} = (1-x)Eg^{ZnSe} + xEg^{CdSe} - b_{ZnCdSe}x(1-x) \quad (2.30)$$

and doing the corresponding calculations, considering the average bowing parameter (0.33) given by reference 20, we obtain:

$$Eg^{Zn_xCd_{1-x}Se} = 2.70 - 1.37x + 0.33x^2 \quad (2.31)$$

Comparing both equations, $\beta = 0.33$ is deduced so the equation for the Eg of the quaternary at RT will be:

$$Eg^{Zn_xCd_yMg_{1-x-y}Se} = 4.0 - 1.3x - 2.34y - 0.33xy \quad (2.32)$$

Applying the relationship considered in reference[38] for $Zn_{1-x}Cd_xSe$ alloy, it is possible to obtain also the Eg of the quaternary at 10K as appears in the reference 39 .

$$Eg^{Zn_xCd_yMg_{1-x-y}Se} = 3.65 - 0.83x - 1.87y - 0.35xy \quad (2.33)$$

Once $Eg^{Zn_xCd_yMg_{1-x-y}Se}$ is known at one of these temperatures, equation 2.32 for RT or equation 2.33 for 10K, and $a(Zn_xCd_yMg_{1-x-y}Se)$ of the epilayer (equation 2.21), composition of the quaternary (x and y) can be achieved just solving this system of two equations.

It should be noted that even though the PL of the samples was measured at 77 K and not at 10 K, this equation could be applied as a useful approximation. The variation of the band gap with the temperature between 10 K and 77 K is about 15 meV and therefore, the error introduced by inputting the band gap at 77K, $Eg_{77K}^{Zn_xCd_yMg_{1-x-y}Se}$, instead of the one at 10K, $Eg_{10K}^{Zn_xCd_yMg_{1-x-y}Se}$, is small.

A slight variation between equation 2.32 and 2.33 is introduced by considering different values reported of the bowing parameter of the ZnCdSe alloy. The equation 2.32 is obtained considering the average of reported values for the bowing parameter of ZnCdSe, while the equation of the reference 39 considered just the reported value in the reference 38.

Determination of crystal strain

The strain state of the epitaxial layer is an important parameter since it influences the lattice constant of the epilayer. To calculate the composition with accuracy, the strain in the epilayer must be known.

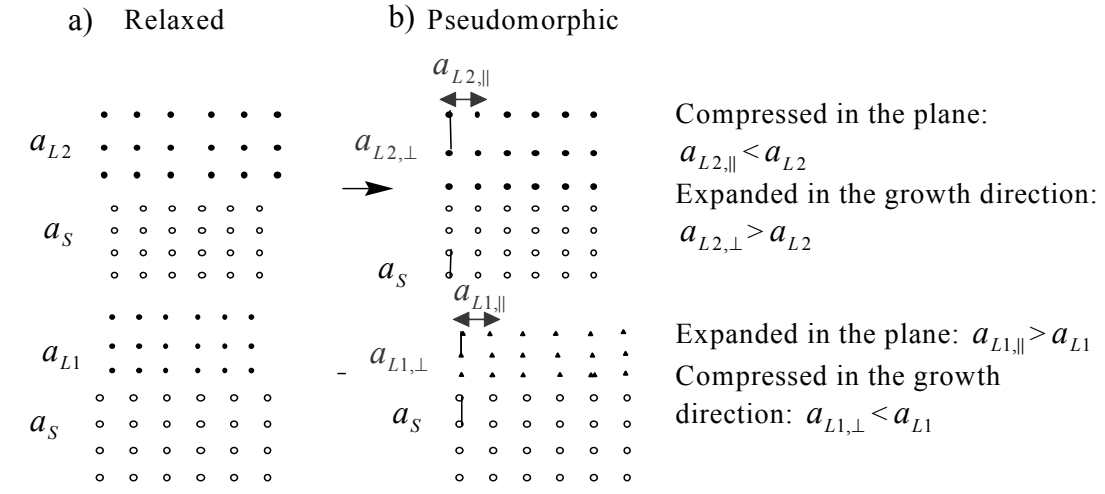

.

Figure 2.19. Possible strain states in the epilayers.

Usually, for a system consisting of an epilayer and a substrate with a different lattice-constant, the epilayer could be fully strained, partially strained, or fully relaxed. When the thickness of the epilayer is less than a certain thickness (critical thickness), the epilayer will be pseudomorphic or fully strained, and the tetragonal structure will be distorted, as shown in Fig. 2.19. The figure shows the two extreme cases: Part a represents the total relaxed epilayers while part b represents the pseudomorphic epilayers. Subscript 1 represents the epilayer with a lattice constant smaller than the substrate lattice constant, i.e. $a_{L1} < a_s$, and subscript 2 identifies the epilayer with a lattice constant bigger than the substrate lattice constant, i.e. $a_{L2} > a_s$. With the same thickness and lattice-mismatch, the layer that is pseudomorphic or commensurate has better quality than a relaxed or partially relaxed layer. For a pseudomorphic epilayer, the in-plane lattice constant is assumed to be the same across the whole crystal, i.e, the parallel lattice constant of the epilayer is equal to the lattice constant of the substrate, $a_{L,\parallel} = a_s$.[40] Therefore, the parallel lattice-mismatch in the plane between the pseudomorphic epilayer and the substrate will be zero. The perpendicular lattice mismatch $[\Delta a/a_s|_\perp = (a_\perp - a_s)/a_s]$ in the growth direction can be obtained by the (400) reflection. When the thickness of the epilayer is larger than the critical thickness, the epilayer will be partially or fully relaxed. In the case of a fully relaxed layer, the parallel and perpendicular lattice-mismatch will be the same and equal to the lattice-mismatch between the free standing epilayer material and the substrate (see Fig. 2.19). Hence, the (400) reflection can be used to obtain the lattice-mismatch (free standing material mismatch) between the fully relaxed layer and the

substrate. For the case of a partially relaxed layer, the (400) reflection cannot be utilized since the lattice mismatch will be different in the parallel and in the perpendicular direction. Consequently, other reflections as (511)a and (511)b, should be used to calculate the parallel and perpendicular lattice-mismatch values.

In the following, I will show briefly how to evaluate both the parallel and perpendicular lattice-mismatch and further free standing lattice constant from (511)a and (511)b reflections.

Let θ be the Bragg angle for the (400) reflection, φ be the angle spanning the (001) and (511) diffraction planes of the substrate (φ=15.7932°). The subscripts a and b represent (511) reflection geometries with x-ray incident angle of θ+φ and θ-φ, respectively. By measuring peak separations ω_a and ω_b, both representing angles separating the epilayer and the substrate in the corresponding (511)a and (511)b x-ray rocking curves, the perpendicular and parallel lattice mismatches can be determined as follows.[23]

$$\left(\Delta a / a_s\right)_{\perp} = \left(a_{\perp} - a_s\right)/a_s = \frac{\sin\theta \times \cos\varphi}{\left\{\sin\left(\theta + \frac{\omega_a + \omega_b}{2}\right)\right\}\left\{\cos\left(\varphi + \frac{\omega_b - \omega_a}{2}\right)\right\}} - 1$$

(2.34)

$$\left(\Delta a / a_s\right)_{\parallel} = \left(a_{\parallel} - a_s\right)/a_s = \frac{\sin\theta \times \sin\varphi}{\left\{\sin\left(\theta + \frac{\omega_a + \omega_b}{2}\right)\right\}\left\{\sin\left(\varphi + \frac{\omega_b - \omega_a}{2}\right)\right\}} - 1$$

(2.35)

To obtain the strain-free lattice constant, we must use the x-ray results from (511) reflections and the elastic theory. According to the solution of Hooke's law

with biaxial stresses, the perpendicular and parallel strains in the epilayer are related by the Poisson effect so that:

$$\frac{\varepsilon_{\perp}}{\varepsilon_{\parallel}} = \frac{2\nu}{1-\nu} \qquad (2.36)$$

$$\varepsilon_{\perp} = \frac{a_{\perp} - a_f}{a_f} \qquad (2.37)$$

$$\varepsilon_{\parallel} = \frac{a_{\parallel} - a_f}{a_f} \qquad (2.38)$$

$$a_f = \left(\frac{1-\nu}{1+\nu}\right) a_{\perp} + \left(\frac{2\nu}{1+\nu}\right) a_{\parallel} \qquad (2.39)$$

where ν is the Poisson ratio of the film and a_f is the free standing lattice constant. According to Bragg's law, θ = 43.0031° for InP substrate and θ = 45.0723° for GaAs substrate. The Mg concentrations in the $Zn_xCd_yMg_{1-x-y}Se$ compounds studied in Chapter 3 were obtained by the combined analysis of (511) reflections, PL, and Vegard's law.

Determination of the thickness

The layer thickness is directly reflected in the integrated intensity of the area under the X-ray peak. The intensity of the layer peak increases monotonically with the thickness. However, when the peaks of the layer and the substrate are close together, the determination of the integrated intensity corresponding to each peak is difficult to be accurately estimated. Furthermore, the integrated intensity depends on the experimental conditions of the measurements. Therefore, another experimental technique must be used.

a) Determination of the thickness using fringes

The fringes, often called thickness fringes, are periodic oscillations around the layer peak. The fringes are a very accurate method to determine the thickness of the layer. Applying the Bragg's Law for the common symmetrical case, the layer thickness is given by the Eq. 2.40:

$$t = \frac{\lambda}{2\Delta\theta_p \cos\theta} \qquad (2.40)$$

where λ is the wavelength, t the thickness and Θ the Bragg's angle and $\Delta\theta_p$ is the interference peak separation.

This is a very useful method since this technique does not depend on the diffraction conditions and any other material parameter that the Bragg's angle. Furthermore, it is not necessary to grow a very thick layer to obtain a reasonable accurate measurement as the determination of the thickness using the radial sectioning instrument. Section 5.3.2.1 will show experimental data of this type of method.

b) Determination of the thickness using the period of a superlattice

A superlattice contains a periodic sequence of layers of alternating composition. The X-ray diffraction derived from this type of structures is usually a sequence of equispaced satellite peaks associated with the period of the superlattice. Section 5.3.2.1 will show the determination of period thickness of a two MQD structures (thirty periods of ZnSe/ZnCdMgSe QWs grown on ZnCdMgSe barriers), which were grown to calibrate the spacer thicknesses of the MQD structures.

The rocking curve will show the following features:

1. A substrate peak from the A substrate (ie. InP for ZnSe-QW/ZnCdMgSe superlattices)
2. A peak caused from the addition of Bragg reflections from A and B components of the MQW. This is the zero-order or average mismatch peak, from which the average composition of the A+B layers may be obtained by differentiation of Bragg's law (zero order peak of ZnSe-QW/ZnCdMgSe superlattice).
3. A set of subsidiary "satellites" peaks symmetrically surrounding the zero-order peak (satellites peaks originating from ZnSe-QW/ZnCdMgSe superlattice), with spacing determined by the periodicity (total thickness of the repeating layers) of the MQW. These may also be regarded as the sum of the interference fringes arising from the interference between each of the layers comprising the MQW.
4. A peak caused by the thick barrier layer can also appear in the spectrum, close to the zero order peak of the MQWs (ie. ZnCdMgSe barrier peak grown before the superlattice structure).

The periodicity or period thickness can be determined using the equation 2.41 or also by the approximation 2.40.

$$\Lambda = \frac{\left(s_i - s_j\right)\lambda}{2\left(\sin\theta_i - \sin\theta_j\right)} \qquad (2.41)$$

where λ is the wavelength of the X-ray beam, s_i and s_j are two diffraction orders (e.g. 1 and 2) and Θ_i and Θ_j are the corresponding angles at which these orders diffract (Bragg's angles).

Using this technique, very good estimations of very thin periods can be obtained. The error of this method is laid, basically, in the determination of the satellite peak positions; accurate measurements of thickness can be achieved.

2.2.2.4. Atomic Force Microscopy Measurements

Several techniques are available for magnifying the microscopic features of a surface. Methods for magnifying surface features originated with magnifying lenses and optical microscopy in the late 18th century. Optical instruments are limited by the wavelength of visible light and can observe objects down to approximately 0.5 microns.

During the 20th century, methods for magnification based on electron and ion beams were developed. Even though these techniques represented an advance with respect to the primitive microscopes used in the earlier centuries, it was still not suitable to provide atomic level information. Operating in a vacuum, the scanning electron microscope (SEM) could resolve features to the level of approximately 30 Å at maximum.

Scanning probe microscopy (SPM) is a recent, innovative technology that relies on a mechanical probe for generation of magnified images. An SPM instrument is operable in ambient air, liquid, or vacuum; and resolves features in three dimensions, down to a fraction of an angstrom. There are two basic modes of SPM: scanning tunneling microscopy (STM) and atomic force microscope (AFM) where the original work was done by G. Binning et al.[24]

Unlike the STM, which monitors fluctuations in currents flowing between the probe tip and a conductive sample, the AFM can provide images of a broad spectrum

of both conducting and insulating materials. The AFM can be divided into two primary scanning modes, *contact* and *non-contact*, which simply refers to whether the scanning probe actually comes into physical contact with the sample surface or not.

The not essential surface preparation and the relative simplicity of AFM technique compared to other techniques like STM or TEM is the cause of the widespread use of the AFM for the characterization of nanostructured surfaces.

One of the well known problems with AFM is the finite size of the probe. A dilation" with the probe geometry must therefore be taken into account[41]. This effect is often called "tip convolution effect" since the AFM scan is normally a convolution of a surface nanoscale object and the probe shape. This effect can be neglected for lateral structure sizes that exceed the tip radius (typically of 10-20 nm) and structure slopes less than half the opening angle of the AFM tip. Hence, for an array of 3D islands on the surface, AFM correctly evaluates the island density and typically overestimates the island lateral size.

One of the main problems in AFM images performed in II-VI materials and, in particular, in CdSe QDs, is the rapid formation of an oxide layer[42]. The formation of the selenite in the surface of these nanostructures has been studied by several groups, either in colloidal solution of CdSe QDs or in epitaxial growth. Sometimes, this formation of the oxide layer was improperly associated with the ripening of the quantum dots, which is caused mainly by the mobility of the atoms in unprotected uncapped surface during cooling down process (see below) and cannot be assumed if a systematic study is not carried out. Possible solutions to avoid the formation of this oxide layer are the performance of the AFM "in situ", inside the molecular beam

epitaxy system, or the delay of the energetically favorable oxide formation by changing some thermodynamic parameter, for example, the temperature.

A more severe disadvantage of the AFM technique is related to the fact that the grown structure normally has to be cooled down to room temperature before the AFM scan is performed (even though the surface morphology is studied " in situ" in the vacuum system). A cooling down from 480 to 420 in the growth of InAs/GaAs structures, already leads to a dramatic changes in the surface morphology of InAs/GaAs structures[43, 44, 45]. This effect was not only found in the III-V semiconductor QDs but also in the other type of semiconductor as the II-VI. In 2003, Munoz et al.[46] analyzed the change of the size in uncapped CdSe/ZnSe QDs compared with the CdSe/ZnSe capped ones based on contactless electroreflectance measurements. A decrease in the wetting layer thickness due to adatom condensation on islands, decreased island density, increased average size volume, and an increase in the height-to width aspect ratio of the islands have been found in different systems. This effect depends on the mobility of the atoms while the sample is cooling down, higher mobility of the atoms, more severe redistribution of material over the surface and more dramatic changes in island density, volume and shape.

In Chapter 3, details of the growth procedure and post-treatment of the uncapped CdSe/ZnCdMgSe will be given to attempt to diminish all these drawbacks of AFM measurements.

Contact AFM

In the contact AFM method (Fig. 2.20), the probe tip (which is mounted to the end of the cantilever) scans across the sample surface, coming into direct physical

contact with the sample. As the probe tip scans, varying topographic features cause deflection of the tip and cantilever. A light beam from a small laser is bounced off of the cantilever and reflected on to a four-section photodetector. The amount of deflection of the cantilever (or the force it applies to the sample) can then be calculated from the difference in light intensity on the sectors.

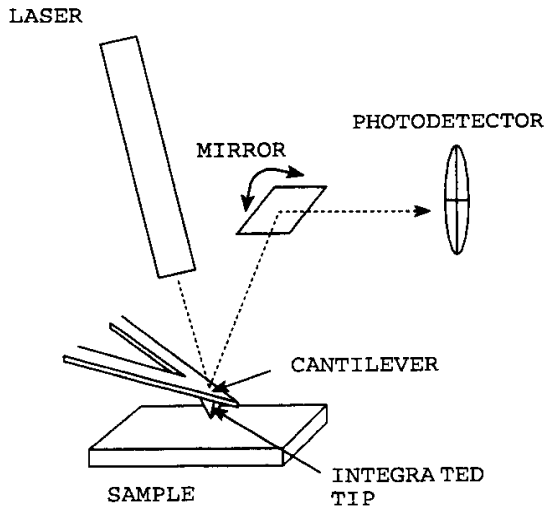

Figure 2.20. Force sensor in contact mode.

Hooke's Law gives the relationship between the cantilever's motion, d, and the force required to generate the motion, F: F=-kd. It is possible to fabricate a cantilever with a force constant, k, of 1 N/m or less. Since motion of less than one angstrom can be measured, forces of less than 0.1 nN are detectable. As the cantilever moves across the sample surface in contact scanning, the lateral motion of the

cantilever may cause damage to soft or fragile samples such as biological specimens or polymers. In the case of semiconductor surfaces, small scratches can be observed after a contact-AFM scan, which is not desirable if the sample would be utilized for other measurements. Because of this phenomenon, as well as, a number of other variables, non-contact scanning is sometimes preferable.

Non-contact AFM

In non-contact operation (Fig. 2.21), the cantilever is oscillated at its resonant frequency. In this mode, the detected force between the tip and the sample changes depending on the morphology of the surface, even though they are not in contact.

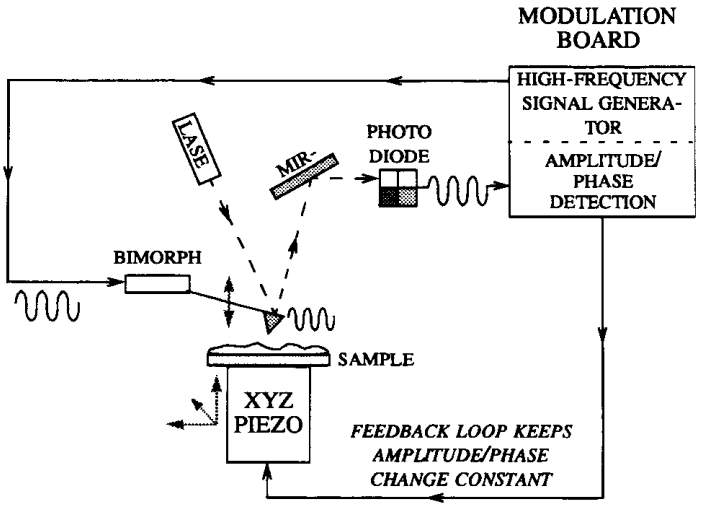

Figure 2.21. Non-contact feedback-loop.

This force change is also referred to as the force gradient. As the probe gets closer to the sample surface, the force gradient varies and with this, changes both the

oscillation *amplitude* and *phase* of the vibrating cantilever. Either the change in amplitude or the change in phase can be detected and used to control the tracking of the probe over the surface (i.e., the feedback-control loop). *Amplitude detection* is the non-contact method usually used for high-amplitude cantilever vibration. *Phase detection* is the method usually used when the cantilever vibration amplitude is relatively small (and/or higher sensitivity is needed for stable feedback).

The AFM measurements of the QDs were performed using a ThermoMicroscopes Explorer AFM of Veeco-Digital Instruments operated in the non-contact mode or contact mode under ambient conditions. For non-contact mode, a Si cantilever with a spring constant of 13-100 N/m and a nominal resonance frequency of 240-420 kHz was used. In the case of contact mode, a NanoProbe of Si_3N_4 with a sping contant of 0.01-0.50 N/m was used. Images were recorded with a resolution of 300 x 300 pixels and a scan rate of 3.69 μm/s for non-contact and 13.78 μm/s for contact mode. Samples for the AFM were removed from the chamber immediately following the QD formation (without the quaternary top and cap layers). To slow down a possible ripening effect and the formation of oxides, the samples were immediately immersed in liquid nitrogen after the growth and kept in this condition until the moment of taking the surface topography.

2.2.2.4. Contactless Electroreflectance Measurements

Since its establishment in 1964, modulation spectroscopy has proven to be a powerful and versatile optical technique for obtaining valuable information about a

large variety of semiconductor systems,[47, 48, 49, 50, 51, 52, 53, 54, 55] including bulk/ thin films, micro- and nanostructures (QWs, multiple QWs, superlattices, QWRs and QDs), surfaces/ interfaces (semiconductor/ air/ vacuum), semiconductor/ semiconductor (hetero- and homojunctions), semiconductor/ metal, semiconductor/ electrolyte, and the effects of growth/processing, as well as the characterization of actual device structures (heterojunction bipolar transistors, pseudomorphic high electron mobility transistor, QW lasers). The idea underlying modulation spectroscopy is a very general principle of experimental physics. Instead of directly measuring an optical spectrum (reflectance or transmission), the derivative of this spectrum with respect to some parameter is measured. This can be easily accomplished by applying a small perturbation in a periodic fashion and measuring the corresponding change in the optical properties with phase sensitive detection (i.e. with a lock-in amplifier). Structure in the conventional optical spectra is considerably enhanced in the derivative spectra and broad, structureless backgrounds are eliminated. Weak structure superimposed on a large background is sometimes difficult to resolve due to statistical noise of the background. Its resolution becomes easier in a modulation measurement since the structureless background is eliminated.

Modulation techniques can be classified into two categories: internal and external. In the internal modulation techniques, a parameter of the monochromatic optical beam, such as the wavelength or the degree of polarization, is modulated. In the external techniques, an independent modulation parameter (e.g. a stress, an electric field, etc.) is applied to the sample. Of the external modulation techniques,

electroreflectance has remained to this date the most popular technique because of its experimental simplicity and the sharpness of the spectra obtained.

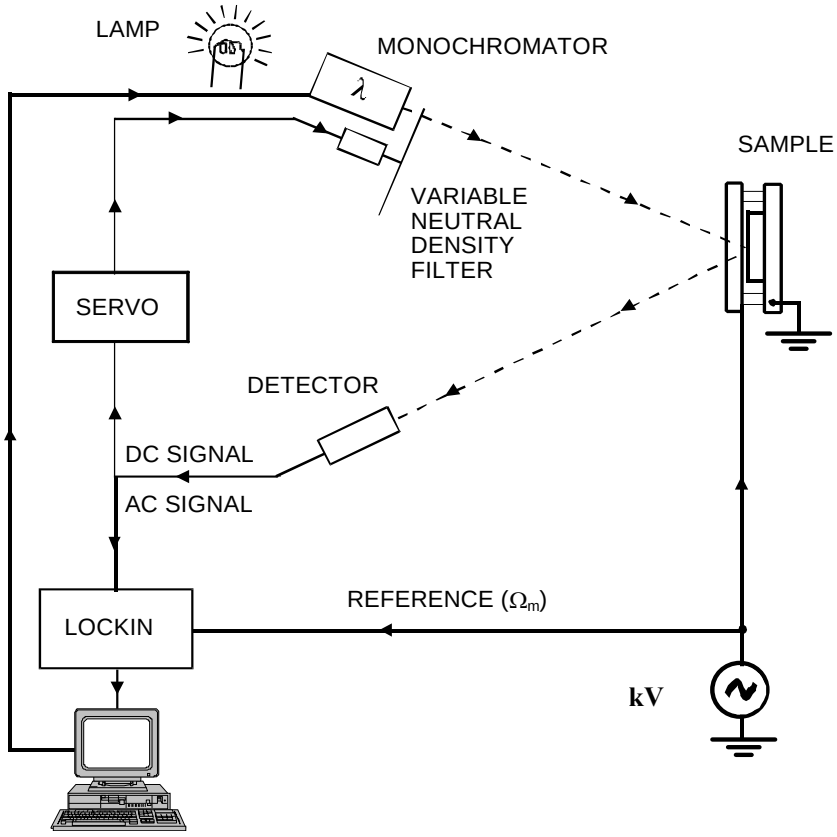

Figure 2.22. Schematic representation of the contactless electroreflectance setup in the City College of New York.

Contacless electroreflectance (CER) setup

The light striking the detector contains two signals: the d.c. (or average value) is given by $I_0(\lambda)R(\lambda)$, where $R(\lambda)$ is the d.c. reflectance of the material, while the modulated value (at frequency Ω_m) is $I_0(\lambda)\Delta R(\lambda)$, where $\Delta R(\lambda)$ is the change in

reflectance produced by the modulation source. The a.c. signal from the detector, proportional to $I_0\Delta R$, is measured by the lock-in amplifier. In order to evaluate the quantity of interest, i.e. the relative change in reflectance $\Delta R/R$, a normalization procedure must be used to eliminate the uninteresting common feature $I_0(\lambda)$. In Fig. 2.22, the normalization is performed by a variable neutral density filter (VNDF) connected to a servo mechanism. The d.c. signal from the detector, which moves the VNDF in such a manner as to keep $I_0(\lambda)R(\lambda)$ as a constant, i.e. $I_0(\lambda)R(\lambda)=C$. Under these conditions the a.c. signal $I_0(\lambda)\Delta R(\lambda)=C\Delta R(\lambda)/R(\lambda)$, the signal to the lock-in amplifier, is proportional to the quantity of interest, i.e. $\Delta R(\lambda)/R(\lambda)$.

The periodic variation of the measurement conditions gives rise to sharp, differential-like spectra in the region of interband (intersubband) transitions. One of the great advantages of modulation spectroscopy is its ability to perform a lineshape fit. Thus, it is possible to account for the lineshapes to yield accurate values of important parameters such as the energies and broadening functions of interband (intersubband) transitions. CER measurements were performed for SQDs and MQDs of CdSe with barriers of ZnCdMgSe. ZnCdMgSe barrier, ZnCdSe LT and InGaAs layers were grown to obtain reference spectra to compare with the data of the QDs. Lineshape fitting were performed and transitions were compared with theoretical calculations.

2.2.2.6. Hall Effect

Hall discovered the Hall effect in 1879, when he investigated the nature of the force acting on a conductor carrying a current in a magnetic field. Hall tried to determined whether the force experienced by a wire with current in a magnetic field was exerted

on the whole wire or only upon the moving electrons in the wire. Hall discovered that when a magnetic field is applied perpendicular to the current flow of electrons, it generates a force perpendicular to both magnetic field and electric current. This force causes the charges to accumulate on opposite sides of the conducting material. The resulting force is called Hall field. The magnitude of the Hall field is proportional to the concentration of charges in the semiconductor. Fig. 2.23 shows a schematic diagram of the Hall effect principle for a p-type semiconductor sample (the n-type case is analogous). As is illustrated in the figure, an electric field is applied along the x-axis while a magnetic field is applied along the z-axis. The electric field is defined the electric force per unit charge:

$$E = F / q \qquad (2.40)$$

Where E is the electric field, F is the force and q is the charge.

For a p-type sample, the Lorentz force, produced by the magnetic field is represented by:

$$F = q\nu_x x\ B \qquad (2.41)$$

where B is the magnetic field, ν_x is the velocity and q is the charge.

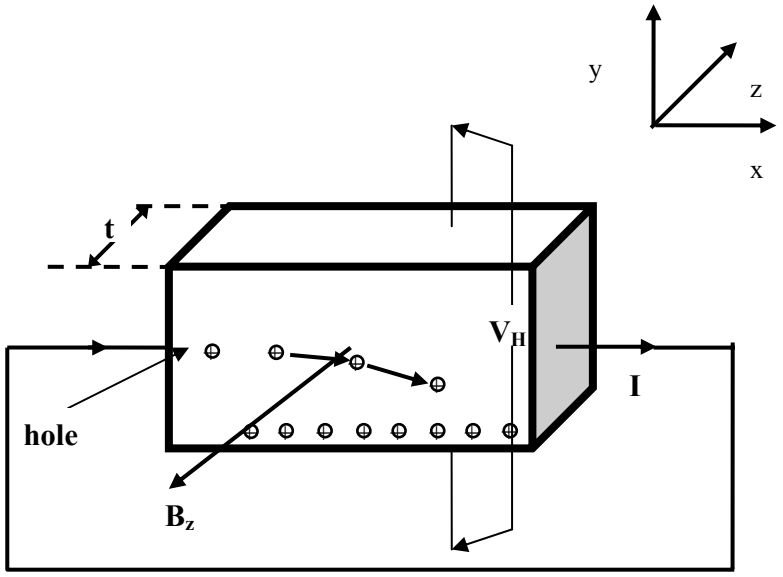

Figure 2.23. Fundaments of the Hall effect. The current and the holes flow in x-direction, the magnetic field is in the z-direction, and the Hall voltage is developed in the y-direction.

This Lorentz force causes an average downward force on the holes, and downward-directed current causes a piling up of the holes at the bottom side of the sample, which in turn give rise to an electric field ε_y. Since there is no net current along the y direction in the steady state, the electric field along the y axis (Hall field) exactly balances the Lorentz force. The relation between the Hall field (ε_H) and the applied current density (J_x) and the magnetic field B_z can be expressed by[56]:

$$\varepsilon_H = R_H J_x B_z \qquad (2.42)$$

where R_H is the Hall coefficient which can be obtained from the given J_x and B_z and the measured ε_H via the equation 2.42.

When both holes and electrons are present in compensated samples the expression that relates the free carriers and the Hall coefficient is:[57]

$$R_H = \frac{\left[\left(p - b^2 n\right) + \left(\mu_n B_z\right)^2 \left(p - n\right)\right]}{q\left[\left(p + bn\right)^2 + \left(\mu_n B_z\right)^2 \left(p - n\right)\right]} \qquad (2.43)$$

Where b is the mobility ratio:

$$b = \frac{\mu_n}{\mu_p} \qquad (2.44)$$

and μ_n are μ_p electron and hole mobilities, respectively. This expression reveals that the Hall coefficient varies with the applied magnetic field. For samples with modest mobility in the 100 to 1000 cm^2/Vs and with mobility ratios of b~3 to 10, the Hall mobility coefficient is generally found to vary little with the magnetic field.

For the case of $\mu_n B_z \ll 1$, equation 2.43 can be simplifies to: [57]

$$R_H = \frac{\left(p - b^2 n\right)}{q\left(p + bn\right)^2} \qquad (2.45)$$

For highly doped samples without significant compensation effect (i.e. n>>p for n-type or p>>n for p-type) and with modest mobility ratios, equation 2.45 can be further simplified to equation 2.46 for p-type or 2.47 for n-type semiconductor samples:

$$R_H = \frac{r}{qp} \qquad (2.46)$$

$$R_H = \frac{-r}{qn} \qquad (2.47)$$

where q is the elementary charge, and r is the scattering factor that lies between 1 and 2, depending on the scattering mechanisms in the semiconductor. Usually, r is assumed to be unity and this assumption generally introduces an error of less than 30

%. Thus, the carrier concentration can be determined via equations 2.46 or 2.47. The carrier type in the sample can be determines from the sign of the Hall coefficient; i.e. n-type if R_H is negative and p-type if R_H is positive.

Moreover, the Hall mobility μ_H can be also obtained by:

$$\mu_H = \frac{|R_H|}{\rho} \qquad (2.48)$$

where ρ is the resistivity of the sample which can be measured independently.

Therefore, Hall Effect is a tool to study the electrical properties of the material such as mobility (measurement of the ease of carrier motion within the crystal) and resistivity (measurement of material's inherent resistance to current flow), as well as to determine the concentration of the major carrier (electrons for the case of n-type semiconductor and holes for the p-type).

Experimental details

In our lab, four ohmic contacts are made by soldering indium and four gold wires to the surface of a symmetric square piece of sample (one extreme of the wire) and to the sample holder (other extreme of the wire). This geometry is called Van der Paaw geometry. The quality of ohmic contacts is determined by a current-voltage (I-V) curve, which must be linear for a contact that follows Ohm's law. If the contacts are symmetric and ohmic, the Hall Effect measurement can be performed. Figure 2.24 shows a schematic representation of sample and holder after making the contacts on the sample surface.

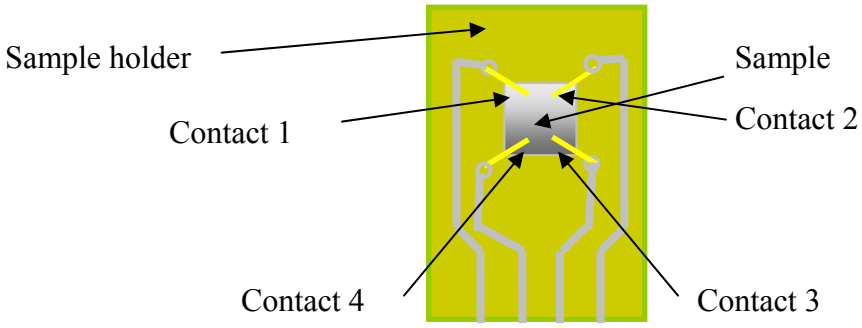

Figure 2.24. Hall Effect measurements. Schematic representation of sample and holder after making the contacts on the sample surface.

The magnetic field B_z used for the Hall effect measurements in the laboratory is fixed at 2.5 kG (=0.25 T) and the samples studied in this thesis have relatively low mobilities in the range of 100 cm^2/Vs. This results in $\mu_n B_z \sim 10^{-3} - 10^{-2} \ll 1$ and equation 2.45 can be utilized. For highly n-type doped $Zn_xCd_yMg_{1-x-y}Se$ where n>>p and p-type doped $ZnSe_yTe_{1-y}$, with high Te content where p>>n, equation 2.46 can be used to determine the free carrier concentration. In this thesis, all values of the free carrier concentration measured by Hall effect were determined from the equations 2.46 or 2.47. It should be noted for samples which contain significant carrier compensation, such as p-type $ZnSe_yTe_{1-y}$, alloys with low Te content, the use of this equation may introduce errors. More detailed characterization such as in high magnetic fields and/or magnetic field-dependent Hall effect measurements may be useful to determine the free carrier concentration[58] in those cases. In this dissertation capacitance-voltage measurements were used for the determination of the carrier

concentration of $ZnSe_yTe_{1-y}$ with low content of Te. Details will be given in the next section and in the section 2.2.2.9 and Chapter 4.

Setup for the Hall Effect

The Hall effect instrument, represented in Fig 2.25, consists of a picoammeter (*Keithley 485*), a voltmeter (*Keithley 182*), a current source (*Keithley 220*), a computer interface and magnetic controller, a sample holder with a magnet (*Abbess Instrument*), a computer with a software that runs the measurement and a water circulating unit for cooling the magnet.

The switching matrix sets the first configuration, then the picoammeter is set to zero. The Keithley 220 applies the desired current between the two contacts for five seconds (the acquisition time should be determined by the user). During this period, the picoammeter measures the current, the computer averages this measurement and records it as the measured current (I). At the same time, the voltmeter measures the voltage between these two contacts for five seconds, then the computer averages this measurement and records it as the voltage value (V). For resistivity measurements, eight voltage measurements are taken in the absence of the manetic field. The voltage is applied alternatively between two contacts following the sequence that is shown in the Table 2.1.

Voltage identification (ID number)	Current applied between contacts numbers:	Voltage measured between contact numbers:
$\mathbf{V_1}$	1-2	4-3
$\mathbf{V_2}$	2-1	4-3
$\mathbf{V_3}$	2-3	1-4
$\mathbf{V_4}$	3-2	1-4
$\mathbf{V_5}$	3-4	2-1
$\mathbf{V_6}$	4-3	2-1
$\mathbf{V_7}$	4-1	3-2
$\mathbf{V_8}$	1-4	3-2

Table 2.1. Sequence of voltage measurement for the determination of resistivity.

After measuring these voltages values, resistance can be calculated using Ohm's law:

$$R_n = \frac{|V_n|}{I} \qquad (2.49)$$

For a perfect ohmic contact, the contact resistance obtained from two oppositely applied currents (such R_1 and R_2) should be equal. The average resistance between a pair of contacts will be:

$$R = \sum_{n=1}^{8} \frac{R_n}{8} \qquad (2.50)$$

Then the resistivity can be determined by:

$$\rho = \frac{F\pi tR10^{-4}}{\ln 2} \qquad (2.51)$$

Where t is the sample thickness in μm and F is the van der Pauw factor (symmetry factor). The van der Pauw factor can be approximated by:

$$F = 1 - \frac{1}{2}\ln 2\left[\frac{R_b - R_a}{R_b + R_a}\right]^2 - \left[\frac{R_b - R_a}{R_b + R_a}\right]^4\left[\frac{(\ln 2)^2}{4} - \frac{(\ln 2)^3}{12}\right] \qquad (2.52)$$

where $R_a = \frac{(R_1 + R_2)}{2}$ (2.53)

and $R_b = \frac{(R_3 + R_4)}{2}$ (2.54)

are the average resistance of a pair of contacts.

For determination of carrier type, mobility and carrier concentration, we need to measure the Hall coefficient as it was shown above. The measurements were performed in the presence of a 2.5 kG magnetic field with + and – fluxes and the voltage measurement sequence is shown in the Table 2.2.

As soon as the voltages (in volts) are measured, the average voltage for each configuration can be obtained by:

$$V_{F1} = \frac{V_9 + V_{10}}{2} \qquad (2.55)$$

$$V_{R1} = \frac{V_{11} + V_{12}}{2} \qquad (2.56)$$

Voltage identification (ID number)	Flux	Current applied between contacts numbers:	Voltage measured between contact numbers:
$\mathbf{V_9}$	+B	1-3	2-4
$\mathbf{V_{10}}$	+B	3-1	2-4
$\mathbf{V_{11}}$	-B	1-3	2-4
$\mathbf{V_{12}}$	-B	3-1	2-4
$\mathbf{V_{13}}$	+B	2-4	1-3
$\mathbf{V_{14}}$	+B	4-2	1-3
$\mathbf{V_{15}}$	-B	2-4	1-3
$\mathbf{V_{16}}$	-B	4-2	1-3

Table 2.2. Sequence of voltage measurement for the determination of the Hall coefficient.

The other set of voltages (V_{F2} and V_{R2}) are similarly defined. Then, the Hall voltage for each configuration is:

$$V_{H1} = \frac{V_{F1} + V_{R1}}{2} \quad (2.57) \quad \text{and} \quad V_{H2} = \frac{V_{F2} + V_{R2}}{2} \quad (2.58)$$

Therefore, the average of the Hall coefficient can be obtained by:

$$R_H = \frac{10t\left(V_{H1} + V_{H2}\right)}{2IB} \qquad (2.59)$$

where t is the sample thickness in m, B is the magnetic flux in kG, and t is the current in A. If R_H is negative, the carriers are n-type. If R_H is positive, the carriers are p-type. After R_H is determined, the carrier concentration can be obtained by either equation 2.46 for p-type or 2.47 for n-type semiconductor layers and Hall mobility will be determine using equation 2.48.

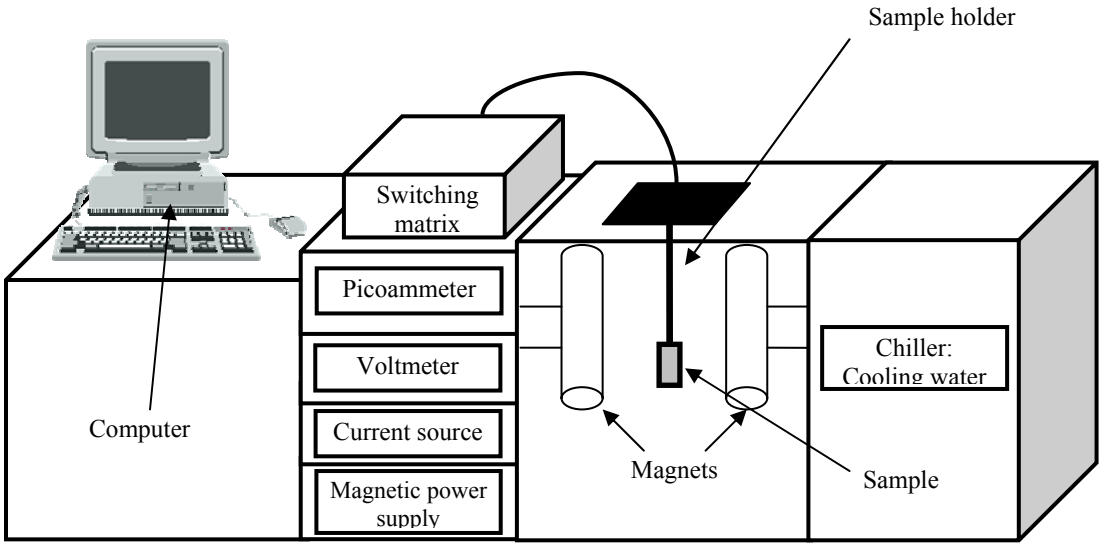

Figure 2.25. Schematic of Hall Effect measurement apparatus.

2.2.2.7. Vapor Deposition

To perform high-quality electrical measurements of a device structure, it is essential the achievement of a high-conductive contact, which could be obtained by depositing thin metal films. Thin metal films, such as gold films, can be deposited "in situ" in the metallization chamber inside the molecular beam epitaxy system or ex-situ, using other techniques to evaporate metals on the sample surface. One of the techniques utilized frequently for this purpose is based on the thermal evaporation of the deposited contact material. The Fig. 2.26 shows the main components of the basic system and the principles of operation of the evaporation apparatus, CVE-15 system, used in the City College of New York. The Table 2.3 shows the valve sequence in the operation steps of this evaporation system. The basic CVE-15 system is primarily a high vacuum evaporator since it contains a pumping system, which can promptly evacuate the bell jar, where is situated the sample and the metal that will be deposited on the sample surface. A low-voltage, high-current power supply provides electrical

energy through resistance heating. In the operation process, the sample with the mask, which is designed to obtain ring shape (or a dot) using a tungsten foil, and the metal are placed on the bell jar shown in the Fig. 2.26. Then the air inlet valve is closed and the vacuum is produced using a roughing pump and a diffusion pump. The system evacuation is accomplished in two steps. The first step, called the roughing cycle, is carried out by the mechanical pump. This step takes about 30 minutes and reduces the bell jar chamber pressure to 50-100 millitorr pressure, measured by an ionization gauge tube inside the chamber. To reduce the pressure further, a diffusion pump is introduced into the pumping system. This step is called diffusion cycle or high-vacuum phase. This diffusion-pump reduces the clean, dry, and empty system (obtained by the roughing cycle) to the high vacuum pressure ranges. The pressure of the system should be about 5×10^{-6} (CVE-15 could reach pressure of about $3\text{-}4 \times 10^{-8}$) after the second vacuum step is finished (approximately, 2 hours and a half). When the correct working pressure has been obtained in the bell jar, the evaporation can be performed. After the evaporation system reaches the desired vacuum, the tungsten filament (resistance element) is turned on using the filament control place on the control center (see Fig 2.26). Voltage of the filament is increased slowly by rising the voltage using a controller connected to an auto-transformer Variac. Electrical feedthroughs connect the filament to the transformer system. When the filament reaches the desired temperature the metal will evaporate and will deposit on the surface of the sample that is exposed by the mask (only a ring or a dot, depending on the shape of the mask).

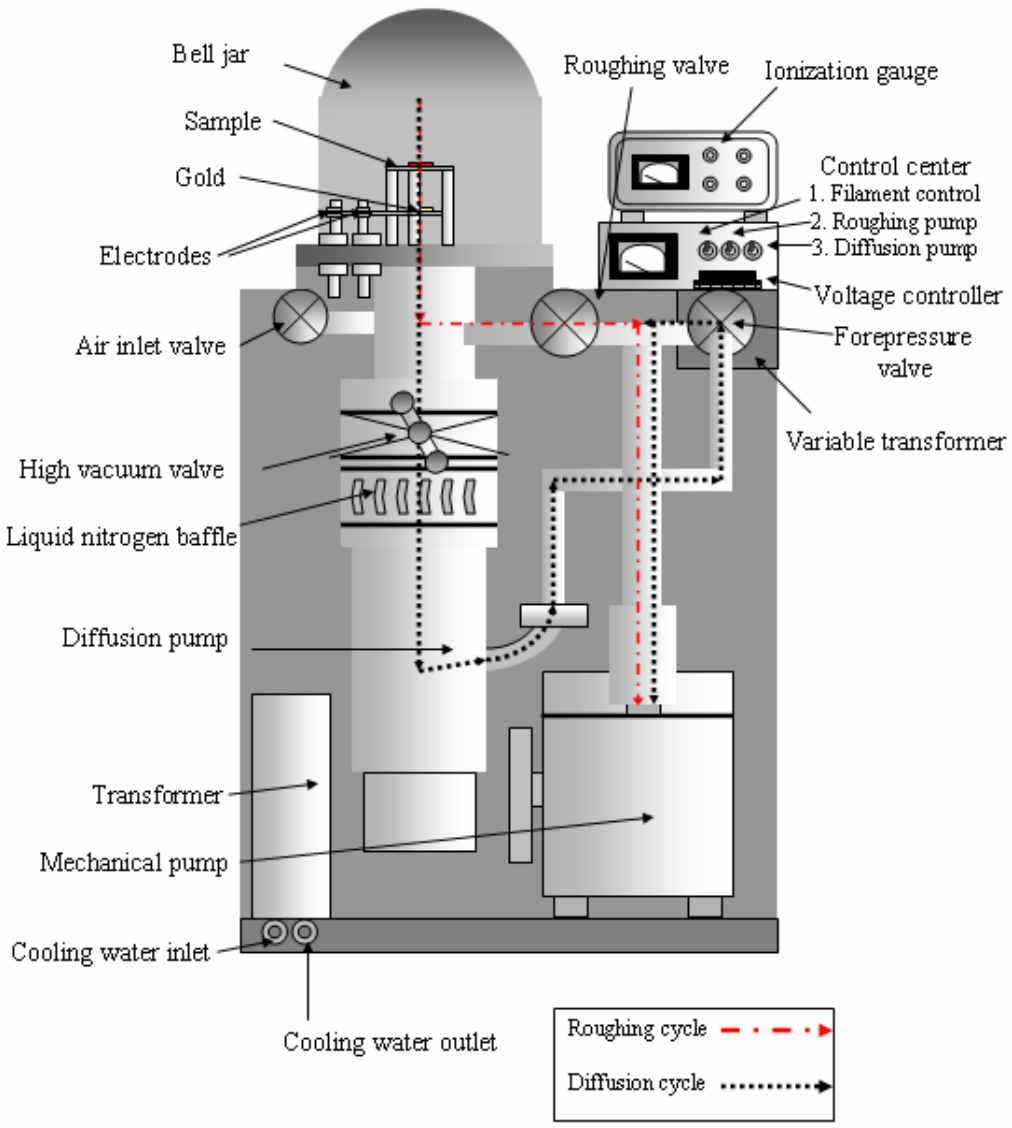

Figure 2.26. Scheme of components of CVE-15 vapor deposition machine.

Phase			Valves Closed			Valves open		
Roughing	High vacuum		Forepressure	Air inlet		Roughing		
Diffusion		Roughing		Air inlet	High vacuum		Forepressure	
Open Bell jar	High vacuum	Roughing					Forepressure	Air inlet

Table 2.3. Valve sequence for the difference operation steps in the CVE-15 evaporation system.

2.2.2.8. Surface profilometry

An alpha-step 200 surface profilometer was used in this research for tracing the surface profiles of the samples after the gold contact deposition in order to determine the thickness of the gold contact. Thick and very thin gold depositions were attempted. The thin ones were performed in order to obtain a transparent contact to pursue the achievement of light emission of the LED structures through the contact. More details will be shown in the Chapter 4.

It operates by moving a stylus arm assembly from the center position to either the left or the right to measure the sample surface. The stylus arm assembly uses a three-position pivot to allow friction free vertical motion as it moves across the sample being measured. The arm is glued to the center pivot, and the two outside sections are glued to a bracket surrounding the stylus arm. The bracket is connected to a bolt that is then used to align the arm and set the stylus force. The stylus motion is measured by means of a transducer. Either a clear quartz rod or a black graphite rod is attached to the stylus arm. This rod isolates the slug of the transducer so that even the slightest vertical motion of the stylus arm can be detected by the transducer. When the slug is in the exact center of the transducer (null position), the needle in the measurement display should also be in the center. The measured linear voltage differential drive (LVDT) signal goes to the computer control unit for display, calibration and leveling.

2.2.2.9. Capacitance-Voltage Measurements

Information of the free carrier or net carrier concentration is important for the study of the doping of bulk semiconductor layers and the performance of devices based on these doped semiconductors. The free electron concentration of n-type-$Zn_xCd_yMg_{1-x-y}Se$ system can be determined from the Hall measurement measurements (section 2.2.2.6) while p-type net acceptor concentration (N_A-N_D) is usually obtained from the capacitance-voltage (C-V) characteristics due to the formation of a Schottky barrier instead of an ohmic contact at the contact-semiconductor interface. In III-V materials the free hole (electron) concentration measured by Hall effect is nearly equal to the net acceptor (donor) concentration determined from the C-V curves at room temperature because donors and acceptors are totally ionized at this temperature. However, for wide bandgap materials, these two values are not identical.[59] For example, the ionization energy of the nitrogen in p-type ZnSe is about 110 meV, four times larger than kT at the room temperature, so the free hole concentration in the valence band should be significantly smaller than the net acceptor concentration. Besides the binding energy, other factors such as compensation mechanisms may also alter the ionization rate of acceptors or donors.[60]

This section is focused on the introduction of the C-V measurement measurements performed to characterize the net acceptor concentration of p-type-$Zn_xCd_yMg_{1-x-y}Se$ and p-type-$ZnSe_yTe_{1-y}$ bulk layers. Electrical C-V will be described since Chapter 4 shows some results derived from these measurements. Electrochemical C-V (ECV) was occasionally utilized for the characterization of

semiconductor layers but it will not describe since the samples are out of the scope of this thesis.

Fundaments of the measurement

The C-V technique relies on the fact that the width of a space-charge region (scr) of a semiconductor junction device depends on the applied reverse-biased voltage. The method is founded on a Schottky barrier created using a metal. To be able to apply this method, the reverse-biased junction must be considered as a parallel plate capacitor. This consideration can only be accepted presuming the "depletion approximation" assumptions: First, an ideal boundary with perfectly sharp limits must be considered in order to evaluate the carrier concentration using electrical C-V measurements and second, the effect of the minority carriers must be supposed negligible, and the region beyond the width of the SCR being perfectly neutral in charge.

Accepting these statements, let us consider a Schottky barrier diode as the Fig. 2.27 where the semiconductor is a p-type doping semiconductor with a doping concentration of N_A. A dc bias V is applied to the metal contact. The reverse bias produces a space-charge region of width W. For the p-type layer $Zn_xCd_yMg_{1-x-y}Se$ (or $ZnSe_yTe_{1-y}$) grown on InP substrates, the equivalent circuit of the resulting structure consists of two barriers: a Schottky barrier (SB) diode formed at the metal contact/p-$Zn_xCd_yMg_{1-x-y}Se$ (or p-$ZnSe_yTe_{1-y}$), and a p-$Zn_xCd_yMg_{1-x-y}Se$ (or p-$ZnSe_yTe_{1-y}$) /p-InP heterojunction (HJ). Because of a large valence band discontinuity in the heterojunction (>1eV) there is a depletion region on the wide band gap side, i.e., p-$Zn_xCd_yMg_{1-x-y}Se$ (or p-$ZnSe_yTe_{1-y}$).

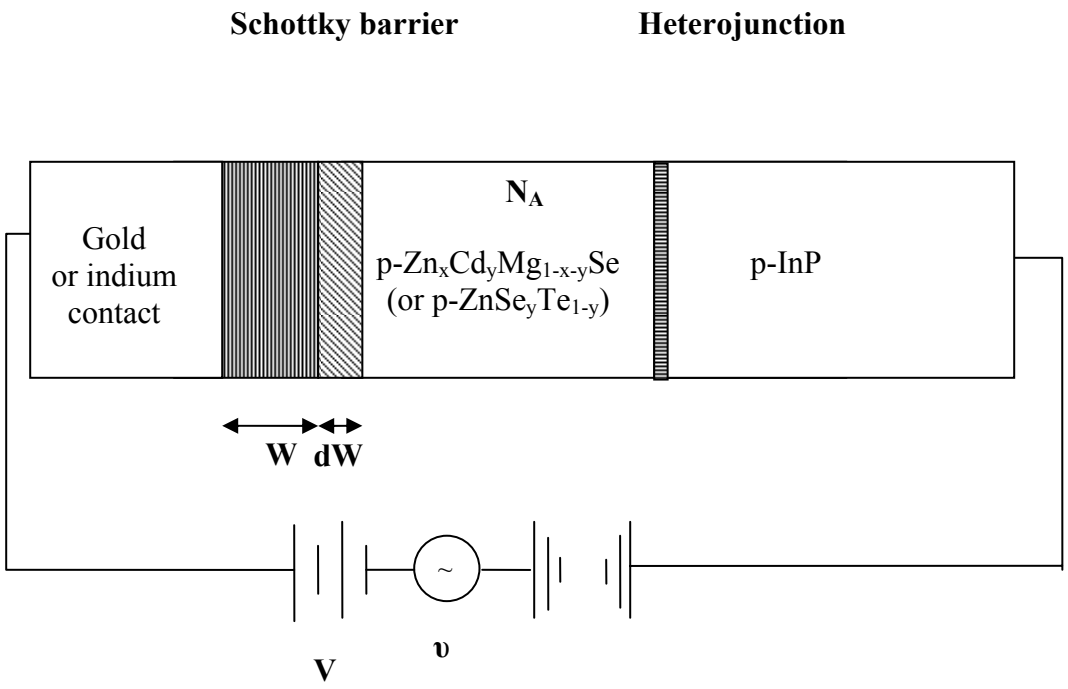

Figure 2.27. Reverse-biased Schottly diode.

The capacitance of the reverse-biased junction can be expressed as:

$$C = \frac{-dQ_s}{dV} \qquad (2.60)$$

where Q_s is the semiconductor charge and V is the applied voltage. The negative charge in the semiconductor scr (negatively charge-ionized acceptors) for increased positive voltage on the metal. The capacitance can be determined by superimposing a small-amplitude ac voltage υ on the dc voltage V. Therefore, let us consider a diode that is biased with a dc voltage plus a sinusoidal ac voltage. Assuming the ac voltage increases from zero to a small positive voltage, adding a charge increment dQ_m to the contact. The charge increment dQ_m must be balanced by an equal semiconductor charge increment dQ_s, for the overall charge neutrality, where dQ_s is given by:

$$dQ_s = -eA(N_A - N_D)WdW \qquad (2.61)$$

Therefore, the charge increment dQs results in a slight increase in the scr width. Combining 2.60 with 2.61, equation 2.62 is obtained:

$$C = -\frac{dQ_s}{dV} = -eA(N_A - N_D)W\left(\frac{dW}{dV}\right) \quad (2.62)$$

The capacitance of a reversed-biased junction, when considered as a parallel plate capacitor, is expresses as:

$$C = \frac{K_s \varepsilon A}{W} \qquad (2.63)$$

where ε is the dielectric constant and A is the contact area.

By differentiating 2.63 with respect to voltage and substituting dW/dV into 2.62, the doping concentration can be determined by 2.64.

$$(N_A - N_D) = -\frac{C^3}{eK_s \varepsilon A^2\left[\frac{d(C)}{dV}\right]} \qquad (2.64)$$

which sometimes is modiffied in form using the identity $\frac{d\left(1/C^2\right)}{dV} = -\left(\frac{2}{C^3}\right)\frac{dC}{dV}$ into:

$$(N_A - N_D) = \frac{2}{eK_s \varepsilon A^2\left[\frac{d\left(1/C^2\right)}{dV}\right]} \qquad (2.65)$$

A C-V curve is measured by a capacitance meter. Both equations, 2.64 and 2.65, can be used to determine the net acceptor concentration. The doping concentration is obtained from a C-V curve by taking the slope dC/dV or by ploting $1/C^2$ versus V and taking the slope $d(1/C^2)/V$. Sometimes the second method is preferred (equation 2.65) since it usually gives a more clear idea of the uniformity of the doping and it is usually easier to take the slope from the curves $1/C^2$-V. Since the

area of the contact appears in the equation 2.63, it is very important that the contact area should be precisely defined for an accurate concentration. After the capacitance has been measured, the scr width (W) can also be calculated by the equation 2.60.

Experimental details

For an electrical C-V measurements, an indium or a gold dot with a diameter varying from 400-600 um and thickness of about 100 nm (Fig. 2.28) was annealed (indium) or evaporated (gold) on the clean surface of a p-type sample using the vapor deposition machine (see section 2.2.2.7).

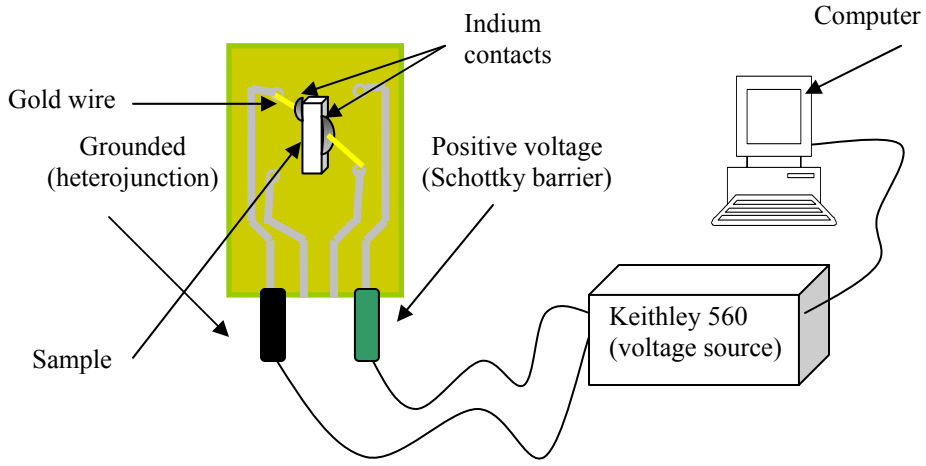

Figure 2.28. Representation of the setup of electrical C-V measurements.

A Keithley model 560 C-V instrument is used for the measurements. A dc voltage was varied from -2 V to 2 V or from -1 to 1 V and applied on the metal contact (Schottky barrier) while the ohmic contact (substrate side) is grounded. The capacitance is measured by superimposing a small-amplitude ac voltage υ on a dc voltage. The ac voltages can vary to different frequencies of 1 MHz, 100 KHz or 3.2 KHz and the amplitude was 10 or 20 mV. In general, a net acceptor concentration measured at lower ac frequency is higher and more accurate than that measured at

higher ac frequency.[58] Net acceptor concentrations are determined by taking the slope of the $1/C^2$ curve versus V and substituting the slope in the equation 2.65. Figure 2.29 shows an example of typical C-V and $1/C^2$-V curves of nitrogen doped ZnCdMgSe measured at ac frequency of 3KHz. By the equation 2.65, the N_A-N_D level of this sample has been calculated to be about $6.8x10^{15}$ cm^{-2}.

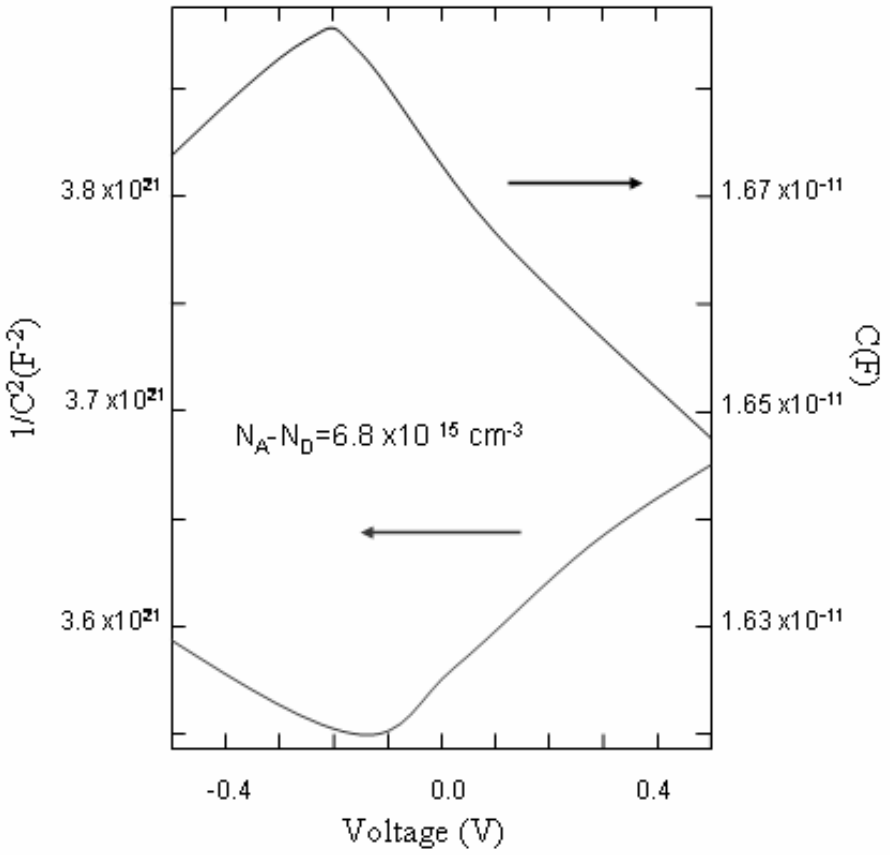

Figure 2.29. C-V and $1/C^2$-V curves of ZnCdMgSe:N sample measured with 3.2 KHz ac frequency.

2.2.2.10. Current-Voltage Measurements

Current-Voltage (I-V) measurements are fundamentally applied to characterize the behavior of contacts (ohmic: either ideal non rectifying barrier

contact or tunneling barrier contact, shottly diode contact and others) or to test the performance of devices or rudimentary (or preliminary) device structures (diode behavior, turn on voltage, device resistance to the current flow and others). The contacts for the Hall effect measurements must be tested before the measurement to determine their I-V characteristics. An ohmic contact is a low-resistance junction providing conduction in both directions between the metal and the semiconductor. Ideally, the current through the ohmic contacts is a linear function of the applied voltage (following the Ohm's law) and the applied voltage should be very small.

Experimental details

To test the I-V characteristics of the contacts, indium was annealed on the semiconductor surface (the entire procedure is explained in the section 2.2.2.6, the Hall measurements). For the I-V characterization of the LEDs, an indium dot or a gold with a ring shape, evaporated on the clean surface of a p-type side (surface) of the LED sample using the vapor deposition machine (see section 2.2.2.7), were used. After the evaporation, a small drop of indium served to solder the gold wire to the surface. Contact in the n-type of the LED structure was just melted indium (see Fig. 2.30). More details about the LED structures and experimental results will be given in the Chapter 4.

A Keithley source unit model 236 for the I-V measurements is employed to determine the I-V characteristics of the samples. The instrument can perform the measurements in two modes: applying the current and measuring the voltage with the voltmeter or applying the voltage and measuring the current with the ammeter, which

is the method used in this thesis. A sense cicuitry is used to constantly monitor the output voltage and executed the adjustments to the voltage source as needed. If the sense (measured) and the programmed value are not the same, the voltage source is adjusted accordingly. The voltage source can provide a voltage from ± 100 μm to ± 100 V while the ammeter can only measure currents of from ±10 fA to ±100 mA. The voltage range is set from -5 V to 5 V although sometimes, the range is smaller -2 V to 2 V or -1 V to 1 V. Setting the appropriate range at the beginning of the measurement is crucial to protect devices that are susceptible to damage by overvoltage (see Chapter 4, LEDs). There are two operations modes "sweep" and "dc operation", in which a constant dc voltage (or current) is applied. The measurement is taken in "sweep" operation mode in which the source measure unit sweeps through a user-defined list of points (usually 100 or 1000) in the voltage range determined previously. The user defines the number of points in the cited range, and the computer calculates the step size that must be considered for the measurement, or vice versa. In “sweep” mode, the waveform that is used in the measurements is “fixed level sweep”. In this mode, when the sweep is triggered to start, the ouput will go from the bias level (bias is the dc level that is maintained at the output when the sweep is not in progress) to the source level. The duration of this sweep is determined by the number of the points that have been selected (from 1 to 1000), the time period of the delay (fixed by the user) and the measurement time.

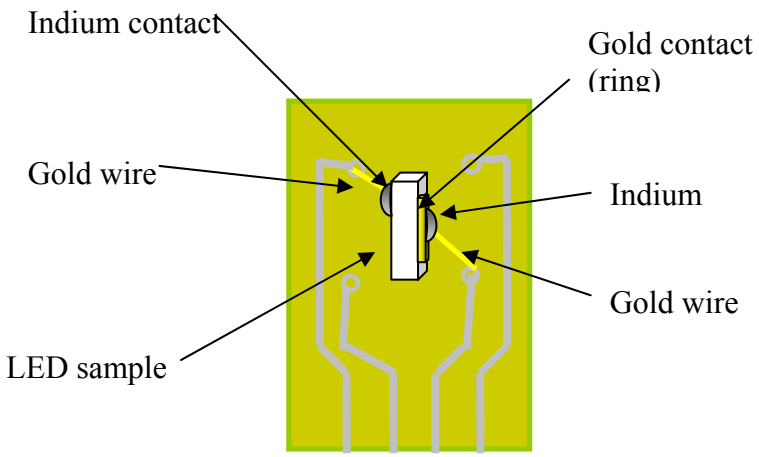

Figure 2.30. Schematic of the contacts on a LED sample.

Chapter 3. Growth of CdSe Single Quantum Dots Layers on ZnCdMgSe

3.1. Quantum Dots

3.1.1. Introduction

A quantum dot is a nanometer-scale inclusion of one semiconductor inside a second semiconductor with larger bandgap. Electrons and holes in the QD can occupy only a given set of states with discrete energies, as in an atom, which permits their utilization to do "atomic physics" experiments in solid state[61].

Extensive research has been carried out in the fabrication and applications of new low-dimensional heterostructures such as QWRs[62], QDs[63] and coupled arrays of MQDs[64] due to their potential advantages[65] (such as excellent lasing characteristics) compared to traditional semiconductor[14, 66] or QW-based devices[16, 17]. Although the advantages of low dimensional semiconductor heterostructures, were predicted about 30 years ago by Dingle and Henry (wavelength tunability, lower lasing threshold, maximum material gain and reduction of temperature influence in the device performance), experimental work and commercial applications of QDs and QWRs based-devices were still lag far behind those of QWs.

During the 1980s, a considerable portion of the physics scientific world was still moved by the applications of the two-dimensional (2D) QW heterostructures. At

this chronological moment, many scientists tried to explore systems of further reduced dimensionality, such as QWRs or QDs. Some experimental advances in the growth on misoriented[67] or patterned substrates[68] reactivated the interest in the growth of heterostructures with size-quantization in more than one direction. In 1982, Arakawa and Sakaki described the impact of the size quantization effects theoretically[69]. They introduced the concept of "three-dimensional quantum wells", which a year later were called "quantum boxes" (quantum dots), as artificial atoms where the electrons are confined in three directions. In this paper, these authors pointed also some of the principal advantages of these quantum-size heterostructures for laser applications. They predicted significant increase in the material gain, and a lower threshold current, less susceptible to temperature dependence than the conventional semiconductor lasers. The authors also investigated the dependence of the threshold current of a QW laser (placed in high magnetic fields) with the temperature. They proposed as possible solution the utilization of one dimensional or zero dimensional heterostructures in the active region of the laser, with the purpose of either decreasing the temperature dependence of the threshold current for the QWR-based lasers, or totally avoiding any dependence (full temperature stability) for the QD case.

It was not until 1983 when the first semiconductor dots based on II-VI microcrystals in glass matrix were proposed and demonstrated by Ekimov and Onushchenko[70]. However, the quality of the interface between glass and semiconductor dot was not high, which limited their device applications. Another approach extensively used for the fabrication of QDs is based on colloidal solutions.

Colloids of CdS and CdSe QDs have been demonstrated and their optical properties have been studied.[71, 72, 73] Fluorescence within the visible range was obtained and associated to the highly tunable nature of the QD size. However, there are still some problems such as the size dispersion, device integration and the stability of some of the semiconductor colloidal solutions.

Possibilities that are much more exciting appeared when QDs grown by a three-dimensional (3D) growth mode (3D QDs) were fabricated in a semiconductor matrix. A great technological revolution happened with the development of new growth techniques, such as MBE or MOCVD. Subsequently, several methods (indirect and direct methods) were proposed for the fabrication of QD structures by means of either the so called top-down or bottom-up approaches. Indirect methods, such as the post-growth lateral patterning of 2D QWs or the well-known growth on patterned substrates[74], obtained for example for selective ion etching, often suffer from insufficient lateral resolution and interface damage caused by the formation of nonradiative defects produced during etching or the patterning procedure. This leads to degradation the material quality, which results in unsuitable structures for device applications. In addition, these methods are usually expensive methods and/ or require complicate processing. A more promising way of fabrication is by direct methods, such as the growth in V-grooves or on corrugated surfaces, which may result in the formation of QWRs or QDs structures[75]. The disadvantage of this kind of techniques is that the number and quality of the grooves, sometimes influence the optical properties of these nanostructures (broad PL emission and low PL intensity)[76].

Although all these methods can be applied for the fabrication of low-dimensional heterostructures, the formation of QDs or QWRs by self-organization process is one of most exciting techniques of formation of these nanostructures. This fact is not only for its technological advantages (reduced cost, low processing time and less fabrication requirements) but also for the interest in the study of the physical phenomena of the QD spontaneous formation. The effect of the spontaneous islanding in the InAs/GaAs system was already known before the mid-1980s. However, the self-assembling technique did not attract much attention for optical devices applications, because it was considered too difficult to produce dislocation-free QDs with sufficiently uniform size and shape. In the 1990's, both selective growth and self-assembled growth techniques which can avoid nonradiative defects were well heavily investigated. Particularly, the Stranski-Krastanow growth mode was shown to be very successful for In (Ga)As/GaAs systems. This self-assembled growth for making nanoscale islands led to a breakthrough to QD devices, specifically, in the scope of the laser applications. Fig. 3.1 shows the development of QDs lasers with respect to the traditional double heterostructure and QW-based semiconductor lasers (a detailed description of the present state-of-the art in QD lasers may be found in different reviews Ledentsov[77] and Bimberg et al[78]).

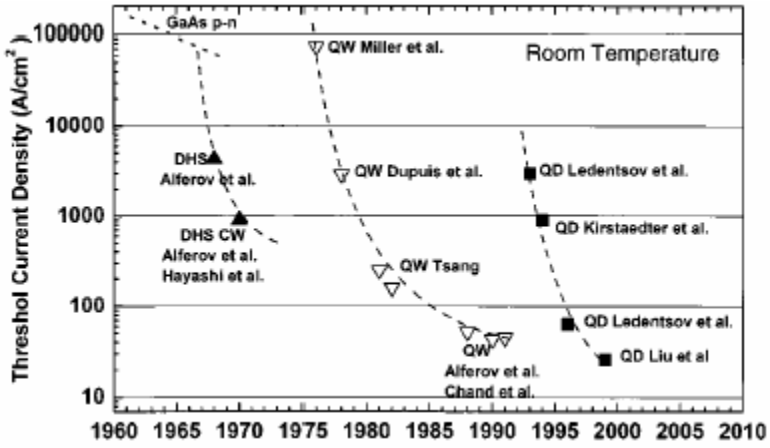

Figure 3.1. Development of the heterostructure lasers. Results marked in the figures were reported in the original papers. Double heterostructure (DHS) lasers.[79, 80, 81] QW lasers. [82, 16, 17, 83, 84, 85, 86] QD lasers.[88, 89, 87] Results are dated according to the year of submission, which is different that the publication date given in the references.

After the experimental demonstration of lasing in self-organized QDs appeared in December 1993,[88] QDs were not only incorporated successfully to laser structures (first laser reported by N. Kirstaedter et al.)[89] but also to other devices, such as light emitted diodes and detectors for both inter-band and inter-subband transitions, quantum cascade lasers, and high-frequency two- and three-terminal devices based on Esaki-Tsu superlattices. In(Ga)As/GaAs QD lasers with high performance lasing characteristics have been successfully demonstrated. Low threshold current density of 21A/cm^2, high T_0 up to 385K, and high differential gain at room temperature were reported. A record in transparency current 6A/cm^2, internal losses as low as 1.5 cm^{-1} and high quantum efficiency of 98% were also demonstrated.[90] Furthermore, 1.3-1.55 μm lasing wavelength range has been achieved, which is significant for low-cost lasers for access network communication systems utilizing GaAs substrates. Vertical cavity surface emitting lasers (VCSELs) with QDs have been also demonstrated[91],

representing a promising technological solution for large MBE production since they do not require specific nitrogen plasma sources (as the competitive InGaAsN system).

Regardless of this fast development and advances in the III-V QD systems and devices, these systems are focused mainly on the infrared technology so other materials systems must be explored to cover the UV and the visible range of the spectrum. Recently, new material systems, such as II-VI semiconductors and GaN-based III-V semiconductors were also studied for for short wavelength range applications. In particular, GaN based have received great attention for applications to blue and UV light emitting lasers. Arakawa et al. have been recently achieved the growth of InGaN QDs on GaN epitaxial layers and the operation at room temperature of a photopumped laser structure based on this type of QDs[92]. The family of (311) faceted surfaces of GaAs and AlAs and corresponding corrugated superlattices were studied for optical applications from the green to red range of visible spectrum[93] while CdSe/ZnSe QDs were fabricated for applications in the blue and green regions.

Despite all the advances in the QD growth formation and the incorporation to devices structures, the possibility of using a single technology to cover the entire visible spectrum and even reach the UV wavelengths with a unique QD material system has not been achieved. A QD system whose size and, consequently, the PL spectrum emission are easily controllable and reproducible by changing slightly the conditions of the growth is desirable in terms of easier incorporation on a large MBE device production. Furthermore, the possibility of combining diverse QDs layers with different QD size (either individually or in the same structure) for the fabrication of integrated red-green and blue optical devices or white light sources through the

mixture of the three primary colors, offers an exceptional and promising way to substitute current complex fabrication designs for this kind of applications.

3.1.2. Physics Background

The understanding of the quantum physics governing the physical properties of these nanostructures is important to be able to obtain the maximum profit from their quantum characteristics. If the size of the periodic potential field (or the crystal) is reduced in any dimension to a scale comparable to some characteristic length L (λ), the electron will posses discrete states in this direction instead of continuous levels as in the energy bands[94]. The quantum nature of these low-dimensional structures can become evident if the separation of the electronic energy levels becomes comparable to the energies themselves, in contrast to the case of a bulk solid where the allowed energy levels within an energy band are essentially continuous. This situation corresponds to quantum confinement of electrons within the structure. Classical mechanics is not able to explain the dependence on dimensionality of wavefunctions, energy levels, density of states, and Fermi wave vectors K_F (maximum value for occupied k's) for spatially confined electrons in two dimensions (QW), one dimension (QWR) and zero dimensions (QD). Quantum mechanics must be used instead of the classical approximation.

Considering the quantum mechanics approximation of "a particle in a box": inside of the box the potential is equal to zero (V=0) while outside the box it increases to an infinite value (V=∞). The wavefunction that describes the electronic motion can undertake only certain standing-wave patterns, with a corresponding discrete set of

energy levels. In other words, the energy of the electron is quantized by the potential well (see Fig. 3.2)

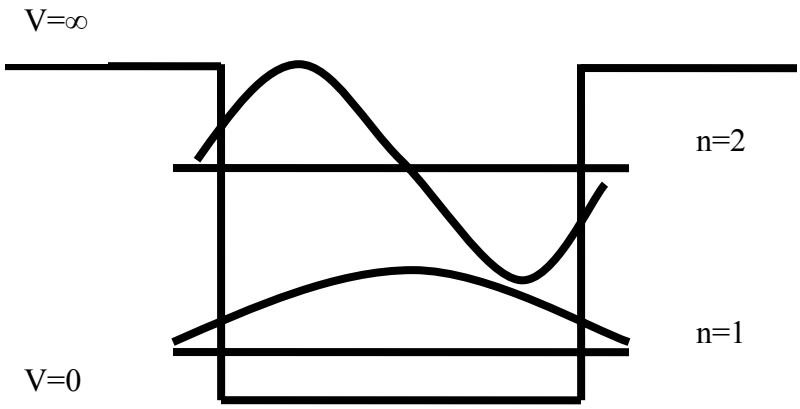

Figure 3.2. Particle in a box.

Structures with reduced dimensionality can be approximated adequately by this "particle in a box" problem (see Fig. 3.3). These nanostructures are semiconductor heterostructures, or composite crystals of at least two semiconductor materials with different bandgaps, where potential profile of the "particle in a box" can be simulated by a variation in the bandgap. For example, a quantum dot consists in a "small dot" or "cage" of a semiconductor material with a narrower bandgap surrounded by another semiconductor material with a wider bandgap. The electrons and holes are confined or trapped in the low-bandgap material by the effective potential well (e.g., in part c of Fig. 3.3, in the limit, particles are confined within the region of the box with potential, V=0).

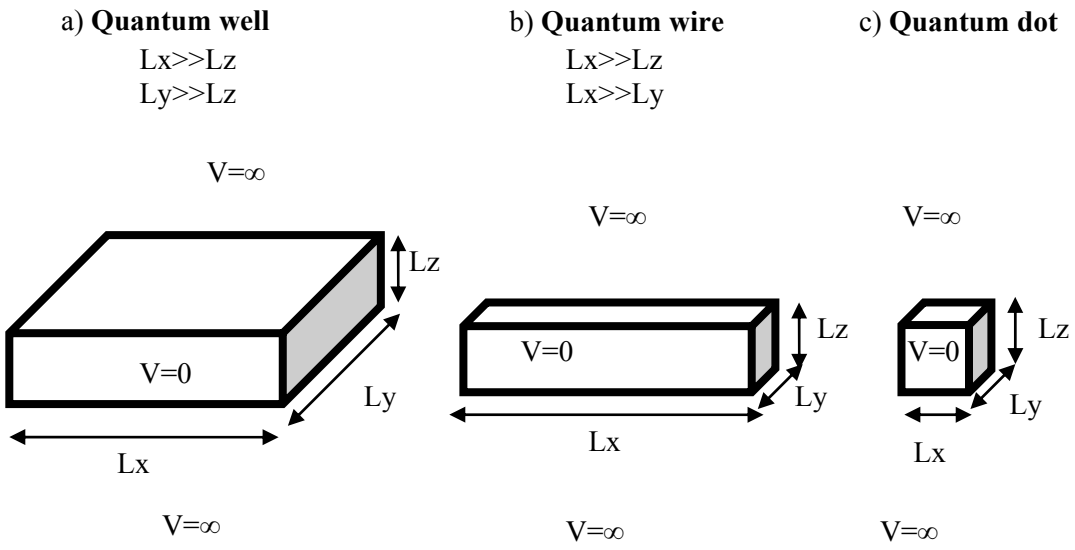

Figure 3.3. Materials with low dimensionaly d in which electrons are confined: a) a quantum well (d=2), b) a quantum wire (d=1), and c) a quantum dot. The outside boundaries of these regions are infinite potential barriers.

Besides the considerations about the confinement of the carriers in the potential well given by the "particle in a box" approximation, the states of electrons and holes in these heterostructures can generally be described using a modified version of the Bloch's theorem, known as the envelope approximation. In this approximation, the particle wavefunction $\psi\left(\vec{r}\right)$ is written as a product of a periodic part $u\left(\vec{r}\right)$ and an envelope wavefunction $\chi\left(\vec{r}\right)$:

$$\psi\left(\vec{r}\right) = u\left(\vec{r}\right)\chi\left(\vec{r}\right) \tag{3.1}$$

On one hand, the Bloch function $u\left(\vec{r}\right)$ repeats with the periodicity of the lattice and can be calculated taking into account symmetry considerations of the crystal lattice. In CdSe, ZnSe and MgSe binaries systems constituents of the

ZnCdMgSe system, the $u(\vec{r})$ is an s-like wavefunction for electrons in the conduction band, and a p-like wavefunction for holes in the valence band.

On the other hand, the envelope function $\chi(\vec{r})$, can often be described using the effective mass approximation:

$$\left[-\frac{\hbar}{2m*}\forall^2 + V(\vec{r})\right]\chi(\vec{r}) = E\chi(\vec{r}) \tag{3.2}$$

$$E(k) = E(k_x) + E(k_y) + E(k_z) \tag{3.3}$$

where E(k) is the carrier energy. This equation of motion is equivalent to the ordinary Schrödinger equation, except that the particle mass has been replaced by an effective mass m*, and the potential $V(\vec{r})$ corresponds to the energy of the appropriate band edge. Thus, $V(\vec{r})$ is the bottom of the conduction band for electrons, and it is the top of the valence band for the holes.

Solving this equation for the QW case, considering infinite potential barriers as "the particle in a box" problem, the electronic wavefunction $\psi(\vec{r})$ and the energy E (k) can be obtained:

$$\psi(\vec{r}) = A(\sin k_z x)e^{i(k_x x + k_y y)} \tag{3.4}$$

$$E(k) = \frac{h^2 n_z^2}{8m_e^* L_z^2} + \frac{\hbar^2(k_y^2 + k_x^2)}{2m_e^*} \tag{3.5}$$

It can be noted that just for confining the electron in one direction L_z, its ground state energy corresponding to n_z=1 is increased above the unconfined value by

an amount equal to $\frac{h^2}{8m_e^* L_z^2}$ due to the quantum confinement. This amount decreases rapidly if L_z decreases. This effect is explained considering the Heisenberg uncertainty principle, which states that a particle confined within a region of size L_z will have a resulting minimum uncertainty in its momentum given by $\Delta p_x \approx \frac{\hbar}{L_x}$. The corresponding minimum in its energy, the zero point energy, will therefore be $\Delta E \approx \frac{(\Delta p_x)^2}{2m_e^*}$, which corresponds to the ground-state given above.

For the QWR case, $\psi(\vec{r})$ and E (k) are:

$$\psi(\vec{r}) = A(\sin k_y y)(\sin k_z z)e^{i(k_x x)} \tag{3.6}$$

$$E(k) = \frac{h^2}{8m_e^*}\left(\frac{n_y^2}{L_y^2} + \frac{n_z^2}{L_z^2}\right) + \frac{\hbar^2(k_x^2)}{2m_e^*} \tag{3.7}$$

and for the QD case:

$$\psi(\vec{r}) = A(\sin k_x x)(\sin k_y y)(\sin k_z z) \tag{3.8}$$

$$E(k) = \frac{h^2}{8m_e^*}\left(\frac{n_x^2}{L_x^2} + \frac{n_y^2}{L_y^2} + \frac{n_z^2}{L_z^2}\right) \tag{3.9}$$

with $n_x, n_y, n_z = 1, 2, 3....$ for the all the equations.

In contrast, the wavefunction and energy for the bulk are given by the expressions:

$$\psi(\vec{r}) = Ae^{i(k_x x + k_y y + k_z z)} \tag{3.10}$$

$$E(k) = \frac{\hbar^2(k_x^2 + k_y^2 + k_z^2)}{2m_e^*} \tag{3.11}$$

For the equations 3.4-3.11, it is assumed the electrons occupied a parabolic band with effective mass m_e*. Replacing m_e* by m_h*, analogous expressions are obtained for the confinement of the hole.

Similarly, the density of states is also affected directly by the dimensionality of the system:

For a three-dimensional system (bulk semiconductor) the density of states has the form:

$$\rho_e(E) = \frac{dN}{dE} \propto \frac{d}{dE} E^{3/2} = E^{1/2} \tag{3.12}$$

However, in a two dimensional system (QW) it is a step function,

$$\rho_e(E) = \frac{dN}{dE} \propto \frac{d}{dE} \sum_{\varepsilon_i < E} (E - \varepsilon_i) = \sum_{\varepsilon_i < E} 1 \tag{3.13}$$

For a one-dimensional system (QWR) it has the form:

$$\rho_e(E) = \frac{dN}{dE} \propto \frac{d}{dE} \sum_{\varepsilon_i < E} (E - \varepsilon_i)^{1/2} = \sum_{\varepsilon_i < E} (E - \varepsilon_i)^{-1/2} \tag{3.14}$$

And for a zero-dimensional system (QD) it has δ-function shape,

$$\rho_e(E) = \frac{dN}{dE} \propto \frac{d}{dE} \sum_{\varepsilon_i < E} \Theta(E - \varepsilon_i) = \sum_{\varepsilon_i} \delta(E - \varepsilon_i) \tag{3.15}$$

where ε_i are discrete energy levels, Θ is the Heaviside step function, and δ is the Dirac function. Obviously, the reduction in the freedom of motion in low-dimensional structures significantly modifies the density of states, as illustrated schematically in Fig. 3.4. In contrast to higher dimensional structures, such as bulk crystal materials,

and even QWs and QWRs, in which the density-of-states is a continuum in energy for at least some directions, QDs have atomic-like discrete energy states, and the physical properties of QDs in many, although not all, respects resemble those of an atom in a cage. A profound size-dependent change of all macroscopic material properties as compared to the bulk occurs. For QDs, as a consequence of the discrete nature of the energy spectrum, optical transitions between these states are expected to be extremely narrow in energy, with their line width becoming much less sensitive to increasing temperature (although the population of the different states will of course depend on temperature). This feature, together with increased carrier localization due to the confinement in all three dimensions, which results in a major enhancement of optical transition matrix elements, holds promise of significant improvements in optical and electronic device applications involving QDs. Indeed, device configurations involving SAQDs fabricated from III-V semiconductors,[77, 78] have already exhibited many superior properties over structures based on QWs.

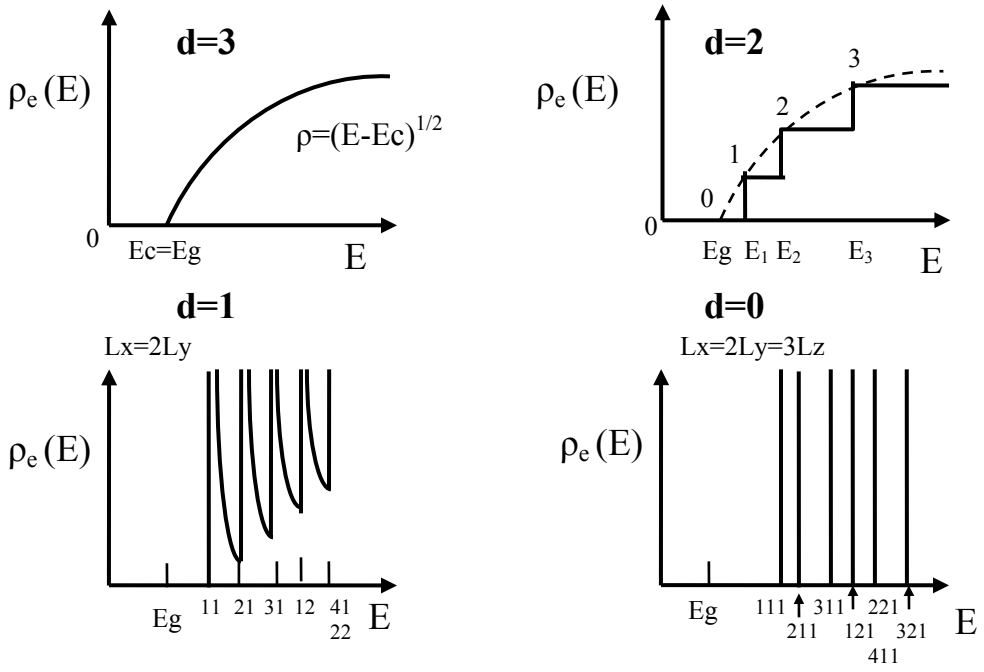

Figure 3.4. Density of states for charge carriers in structures with different dimensionalities.

3.1.3. Modes of Growth

In the equilibrium theory of the heteroepitaxial growth, three growth processes are traditionally distinguished[95]. They are the Frank-van de Merwe (FM)[96], Volmer-Weber (VW)[97] and Stranski-Krastanow (SK)[98] growth modes. These growth modes may be described, respectively, as layer-by layer growth (2D), island growth (3D), and layer-by-layer growth plus islands (see Fig. 3.5). The particular growth mode for a given system depends on the interface energies and the lattice mismatch.

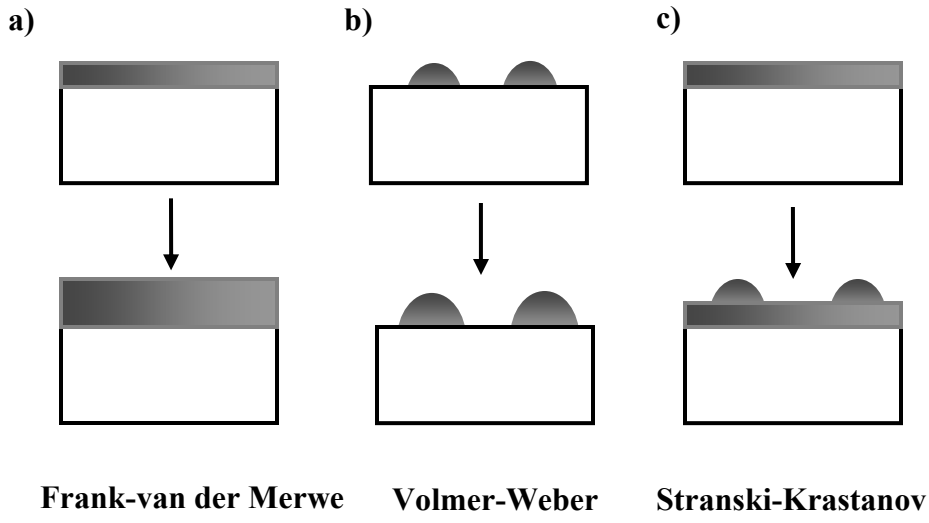

Figure 3.5. Schematic of the three growth modes for heteroepitaxial systems. a) Frank-van der Merwe (FM), b) Volmer Weber (VW), and c) Stranski-Krastanow.

In the lattice-matched systems, the growth mode is governed by the interface and surface energies only. If the sum of the epilayer surface energy γ_2 and the interface energy γ_{12} is lower than the energy of the substrate surface, $\gamma_2 + \gamma_{12} < \gamma_1$, i.e., if the deposited material (2) wets the substrate (1), the FM mode occurs. A change of $\gamma_2 + \gamma_{12}$ value may drive a transition from the FM to the VW growth mode where 3D islands are formed on the bare substrate. For a strained epilayer with small interface energy, initial growth may occur by layer-by-layer, but a thicker layer has large strain energy so the elastic energy tends to be reduced via formation of isolated islands. In these islands the elastic strain is released and, correspondingly, the elastic energy decreases. Thus the SK growth mode occurs. The characteristic size of the islands is determined by the minimum in the energy of the array of 3D coherently strained islands per unit surface area as a function of the island size. Due to the stringent requirements of such controlled thin layer deposition, the SK growth mode eluded the

crystal growth community for a long time. Recent developments in epitaxial techniques, such as metal-organic chemical vapor deposition (MOCVD) and MBE, have finally made it possible to control layer deposition to the degree required by the SK process. By making the self-assembling processes possible, these advances have in effect opened a new era in nanostructure fabrication, making zero-dimensional geometries a very practical reality.

3.2. Equilibrium and Kinetics of SAQDs Formation

3.2.1. Introduction

Spontaneous formation of nanostructures is subject of intense experimental and theoretical studies. The first theoretical models to describe spontaneous formation of nanostructures were given to explain the formation of the periodic faceting of vicinal[99, 100], low index and high index surfaces[101]. The formation of three-dimensional islands was explained in later theoretical review papers. V. A Shchukin[102] et al. studied the spontaneous ordering of arrays of coherent strained islands neglecting the presence of the wetting layer. These authors found that the equilibrium of the system will go towards the formation of stable islands or towards the ripening, depending on the material constants and the misfit. By contrast, I. Daruka et al.[103] incorporated the existence of the wetting layer and predicted the growth mode, phase diagram, and stability of the three dimensional SAQDs dependent on the coverage and the misfit.

This section will illustrate two models for the formation of CdSe SAQDs over ZnCdMgSe barriers, providing a guide to explain the results obtained with this new QDs system.

3.2.2. Models and Energetic Considerations

The formation of SAQDs usually comprises two parts: formation of the wetting layer (which is sometimes missing) and development of the spontaneous islands. If both are present, both should be taken into account consideration to explain the properties of the dots.

In the first part of this section, a model considering the binding energies of the materials will be discussed to explain some of the factors that can contribute to the formation of different thicknesses of wetting layer. The second part of this section will present a model from the thermodynamics point of view that will illustrate the parameters that control the size and density of the QDs.

3.3.2.1. Wetting Condition Model

As mentioned in the above section, the growth on lattice-mismatched substrate can result in the formation of three-dimensional islands, either on the bare substrate surface for Volmer-Weber growth mode or on the wetted surface for coherent Stranski-Krastanov. The formation of SAQDs is often described as a process where M monolayers (ML) of atoms of one material (A) are deposited on a substrate (material B) with a different equilibrium lattice constant than the deposited material.

Therefore, the lattice mismatch between these materials is $\varepsilon = \frac{(d_A - d_B)}{d_B}$. Assuming, the desorption rate is very low. Thus, it is possible to define a "surface equilibrium" in which the substrate works as a thermal bath with a fixed temperature T, the number of adsorbed atoms on the surface is fixed, atoms do not desorb, and no exchange processes occur between adatoms and substrate atoms. Therefore, the condition for the existence of this surface equilibrium can be expressed as:

$$t_{eq} << t_{des} \qquad (3.16)$$

The equation 3.16 states that the time needed for the surface to reach this equilibrium, t_{eq}, should be considerably shorter than the desorption time, t_{des}. This basic assumption, which is a reasonable approximation in QDs fabricated by self-assembly (SA) using MBE at low temperatures, is implicit in this model and in the model described in the section 3.3.2.2 .

Then, it is possible to introduce a growth interruption (GI) such that:

$$t_{eq} << t_{GI} << t_{des} \qquad (3.17)$$

Therefore, a growth interruption t_{GI} will drive the system to the "surface equilibrium" described above. In this equilibrium, a certain fraction of the atoms A will form a wetting film of n_A monolayers and the remaining of the material (M-n_A) monolayers will be distributed in the 3D islands. Let us assume that n_B represents the number of atoms in fully coherent islands. Therefore, the atoms in the ripened islands will be given by M-n_A-n_B. Neglecting evaporation and considering that the deposited material represents a conserved system in equilibrium with a thermal reservoir, the relevant thermodynamical potential density is the free energy per atom:

$$f = u - Ts \qquad (3.18)$$

where u is the internal energy density (total energy per unit cell of the substrate), T is the temperature, and s is the entropy density of the system. The entropy contribution can be demonstrated negligible.[103] Therefore, equation 3.19 is obtained:

$$f \approx u \qquad (3.19)$$

The u can be defined as:

$$u(M, n_A, n_B, \varepsilon) = n_B E_{island} + (M - n_A - n_B)E_{rip} + E_{WL}(n_A) \qquad (3.20)$$

The first term describes the free energy per atom of the QDs islands and island-island interaction. This term is function of the number of the atoms in the islands, n_B. The second term takes into account the total energy density of the ripened islands and is a function of the total number of atoms stored in these ripened islands ($M-n_A-n_B$). An extensive explanation about the first two terms can be found in references 102, 103, 100, 104.

The last term is the one related to the wetting layer formation, its energy and its thickness. The third term provides the energetic contribution of the n_A strained monolayers (wetting layer) to the internal energy density of the system. Equation 3.21, takes into account the different parameters that must be included in this term, implying an integral over the binding and elastic energy densities[103]:

$$E_{WL}(n_A) = \int_0^{n_A} \left\{ G + \Delta \left[\Theta(1-n) + \Theta(n-1)e^{\frac{-(n-1)}{a}} \right] \right\} dn \qquad (3.21)$$

where $\Theta(x)$ is a function of the x value inside its parenthesis:

$$\Theta(x) = 0 \text{ if } x<0 \qquad (3.22)$$

$\Theta(x) = 1$ if x≥0 (3.23)

The parameter *a* is associated to the short range forces. Its physical meaning is the characteristic attenuation length of the interatomic interaction. The limit a=0 corresponds to the absence of these forces.

The parameter G is the energy density of a uniformly strained layer, which given by equation 3.24:

$$G = C\varepsilon^2 - \phi_{AA} \qquad (3.24)$$

where $-\phi_{AA}$ is the energy of a chemical bonds, A-A bonds, in the bulk of the deposited material A, defined per atom and C is the material constant, being a function of the Young's modulus and the Poisson ratio. At the wetting layer-substrate interface, chemical bonds between the substrate atoms and film atoms, A-B bonds, are formed. The binding energy of the AB bonds is $-\phi_{AB}$. Therefore, the wetting condition is:

$$\Delta = -\phi_{AB} - (-\phi_{AA}) = \phi_{AA} - \phi_{AB} < 0 \qquad (3.25)$$

Due to the finite range of intermolecular interactions, the binding energies of the atoms in the film in the second and successive monolayers are also modified. As the atoms that form part of the material A are getting away from the substrate their binding energy density increases from $-\phi_{AB}$, in the first monolayer of deposited material A on the substrate B, to an asymptotic value that represents the binding energy of only material A, $-\phi_{AA}$. This explains the reason that the critical thickness of the growth of heteroepitaxial QDs is usually more than one monolayer. In addition, this expression can be useful to describe some factors that influence the thickness of

the wetting layer. Changing the binding energy density in the interface between the substrate and the material ($-\phi_{AB}$), the wetting layer condition will be modified. For the same deposited material A and for no fundamental change in the binding energy of the material ($-\phi_{AA}$), if the absolute value $\left|-\phi_{AB}\right|$ is increased the thickness of the wetting layer will be larger. The inequality 3.25 will be more negative for a higher value of $\left|-\phi_{AB}\right|$, more material A must be deposited to reach the value $-\phi_{AA}$ (critical thickness).

To summarize, equation 3.20 defines the total energy of the wetting layer and three dimensional islands, where the latter exhibits bimodal behavior, i.e., both small islands with a optimal size (coherently strained) and large islands of a size considerably larger than this optimal size (ripened islands) may be present in the system. By minimizing the energy 3.20 with respect to n_A (weeting layer atoms) and n_B (atoms that form 3D coherently strained islands) and considering the corresponding parameters of island shape, the equilibrium phase diagram of the lattice-mismatched heteroepitaxial system as a function of the lattice mismatch and the total amount of the deposited material M can be obtained.

The Fig. 3.6 represents the phase diagram for 3D pyramidal shape islands obtained by Dakura et al.

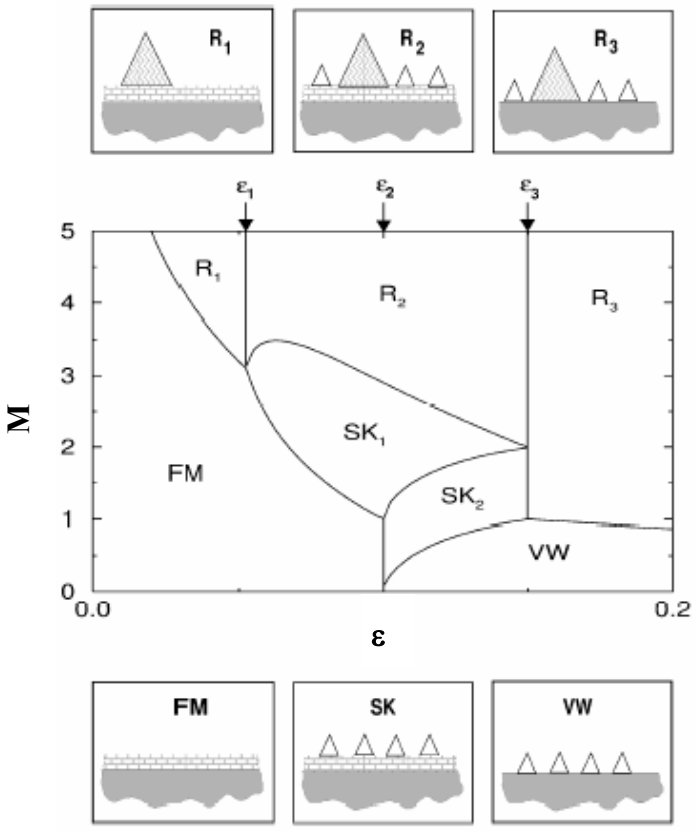

Figure 3.6. Equilibrium phase diagram of a lattice-mismatched heteroepitaxial system as a function of the total amount of the deposited material M and the lattice mismatch ε. The small panels at top and bottom illustrate the morphology of the surface in the six growth modes. Small islands indicate the presence of coherently strained islands without dislocations while large shaded ones refer to ripened islands. The figure was obtained from the reference 103.

3.3.2.2. Thermodynamic Model

A thermodynamic model is necessary to understand not only the critical size and density of the islands that are formed by SA but also the factors that can be modified (or controlled) to obtain other critical parameters, smaller island size or higher density, which are fundamental for optical applications.

Considering a solid nucleation process from the vapor phase, small nuclei are thermodynamically unstable since the surface energy cost of forming small nuclei exceeds the energy gain coming from the crystallization from a vapor phase. This result, in fact, resembles the same phenomenon of a liquid drop in a solid surface. The large-surface-to volume ratio drops will be energetically more unstable. Therefore, the small nuclei will become smaller and smaller and, finally will disappear while large nuclei continue to grow. In other words, there is a size of nuclei capable of forming thermodynamically stable clusters, called critical radius, and other sizes that are unstable.

Gibbs was the first to realize that the formation of a new phase requires the appearance of clusters beyond a certain size as the prerequisite of forming the new phase.[121]

Considering the formation of QDs, for example CdSe QDs over ZnCdMgSe barriers, the variation of the Gibbs free energy, ΔG, as a result of the formation of the nuclei from the vapor phase, principally implies four terms: a bulk term, a surface term, an interface term, and a strain energy term.

$$\Delta G = \Delta G_{bulk} + \Delta G_{surface} + \Delta G_{\text{interface}} + \Delta G_{\text{strain}} \qquad (3.26)$$

The bulk term is originated from the energy gain resulting from the vapor crystallization process. The surface term is due to the energy cost upon creating surfaces of nuclei (i.e. surface energy). In the reference 105, the change of the Gibbs free energy, ΔG, upon the formation of the nuclei from a vapor phase is given by:

$$\Delta G = -N\Delta\mu + \sum_i S_i\sigma_i + \Delta G_{\text{interface}} + \Delta G_{\text{strain}} \qquad (3.27)$$

where N is the number of atoms in the nuclei, $\Delta\mu$ a chemical potential difference between the vapor and solid phase, σ_i a surface energy density of a plane i, and S_i an area of a plane i.

For simplicity, suppose the nucleation process of liquid droplets on a structureless substrate with a supersaturated vapor phase. The liquid droplet represents a segment of a sphere with radius r and a projected radius $r\sin\theta$, where θ is the wetting angle. For this system, the equation 3.27 is written as:

$$\Delta G(r) = -\frac{4\pi r^3}{3}\frac{(1-\cos\theta)^2(2+\cos\theta)}{4}\frac{\Delta\mu}{\upsilon} + 2\pi r^2(1-\cos\theta)\sigma + \pi r^2\sin^2\theta(\sigma_{\text{int}} - \sigma_{sub}) \tag{3.28}$$

where υ is the molar volume of the liquid, σ and σ_{sub} are the surface energies of the droplet and the substrate, respectively. The σ_{int} is the substrate-droplet interface energy. Here, the strain term is neglected. Taking into account the Young relation given in the reference, $\sigma_{\text{int}} - \sigma_{sub}$ can be expressed as equation 3.29:

$$` \ (\sigma_{\text{int}} - \sigma_{sub}) = -\sigma\cos\theta \tag{3.29}$$

Then, equation 3.28 will be :

$$\Delta G(r) = -\frac{4\pi r^3}{3}\frac{f(\theta)}{\upsilon}\Delta\mu + 4\pi r^2 f(\theta)\sigma \tag{3.30}$$

where $f(\theta)$ is called the wetting function:

$$f(\theta) = \frac{1}{4}(1-\cos\theta)^2(2+\cos\theta) \tag{3.31}$$

The wetting function $f(\theta)$ accounts for the catalytic potency of the substrate with respect to nucleation formation, and is identical to the ratio of the volume of the segment (droplet) to that of the entire sphere. The Fig. 3.7 shows how $\Delta G(r)$ changes as a function of r. From Fig 3.7, it is found that the function $\Delta G(r)$ reaches a maximum at $r = r_g^*$ given by:

$$r_g^* = \frac{2\sigma\upsilon}{\Delta\mu} \qquad (3.32)$$

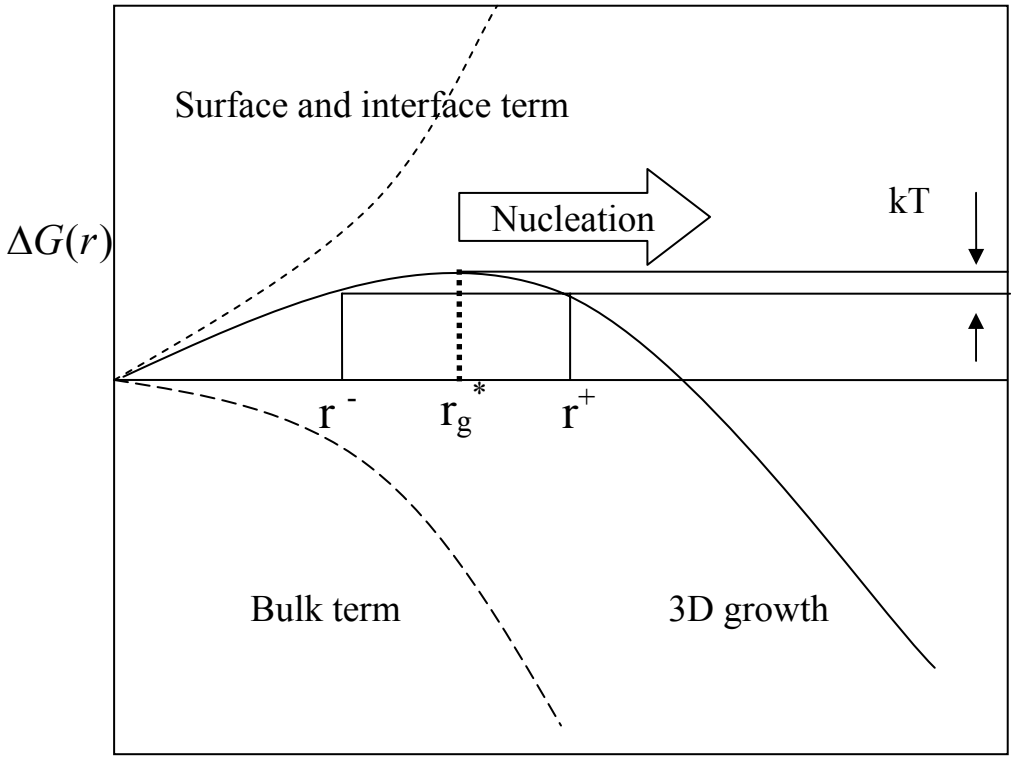

Figure 3.7. Plot of the change of the Gibbs free energy $\Delta G(r)$ upon the formation of nuclei from a vapor phase as a function of a radius *r* of liquid droplets.

without depending on the wetting layer angle θ, r_g^* gives the condition for the equilibrium of the droplet with the vapor, and is called critical radius. Of course, this equilibrium is unstable. When a droplet has a smaller radius than r_g^*, decreasing the size of the droplets is an energy gain process. In contrast, when a droplet has a larger radius than r_g^*, the probability of size reduction becomes smaller than that of growth. Therefore, droplets continue the growth.

In addition, from the equation 3.32 and from the Fig. 3.7, we can see that if the surface term and the interface term change, the critical radius of the droplet will be affected. If the value of σ is substituted in equation 3.32, the equation 3.33 is obtained:

$$r_g^* = \frac{-2\upsilon(\sigma_{\text{int}} - \sigma_{sub})}{\cos\theta\Delta\mu} = \frac{2\upsilon(\sigma_{sub} - \sigma_{\text{int}})}{\cos\theta\Delta\mu} \quad (3.33)$$

A smaller σ_{sub} (surface energy of the substrate) or higher σ_{int} (substrate droplet-surface energy), the r_g^* will be smaller. In other words, if a growth parameter or chemical factor will affect one of these components in the correspondent direction, the critical radius will be smaller.

Taking into account all this, it is possible to discuss which are the growth factors that affect the size of the islands. After the 3D nucleation takes place, the islands will be distributed around the vicinity of the critical radius size r_g^*. Considering all the parameters in the equation 3.33, it turns out that the issue is to understand how $\Delta\mu$ depends on the growth conditions.

Using the pressure of a vapor phase P_v and the equilibrium pressure of infinite large crystal P_c^e at a given temperature, $\Delta\mu$ is represented in the form:

$$\Delta\mu = K_B T \ln \frac{P_v}{P_c^e} \qquad (3.34)$$

As it can be inferred from equation 3.33 and 3.34, the size of the islands depends on the growth temperature. Increasing the growth temperature, P_c^e becomes higher and higher. The resultant decrease of $\Delta\mu$ causes a larger critical radius r_g^*. In other words, increasing the growth temperature at a fixed growth rate leads to the nucleation of larger islands. Another growth factor that is also relevant for the value of $\Delta\mu$ is the growth rate. Higher growth rate means higher vapor pressure P_v, (higher flux) resulting in smaller critical radius through the increase of $\Delta\mu$. Higher flux is reflected in a higher density of mobile adatoms in the surface, which will rather nucleate new islands instead of attaching to the existing ones. Therefore, an increase of the growth rate will yield a higher density and smaller islands. The change of the vapor pressure of a determined element in excess is other way to modify the size of the islands that can also be explained using this thermodynamic relationship.

In summary, any growth factor that affects directly the $\Delta\mu$ will be a direct factor to consider in the formation of SAQDs. The next section will illustrate some results obtained in this research related to the control of the morphological properties of CdSe QDs over ZnCdMgSe barriers demonstrating the applicability of some of these parameters.

3.3. The Control of the Morphology in CdSe/ZnCdMgSe SAQDs

As mentioned in the introduction, important advances in the fabrication and incorporation of QDs to devices structures have been recently achieved using different methods[106, 107, 108]. Among these, SAQDs grown by MBE growth offer some advantages. The MBE technique allows the control of the alloy composition and growth rate of the QDs and in addition, permits the monitoring of the growth in real time by using RHEED. The SAQDs formed by the Stranski-Krastanow mode have been fabricated by MBE in group-IV[109, 110] and group III-V semiconductors[111,112,113]. The II-VI semiconductors, such as CdSe/ZnMnSe[114], CdSe/ZnSe[46, 115, 116], CdSe/ZnBeSe[9, 115, 116], ZnCdSe/ZnSe[117], CdTe/ZnTe[118] and ZnSe/ZnS[119] have recently been extensively explored due to the higher exciton binding energy and the wider energy band gap that these materials offer[120]. However, the control and reproducibility in the size of the QDs in this type of materials continue to be drawbacks as regards future device applications. Worldwide research efforts have been directed toward understanding, controlling, improving, and exploiting shape, size, density, and spatial arrangement of islands, since such geometric properties of QDs are closely related to their electronic properties[121]. Some material characteristics such as surface energies, surface stress, and lattice mismatch between material deposited and substrate (matrix material) and other chemical parameters often govern the density, shape and dimension of quantum dots arrays. It has been found that substrate temperature, amount of material deposited on the matrix, growth

interruption after the QD material deposition and sometimes vapor pressure of a determined element (for a III-V material, vapor pressure of the group V and for a II-VI material, vapor pressure of group VI) conditioned the size and shape of the quantum dots sheets. This section presents a new II-VI QDs system, CdSe QDs with ZnCdMgSe barriers, grown by MBE on InP substrates, as well as, describes the experimental results and the achievements in the control of the morphological properties of CdSe QDs over ZnCdMgSe barrier layers.

3.3.1. Introduction: Development of a New QD Material System

Initial studies of CdSe QDs on $Zn_xCd_yMg_{1-x-y}Se$ barriers were developed based on the variation of two growth parameters: substrate temperature and CdSe deposition time. Both studies were carried out at the same time to try to find the right growth conditions for the growth of a promising CdSe QDs on $Zn_xCd_yMg_{1-x-y}Se$ barriers. The Fig. 3.8 illustrates the bandgap energy versus the lattice constant for some QDs materials systems. It can be noticed that the traditional III-V, InAs QDs grown over GaAs substrate, and the traditional II-VI QD system, CdSe QDs grown over ZnSe substrates follow the same trend (parallel lines) with respect to the lattice mismatch (difference of lattice constants) between the QD material and the substrate barrier.

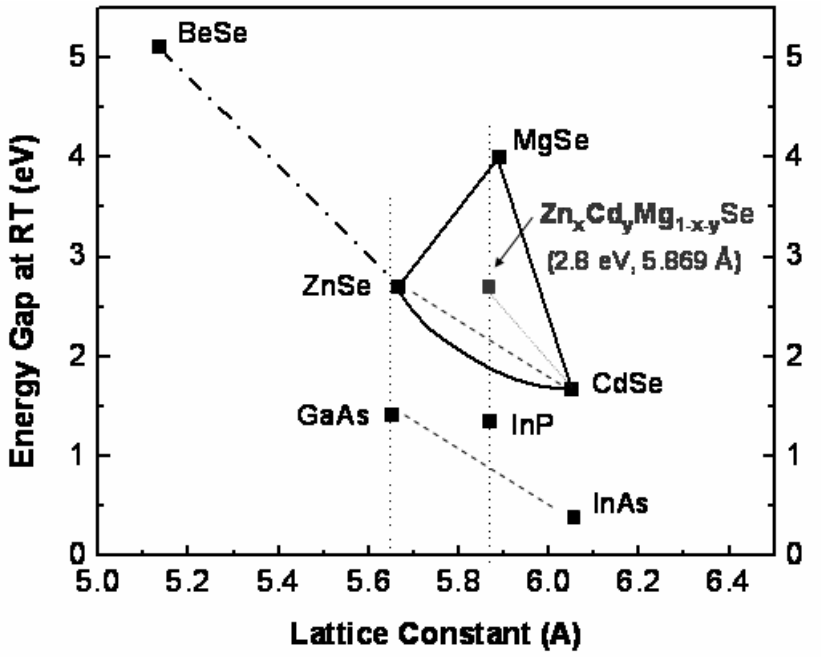

Figure 3.8. Energy of the bandgap versus the lattice constant for some QDs systems.

Another attractive QD system shown in this figure is the CdSe/$Zn_xBe_{1-x}Se$ system, which was originally grown by S. Guo and X. Zhou, in the MBE lab in City College of New York. The dashed line between the binaries ZnSe and BeSe represents the compositions of the $Zn_xBe_{1-x}Se$ ternary system. Initially, small amounts of Be were introduced in the ZnSe barrier to obtain a matched condition to the GaAs substrate, expecting an improvement in the quality and properties of the ZnSe barrier material. Effects of the Be in the formation and size of the QDs were found, reported and compared with the traditional CdSe QDs over ZnSe barriers grown also in our group[9]. The CdSe QDs on $Zn_xBe_{1-x}Se$ was demonstrated to be an interesting system because tiny amounts of beryllium in the barrier caused a significant effect in the QD formation, pointing out beryllium as a chemical element that influences the QD formation. However, this system turned out to be an extremely difficult to control.

For example, slight variations of the substrate temperature by using different blocks (sample holders) produced a large disparity in the size. Therefore, QD PL emission was hard to control and reproduce using analogous growth conditions. Moreover, time-resolved PL studies revealed that non-radiative processes were dominant at RT for the CdSe/$Zn_{0.97}Be_{0.03}Se$ QDs structure, which is an inherent shortcoming of this material system for RT devices applications.[116] In addition, the study of the effect of the beryllium in the QD formation required careful design of structures not to introduce any additional influence of the strain in the formation of the CdSe QDs on $Zn_xBe_{1-x}Se$.

In order to introduce QDs in device structures for visible applications, a II-VI QD system with a systematic control in QD formation and properties must be developed. For the fabrication of new QD material system by the SK growth mode, the materials involved in the growth must usually satisfy two requirements. First, the lattice mismatch (strain) between the QD material and the substrate must be different. This forces the growth mode to transform from pseudomorphic 2D layer growth into 3D island formation when the critical thickness is reached, without forming defects or dislocations. Second, the QD material must have a smaller band gap than the surrounding "matrix" material, so that the dots constitute, in effect, zero-dimensional potential wells, energetically favorable for quantum confinement of the carriers. As observed in the Fig 3.7 and Table 3.1, a system formed by CdSe and $Zn_xCd_{1-x}Mg_{1-x-y}Se$ matched to InP substrate (same lattice constant that InP) follows these two requirements. In addition, as already discussed in the introduction of this dissertation,

a wide range of bandgaps can be obtained just by changing the Mg composition and adjusting slightly the conditions of the quaternary growth.

Material	**Band Gap**	**Lattice constant**
InAs	0.418	6.058
GaAs	1.520	5.653
CdSe	1.765	6.05
ZnSe	2.820	5.668
BeSe	4.720	5.137
ZnCdMgSe	2.1-3.6	5.869
InP	1.424	5.869

Table 3.1 Bandgap at 77 K and lattice constant of different II-VI and III-V semiconductors interesting for QD development.

By analogy with the CdSe/ZnSe system, the new system, CdSe QDs over $Zn_xCd_{1-x}Mg_{1-x-y}Se$ was grown with a number of alike parameters. The composition was adjusted to obtain a comparable bandgap value for the $Zn_xCd_{1-x}Mg_{1-x-y}Se$ barrier matched to InP as that of ZnSe (2.8 eV versus 2.82 of the ZnSe at 77K). The growth interruption after the deposition of CdSe QDs was fixed at the same time, t_{GI}=30 sec. In addition, a reference sample was grown with the same growth conditions as for CdSe/ZnSe QDs in terms of CdSe deposition time, substrate temperature (320ºC) at which CdSe was deposited, as well as, the barrier temperature growth and cooling down time (or heating up time) between the growth of the QDs and the top barrier (bottom barrier). Considering the strain factor, the critical thickness for the CdSe on ZnCdMgSe is expected to be larger since the lattice-mismatch between CdSe and

ZnCdMgSe is nearly half of that between CdSe and ZnSe. Therefore, the appropiate growth parameters could be also different in both systems. For this reason, two sets of experiments were performed. In the first experiment, the substrate temperature was fixed at 320 ºC and CdSe deposition time was changed, while in the second experiment, the deposition time was fixed at 26 sec and the substrate temperature was varied.

3.3.2. Temperature control: Initial Studies

3.3.2.1. Experimental details

The QDs samples were grown by MBE on semi-insulating epiready InP (001) substrates on the dual chamber Riber 2300P MBE system. Substrates were mounted on 2 in. molyblocks and introduced in the MBE system. First, the oxide layer of the InP substrate is removed by heating the substrate with an As flux impingent on the substrate surface. The oxide desorption of the substrate was monitored using the RHEED. The removal of the oxide layer was determined by the transition from a (2 x 4) to a (4 x 2) surface reconstruction at about 495 ºC. Immediately after the deoxidation temperature was reached, the substrate temperature was decreased to 470 ºC to recover the (2 x 4) surface reconstruction and then, a 150 nm lattice-matched InGaAs buffer layer was grown in order to obtain an atomically flat surface for the growth of the II-VI layers. The substrate temperature was gradually increased to about 485 ºC during the InGaAs layer growth. The RHEED showed a streaky (2 x 4) surface reconstruction during growth, indicating a good quality of the epilayer and the

formation of an As-terminated surface, which is essential to obtain a good II-VI/III-V interface.[20] After the III-V buffer layer growth, the samples were transferred into the II-VI chamber in UHV. Prior to the growth of II-VI layers, a Zn exposure for a duration of 40 sec at 170 ºC was performed to reduce defect density of the $Zn_xCd_yMg_{1-x-y}Se$ epilayer, which is related to the formation of undesired compounds between Se atoms and In/Ga atoms, such as Ga_2Se_3[3] (described in Chapter 2). This Zn exposure was followed by ~60 Å ZnCdSe to promote the two dimensional nucleation and to allow an ordered deposition of the $Zn_xCd_yMg_{1-x-y}Se$ layer. Then the substrate temperature was increased to 250 ºC and a 13 nm-$Zn_xCd_yMg_{1-x-y}Se$ buffer layer was grown. After this, the substrate temperature was set at 270 ºC for the remainder of the growth. The total thickness of the quaternary barrier is 130 nm for this set of samples, the RHEED showed a streaky Se-terminated (2 x 1) surface reconstruction indicating a good quality epilayer formation during the $Zn_xCd_yMg_{1-x-y}Se$[20] This initial part of the growth is a common part for all the CdSe QDs samples grown over $Zn_xCd_yMg_{1-x-y}Se$ barriers.

After this, the temperature of the substrate (T_s) was increased until desired CdSe growth temperature (432 ºC, 380 ºC, 350 ºC, 320 ºC, 270 ºC). Growth pause varied, depending on the temperature desired, from 9 minutes (320 ºC) to 18 minutes (432 ºC). A deteriorated RHEED pattern was gradually appeared during this substrate heating time (t_H). The streak pattern seemed more distorted with the increase of the t_H. For the sample that was grown at 270 ºC, since the substrate temperature was not changed, the growth interruption existed but was not controlled. Once the desired temperature for the growth of CdSe was reached, the Cd and Se shutters were opened

and CdSe deposition was performed. After the time of deposition, the Cd shutter was closed for 30 seconds (growth interruption) to permit the mobility of the atoms and the formation of the islands. Once this growth interruption was completed, the substrate temperature was immediately set to 270 ºC and when the temperature was attained, a top barrier layer was grown during 10 minutes (130 nm) to cap the QDs. The time for substrate cooling down (t_C) was again variable depending on the higher initial temperature in which the CdSe was deposited. A 60 Å-pseudomorphic ZnCdSe cap layer was grown to prevent the oxidation of the $Zn_xCd_yMg_{1-x-y}Se$ top layer. The Se/Cd, Cd/Zn and VI/II ratios were kept at 5.7-5.8, 1.4 and 3.0 respectively during the entire II-VI growth. Selenium vapor pressure read on the manipulator gauge was about 1.8-1.9 x 10^{-6} Torr.

Two sets of samples were initially grown the first set at 320 ºC with depositions times of 13, 22, 26 and 30 sec, the second set was grown with the same t_D, 26 sec, but with different T_s: 432 ºC, 380 ºC, 350 ºC, 320 ºC, and 270 ºC.

3.3.2.2. Results and Discussion

The Fig. 3.9 (from *a* to *d*) and Fig. 3.10 (from *a* to *e*) shows the PL emission spectra of samples grown under the conditions described above. The T_s and the t_D are indicated on the top of the figures. The Fig. 3.9 illustrates the PL spectra of four samples grown at the same Ts (320 ºC) but with different t_D and the Fig 3.10 shows the PL spectra of five samples grown with the same t_D (26 sec) but with different Ts.

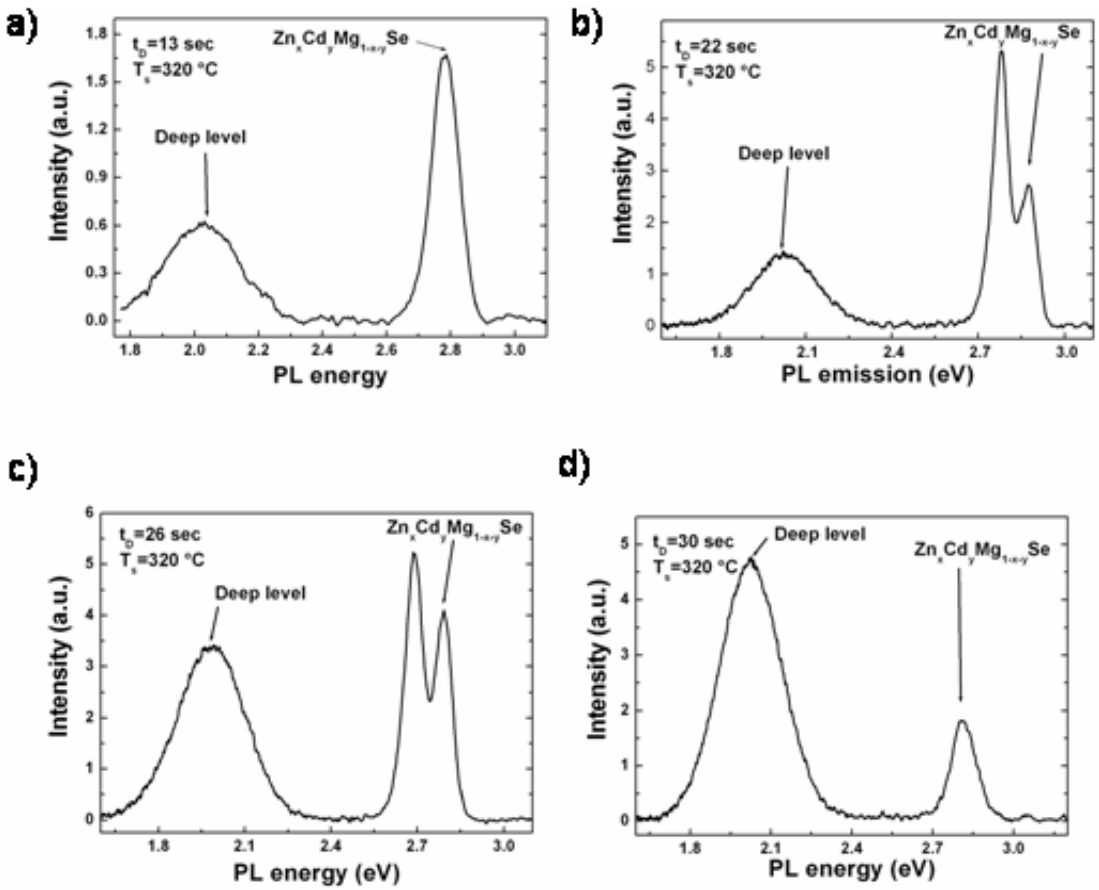

Figure 3.9. Deposition time variation studies of samples growth with the same substrate temperature Ts=320 ºC but different CdSe deposition times: a) t_D=13 sec, b) t_D=22 sec, c) t_D=26 sec, and d) t_D=30 sec.

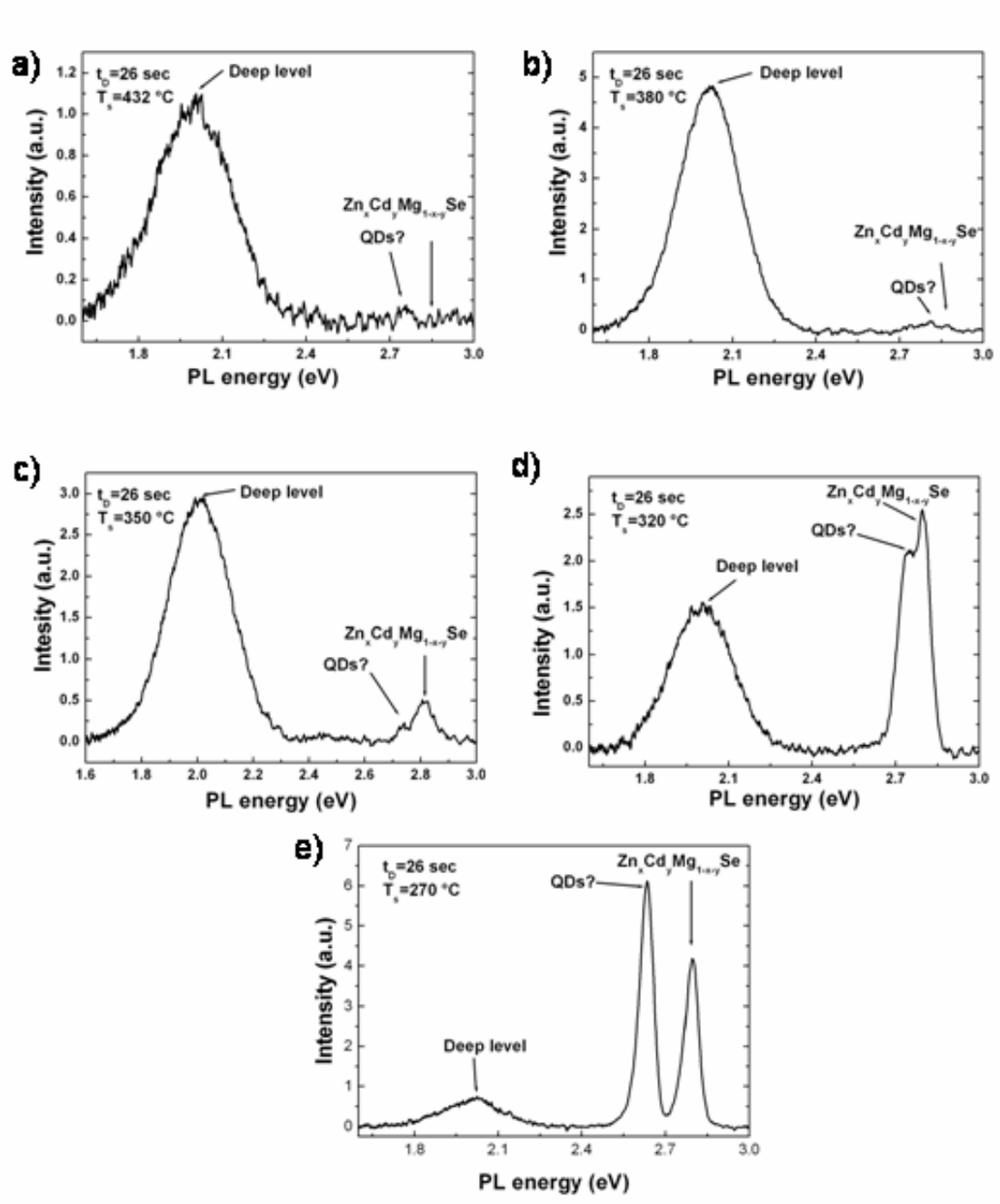

Figure 3.10. Substrate temperature variation studies of samples growth with the same CdSe deposition time, t_D=26 sec. a) T_s=432 ºC, b) T_s=380 ºC, c) T_s=350 ºC, d) T_s=320 ºC, and e) T_s=270 ºC.

Fig ID	Deposition time (sec)	Peak 1 Position (eV)	FWHM of peak 1 (meV)	Peak 2 Position (eV)	FWHM of peak 2 (meV)	Peak 3 Position (eV)	FWHM of peak 3 (meV)
a	**13**	2.019	233			2.777	86
b	**22**	2.026	229	2.776	63	2.872	55
c	**26**	1.981	240	2.686	69	2.790	57
d	**30**	2.023	233			2.794	98

Table 3.2. Peak positions and FWHM for the three types of peaks that appeared in the spectra of the four samples of Fig. 3.9, grown with the same T_s=320 ºC but different t_D.

Fig ID	Temp Substrate (ºC)	Peak 1 Position (eV)	FWHM of peak 1 (meV)	Peak 2 Position (eV)	FWHM of peak 2 (meV)	Peak 3 Position (eV)	FWHM of peak 3 (meV)
a	**432**	2.007	280	2.754			
b	**380**	2.015	232			2.806	
c	**350**	2.007	236	2.746	62	2.808	78
d	**320**	2.002	221	2.743	61	2.794	54
e	**270**	2.007	189	2.630	49	2.793	51

Table 3.3. Peak positions and FWHM for the three types of peaks that appeared in the spectra of five samples of Fig. 3.10, grown with the same t_D=26 sec but different T_s.

Three types of peaks can be distinguished in the spectra. Sometimes, some of them are absent or (almost) not perceptible. The tables 3.2 and 3.3 summarize PL emission energy and the full-width at half-maximum (FWHM) values for those peaks in which the values can be registered.

From the first experiment (Fig. 3.9 and table 3.2), it can be inferred that there is always a broad peak (called *peak 1* in the tables) that appears, consistently, around the same value, from 1.981 to 2.026 eV. No particular trend is observed in the PL emission energy of this broad peak with the variation of t_D, so this peak was assigned to a deep level and not to the QDs. The *peak 3* appears at the highest energy in the spectra, at about 2.8 eV. This peak was assigned to the $Zn_xCd_yMg_{1-x-y}Se$ barrier since the fluxes were adjusted to obtain this barrier PL emission energy. The last peak, named *peak 2*, appeared at lower energy besides the peak at about 2.8 eV and was only visible in certain samples. This peak was assigned to the QDs.

To confirm the assignments, a second experiment was carried out. In this experiment, the temperature of the substrate was varied while the deposition time was kept constant (Fig 3.10 and Table 3.3). A dramatic raise of the intensity ratio of the *peak 1* with respect to the others and an enlargement of its FWHM were observed. Furthermore, the *peak 1* was invariable in energy regardless of the growth temperature, which is a behavior expected for a defect-related peak. In addition, the intensity of the PL emission of the $Zn_xCd_yMg_{1-x-y}Se$ barrier (*peak 3*) was reduced when the temperature was increased (or/and waiting time) while its FWHM increased, which indicated an enhancement of degradation of the quaternary layer. To further demonstrate the origin of the *peak 1*, a reference experiment was performed.

In this experiment, the sample structure was grown without the CdSe deposition (bottom and top quaternary layers), but subjecting it to the same growth interruptions and temperature cycles that a sample grown at T_S=320 ºC. The PL emission from this sample is shown in the Fig. 2.11. Again, the appearance of a strong peak at 2.0 eV, clearly demonstrated that the 2.0 eV peak was actually due to a deep level defect and not to the QDs. We concluded material degradation was caused because of the enhancement of the formation (or growth) of deep level defects, which in turn is influenced by the increase of the temperature or/and the waiting time (t_H and/or t_c) between the growth of the different layers.

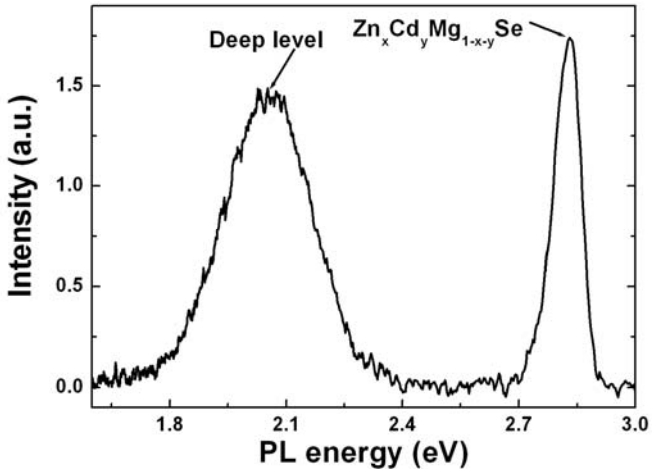

Figure 3.11. ZnCdMgSe reference layer without QDs grown under the same condition than a sample of CdSe QDs on $Zn_xCd_yMg_{1-x-y}Se$ barriers with t_D=26 sec, Ts=270 ºC and waiting time=7 minutes.

The lower energy peak (*peak 2*) near the 2.8 eV peak was investigated to determine if it was associated to the QDs. A comparison of the quaternary reference layer without QDs (Fig 3.11) with the analogous sample where the CdSe deposition

(see *part d in* Fig. 3.9) confirmed the assumption that this second-high energy peak was not originated from composition fluctuations of the $Zn_xCd_yMg_{1-x-y}Se$. In addition, it is interesting to compare the peak positions of the CdSe QDs on ZnSe or CdSe QDs on ZnBeSe barriers with the ones of the samples of $CdSe/Zn_xCd_yMg_{1-x-y}Se$ grown under the same substrate temperature (Fig. 3.12). A dramatic blue shift is observed for the *peak 2* even though much higher deposition times were used[1]. This result is surprising taking into account that the barriers layers are tuned to obtain comparable bandgap energy. Furthermore, the PL energy of the *peak 2* increases at higher temperatures, which is not expected considering the thermodynamic model of the section 3.3.2.2.

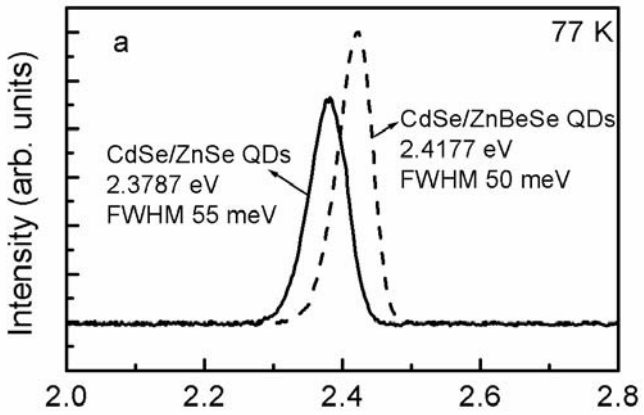

Figure 3.12. PL emission spectrum for two samples of CdSe QDs on ZnSe (solid line) and ZnBeSe (dashed line) grown with t_D=13 sec and T_s=320 ºC.

We propose that this large shift and the influence of the temperature can be originated from a combination of two effects: sticking coefficient of cadmium dependent on selenium flux and its dependence with the temperature. The section

[1] A blue shift is expected since the strain (lattice mismatched) between CdSe and ZnCdMgSe is the half of CdSe on ZnSe. Reduction of lattice mismatched usually results in an increase of the critical thickness and consequently, in smaller QDs.

3.3.2 describes two models, in both of them desorption process is neglected. A higher temperatures, this approximation is not completely correct as explained in the reference 122, since the cadmium desorption process is started to be relevant. In this reference, the postgrowth stability of the InAs quantum dots is studied under variation of the temperature and of the arsenic flux. The authors observed that an additional process of desorption and a resulting dissolution of the QDs takes place a higher temperatures. They also demonstrated that a higher As flux stabilizes the indium in the surface increasing its sticking coefficient. We suggest this behavior can be also the origin of our data. The desorption of cadmium is favored at higher temperature as well as for lower selenium fluxes. In addition, the desorption process is also stimulated by the postgrowth waiting time (during cooling down process) between the CdSe deposition and the growth of the ZnCdMgSe top barrier.

Taking into account all these details about the factors that influence the desorption, the blue shift of CdSe QDs on ZnCdMgSe can be explained if we compare the Se/Cd ratio of the CdSe QDs over ZnCdMgSe ($Q_{Se/Cd}$=5.86) with the one of CdSe QDs over Zn(Be)Se ($Q_{Se/Cd}$=12.6). For the same CdSe temperature growth conditions, the smaller ratio will stabilize less the cadmium in the substrate surface so the desorption or dissolution of the islands will be more favorable, and consequently the islands will be smaller. Other possible explanations about this mechanism could be considering a probable unintentional intermixing between the Zn/Mg from the barrier and the cadmium caused by temperature-dependent segregation during growth[123]. Assuming a homogeneous composition, the intermixing would result in strain reduction so the critical thickness for the formation of the islands will be bigger

and consequently, the size of the islands will decrease with the raise of the temperature.

The next section will show data of QDs grown at lower temperature and a higher selenium flux that will support this explanation.

3.3.3. Deposition Control

After these initial experiments, the effort was concentrated in improving the quality of the $Zn_xCd_yMg_{1-x-y}Se$ barrier layer since it was an important factor to obtain good quality QDs. It must be noticed that the QDs grown at 270 ºC with a smaller growth interruption between the growth of the $Zn_xCd_yMg_{1-x-y}Se$ layer and the QD deposition, presented a smaller deep level. The deep level increased in intensity and the quality of $Zn_xCd_yMg_{1-x-y}Se$ became much inferior (FWHM increased and PL intensity decreased) when the growth interruption was longer. Therefore, avoiding the growth interruption between the deposition of the $Zn_xCd_yMg_{1-x-y}Se$ bottom layer and the CdSe deposition might result in an improvement of the quality of the material. This next section presents results of samples grown without this growth interruption.

3.3.3.1. Experimental Details

The QDs samples were grown by MBE on semi-insulating epiready InP (001) substrates. After the deoxidation of the InP substrate, by heating the substrate with an As flux impingent on the substrate surface, a 150 nm-InGaAs buffer layer was grown. Then, the samples were transferred to the II-VI chamber to perform the growth of the

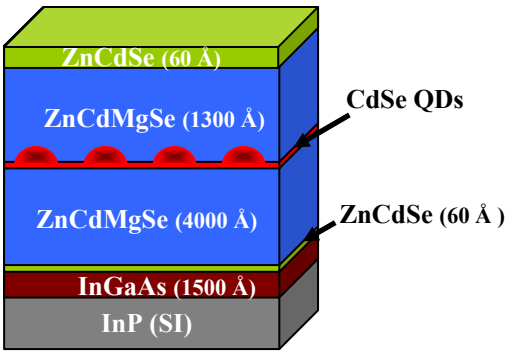

Figure 3.13. Representation of the sample structure for the studies of the CdSe deposition time effect.

II-VI desired layers. The InGaAs buffer, the Zn-irradiation step, the ZnCdSe-LT and ZnCdMgSe bottom layers are grown following the same procedure that the one described in section 3.3.2.1. Fig. 3.13 shows a schematic representation of sample structure. The total thickness of the quaternary bottom barrier layer was increased up to 400 nm to improve the quality of the $Zn_xCd_yMg_{1-x-y}Se$. The RHEED showed a streaky Se-terminated (2 x 1) surface reconstruction indicating a good quality epilayer formation.[20] To initiate the CdSe deposition, the Zn and Mg shutters were closed (no growth interruption). The different CdSe QDs were formed on the $Zn_xCd_yMg_{1-x-y}Se$ barrier by variation of the t_D from 6 to 36 sec, followed by a t_{GI} of 30 sec with only the Se shutter open. Inmediately after the t_{GI}, Zn, Cd and Mg shutters were opened again to perform the growth of a top 130 nm-$Zn_xCd_yMg_{1-x-y}Se$ barrier. The RHEED pattern was streaky from the beginning to the end of this layer growth. Finally, a 60 Å ZnCdSe cap layer was grown to prevent the oxidation of the $Zn_xCd_yMg_{1-x-y}Se$ top layer. The Se/Cd, Cd/Zn and VI/II ratios were kept at 7.5, 1.3 and 3.9 respectively during the entire II-VI growth. The BEP of selenium was 2.4 x 10^{-6} Torr.

3.3.3.2. Results and Discussion

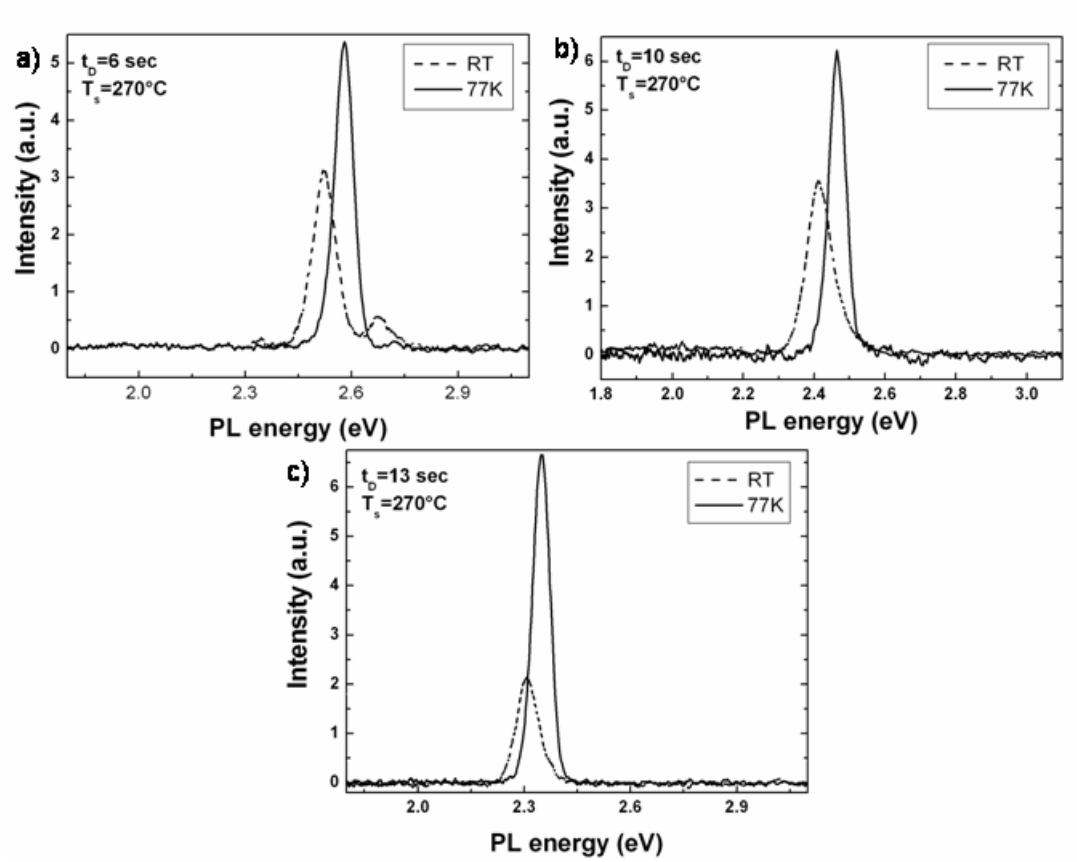

Figure 3.14. PL spectra of three samples grown at the same substrate temperature (T_s=270 ºC) and without waiting time between the quaternary layers and the CdSe deposition. a) t_D=6 sec b) t_D=10 sec and c) t_D=13 sec.

The Fig. 3.14 shows the PL spectra of three samples with different deposition times t_D= 6 sec (part a), t_D= 10 sec (part b), and t_D=13 sec (part c) grown under the conditions described in 3.3.3.1. The T_s during the CdSe deposition was 270 ºC. No waiting time existed between the $Zn_xCd_yMg_{1-x-y}Se$ growth and the CdSe deposition. Solid line shows the PL spectra at 77 K while the dashed line is the PL spectra at RT. There was only one narrow peak for each sample at 77 K with lower energy than the $Zn_xCd_yMg_{1-x-y}Se$ barrier (2.8 eV). This peak was shifted in energy for the different

deposition times. No barrier or deep level emission was observed at 77K, which indicated an improvement in the quality of the material. For the sample with t_D=6 sec, the barrier peak is noted at higher energies that the QD peak for the spectrum a RT.

To further investigate the behavior of the peak that appears at lower energy that the barrier, the peak position and the FWHM of these three samples was represented versus the deposition time. The Fig. 3.15 shows the results of the plotting.

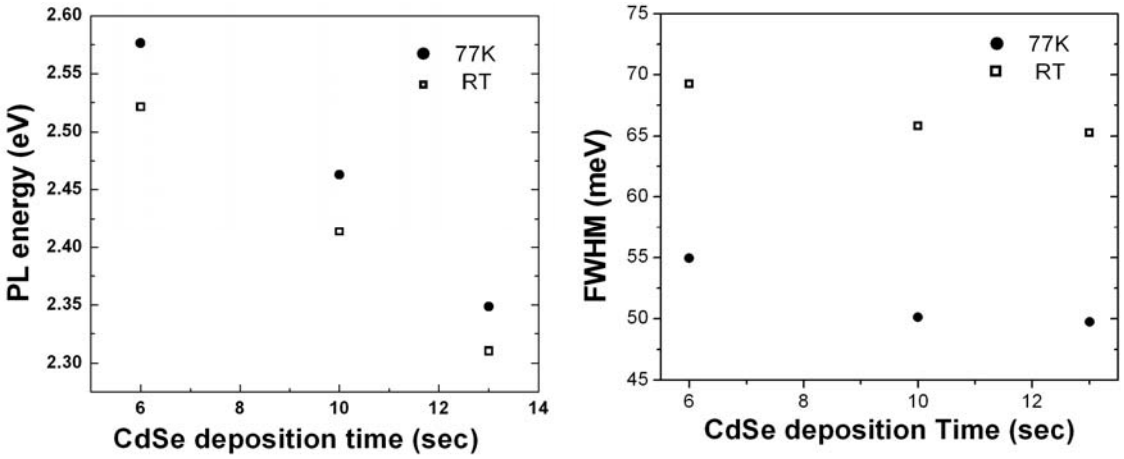

Figure 3.15. PL emission energy and FWHM versus the CdSe deposition time for the three samples represented in the Fig. 3.14.

As observed from the Fig 3.15, the behavior the peak and the FWHM are completely different to those that are expected from the bulk or the QWs[20]. Peak position is shifted a little with a change of the temperature from 77K to 298K (RT). The shift is consistent with other reported experimental data[9] and it is slightly different by different depositions times (see below). The FWHM of the QD peak appears almost independent on the temperature as expected ideally by the QDs with just an increase of about 14-15 meV for all the samples.

To further verify the QD assignment to this peak and to understand its dependence with the CdSe deposition time, we performed systematic PL studies by repeating the growth in different days, using different CdSe deposition times. In addition, the morphology of the uncapped QDs with different deposition times was also studied by the analysis of the AFM microscopy images of different samples.

An example of a three dimensional image of an uncapped CdSe QDs on $Zn_xCd_yMg_{1-x-y}Se$ barrier structure is shown in Fig 3.16. The AFM measurements of the QDs were performed using a ThermoMicroscopes Explorer AFM of Veeco-Digital Instruments operated in the non-contact mode under ambient conditions. The AFM cantilever is a Si cantilever with a spring constant of 13-100 N/m and a nominal resonance frequency of 240-420 kHz. Images were recorded with a resolution of 300 x 300 pixels and a scan rate of 3.69 μm/s. Samples for the AFM were removed from the chamber immediately following the QD formation (without the quaternary top and cap layers). The microscope was placed on a pneumatic anti-vibration table, under a damping cover. The processing was conducted using the SPMLab software.

To slow down a possible ripening effect[20] and the formation of selenite (section 2.2.2.4), the samples were immediately immersed in liquid nitrogen after the growth and kept in this condition until the moment of taking the surface topography.

The CdSe QDs deposition time for this sample was 10 seconds, equivalent to 2ML of nominal thickness (1ML is considered equivalent to 0.3 nm). The PL spectrum of a capped sample grown under the same conditions appeared in the green region at 2.633 eV. The inset in the Fig 3.16 is a representative histogram of the QDs height distribution in the sample. The histogram shows an approximately Gaussian

lineshape, with 4.5 ± 0.5 nm being the most abundant value. The average radius of the QDs base is 47 nm. However, the radius should be cautiously considered due to the AFM tip convolution which can make the radius of the QDs base appear bigger than the real value (as described section 2.2.2.4). The average QDs density was $7x10^{8}$ cm^{-2}.

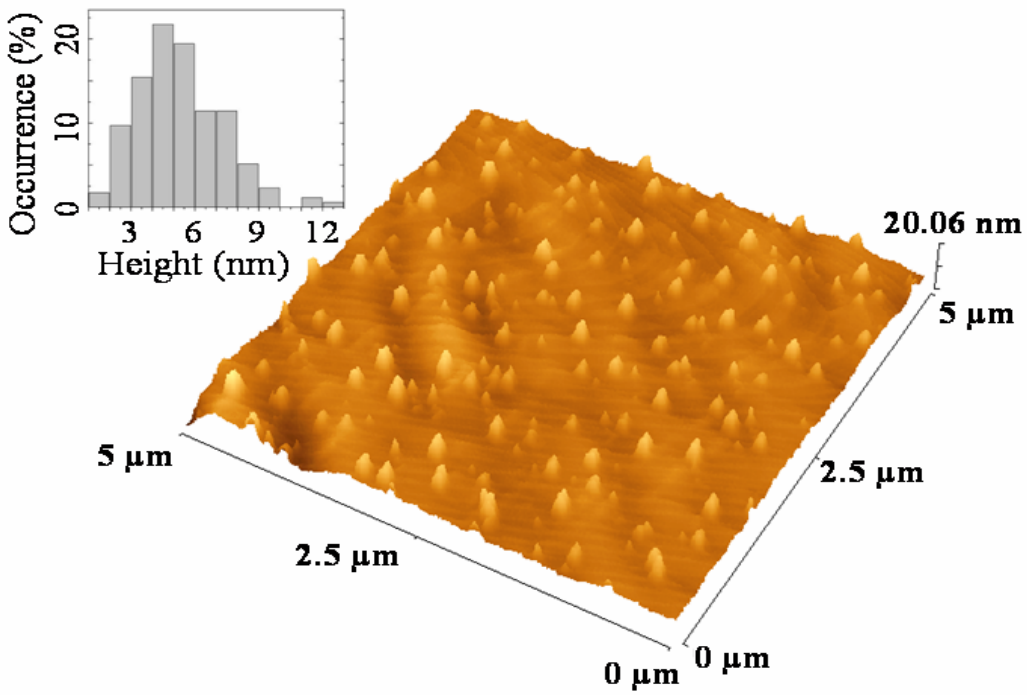

Figure 3.16. Three-dimensional AFM image of CdSe QDs deposited on ZnCdMgSe barrier (t_D=10 sec). Inset shows a histogram of the QD height.

The PL spectra of the five samples grown under the conditions described above and having t_D of 6, 13, 18, 24, and 29 sec, which would correspond to the deposition of layers with nominal thicknesses of 1.2, 2.5, 3.6, 4.8, 5.8 ML, is shown in the Fig. 3.17. The $Zn_xCd_yMg_{1-x-y}Se$ barrier layers were grown with the same

composition, thickness and band gap, of about 2.8 eV, for all the samples. The $Zn_xCd_yMg_{1-x-y}Se$ barrier band gap was measured in a reference layer grown under the same conditions as the QD barrier layer. The PL peak intensities were normalized. A weak PL emission from the $Zn_xCd_yMg_{1-x-y}Se$ barrier is observed in the sample that exhibits blue emission.

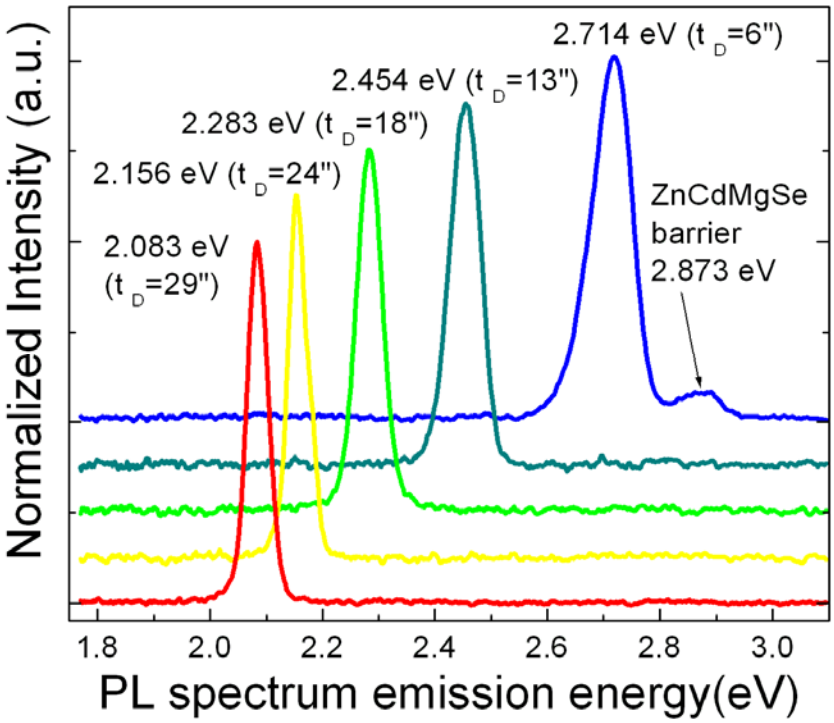

Figure 3.17. PL spectra of five samples grown with different t_D. The PL peak emission and t_D for each sample is indicated in parenthesis.

As in shown in figure 3.17, by appropriate choice of the t_D, the size of the QD and consequently, the emission wavelength from the CdSe QDs can be adjusted to fall anywhere within the visible range. Ivanov et al.[124] have recently reported a similar study in the case of CdSe QDs on ZnSe barriers. However, in their work, they reported emission only from the blue to the green and not in the entire range of the visible spectrum as in our case. Furthermore, they observed a very dramatic decrease

in the QD emission intensity for the sample with emission at about 2.29 eV which was attributed to the fact that in that case, after deposition of 3.2 ML, the critical thickness was exceeded, and thus there was formation of defects that reduced the efficiency of the luminescence. In our system we are able to reach the red (1.964 eV) with a CdSe deposition time t_D=36 sec and an equivalent nominal thickness of 7.2 ML, without such a reduction of emission intensity. This result was attributed to the fact that the critical thickness of this II-VI SAQDs system is greater than in the CdSe/ZnSe system due to the much smaller lattice-mismatch (3.08 %) between the $Zn_xCd_yMg_{1-x-y}Se$ lattice-matched to InP (a=5.869 Å[20]) and CdSe (a= 6.050 Å[20]).

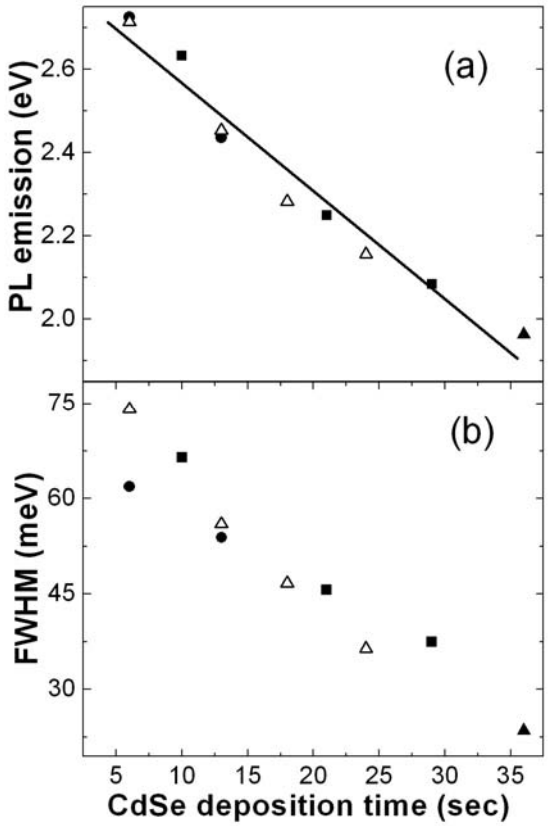

Figure 3.18. (a) Variation of the PL emission energy and (b) of FWHM as a function of t_D for several samples grown on different days. The different symbols indicate the different days the samples were grown.

In Fig. 3.18, the PL emission peak position and FWHM are plotted as a function of t_D. The relationship between PL peak energy and the t_D is nearly linear (the straight line shown is given to guide the eye) and has been observed in sets of samples grown on different days, indicating that good control and reproducibility in the optical properties were achieved. A similar linear relationship was obtained by Ivanov et al. for CdSe/ZnSe.[124] By choosing properly the t_D, light emission at any wavelength within the visible range can be obtained, which may be useful for full color R-G-B light emitters and white light sources.

Figure 3.18 (b) shows the FWHM of the same samples represented on figure 3.18 (a). The linewidth increases with increasing band gap (smaller size). By contrast, Ivanov et al.[125] reported a reduction of the FWHM with QD size, which he attributed to higher uniformity of QD size in the samples with smaller QDs. This comparison suggests that the dominant effect determining the linewidth variation with QD size in our case is not a change in uniformity of the QDs size, but rather that the intrinsic linewidth of the QD increases a the dot size decreases due to enhanced interface effects in the smaller dots.

The new system QD system that we have being investigated, $Zn_xCd_yMg_{1-x-y}Se$/CdSe SAQDs provides an interesting comparison to the well-studied system among the II-VIs, CdSe/ZnSe SAQDs. In this case, the bandgap of the $Zn_xCd_yMg_{1-x-y}Se$ barrier (Eg~2.8 eV) used is comparable to the bandgap of ZnSe. However, the lattice-mismatch between the CdSe QD material and the barrier material is approximately half (~3.1 % vs 6.7 %) of the mismatch between ZnSe and CdSe. Thus, we can compare directly the effects of mismatch on QDs formation.

Comparison of the PL emission energy for a given deposition of CdSe between our experiments and those of Ivanov reveals that the results are strikingly similar, suggesting that the CdSe QD sizes are similar. This is surprising if we assume that lattice-mismatch (strain) is the principal mechanism controlling the QD size, and points to other factors due to the different chemical composition of the two barrier layers as being dominant. Chemical effects have been reported before that show that even small quantities of certain elements (such as Be[9] or Mn[1]) in the ZnSe barrier cause significant change in QD size. In our case, large quantities of the Mg and/or Cd in the barrier layers are clearly affecting the dynamics of QD formation by the SA process.

3.3.4. Growth Interruption

3.3.4.1. Introduction

The nature of the narrow island size distribution obtain by some QD systems, sometimes with the absent of Ostwald ripening, is subject of intense debate. The effect is described kinetically or thermodynamically. Thermodynamic theory states that, under certain conditions, the equilibrium state of a lattice-mismatched heteroepitaxial system is an ordered array of 3D coherently strained islands. No Ostwald ripening will occur after reaching this stage. Kinetic theories state that, once 3D islands have formed, there exists a thermodynamic tendency towards ripening, but that the growth of islands above a certain size can be kinetically slowed down due to strain-induced barriers. However, the kinetics of equilibration may be rather slow, and the system may still not reach its final state on an accessible time scale

(experimentally, growth interruption time). Therefore, this state is not the equilibrium state is an intermediate path towards the equilibrium.

In order to study the effect of the growth interruption in the equilibrium of the islands, an experiment with variation of the growth interruption time was carried out for a large CdSe deposition time.

3.3.4.2. Experimental Details

The QD Samples for the growth interruption studies were grown using the same procedure as the one described in section 3.3.3.1. The t_D for these samples was 31 sec, i.e. 6.1 ML of nominal thickness, and the t_{GI} was varied between 12 sec and 30 sec (equilibration time).

3.3.4.3. Results and Discussion

The Fig. 3.19 illustrates the PL spectra of two samples grown under conditions but with different t_{GI}. A large shift from the red side to the blue-green side of the spectrum is obtained just by reducing the t_{GI} from 30 sec to 12 sec.

Previous studies in other II-VI systems, as CdSe QDs on ZnSe indicated that CdSe islands reach a narrow size distribution around a certain size upon a growth interruption of 30 sec, and that the distribution of capped islands sizes does not change significantly upon further growth interruption. If the growth interruption is shorter, there is not enough time to reach the size of equilibrium so a smaller size (intermediate equilibrium stage) is obtained. On the other hand, this result also supports the achievement of larger QDs with PL emission on the red range of the

visible spectrum since QW behavior is expected not to change with the growth interruption.

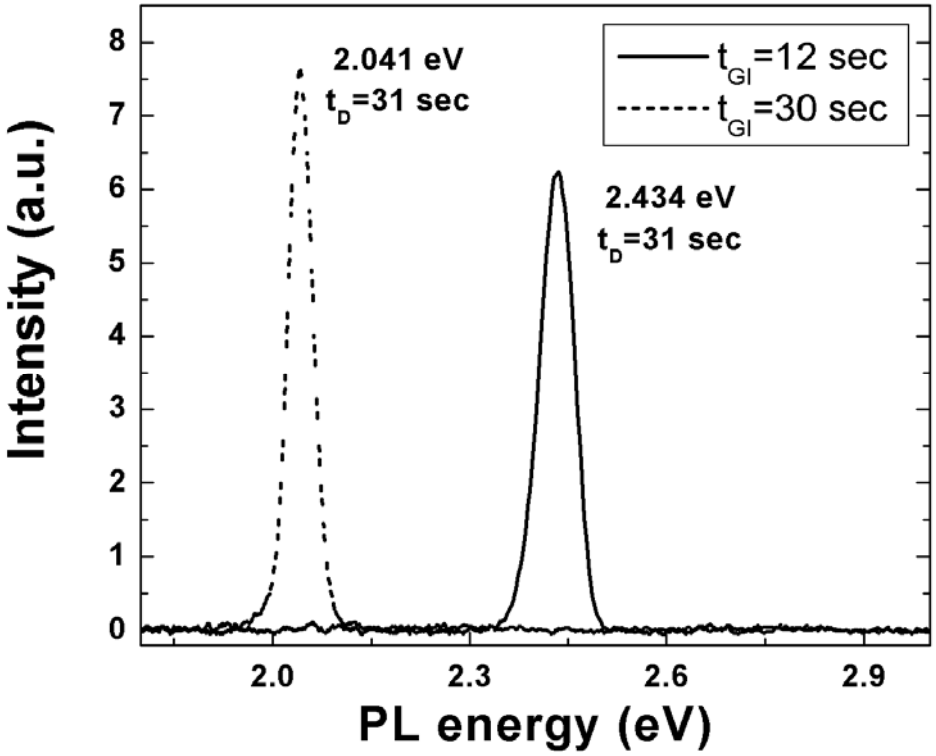

Figure 3.19. Growth interruption variation studies for two samples of CdSe QDs on ZnCdMgSe grown under the same growth conditions but with t_{GI}. The different t_{GI} for the samples are represented on the top right side of the figure.

3.3.5. Chemical factors: Mg effect

3.3.5.1. Introduction

The section 3.3.3 showed that changing the CdSe deposition time, PL and consequently, size of the CdSe QDs grown on $Zn_xCd_yMg_{1-x-y}Se$ can be tuned from the blue to red, covering the whole visible spectrum and even more, offering the promising characteristic of reaching the near-UV when the $Zn_xCd_yMg_{1-x-y}Se$ bandgap is tuned to UV wavelength. The PL emission energy for a given CdSe deposition was

also compared with those reported for the traditional II-VI system, CdSe QDs grown on ZnSe barriers. It was suggested that structural parameters, such as lattice mismatch (or strain) were not the only parameters that play a role in the formation of the CdSe QDs over $Zn_xCd_yMg_{1-x-y}Se$. Chemical factors, such as Mg or/and Cd concentrations on the $Zn_xCd_yMg_{1-x-y}Se$, were proposed as a possible explanation to the behavior of this QD system. To study the effect of Mg concentration of the $Zn_{1-x}Cd_yMg_{1-x-y}Se$ on the size of CdSe SAQDs, experiments based on both capped and uncapped samples were performed. Capped samples were grown to observe the variation of the MgSe content in the PL spectra while uncapped samples were grown to examine the impact of MgSe content in the morphology of the QDs, studied by AFM measurements. Experimental details and results of these experiments are described in the section 3.3.5.1 and 3.3.5.2, respectively. The last section of 3.3.4.2 illustrates also a detailed explanation about the MgSe effect, considering either theoretical approach or a more experimental-based one.

3.3.5.2. Experimental Details

The SQDs samples grown to study the effect of the Mg in the nucleation of the QDs were obtained using the same procedure described in the previous section (3.3.3.1). The difference between the samples is just the MgSe content on the $Zn_xCd_yMg_{1-x-y}Se$ barriers. Variation of the MgSe content on the $Zn_{1-x}Cd_yMg_{1-x-y}Se$ barrier layer was accomplished by changing the Mg cell temperature with almost no alteration of other growth parameters (sometimes, Zn temperature was slightly adjusted). Uncapped samples were grown to observe, by AFM, the variation in the

dimensions and density of uncapped QDs. Calculations of the MgSe content of these samples were obtained based on a $Zn_xCd_yMg_{1-x-y}Se$ reference layer. From the X-ray measurement, Θ of the epilayer is obtained, and then, if Bragg's equation is applied, its lattice constant. PL measurements were used to estimate the bandgap of the quaternary. Then, as described in the section 2.2.2.3, the composition of quaternary layers could be found by solving a system of two equations, one that relates linearly the lattice constant of the $Zn_xCd_yMg_{1-x-y}Se$ epilayer with the composition (assuming the Vegard's law):

$$a(Zn_xCd_yMg_{1-x-y}Se) = 5.668x + 6.050y + 5.890(1-x-y) \quad (3.35)$$

and other, a second degree equation that relates the band gap of the material at 10K with the composition (for the RT measurements, equation 2.32)

$$Eg^{Zn_xCd_yMg_{1-x-y}Se} = 3.65 - 0.83x - 1.87y - 0.35xy \quad (3.36)$$

3.3.5.2. Results and Discussion

To monitor the effect of the variation of MgSe content of the $Zn_xCd_yMg_{1-x-y}Se$ on the electronic properties of the QDs, we compared PL measurements of the capped samples with the same t_D but with different concentration of MgSe in the barrier. The *part a* in the Fig. 3.20 shows the QD PL peak energy for different percentage of MgSe content in the $Zn_xCd_yMg_{1-x-y}Se$ barrier. Different symbols indicate different deposition times. The part b ilustrates the comparison between samples with the same t_D. The variation of the QD PL peak position between two samples is represented with respect to the difference of the MgSe content in the same

samples. The samples that are compared are grown under the same conditions with only one difference, the MgSe content. A higher Mg concentration in the $Zn_{1-x}Cd_xMg_{1-x-y}$ Se layer shifts the PL peak position of the QDs to the blue (higher PL peak energy), which is consistent with smaller QD size. From *part b* of Fig. 3.20, it can be inferred that tiny variations of Mg composition in the $Zn_{1-x}Cd_xMg_{1-x-y}Se$ barrier result in a significant effect in QD PL peak position shift (170 meV for 3.3 % variation). This effect is not attributed to the intermixing between the Mg of the ZnCdMgSe and the Cd or the CdSe QDs. The reason for that is that even though the Mg incorporation in the QDs will increase the QD PL emission energy, it is also expected a decrease of the optical quality of the material.

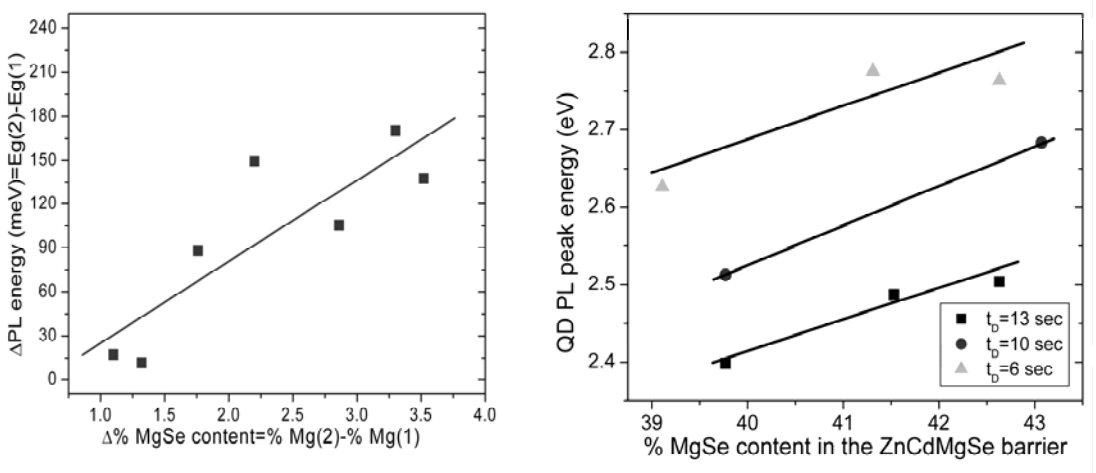

Figure 3.20. a) QD PL peak energy versus percentage of MgSe content in the $Zn_xCd_yMg_{1-x-y}Se$ barrier for different deposition times. b) Difference of PL energies versus percentage of MgSe content variation for a set of samples grown under the same conditions. A point represents the variation in the PL energy between two samples grown with the same deposition time but different MgSe content on the $Zn_xCd_yMg_{1-x-y}Se$ barrier.

Therefore, broadening of the QD PL peak (FWHM increase) and a significant decrease of QD peak intensity are expected. In fact, the intermixing effect of Al in the

InAs QDs grown on InGaAs barriers resulted in an increase of the QD density and a decrease of QD size but also in a substantial degradation of the optical properties of the material [126, 127]. The CdSe QDs grown on ZnCdMgSe with higher Mg content do not exhibit any optical or quality degradation so we assume the intermixing is not (or almost not) probable. This Mg variation can be also compared with previous results in the CdSe QDs with $Zn_xBe_{1-x}Se$ barriers, where a variation of 3% of Be content introduced a blue-shift of only 39meV. This effect can not be explained as only QD energy levels shift ensuing from the increment of the height of the barrier (more Mg). Small variations of magnesium modify slightly the band structure of the barrier and consequently, it should not affect considerably the nature of the energy levels of the QD. Therefore, the change in the PL position must be originated from effects in the QD morphology.

The Fig. 3.21 and Fig. 3.22 show two 3D-AFM images of two uncapped samples with different MgSe content in the barrier. A bigger variation in the MgSe content was carried out in order to be able to perceive a major effect in the image of the size and density of the QDs. Both samples were grown with the same t_D=10 sec, which correspond to a nominal thickness of 2ML. The first sample, represented in the Fig. 3.21, contains a MgSe concentration of 39% on the $Zn_{0.38}Cd_{0.23}Mg_{0.39}Se$ barrier of while the MgSe content of the sample in the Figure 3.22 is 59%.

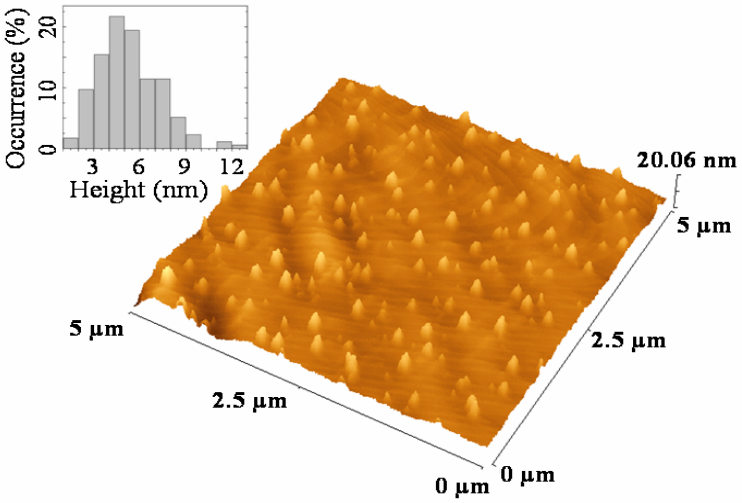

Figure 3.21. Three dimensional AFM image for a sample with a CdSe nominal thickness of 2ML and 39% of MgSe content in the barrier.

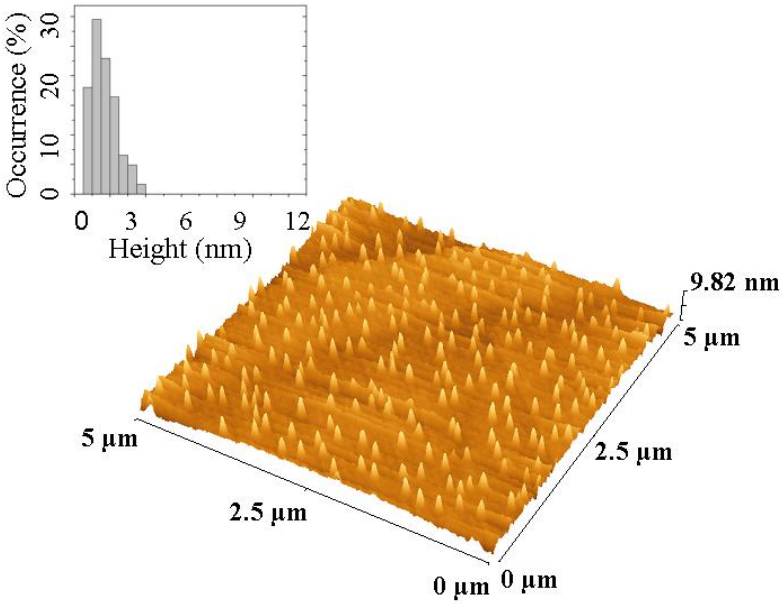

Figure 3.22. Three dimensional AFM image for a sample with a CdSe nominal thickness of 2 ML and 59% of MgSe content in the barrier.

The insets in the Fig. 3.21 and Fig 3.22 are representative histograms of the QDs height distribution in each sample. The histogram in Fig. 3.21 shows an approximately Gaussian lineshape, with 4.5 ± 0.5 nm being the most abundant value.

The average radius of the QDs base is 47 nm. The average QDs density was $7x10^{8}$ cm^{-2}. In contrast, in the Figure 3.22, the most abundant QD height given by the histogram was 1.6 ± 0.5 nm, the lateral size was reduced at 30 nm and the average in density was increased up to 1.02 $x10^{9}$ cm^{-2}. It was noticed that not only height, radius and density were affected by an increase of MgSe content in the $Zn_{0.18}Cd_{0.23}Mg_{0.59}Se$ barrier but also resulted in more uniform size distribution in the sample, shown in the histogram, which is desirable for some optical applications.

On one hand, we propose this result can be explained by a thermodynamic Mg influence in the CdSe QDs formation. A higher Mg concentration changes the surface energy of the $Zn_xCd_yMg_{1-x-y}Se$, which influences the wetting characteristics (binding energy between the substrate and the material deposited on the top) and, consequently, the size of the QDs. The section 3.3.2.1 considered the dependence the thickness of the wetting layer of the binding energies of the deposited material and the barrier material. From the Eq. 3.25, a higher binding energy density in the interface between the substrate and the material, ($-\phi_{AB}$), will result in higher thickness of the wetting layer and consequently, smaller critical radius of the islands formed (see section 3.3.2.2). From a chemical point of view, magnesium is much more electropositive atom than cadmium or zinc, so higher binding energies are expected between the selenium atoms and the magnesium.[20] If the density of magnesium atoms is much higher on the bottom barrier, more magnesium atoms will be bare on the surface to make bonds with the material that is being deposited. Therefore, the total binding energy between both materials, sum of the binding

energies of all the bonds formed, will be higher which it turns in a thicker wetting layer.

On the other hand, considering the AFM studies, a kinetic explanation derived from the experiments can also given. We observed always that the QDs grow in the edges of the surface atomic steps, acting as a nucleation centers. Comparing Fig 3.21 and 3.22, we noticed that the density of these atomic steps increased for the sample with more magnesium content so a denser QD layer with smaller size QDs was obtained. Magnesium as beryllium is a hard element that is characterized by the higher bonding energies with other elements. This element property often result in a rougher surface for Mg or Be based systems, which is a consequence of the lower adatom mobility (migration) on the surface. If higher magnesium concentration is on the ZnCdMgSe epilayer, we expect a considerable decrease in the total atom surface migration so more atomic steps will form and will not be dissolved, previously, to the CdSe deposition. This step bunching formation is well-known in III-V material systems[128]. This approach is already a successful method to obtain ordering in InAs/GaAs QDs arrays, either by MBE or by MOCVD[129]. Usually, in these techniques a barrier layer with multi-atomic steps is formed by using a vicinal surface (GaAs), i.e., a surface with atomic (1ML thick) steps. The multi-atomic step edges on the surface (GaAs) are formed by the so-called step bunching process. Since QDs (InAs) form preferentially at the step edges rather than on the terraces, QDs are grown selectively in rows at the multi-atomic steps edges.

This spontaneous formation of ordering atomic steps in the ZnCdMgSe has never been reported in other II-VI material. This is a promising achievement for the control in the size, density and position of the CdSe QDs.

In summary, the chemical effect of MgSe content on the formation of the CdSe QDs grown on $Zn_{1-x}Cd_xMg_{1-x-y}$ Se has been observed. A reduction of the QD size, as well as, a blue shift of the QD PL peak position by increasing Mg concentration in the $Zn_{1-x}Cd_xMg_{1-x-y}$ Se barrier has been demonstrated by changing the Mg temperature. In addition, a more uniform and denser layer has been found with an increase of the percentage of MgSe in the $Zn_{1-x}Cd_xMg_{1-x-y}$ Se barrier layer. Results pointed to Mg as chemical factor that induced QD formation, either by increasing the atomic steps or by changing the energy of the $Zn_xCd_yMg_{1-x-y}Se$ surface.

3.4. Contacless Electroreflectance of Single Quantum Dot Layer Structures

3.4.1. Introduction

The results based on luminescence measurements provide only partial information about the electronic properties of the materials. In the case of the QDs, this information is limited to the lower energy states and does not allow studying the shape of the QD potential or the coupling effects in stacked structures[46]. This section presents the preliminary CER studies that have been performed in SQDs and MQDs of CdSe with $Zn_xCd_yMg_{1-x-y}Se$ barriers.

3.4.2. Experimental Details

Single layer QD samples for contactless electroreflectance experiments were grown using the same growth conditions as the ones specified in the section 3.3.3.1.

3.4.3. Results and Discussion

The RT-CER measurements were carried out initially in the CdSe-SQDs grown on $Zn_xCd_yMg_{1-x-y}Se$. No information about higher energy QD transitions has been reported. In addition, the $Zn_xCd_yMg_{1-x-y}Se$ material system utilized as barrier for the growth of the QDs is still a novel material in which not much work has been done to study the critical points of its band structure.

Figure 3.23 shows an example of a measured RT-CER spectrum of a sample of CdSe SQD grown on $Zn_xCd_yMg_{1-x-y}$ Se with a CdSe nominal thickness of 4.8 MLs. The dashed line represents the experimental fitting of the spectrum. The energies corresponding to the observed transitions were obtained by the fitting and marked in the figure by arrows. The transitions originating from the structure, were fit using the first derivative of a Gaussian line shape due to their bound origin[55]. Table 3.4 shows the interband transitions obtained by the experimental fitting and their assigments. Some theoretical calculated values using envelope approximation[130] considering the strain and the values measured by PL are also given.

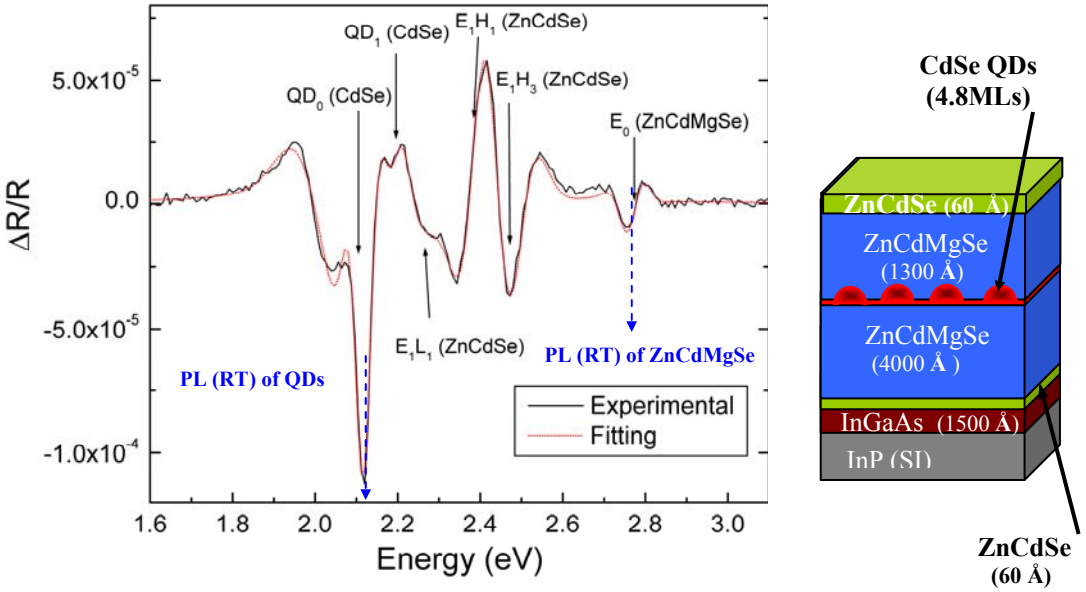

Figure 3.23. The RT-CER spectrum of a CdSe-SQD grown on $Zn_xCd_yMg_{1-x-y}Se$ where the nominal thickness of CdSe was 4.8 MLs. A schematic of the sample layer structure is represented on the right side of the spectrum.

Transition	Experiment (eV) (± 0.005)	Theory (eV)	PL (eV) (±0.002)
QD_0	2.107		2.107
QD_1	2.196		
E_1L_1 (ZnCdSe)	2.267	2.279	
E_1H_1 (ZnCdSe)	2.399	2.386	
E_2H_2 (ZnCdSe)	2.467	Footnote 2	
E_0 ($Zn_xCd_yMg_{1-x-y}Se$)	2.771		2.771
III-V related	2.042		

Table 3.4. Experimental and calculated interband transition energies for a CdSe SQD structure grown on $Zn_xCd_yMg_{1-x-y}Se$ with a CdSe nominal thickness of 4.8 MLs.

The assignment of the band gap of the quaternary layer, E_0 ($Zn_xCd_yMg_{1-x-y}Se$), and the lowest energy level of the QDs, QD_0, were straightforward when compared with the values obtained by the PL measurements at RT. Due to the complexity of the

[2] The transition is assigned to E_2H_2 based on the comparison with reference 132, taking into account the probability of the transitions.

spectrum, different reference layers were grown to clarify the origin of the other transitions. To identify the remaining transitions, two references layers were grown in analogous conditions than the SQDs structures: a $Zn_xCd_yMg_{1-x-y}Se$ structure without the QDs but with the remaining layers (structure is shown on the right side of the CER spectrum in the Fig. 3.24) and a single ZnCdSe-LT layer with the same thickness as the one in the SQD structure.

The Fig. 3.24 illustrates the CER spectrum of this $Zn_xCd_yMg_{1-x-y}Se$ reference layer while Table 3.5 summarizes the interband transitions obtained by the fitting shown by the dashed line. The notation *EnH*(*L*)*m* in Fig. 3.20 and Fig. 3.24 indicates that the transitions are from the *n*th conduction subband to the *m*th valence subband of heavy (*H*) or light (*L*) hole character, respectively. Again, the assignment of the band gap of the quaternary layer, E_0 ($Zn_xCd_yMg_{1-x-y}Se$), is straightforward if compared with the PL experimental data. No peaks were assigned to the III-V portion of the structure, considering literature values reported for $In_xGa_{1-x}As$ and InP materials [131]. Therefore, the transitions corresponding to 2.267, 2.399 and 2.467 eV must be arising from the ZnCdSe layers. The ZnCdSe layers were very thin pseudomorphic mismatched layers to InP. The reason we used a mismatched layer is that we used the same source temperatures for Zn and Cd as the temperatures used for the growth of the $Zn_xCd_yMg_{1-x-y}Se$ and the CdSe QDs. This mistmatch does not introduce a significant strain in the entire structure since the LT-ZnCdSe layer is kept very thin and therefore, pseudomorphic. However, this mismatch changes the band structure of the ZnCdSe and, consequently, the transitions that are observed in the CER spectrum.

The Fig. 3.25 illustrates the splitting originated in the energy levels of the valence band as a consequence of the strain. The EHH and ELH represent the transitions from the lowest level of the conduction band to the heavy hole and the light hole in the valence band, respectively. An envelope approximation calculation considering the strain has been performed for the results illustrated in Fig. 3.25.

Transition	Experimental (eV ± 0.005)	Theory (eV)	PL (eV±0.002)
E_1L_1 (ZnCdSe)	2.303	2.279	
E_1H_1 (ZnCdSe)	2.362	2.386	
$E_0 + \Delta$ (ZnCdSe)	2.628	2.525[3]	
E_0 ($Zn_xCd_yMg_{1-x-y}Se$)	2.889		2.891

Table 3.5. Experimental and calculated interband transition energies for a $Zn_xCd_yMg_{1-x-y}Se$ layer grown under the same conditions than the $Zn_xCd_yMg_{1-x-y}Se$ barrier layer used for the growth of CdSe QDs.

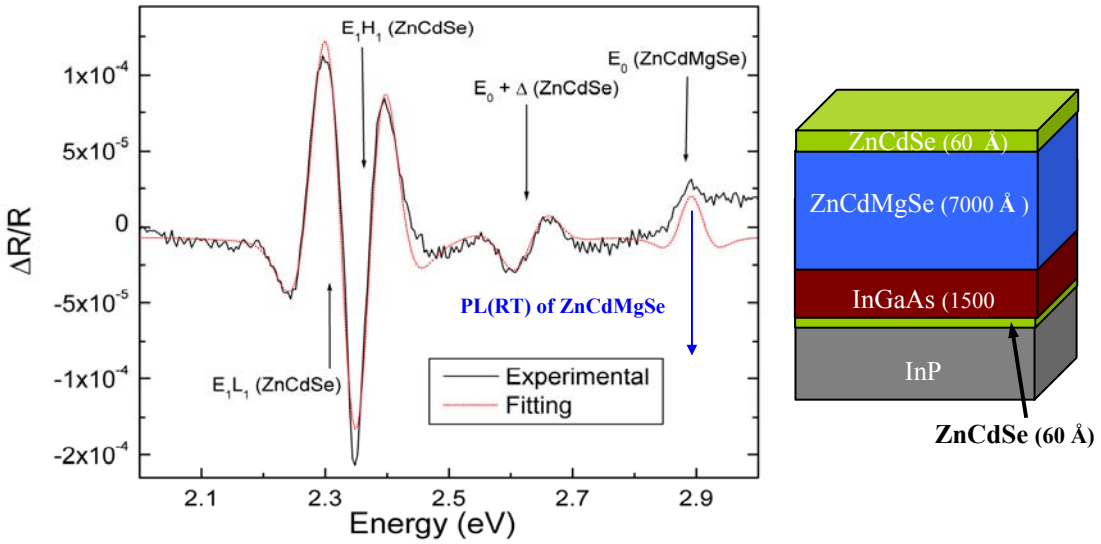

Figure 3.24. The RT-CER spectrum of a $Zn_xCd_yMg_{1-x-y}Se$ layer with the same structure as the $Zn_xCd_yMg_{1-x-y}Se$ barrier used for the growth of the CdSe-SQDs layers. A schematic of sample layer structure is represented on the right side of the CER spectrum.

[3] Value estimated for a matched ZnCdSe layer. This value should be higher than in the matched case due to the higher content of Zn.

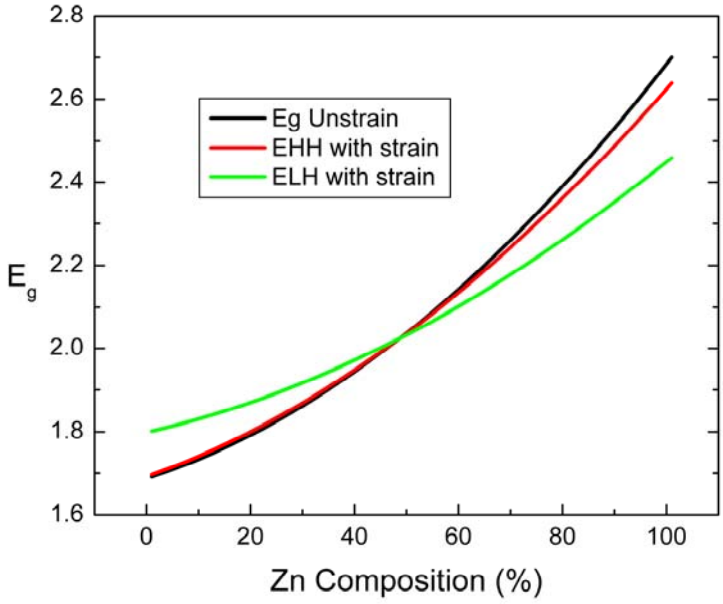

Figure 3.25. Variations of ZnCdSe QW energy levels for different layer compositions. EHH and ELH represent the transitions from the lowest level of the conduction band to the heavy hole and the light hole in the valence band, respectively.

In these calculations it is necessary to know the values of the effective masses as well as Δ_0. However, there are no reports for the effective masses of these compounds. Therefore, required values were estimated as in the reference [132]. It can be inferred from the figure that no splitting is noted for the totally matched structure, for which the percentage of Zn (or Cd) is approximately 50 %. Based on these calculations and considering that the percentage of Zn content in the $Zn_xCd_{1-x}Se$ layers for the $Zn_{0.38}Cd_{0.20}Mg_{0.42}Se$ reference layer represented in the figure 15 was about 81%, we can estimate the transitions for the low temperature layer as 2.279 and 2.385 eV for the heavy and the light hole. Comparison between the experimental values obtained by the fitting and the theoretical values are in good agreement if we take into account

that the calculations are based on the estimations of parameters of these materials. The last critical parameter to identify in the Fig. 3.23 was associated with ZnCdSe layers and appeared at 2.628 eV. This transition could be the $E_0+\Delta_0$ transition for the ZnCdSe cap. The value reported (see Table 3.5) is for matched $Zn_{0.53}Cd_{0.47}Se$, so it is a discrepancy between the value given by the fitting and the experimental value obtained in the reference 132. This disagreement may be explained by the higher content of Zn of the ZnCdSe layers in the sample, which moves the position of this transition to higher energies.

In the CER spectrum of the Fig. 3.23 transitions from the heavy and light hole of the LT-ZnCdSe were also observed. The interband transition that appeared at 2.467 was assigned to a higher energy transition of the ZnCdSe, E_2H_2 instead of the $E_0 + \Delta_0$, but this assignment needs to be considered further. Fig. 3.23 shows a weak transition at 2.196 eV, which is assigned to a high-energy transition in the QDs (QD_1). It is interesting to compare the energy of the QD_1 transition here and QD_1 transition reported in reference 46 for CdSe QDs grown over ZnSe barriers. The PL peak position for QD_0 was 2.107 for the CdSe QDs with $Zn_xCd_yMg_{1-x-y}$ Se barriers while it appears at higher energy, 2.319 eV, for the CdSe QDs with ZnSe barriers. This result is consistent with a difference in energy between the two transitions (E_{QD_1}-E_{QD_0}) equal to 89 meV for CdSe QDs on $Zn_xCd_yMg_{1-x-y}Se$ barriers while it is 125meV for CdSe QDs on ZnSe barriers. We propose that this may be explained by the fact the energy levels are closer to each other when the QD size becomes larger.

The transition at 2.042 eV is given by the experimental fitting. Although this transition is still not identified, we think this point could be related with the deeper

layers of the structure (III-V layers or III-V/II-VI interface). A possible explanation could be a thin III-V layer of InGaAsP resulting in a intermixing between the Ga and As of the InGaAs buffer and the In and P of the InP substrate. Further research must be performed to confirm this proposal.

Chapter 4. White Light

4.1. Introduction

Advanced new technological applications such as medical and biomedical ones, information storage, telecommunication, audio-visual, and military applications require often the use of integrated and compact display technology. Semiconductor based display devices, such as LEDs and lasers offer important advantages over competing technologies such as inorganic based lasers and dye lasers. Recently, advances in LED materials and technology have made the full-color range available from semiconductor-based devices. For example, red, yellow and green LEDs fabricated from different materials systems are being used in traffic lights with much longer lifetime, brighter emission using less power, and more profitability resulting from less operational maintenance than the traditional light bulbs. In addition, semiconductor-based white-LEDs have several advantages compared to the traditional incandescent sources of white light for illumination, including their compactness and longer lifetimes (>10000 hours for LEDs compared to 2000 hours for incandescent light bulbs), while consuming only 15-20% of the power for the same luminous flux, resulting in significant energy savings. However, current semiconductor based full-color displays and semiconductor based white light sources, using the three basic colors: red, green and blue, must be achieved by combining discrete devices made from three different materials, making the technology complex and expensive. Most often, these materials are also grown in different substrates, which make device integration more complex, and limiting the device resolution and

its size. For example, room temperature cw blue lasers of GaN grown on sapphire substrates are commercially fabricated, while green lasers can be fabricated from ZnSe-based materials on GaAs, and red/infrared lasers are based on the InGaAsP material system grown usually on InP substrates. Thus, in order to fabricate an integrated system, it is of interest to develop compatible materials that produce the three colors and that may be grown on high quality on a single crystal.

ZnCdMgSe alloys show great potential for applications in R-G-B devices. ZnCdMgSe-based QWs are used to produce lasers and LEDs that have the unique characteristic of emitting the three primary colors (R-G-B) from almost identical epitaxial heterostructures that can be grown in high quality on the same substrate. Furthermore, they can be easily be integrated in a one-step epitaxial growth process as a single monolithic unit. This simplifies fabrication and greatly enhances the potential for miniaturization of integrated R-G-B display devices. In fact, a design of an integrated three-color device was achieved by using an in-situ patterning of the QW structure by shadow-mask selective area epitaxy.[133] However, QW based devices have the limitations coming from their quantum efficiency and tunability. The SAQDs are expected to not only enhance luminescence efficiency and wavelength selectivity but also reduce the operating threshold of the devices and have less temperature dependence of the device response, which leads to less heat buildup in the operational mode. Heat buildup frequently favors the device degradation and decreases the device lifetime. Moreover, as discussed previously, the coherent SAQDs are expected to impede the propagation the dark-line defects that are often associated with the device degradation of the II-VI based devices.

The objective of Chapter 4 is to advance the QD material technology in order to develop reliable white-light-sources. MQDs structures were studied to explore the possibility of combining diverse QD layers with different QD size for the fabrication of white light-emitting structures through the mixture of the three primary colors.

4.2. R-G-B Multi-Quantum Dot structure to obtain white light

4.2.1. Experimental Details

The MQDs samples were grown by MBE on InP (001) substrates in an ultrahigh vacuum (UHV) system that has two Riber 2300 growth chambers, one dedicated to III-V materials and another to II-VI materials. InP oxide removal, InGaAs buffer layer growth, ZnCdMgSe bottom and top barrier layers were grown using the same procedure described, previously, in the section 3.3.3.1. The MQD inclusion sandwiched between the bottom and the top barrier layers were composed by different layers (usually three) of CdSe QDs with a different $t_{D,}$ separated by $Zn_xCd_yMg_{1-x-y}Se$ spacers.

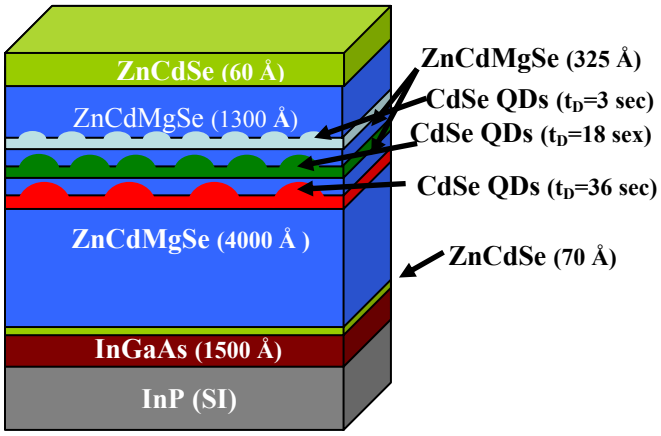

Figure 4.1. Schematic of a MQD sample structure to obtain white light emission.

The Se/Cd, Cd/Zn and VI/II flux ratios were kept at 7.3, 1.2 and 3.5, respectively, during the entire II-VI growth. The $Zn_xCd_yMg_{1-x-y}Se$ barrier layers were grown with the same composition, thickness and band gap (~2.8 eV), for all the samples. The $Zn_xCd_yMg_{1-x-y}Se$ barrier band gap was measured on a reference layer grown under the same conditions as the QD barrier layer. The Fig. 4.1 shows a schematic representation of the structure of a MQD sample. The MQD inclusion consisted of three CdSe QD layers, each one with a different t_D, separated by 325 Å-$Zn_xCd_yMg_{1-x-y}Se$ spacers. CdSe depositions were 7.2 (t_D = 36 sec), 3.6 (t_D = 18 sec), 0.6 (t_D = 3 sec) ML.

4.2.3. Results and Discussion

As discussed in the last chapter, for appropriate choice of the CdSe t_D, the size of the QD and consequently, the emission wavelength from the CdSe QDs can be adjusted to fall anywhere within the visible range. Taking advantage of the control, quality and reproducibility obtained by CdSe SAQDs on ZnCdMgSe barriers, we tried to combine and integrate different QDs layers in a single structure to obtain white light emission.

For photoluminescence structures and for surface emitting LEDs, it is important to ensure the appropriate order of the three QD layers. This is so because if the QD layer with red PL emission is the layer closer to the surface carriers will be absorbed by that layer before they arrive at deeper QD layers inside the structure. Furthermore, during the emission process, if the carriers in deeper QDs recombine emitting light,

part of this light will be reabsorbed by the QD layers with smaller bandgap that are on the top part of the structure.

This significance of the layer order was demonstrated with the first three-MQD-layer structure grown, where three QDs layers were grown in reverse order than in Fig. 4.1. From substrate to surface, the CdSe depositions in each layer were 1.2 ML (t_D = 6 sec), 3.6 (t_D = 18 sec) and 7.2 (t_D = 36 sec), separated by 325 Å-$Zn_xCd_yMg_{1-x-y}Se$ spacers. The Fig. 4.2 is the PL spectrum at 77K of this (R-G-B)-MQD structure. The inset on the right-top side of the figure is another spectrum taken with higher excitation density in the blue-green region (from 2.2 to 3.1 eV). The intensities of the QD peaks diminish noticeably from the red to the blue. Therefore, the mixing of the colors resulted in red-greenish emission but not white light emission.

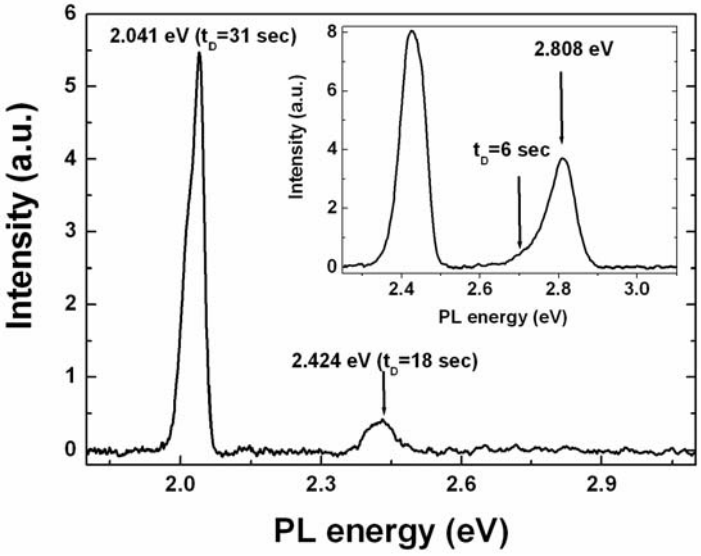

Figure 4.2. The PL spectrum of an R-G-B MQDs sample at 77 K. PL peak emissions with their corresponding t_D assignments are indicated in the figure (red QDs layer t_D = 36 sec, green QDs layer t_D = 18 sec, blue QDs layer t_D = 6 sec). The inset in the right side of the figure is another spectrum taken with higher excitation density. The $Zn_xCd_yMg_{1-x-y}Se$ barrier peak can be noticed in the figure at 2.808 eV with a lower energy shoulder assigned to the blue QDs (t_D = 6 sec).

To optimize the structure that we should choose to obtain the appropriate combination of colors to produce white light we first reversed the order of the three QD layers, according to the order shown in Fig 4.1. In addition, the following two experiments were performed: first, balance the quantity of material deposited for each color and second, change the spacer thickness to enhance interaction between the QD layers.

For the first experiment, a structure with same quantity of material (same number of CdSe deposited monolayers) for each color and with the same QD layer order of colors than the Fig. 4.1 was grown. The structure consisted of nine QDs layers. One QD layer with the red emission, t_D =36 sec, 7.2 ML of nominal thickness; two QDs layers with emission in the green range, t_D =18 sec, 3.6 ML of nominal thickness, (2 x 3.6=7.2 ML); and finally, six layers of QDs with a deposition time of 6 sec, 1.2 ML of nominal thickness, (6 x 1.2 = 7.2 ML). The ZnCdMgSe spacer thickness is 1300 Å between different layers. The Fig. 4.3 shows the PL spectrum for this sample. Once more, one peak is dominating the spectrum, which is attributed to the top QDs layers with a t_D = 6 sec (1.2 ML). Thus, the predominant color of the emission of the sample is blue. No other peaks can be perceived in the spectrum from the other QDs, the two QD layers with t_D = 18 sec (3.6 ML) and the one with t_D = 36 s (7.2 ML), in this sample. The fact that no emission from the deeper QDs is observed is probably due to the larger number of blue QD layers, six layers with t_D=6 sec, with respect to the other two types of QDs layers, as well as to the large $Zn_xCd_yMg_{1-x-y}Se$ spacer thickness, which makes the active region in this sample very thick. Thus, very little light is likely to be penetrating to the deeper QDs.

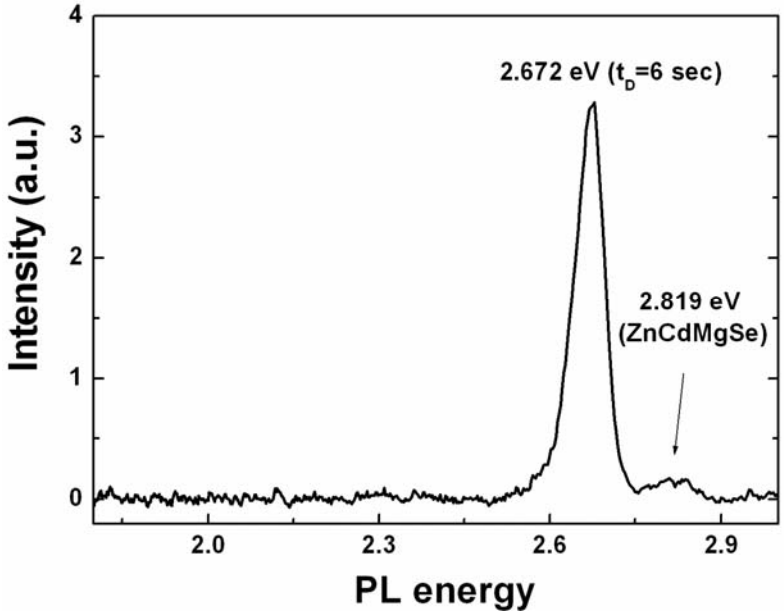

Figure 4.3. PL spectrum of an R-G-B MQDs sample obtained at 77K. The sample structure consisted of one QD layer with the red emission, t_D =36 sec, or 7.2 ML; two QDs layers with emission in the green range, t_D =18 sec (3.6ML); and six layers of QDs with a deposition time of 6 sec (1.2ML). The predominant PL emission is the correspondent to the six QDs layers (t_D =6 sec) with blue emission at 2.672 eV. The ZnCdMgSe barrier peak appears in the spectrum at 2.819 eV.

For the second experiment, the spacer thickness between the QD layers was varied for different samples. The composition and arrangement of QD layers are the same for the three MQD samples grown (as illustrated in Fig. 5.1). The structure consists of three QD layers arranged according to the growth direction in the following way: First, a layer with a t_D = 36 sec was grown, second a QD layer with a t_D = 18 sec and finally, the last QD layer with t_D = 6 sec grown before top barrier. The Fig. 4.4 shows the PL spectra for these three samples. The spacer thicknesses were 1300 Å, 650 Å and 325 Å, respectively, for the part a, b and c of the Fig. 4.4.

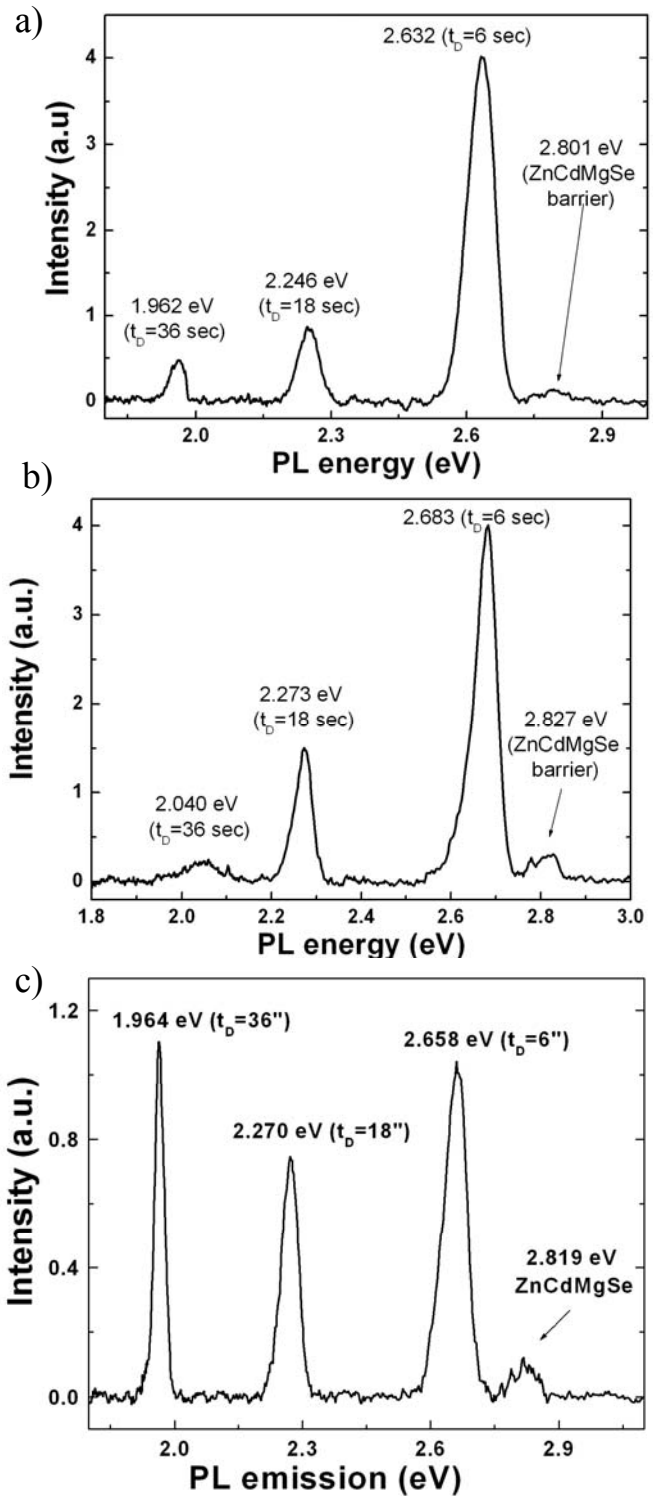

Figure 4.4. PL spectra of three R-G-B MQDs samples obtained at 77K. The structure of all the samples consisted of three QD layers with t_D equal to 36 sec (red emission), 18 sec (green emission) and 6 sec (blue emission). The different spacer thicknesses were 1300 Å for part a, 650 Å for the part b and 325 Å for the sample in part c.

The three samples exhibited bright white emission that could be observed by eye, at 77 K, because of the mixing of the three lines. For the *part a* and *part b*, the white is slightly bluish reflecting the intensity predominance of the blue peak. Figure c shows the PL spectrum of a MQD structure having pure white emission (as seen by eye) at 77 K. Three peaks corresponding to the red (1.964 eV), green (2.270 eV) and blue (2.658 eV) emissions were observed from the QDs layers grown with the following deposition times: $t_D = 36$ sec, $t_D = 18$ sec and $t_D = 6$ sec, respectively.

The FWHM for the 77 K PL emission lines of part c are 23.6 meV for the red, 40.2 meV for the green and 53.1 meV for the blue emission. Both the PL emission energy and the FWHM of the three QDs layers in the MQD structure follow the same trend with t_D (see Fig. 4.5) as the samples represented in Fig. 3.18, which indicates that there is not any disruption of the growth due to a correlation between layers of QDs.

As the sample temperature is raised to RT, the emission appears greenish for all the samples because of the slight shift of the QDs PL emission with the temperature. PL emission moves towards longer wavelengths with temperature. This shift is about 50 meV. To overcome this effect, another sample was grown with a slightly different CdSe deposition time for the blue layer (t_D=3 s). In this case, white emission was achieved at RT. The PL spectrum at RT of this sample is represented in Fig. 4.6. The Fig. 4.7 shows the photographs of a sample that emits white light by the mixing of R-G-B colors. The sample was mounted on a cold finger of a Janis cryostat, which can be appreciated in the figure.

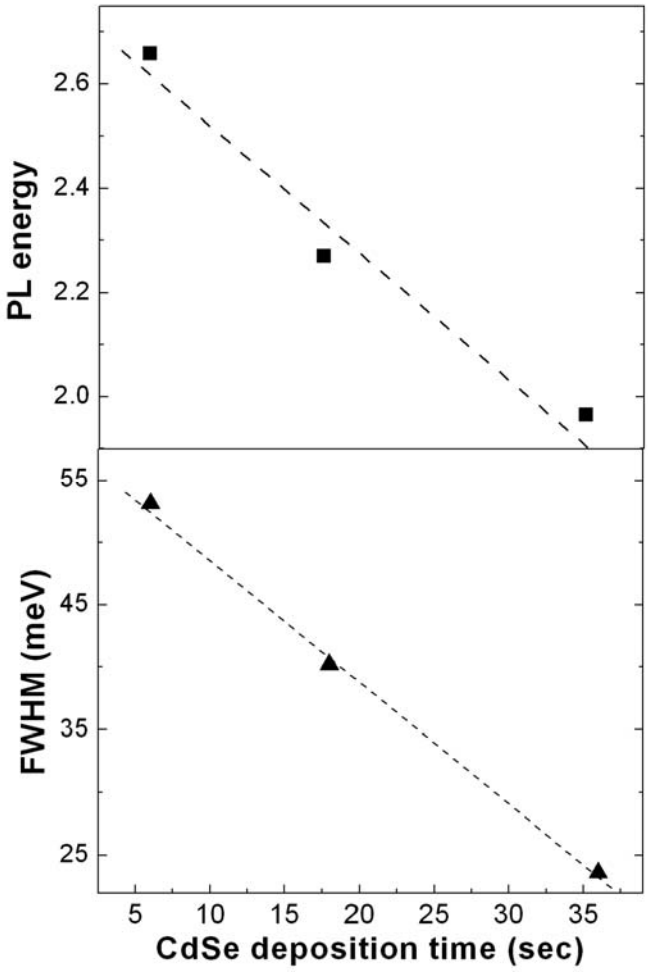

Figure 4.5. PL emission energy and the FWHM versus t_D for the three QDs layers of the MQD structure represented in part c of Fig. 4.4

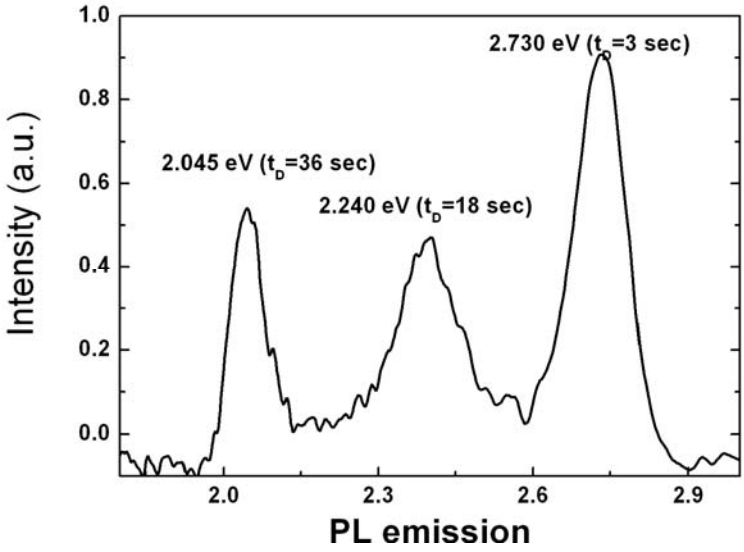

Figure 4.6. PL spectra of a R-G-B MQDs sample obtained at RT with light emission observed by eye. The structure of the sample consisted of three QD layers with t_D equal to 36 sec (2.045 eV, red emission), 18 sec (2.240 eV, green emission) and 3 sec (2.730 eV, blue emission). The spacer thickness between QD layers was 325 Å.

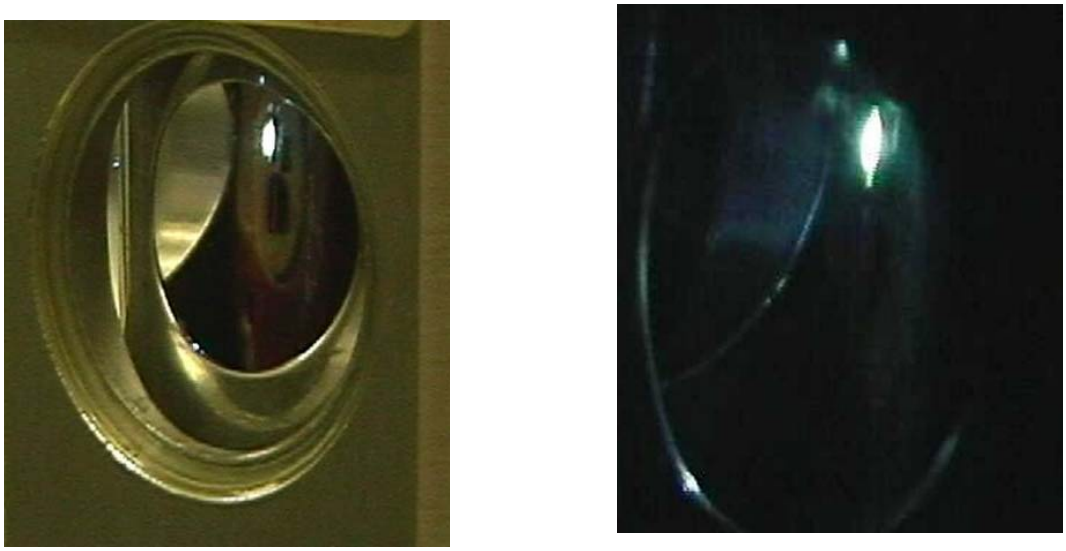

Figure 4.7. White light emitted for the R-G-B-MQDs structure composed of three CdSe QDs layers with different t_D (red QDs layer t_D =36 sec, green QDs layer t_D =18 sec, blue QDs layer t_D =6 sec). The sample was mounted on the cold finger of a Janis cryostat, which can be appreciated in the figure.

These results indicate that this material is not only attractive for optical applications in the R-G-B range but also it may be useful for the fabrication of white light sources, which have not been obtained yet by a single material grown on the same substrate (in a single structure). Futhermore, this is the first approach to obtain white light sources coming from mixing of QDs emission.

4.3. Light-Emitting Diode based on R-G-B-MQD structure for white light emission

It has been shown that the CdSe SAQDs grown on ZnCdMgSe barriers matched to InP substrates can be tuned to obtain emission wavelength adjusted to fall anywhere within the visible range. The simple linear behavior and the reproducibility of the QD PL emission with the CdSe deposition time permit the accurate design of the PL emission originating from QDs. In fact, combinations of three stacked QDs layers with CdSe deposition time corresponding to the red, green and blue emission were demonstrated as photopumped white light sources. These results indicate that this QD material system shows potential to fabricate light emitting devices to obtain any color of the visible spectrum or to achieve white light at room temperature. Through earlier results and those presented in the previous chapters, we have achieved the essential requirements for the fabrication of a LED prototype based on CdSe SAQDs on ZnCdMgSe barriers. In this section, we present some preliminary studies of CdSe/ZnCdMgSe QDs based-p-n junctions designed to obtain white emission.

4.3.1. Experimental Details

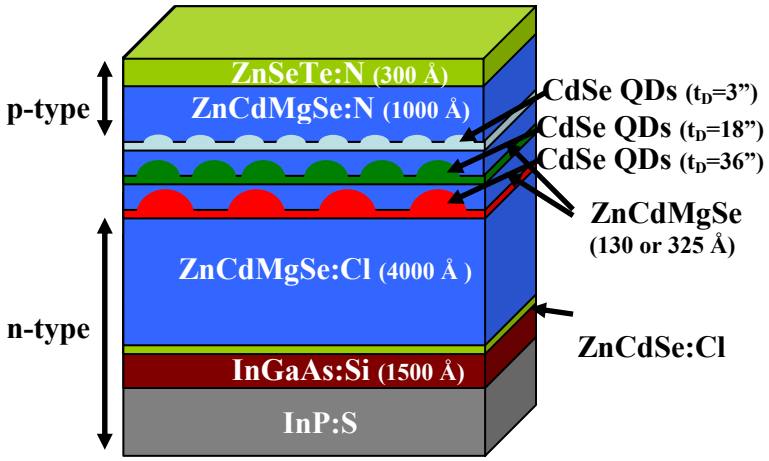

Figure 4.8. Schematic of the light emitting diode layer structure for white light emission

The LED p-n junction structure based on CdSe SAQDs on ZnCdMgSe barriers for the achievement of white light was grown in the same bottom barrier conditions that the ones described in section 3.3.3.1 with the only different that the structure is doped n-type as is indicated in the Fig. 4.8. Two LED structures were grown one with 130 Å and another with 325 Å-ZnCdMgSe undoped spacers. CdSe insertions were 7.2 (t_D=36 sec), 3.6 (t_D=18 sec), and 0.6 (t_D=3 sec) ML as the MQDs structure for white light emission at RT. The CdSe QDs were capped with a 1000-Å ZnCdMgSe cladding layer doped with nitrogen (p type). The growth ended with a 300 Å- ZnSeTe layer highly doped with nitrogen to obtain a good p-type contact. A $ZnCl_2$ cell was used as source of Cl dopant. Doping levels were for the n-type layer following the growth direction: 10^{19} cm^{-3} for the n+-InP substrate doped with sulfur (facilitated by the company), $1.8x10^{18}$ cm^{-3} for the InGaAs doped with silicon, $1.0x10^{18}$ cm^{-3} for the ZnCdSe low

temperature buffer layer, $2x10^{18}$ cm^{-3} for the ZnCdMgSe barrier layer doped with chlorine. All these values were based on Hall effect measurements.

Doping levels for the p-type layer doped with nitrogen source were ~10^{16} cm^{-3} for the ZnCdMgSe top barrier and ~10^{18} cm^{-3} for the ZnSeTe contact layer. Both values were approximated using capacitance-voltage measurements on calibration samples. The composition of both cladding ZnCdMgSe layers (n-type ZnCdMgSe: Cl and p-type ZnCdMgSe: N) was such that it was lattice-matched to the InP. Their bandgaps were about 2.8 eV.

4.2.3. Results and Discussion

The contacts of the LEDs were fabricated by depositing either gold or indium on the surface and attaching gold wires to the back of n-InP substrate surface and the top metal contact using melted indium. The section 2.2.2.10 explains how the contacts are fabricated. An indium dot is deposited to preliminary tests of the I-V characteristics of the LEDs. To obtain a better contact with which surface emission might be observed a gold ring is evaporated on the p-side of LED sample using the vapor deposition procedure described in the section 2.2.2.7. The size of the indium dot is variable while the gold ring mask has been designed to have approximately 0.5 mm diameter. Both gold and indium can form ohmic contacts on the highly p-type doped lattice-matched ZnSeTe: N contact layer, as described in the reference 58. The highly p-type doped thin layer of ZnSeTe: N was used to improve the p-type contact since a direct metal contact on the p-type ZnCdMgSe cladding layer will not behave as an ohmic contact due to relatively low doping level of this layer (~10^{16} cm^{-3}). In

the next two subsections, the Hall Effect and the capacitance voltage results for detemination of the doping levels in p-type and in the n-type sides of the LED structure are shown.

4.2.3.1 The n-type doping: Hall Effect measurements

For the fabrication of LEDs and LDs, effective p-type and n-type dopings of cladding and waveguide layers (just in the LD case) are essential. Typically, a doping in the range of 10^{17} cm^{-3} or higher is required for commercial device applications.

Chlorine as a substitutional atom on a Se site can form a shallow donor in ZnSe based materials. The source of chlorine is a $ZnCl_2$ in the II-VI growth chamber. The n-type doping of the LT $Zn_xCd_{1-x}Se$ buffer and $Zn_xCd_yMg_{1-x-y}Se$ layers was performed with a temperature of the $ZnCl_2$ cell of 65 ˚C.

On the other hand, silicon can be added to InGaAs layers as a shallow donor, substituting a III-element in a InGaAs epitaxial layer. Silicon temperature used for the doping of the InGaAs was 990 ˚C.

Hall Effect measurements were applied to characterize the electrical properties of the three reference bulk layers of n-type InGaAs: Si, n-type ZnCdMgSe: Cl and n-type ZnCdSe: Cl, grown under the same conditions that the correspondent layers on the LED structure. Free electron concentration, mobility, resistivity and Hall coefficient were obtained from the Hall measurements (section 2.2.2.6), after the testing and achievement of the right current-voltage characteristics (ohmic behavior) of the indium contacts. The Table 4.1 summarizes the values of the carrier concentration and mobility for these layers.

Material	Carrier concentration (cm^3)	Mobility (cm^2/ Vs)
InGaAs: Si	1.8 x10^{18}	3157
ZnCdSe: Cl	1.0 x 10^{18}	201
ZnCdMgSe: Cl	2.0 x 10^{18}	200

Table 4.1 Carrier concentration and mobility for n-type InGaAs: Si, n-type ZnCdMgSe: Cl and n-type ZnCdSe: Cl, grown under the same conditions that the correspondent layers on the LED structure.

4.2.3.2 The p-type doping: capacitance-voltage measurements

Two bulk reference layers of N: ZnCdMgSe and N: ZnSeTe were used to determine the doping level concentration of the p-type-ZnCdMgSe and the p-type ZnSeTe layers in the LED structure. Both layers were grown in the same day than the LEDs structures and using the same doping conditions. The ZnCdMgSe reference layer was grown following the same procedure described previously in the section 3.3.3.1. The only difference is that the InGaAs buffer was doped with beryllium (p-type) and grown in a p-type InP substrate. The ZnCdMgSe bulk thickness was 1.5 μm. The nitrogen conditions for this sample were a RF discharge power of 390 W and a background pressure of 2.3 x10^{-6} Torr.

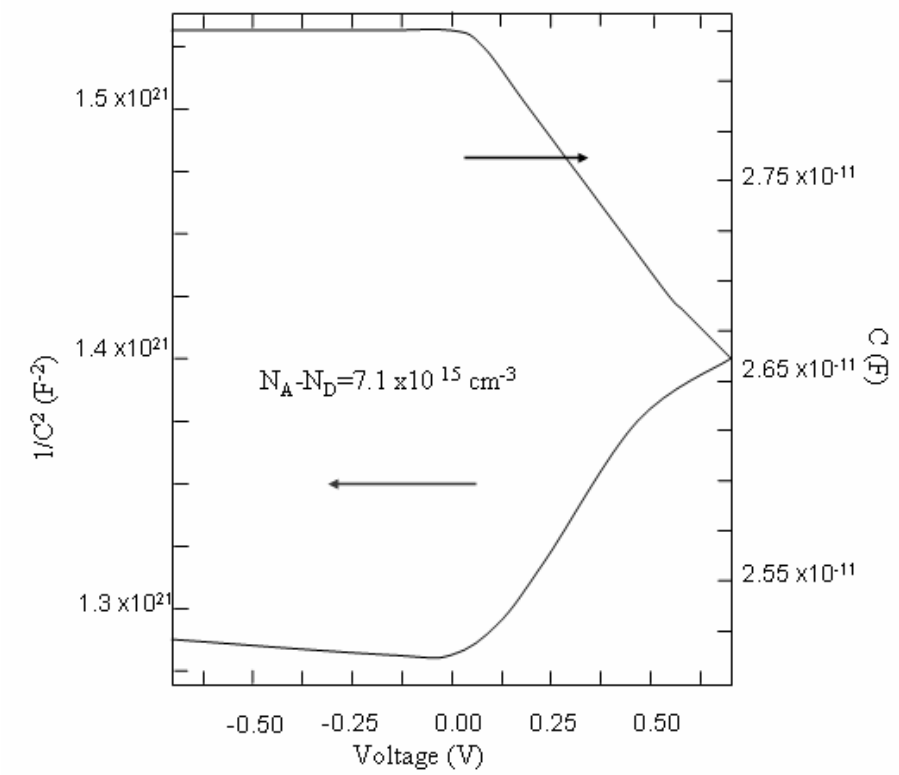

Figure 4.9. Capacitance-voltage and the inverse of the square of the capacitance versus the voltage for a reference $Zn_xCd_yMg_{1-x-y}Se$ bulk layer with the same doping concentration than the p-type $Zn_xCd_yMg_{1-x-y}Se$ in the LED structures. Net acceptor concentration was obtained using the curve $1/C^2$ versus the voltage.

These conditions were not only chosen for the optimization of the nitrogen doping on the ZnCdMgSe layer but also for the growth of a good surface quality. As described in the reference 58, higher discharge power or larger nitrogen flows corresponding to higher background pressure in the chamber results in higher nitrogen incorporation. However, too much nitrogen incorporation may cause serious carrier compensation in the Se-based II-VI materials and degradation of the quality of the surface of ZnCdMgSe. The voltage of the nitrogen source was monitored with a voltmeter and was stable at 450 mV during all the growth. The Fig. 4.9 shows the capacitance-voltage and the inverse of the square of the capacitance versus the voltage for this

sample. Net acceptor concentration of N_A-N_D=7.1 X 10 ^{15} cm^{-3} was obtained taking the slope, d ($1/C^2$)/V, of the curve $1/C^2$ versus the voltage and applying the equation 2.65 with a contact area of approximately 0.3 mm^2.

The N doped $ZnSe_{1-x}Te_x$ bulk reference layer was grown on a p-type InP substrate with a Be: InGaAs buffer. The condition of the discharge nitrogen plasma source was 390 W for the input power with a background pressure in the chamber of 1.95 x10^{-6} Torr. Once more, the voltage of the nitrogen source was monitored with a voltmeter and was stable at 450 mV during all the growth. The Fig. 4.10 represents the capacitance-voltage and the $1/C^2$-voltage profiling of this sample and its net acceptor concentration N_A-N_D=~1 X 10 ^{18} cm$^{-3.}$

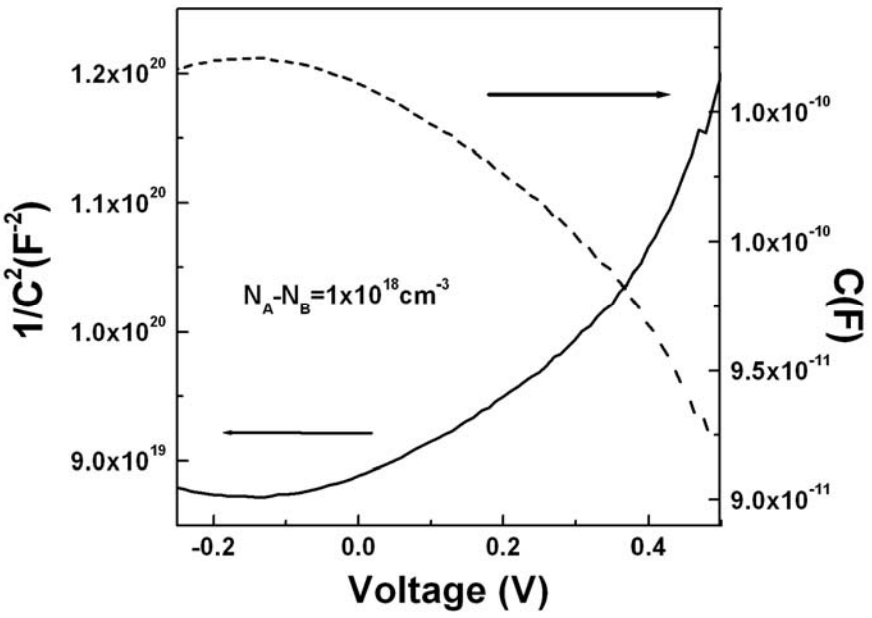

Figure 4.10. Capacitance-voltage and the inverse of the square of the capacitance versus the voltage for a reference $ZnSe_{1-x}Te_x$ bulk layer with the same doping concentration than the p-type $ZnSe_{1-x}Te_x$ contact in the LED structures. Net acceptor concentration was obtained using the curve $1/C^2$ versus the voltage.

4.2.3.3 Current-Voltage Characteristics

The Current-voltage (I-V) measurements were performed in both LED structures with three stacked R-G-B QD layers grown under the same conditions as the structure that emitted white light at RT. Both gold dot contact and melted indium contacts were used for these measurements and similar results were obtained for both. The I-V characteristics of the LEDs were measured with a Keithley 236 source unit (section 2.2.2.10).

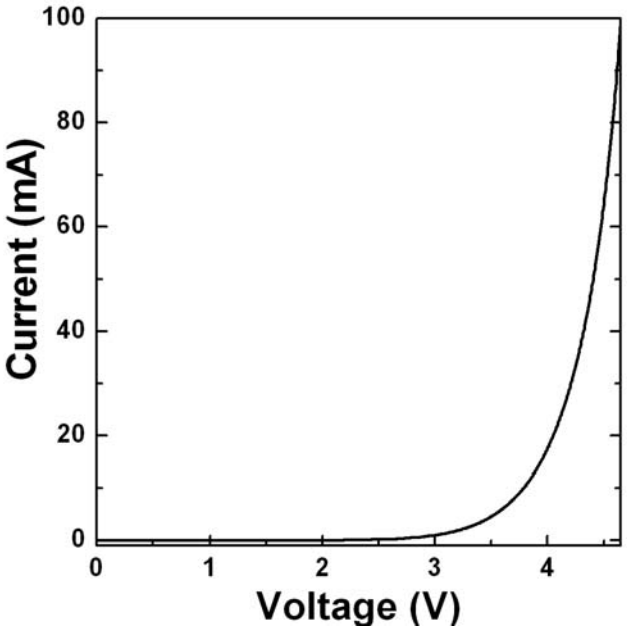

Figure 4.11. Current-Voltage characteristics for a LED structure designed to emit white light.

The I-V characteristics shown in the Fig. 4.11 indicate good diode behavior, low turn-on voltage (<4V), low resistance of the device to the current flow, output currents of ~100mA were obtained for an applied voltage of at 4.6 V (output current is limited of that can be detected by Keithley 236 source unit); and no reverse breakdown devices even at voltages below 10V were observed. Based on this curve the resistance of the device is similar to actual commertial LED devices based on III-V materials.[58]

4.2.3.4 Luminescence: Engineering Challenges of the Designed Structure

One of the most important issues of a LED performance is the quality of the emitted light (luminescence) during the current injection. Every so often, luminescence of previous LED based on QWs of ZnCdMgSe familiar system was observed during the performance of the current-voltage measurements. However, the electroluminescence from the surface was weak since the gold or indium contact absorbed a large part of the light emitted from the LED structure.

Initially, indium melted on the surface was used as contact for the LED samples grown to obtain white light emission. No light emission was observed from both LED samples during the current-voltage measurements when an indium contact was used. This result may be attributed to the light absorption from the contact or the poor contact quality since annealing to high temperatures was not performed. Therefore, to improve the contact characteristics, gold metal was evaporated on the surface of the LED samples (section 2.2.2.7 and section 2.2.2 10). However, no light could be appreciated by eye coming from the surface of the samples when the current was injected in the LED structures even though the thickness of the gold contact was just few angstroms, 200 Å, (almost transparent). This can be explained considering the thickness of the ZnSeTe: N contact. If the thickness of ZnSeTe layers is too large all the light originating from the QD layers will be reabsorbed by this contact on the surface. In fact, reference 58 gives a detailed explanation about the origin of this absorption. A broad red emission was observed in the electroluminescence

measurements regardless of the QW thickness. The transition was assigned to a recombination occurring at the type-II interface between the $Zn_xMg_yCd_{1-x-y}Se$ barrier layer and the $Zn_xSe_{1-x}Te$ cap. The author explains that in spite of the band alignment between these two materials is not known; a type II band alignment is expected. In fact, strong luminescence has been previously observed from II-VI type-II heterostructures.[134] In other to minimize the influence of a thick ZnSeTe contact on the electroluminescence of the LED, an etching of the ZnSeTe cap layer can be performed to thin out this layer[58] but this procedure results, occasionally, in the damage of the crystal quality.

The observation of the luminescence by the edge is complex to complete but it was the alternative to the etching of the ZnSeTe contact. On the other hand, if the contact is in the center of the surface of the sample, edge luminescence is unlikely to be achieved since the carrier transport and carrier recombination occur around the vertical area were the contact is placed.

To test the luminescence coming from the QDs as well as to be able to perform electroluminescence measurements from the edge, we designed a mask to evaporate the gold with the shape of a ring (see Fig. 4.12). After the evaporation of the gold metal on the ZnSeTe: N contact, we performed a cleavage to divide the ring in two halves. As inferred from the cross section of the representation of one of these halves in Fig. 4.12, the contact is just on the edge of the sample. Therefore, the requirement of having the contact right on the edge of the sample was fulfilled to be able to observe if the sample emitted any light from the edge of the structure. No light was observed using two methods: applying a pulse of current and waiting for the

light emission or increasing the voltage continuously until that the turn voltage is overcome and the light is generated.

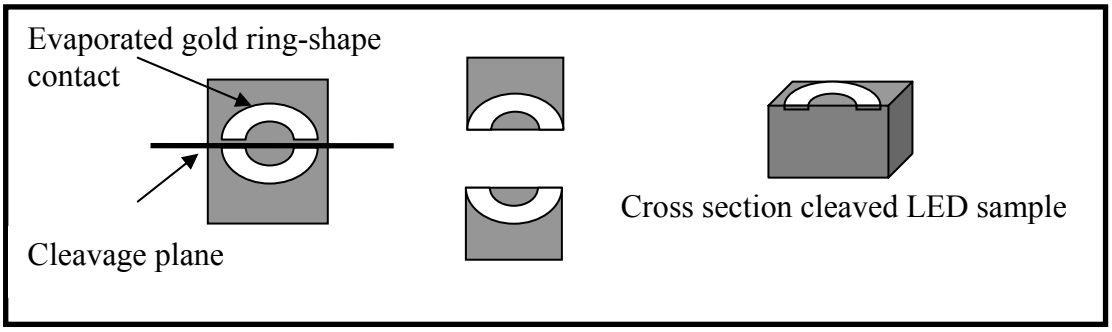

Figure 4.12. Schematic of the cleaved sample to obtain a gold half-ring contacts on the edge of the sample.

We suggest that the reason that any light emission was detected is because the expected intensity of the light coming from the structure is low and, further, a portion of it is reabsorbed by the contact. We propose that more than three layers must be employed for the fabrication of LED, R-G-B multi-quantum dot structures, to balance the low intensity of the emission and the absorbance of the contact. The next chapter will address in detail the fabrication of MQD structures.

It will also be interesting to try to replace this ZnSeTe contact by another material that does not absorb light in the visible range, and consequently the light emitted by the device, but that still permit a high p-type doping. We propose also the study of LED structures with p+ ZnBeTe contacts.

Chapter 5. The Growth of CdSe Multi-Quantum Dots Layers on $Zn_xCd_yMg_{1-x-y}Se$ barriers

5.1. Introduction

Transitions of carriers (electrons or holes) in QDs between two confined states belonging to the same band are called inter-sublevel (ISL) or inter-subband (ISB) transitions. These transitions are involved in important devices applications of QDs, such as QDs infrared (IR) photodetectors (QDIPs) and lasers, and usually take place in the mid- (MIR) or far infrared (FIR) wavelength range. The anticipated large CdSe/$Zn_xCd_yMg_{1-x-y}Se$ conduction-band offsets up to 1.5 eV highlights the potential of these materials to address new important technological directions, such as QDIPs with functionality extended into near-IR, and even up to the visible region; and ISB quantum cascade lasers (QCLs) with emission wavelength significantly shorter, (i.e.1.5 μm at RT) than what is currently available in such devices.

The QDIPs are based on the excitation of carriers from bound QD states to higher energies by means of absorption of IR radiation, so that the carriers can be swept away from the QD by applied external electric field and thus originate photocurrent. The QDIPS compete with the present detection technologies in the IR range, which are mainly based on intrinsic mercury-cadmium tellurite (MCT)

photoconductive detectors and quantum well infrared photodetectors (QWIPs). QWIPs show relatively low quantum efficiency, large dark currents, a narrow bandwidth and the disadvantage of intrinsically detecting only off-normal incidence radiation. In addition, QDIPs can be intrinsically sensitive to normal incidence photoexcitation. Furthermore, they have larger phonon scattering times (phonon bottleneck effect), leading to an efficient detection of radiation since the photoexcited carriers are less likely to be captured into the QDs or to relax to the ground state before being swept away as a photocurrent. This results in increased extraction efficiency and increased operating temperatures.[121]

On the other hand, QCL is a unipolar laser that relies on the ISB transitions between conduction band states arising from the size quantization in a semiconductor heterostructure. Its cascade principle based on the unipolar transport (only injection of electrons) makes the QCL a device with extremely higher quantum efficiency. However, there is not availability of QCLS in CW mode at RT due to limitations to minimize the threshold current, which depends inversely from the quantum confinement. QDs will increase the confinement of the electrons and so, will improve the device characteristics.

Development and control of stacked QDs structures is crucial for the progress of these intersubband devices. The volume density of a single QD layer is rather low, so laser and detector applications result practically unfeasible with no more than an individual layer. Stacked or MQDs[135] have already been fabricated by SA using MBE and have also been integrated into device structures, such as laser structures. However, there are still some engineering disadvantages, such as control in the

location, density, size and shape of SAQDs. In particular, applications such as QCLs and QDIPs require careful of these properties, which influence the energy states and the optical properties of these devices. Despite we were able to tune the PL emission (changing the size of the QDs) from the blue to the red in the visible range, by only changing the t_D of CdSe SAQDs grown on $Zn_xCd_yMg_{1-x-y}Se$ barriers,[136] the possibility of changing the PL emission and/or electronic properties is restricted to decreasing (or increasing) the amount of CdSe that is deposited to form the CdSe QDs. This change every so often affects considerably the QD density and consequently, the PL intensity of the CdSe QDs. Recently, methods to solve these QD shortcomings have been reported. Considering all these attempts, we can distinguish two approaches without an alteration of the growth conditions of the deposited material that will control the formation of the QDs (substrate temperature, deposition time, pressure of the excess element, As in III-V QDs or Se in II-VI…). One approach is by modifying chemically the formation and growth of the QDs, either by altering the lattice mismatch (strain) between the QDs and the substrate layer (or barrier) or/and by adding an external chemical element (such as Mg). Another approach is by modifying the structural properties of the substrate were the QDs would be grown. Some structural methods that have being used are seeding of QDs, patterned substrates, or correlated stacked MQDs[137]. Among these, the use of MQDs offers, in addition, the possibility of controlling the polarization of the light emitted by the QDs layers,[76] which plays a significant role for some devices applications such as surface-emitting, edge-emitting lasers and single-photon based devices.

In this Chapter, optical and morphological studies of MQDs layers are presented. The effect produced by the variation of Mg content in the $Zn_xCd_yMg_{1-x-y}Se$ barrier on the optical and structural properties of MQDs layers is reported. Vertical correlation of MQDs layers is also studied with respect to the $Zn_xCd_yMg_{1-x-y}Se$ spacer thickness and magnesium content. Finally, CER measurements are shown, helping to understand the band structure and properties of the MQDs layers which is essential for the development of ISB devices.

5.2. Initial Studies in MQDs Structures

To take full advantage of the CdSe/$Zn_xCd_yMg_{1-x-y}Se$ QDs outstanding properties for use in optoelectronic emitters and detectors, a detailed and comprehensive understanding of the electronic and optical properties of these materials is necessary. To address this need, optical transmission and reflectivity experiments from the UV to the IR, room and liquid-nitrogen temperature CW-PL experiments from 400 nm to 700 nm, and time-resolved PL experiments were performed on a set of three initial CdSe/$Zn_xCd_yMg_{1-x-y}Se$ MQD samples.

5.2.1. Experimental details

The CdSe/$Zn_xCd_yMg_{1-x-y}Se$ MQD structures were grown with the same $Zn_xCd_yMg_{1-x-y}Se$ barrier and top layer growth conditions as those described in the section 3.3.3.1. The only difference between the samples presented in the section 3.3.3.1 and the samples described in this paper is the active region. The MQD active

regions of samples A2078 and A2081 are composed of ten stacked CdSe QDs layers with the same t_D = 13 sec, 2.5 ML, corresponding to green emission, separated by $Zn_xCd_yMg_{1-x-y}Se$ spacers with different thickness, 32.5 nm for A2078 and 5.2 nm for A2081. The sample A2048 is the same MQDs structure that was described in the Chapter 4, Fig. 4.3. This sample consists of nine QD layers of stacked QDs with a 130 nm ZnCdMgSe spacers: from the top to the bottom, six QD layers with t_D = 6 sec (1.2 ML), two QDs layers with t_D = 18 sec (3.6 ML), and one layer of QDs with t_D = 36 sec (7.2 ML).

5.2.2. Results and Discussion

The study of the interband QDs absorption for CdSe/$Zn_xCd_yMg_{1-x-y}Se$ MQD samples grown on InP substrates is impaired by the III-V layers (the InP and InGaAs bandgaps are lower than that of the interband QDs absorption energy). Thus, InP substrate and InGaAs buffer layers were removed from the CdSe/$Zn_xCd_yMg_{1-x-y}Se$ QDs active structure by selective chemical etching.[138] After this removal, optical transmission and reflectivity measurements were performed on all three QD samples for the spectral range of 180 nm to 3200 nm. The absorption spectrum at RT of the sample A2048 is shown in Fig.5.1. The feature at 470 nm corresponds to the interband QDs absorption whereas the one at 440 nm corresponds to the bandgap of the $Zn_xCd_yMg_{1-x-y}Se$ barrier. For the sample A2078 the features corresponding to QDs interband absorption and $Zn_xCd_yMg_{1-x-y}Se$ bulk absorption are observed at 499 nm and 440 nm, respectively. Reflectivity measurements between 300 nm and 800

nm, at 300 K have been performed on all samples. Reflectivity spectra on all samples show clearly the $Zn_xCd_yMg_{1-x-y}Se$ band-gap signature at about 440 nm.

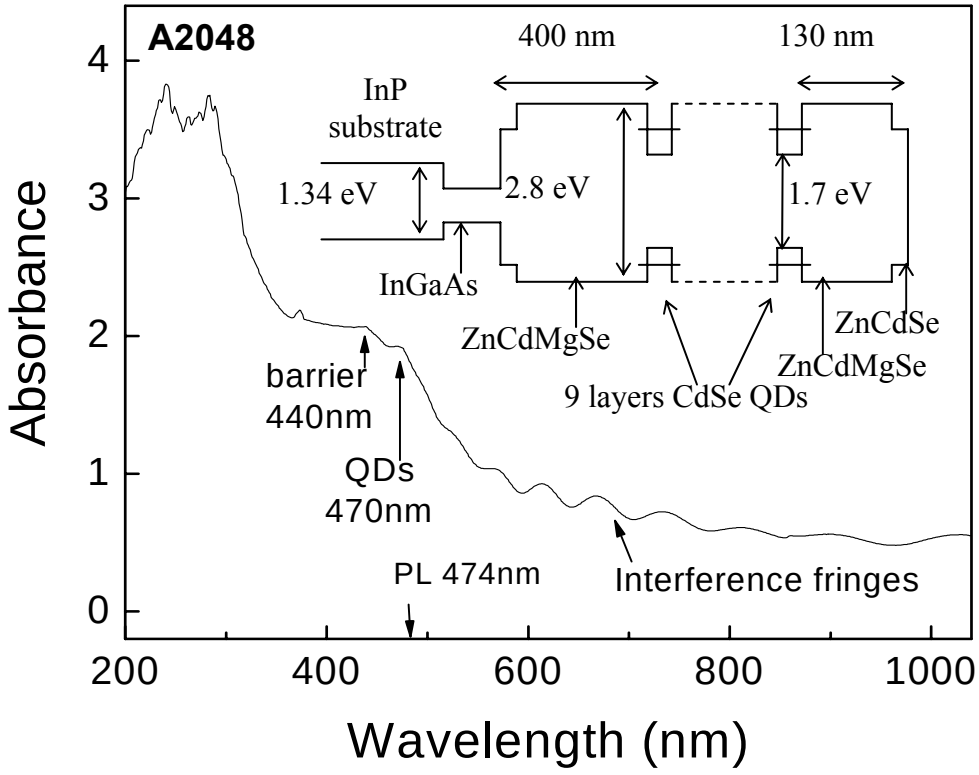

Figure 5.1. Absorption spectrum of the sample A2048 at 300 K. The position of the absorption peaks is indicated with the corresponding transitions. The inset shows the band structure of the QD samples.

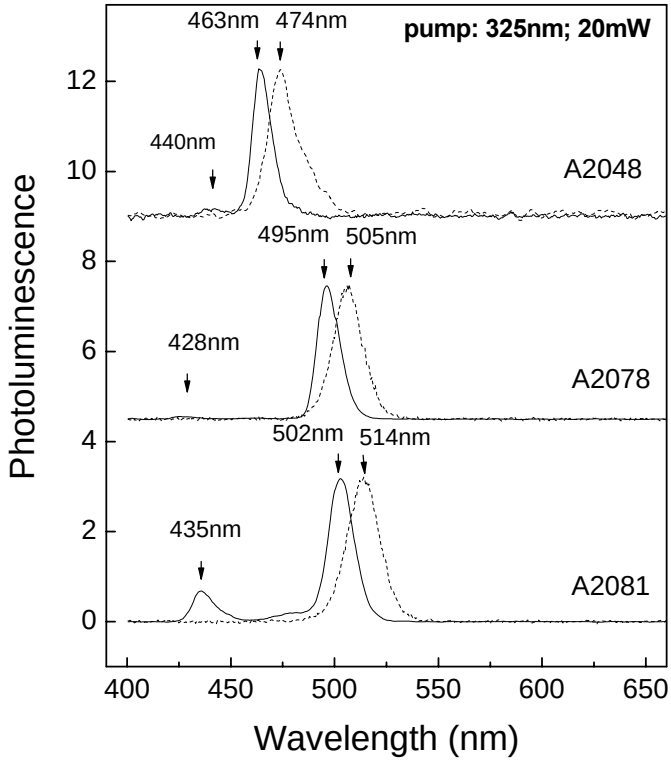

Figure 5.2. Photoluminescence spectra at 77K and at RT for the three MQD samples: A2078, A2081 and A2048.

PL spectra at 300 K and 77 K have been measured on all QD samples, as shown in Fig. 5.2. For PL measurements a He-Cd laser was used with an excitation intensity of 20 mW. The peaks corresponding to interband transitions in the QDs and the bulk $Zn_xCd_yMg_{1-x-y}Se$ barriers are observed. Sample A2048 at 77 K shows a strong luminescence peak at 463 nm corresponding to the QDs interband transitions and a weak peak at 440 nm from the $Zn_xCd_yMg_{1-x-y}Se$ barrier. At 300K the QD peak shifts to 474 nm and the barrier peak disappears. We attribute this PL peak to the first six QDs (t_D = 1.6 sec, equivalent to 1.2 ML of nominal thickness). No other peaks

could be seen from the other QDs, the two QD layers with t_D = 18 sec (3.6 ML) and the one with t_D = 36 sec (7.2 ML), in this sample. As we described previously, the fact that no emission from the deeper QDs is observed is probably due to the larger number of blue QD layers (six layers with t_D = 6 sec), with respect to the other two types of QDs layers, as well as to the large $Zn_xCd_yMg_{1-x-y}Se$ spacer thickness.

Samples A2078 and A2081 show strong emission at 505 nm and 514 nm, respectively, at 300 K. The difference between the PL peak positions of these two green samples could be due to the slight shift in the barrier composition (more magnesium in the barrier of sample A2078). The QDs emission of these samples is slightly blue-shifted to 495 nm and 502 nm, respectively, for PL collected at 77 K. Sample A2081 shows a substantially stronger barrier emission than Sample A2078. This can be explained when we consider the very different total thickness of the QD active region (spacers and QDs) for the two samples, 10 x 5.2 nm = 52 nm for A2081 and 10 x 32 nm = 320 nm for A2078. Thus, electrons photo-excited into the $Zn_xCd_yMg_{1-x-y}Se$ material surrounding the QDs (~ 700 nm) spend more time in the active region for the A2078 sample than for the A2081 sample because the active region in A2078 is much thicker than in A2081. As a result, a larger percentage of the photo-excited electrons recombine in the bulk $Zn_xCd_yMg_{1-x-y}Se$ for sample A2081 than for sample A2078. The fact that the 300K PL for all the samples does not exhibit features corresponding to $Zn_xCd_yMg_{1-x-y}Se$ bulk emission while the 77K PL for the same samples exhibit $Zn_xCd_yMg_{1-x-y}Se$ bulk emission indicates that the carriers photo-excited into the $Zn_xCd_yMg_{1-x-y}Se$ are captured into the QDs faster at higher temperature. This is expected because the electron kinetic energy is higher at 300 K

than at 77 K. The peaks in the PL at 300 K in all samples are Stokes-shifted about 25 meV towards lower energy with respect to the corresponding absorption peak. These Stokes shifts are consistent with other studies on QDs [139].

Time-resolved PL measurements were performed at 300 K for all three samples. The electrons and holes photo-excited (400 nm, 100 fs pulse) into the $Zn_xCd_yMg_{1-x-y}Se$ relax into the QDs sub-bands, recombine and emit photons. Fig. 5.3 shows the PL intensity as function of time for all the samples. The rise-time gives information about capture of electrons and holes into the QDs, whereas the decay time reflects the electron-hole recombination inside the QDs. All three samples exhibit a fast and a slow PL decay component.

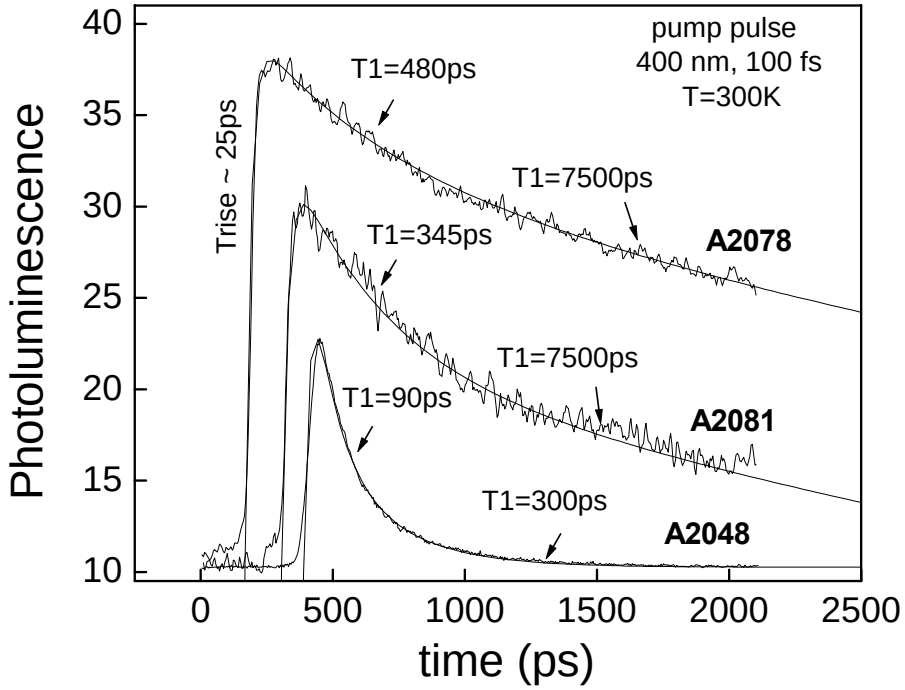

Figure 5.3. Time-resolved photoluminescence spectra at 300K and fit lines for samples A2078, A2081, and A2048.

The time-resolved traces in Fig. 5.3 are fit to a sum of two exponential decays and one exponential rise. Table 5.1 summarizes the decay times, the rise time and the corresponding monitored PL peaks for each sample. The existence of multiple exponential decays is consistent with observing multiple independent but energetically overlapping decays. Similar bi-exponential decays in the PL experiments of CdSe QDs have been observed [10-13]. The bi-exponential decays can be explained either by the existence of two independent recombination channels inside the same QDs [10-13] or, in the case of SAQDs grown by MBE, by the co-existence of two types of QDs, of slightly different shapes, in the same sample.[14] Further investigation is necessary to understand the mechanism of bi-exponential decay.

Sample	Fast decay time (ps)	Slow decay time (ps)	Rise time (ps)	PL at 300K (nm)	QD layers interspacing (nm)
A2048	90	310	~ 30	474	130
A2078	480	7500	~ 22	505	32.5
A2081	345	7500	~ 25	514	5.2

Table 5.1. PL decay times, rise times, and monitored PL peak for all samples.

All the samples studied exhibit strong PL even at RT, which indicates that they have good structural quality. The fact that both recombination processes in sample A2048 are substantially faster (90 ps, 310 ps) than the ones for samples A2078 and A2081 (400 ps, 7.5 ns) suggests that the recombination processes are

inherently faster in smaller QDs (the QDs emitting in blue are smaller than the ones emitting in green) because of large influence of the QD surface on the electronic states. It is interesting to compare the PL and the time-resolved PL from these two samples because of the two samples have the same layer composition but different QD layer interspacing (32.5 nm of the sample A2078 versus 5.2 nm of A2081). The slow relaxation process is almost the same for both samples, ~ 7.5 ns, whereas the fast relaxation process is substantially faster for the sample with smaller interspacing between QD layers than that for the sample with larger interspacing between QD layers. This data suggest that the fast relaxation process may be influenced by the perturbation between adjacent QD layers, whereas the slow relaxation process is not influenced by factors outside the QDs.

The next section will show results that describe the influence of adjacent layers of QDs in MQD structures. Systematic studies were carried out to observe the vertical correlation and the coupling of the QDs in MQD structures.

5.3. Vertical Correlation of Stacking QDs

5.3.1. Experimental details

In this work, two sets of structures having thirty MQD layers of CdSe SAQDs were grown with different MgSe content in the $Zn_xCd_yMg_{1-x-y}Se$, the first with 59 % of MgSe (3.065 eV) and the second with 35 % (2.737 eV). The 187 nm-InGaAs buffer and bottom $Zn_xCd_yMg_{1-x-y}Se$ barrier layers were grown following the

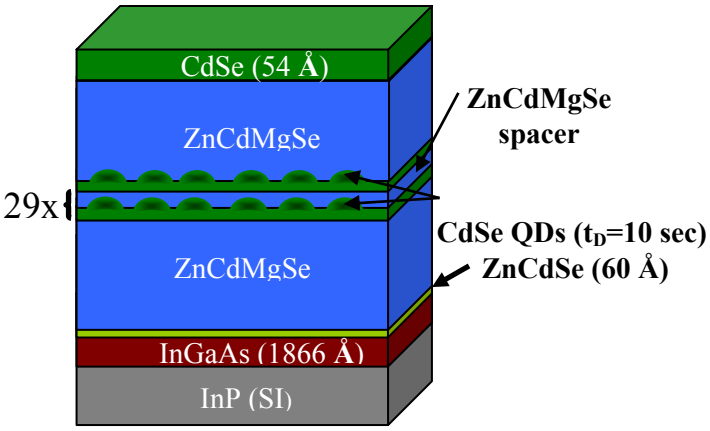

Figure 5.4. Schematic of a thirty-stacked or multi-QD structure for the QD coupling studies.

procedure described in the section 3.3.3.1. Thicknesses of $Zn_xCd_yMg_{1-x-y}Se$ bottom layer were 449 nm for the case of 35 % of Mg and 502 nm for the case 59 %. The CdSe t_D of the QD layers is equal to 10 sec, which correspond to a nominal thickness of 2 ML. The CdSe t_D is kept the same in all the thirty layers of the same structure and inside the different sets of samples. Structures for PL studies were capped with 37 nm-$Zn_{0.32}Cd_{0.33}Mg_{0.35}Se$ for the first set of samples and 42 nm-$Zn_{0.18}Cd_{0.23}Mg_{0.59}Se$ for the second set of samples. Finally, a 54 Å-thick CdSe layer grown to protect Mg from oxidation and to avoid the complication of the interpretation of the CER spectrum introduced when the cap is a ZnCdSe layer (described in section 3.4). Structures without the last top barrier (thirty layer) and the cap were also grown to observe the surface topography of the MQDs.

5.3.2. Results and discussion

5.3.2.1. Growth of Reference Superlattices: Thickness and Composition of MQDs

Two reference superlattice structures were grown with $Zn_xCd_yMg_{1-x-y}Se$ barriers with the same composition and thicknesses than the two different barriers used in the two sets of MQD structures. These two superlattices were formed by 30 periods of layers consisting of 3Å-ZnSe QWs separated by $Zn_xCd_yMg_{1-x-y}Se$ barriers, whose composition and bandgap is the same as the one of the $Zn_xCd_yMg_{1-x-y}Se$ barrier in the MQD structure that requires being calibrated (i.e, $Zn_{0.32}Cd_{0.33}Mg_{0.35}Se$ and $Zn_{0.18}Cd_{0.23}Mg_{0.59}Se$). The growth time of the $Zn_xCd_yMg_{1-x-y}Se$ barriers were estimated from two thick reference layers to obtain approximately a thickness of about 150 Å for the $Zn_xCd_yMg_{1-x-y}Se$ barriers while a ZnSe bulk layer was used for the assessment of the thickness of the ZnSe QW (3 Å). The thick layer thicknesses were previously determined, roughly, using the method of the radial sectioning instrument, described in the section 2.2.2.1.

The single and the double X-ray diffraction data of the superlattices showed a sequence of equally spaced satellites peaks, each one corresponding to a period of the superlattice. The Fig 5.5 illustrates the (400) DCXRD spectra for a superlattice with a barrier layer of bandgap equal to 3.065 eV (59 % of MgSe content). The $Zn_xCd_yMg_{1-x-y}Se$ barrier layer in the superlattice has the same composition than in the corresponding set of the MQD samples of bandgap of 3.065 eV. In the Fig. 5.5, the

assignments of the peaks are represented with the Θ value (arcseconds) for each peak in parenthesis. The FWHM for the $Zn_xCd_yMg_{1-x-y}Se$ and the InGaAs buffer were determined by using a Gaussian line fitting. The FWHM for the $Zn_xCd_yMg_{1-x-y}Se$ was 47 arcsec and the FWHM for the InGaAs buffer layer was 106 arcsec, indicating the good crystal quality for both layers. Both layers, InGaAs and the $Zn_xCd_yMg_{1-x-y}Se$ have a little mismatch to the InP but as observed from the values of the FWHM, it does not affect the quality of the epilayer, which is due to that these layers are still under the critical thickness to initiate the relaxation (fully strained or pseudomorphic layers).

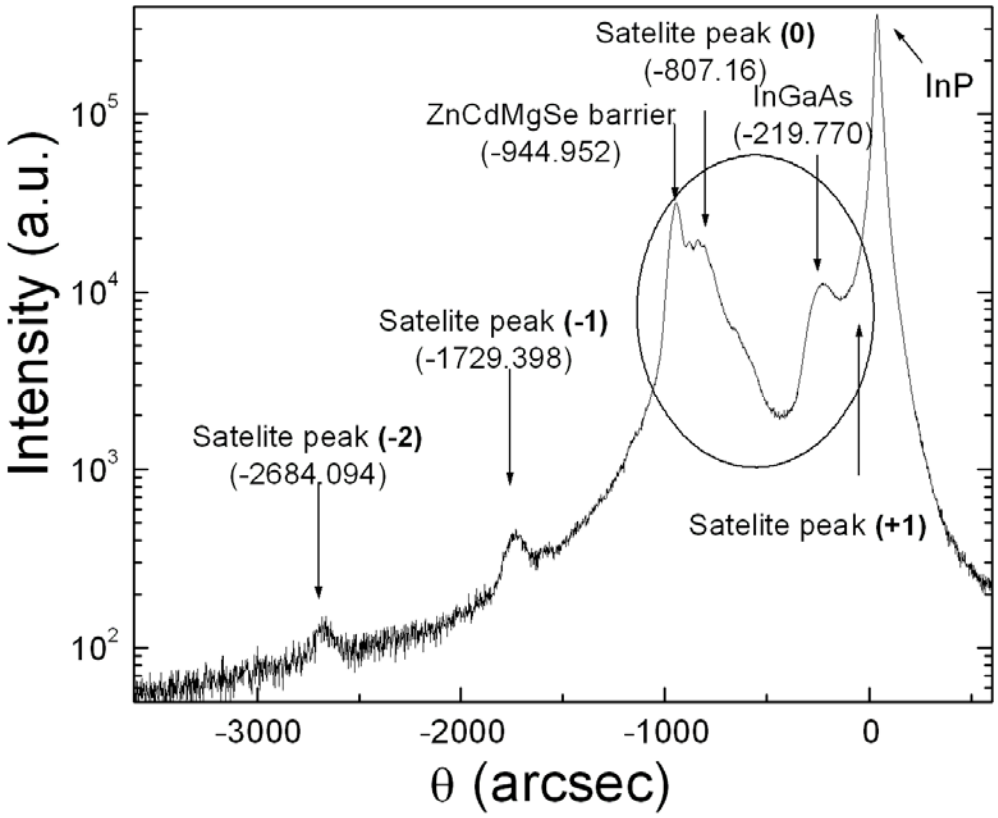

Figure 5.5. (400) DCXRD spectrum of a ZnSe/$Zn_xCd_yMg_{1-x-y}Se$ superlattice with a bandgap energy of 3.065 eV.

Measuring the difference between two vicinal periods and applying Bragg's law (section 2.2.2.3), the exact period of the superlattice was determined and from this, the growth rate for each specific composition of $Zn_xCd_yMg_{1-x-y}Se$ was calculated. The period for the superlattice represented in the Fig. 5.5 was 195.516 Å, so subtracting the ZnSe thickness, the thickness of the $Zn_xCd_yMg_{1-x-y}Se$ spacer was 192.516 Å. Therefore, considering that the $Zn_xCd_yMg_{1-x-y}Se$ spacer was grown during 69 sec, the growth rate of the $Zn_xCd_yMg_{1-x-y}Se$ was 2.790 Å/sec. For the other superlattice with 35 % of magnesium, the calculations are analogous. The superlattice period was 197.145 Å. The thickness of the $Zn_xCd_yMg_{1-x-y}Se$ spacer grown during 79 sec was 194.145 Å and so, the calculated growth rate was estimated as 2.496 Å/sec.

Simulation results were used to understand where the satellites peaks are expected and to verify the results. Simulation results agreed with the estimation of the period thickness. The Fig. 5.6 shows good agreement between the simulation results and the experimental data for the superlattice with 59% of Mg. The dashed line represents the simulation data while the solid line represents the experimental (400) DCXRD data for the sample (same experimental data was represented in Fig. 5.5).

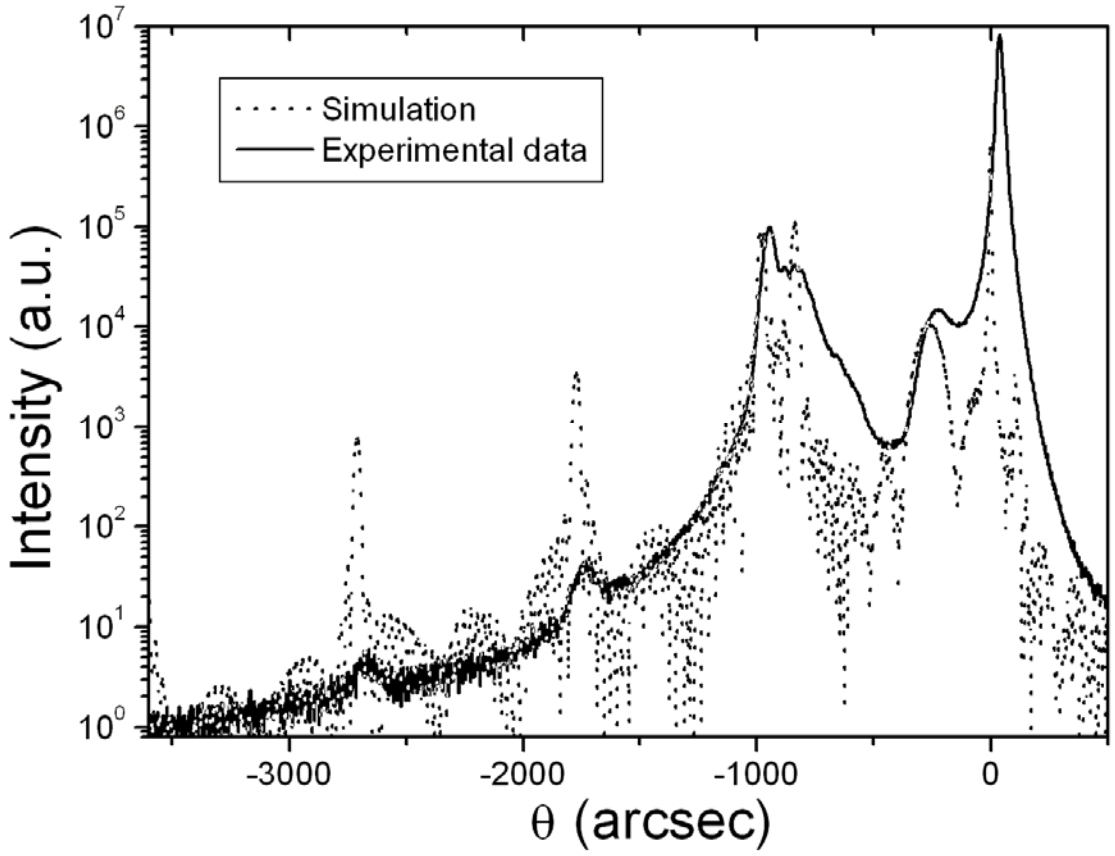

Figure 5.6. Simulation results for the (400) DCXRD spectrum of a ZnSe/$Zn_xCd_yMg_{1-x-y}Se$ superlattice with a bandgap energy of 3.065 eV and 59% MgSe content.

In addition, InGaAs buffer layer was also calibrated using the sequence of the fringes that appeared in the circular region of the Fig 5.5. The Fig 5.7 is a more detailed (400) DCXRD that was taken to observe more clearly the fringes originating from this layer.

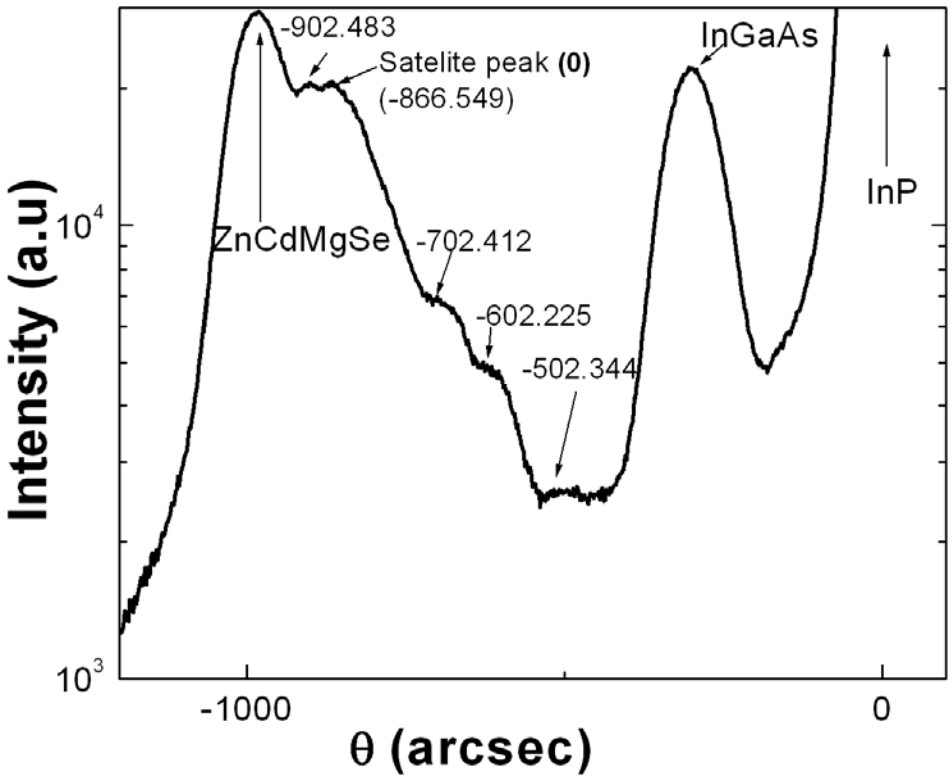

Figure 5.7. (400) DCXRD spectrum from a detail of the fringes derived from the InGaAs buffer layer. The circle in the Fig. 5.5 indicates the portion of the spectrum that has been taken in more detail.

A thickness of 187 nm was obtained (applying 2.40) for an InGaAs buffer layer that was estimated initially to be 150 nm thick using the radial sectioning instrument method (described in section 2.2.2.1). As inferred from the data, the determination of the thickness using the radial sectioning instrument is a rough approximation that must not be utilized if accurate measurements of the thickness are required.

It has been demonstrated that nearly lattice matched ZnCdMgSe layers of about 1 μm can be grown pseudomorphically to InP[39]. Therefore, it is expected that ZnCdMgSe barrier of the superlattices are pseodomorphic or partial-relaxed epilayers. To calculate the composition of the barrier layer, the system of equation

2.33 and 2.21 must be applied. However, the equation 2.21 relates the composition to the free standing lattice constant, which can only be obtained by the (400) reflection when the layer is fully relaxed (the parallel and perpendicular lattice-mismatch will be the same and equal to the real lattice-mismatch between the epilayer and the substrate). For the case of a partially relaxed layer or pseudomorphic layer, (400) reflection cannot be utilized since the lattice mismatch will be different in the plane and in the perpendicular direction. Consequently, other reflections as [511]a and [511]b, should be used to calculate the parallel and perpendicular lattice constant and then, the free standing lattice constant of the epilayer that should be inputted in the equation 2.21 to calculate the composition.

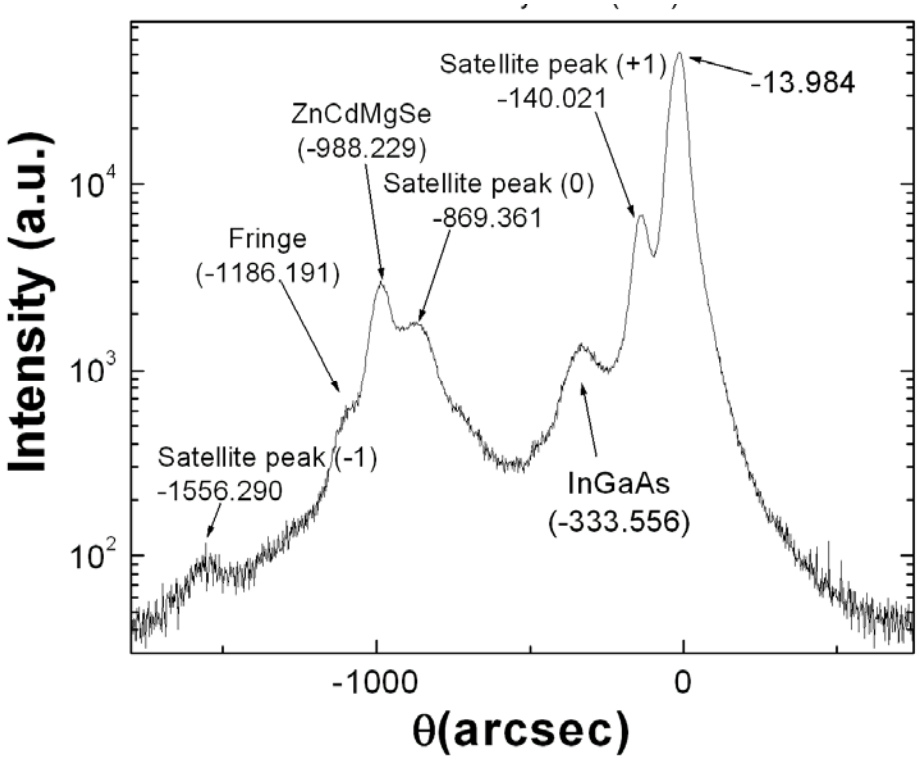

Figure 5.8. (511)a DCXRD spectrum of the ZnSe/ZnCdMgSe superlattice with a bandgap of 3.065 eV.

The Figures 5.8 and 5.9 show, respectively, the [511]a and [511]b of the same superlattice with a bandgap of 3.065 eV (59 % of MgSe). The perpendicular and parallel lattice mismatches was determined by the equations 2.35 and 2.36 and the correspondent values were 100 x $[\Delta a/a_s]_{\perp}$ =0.7566 % and 100 x $[\Delta a/a_s]_0$ =-0.0068 % (almost fully pseudormorphic). The perpendicular and parallel lattice constants were obtained applying the equations 2.37 and 2.38 and their correspondent values were 5.9131 Å and 5.8683 Å. The free standing lattice constant, $a_{f=}$5.8933 Å, was finally obtained by 2.39. Therefore, the system of equations 2.33 and 2.21 were solved and composition of the layer was achieved: $Zn_{0.18}Cd_{0.23}Mg_{0.59}Se$. For the other superlattice with bandgap equal to 2.737 eV, the same calculations were performed achieving a composition of $Zn_{0.32}Cd_{0.33}Mg_{0.35}Se$.

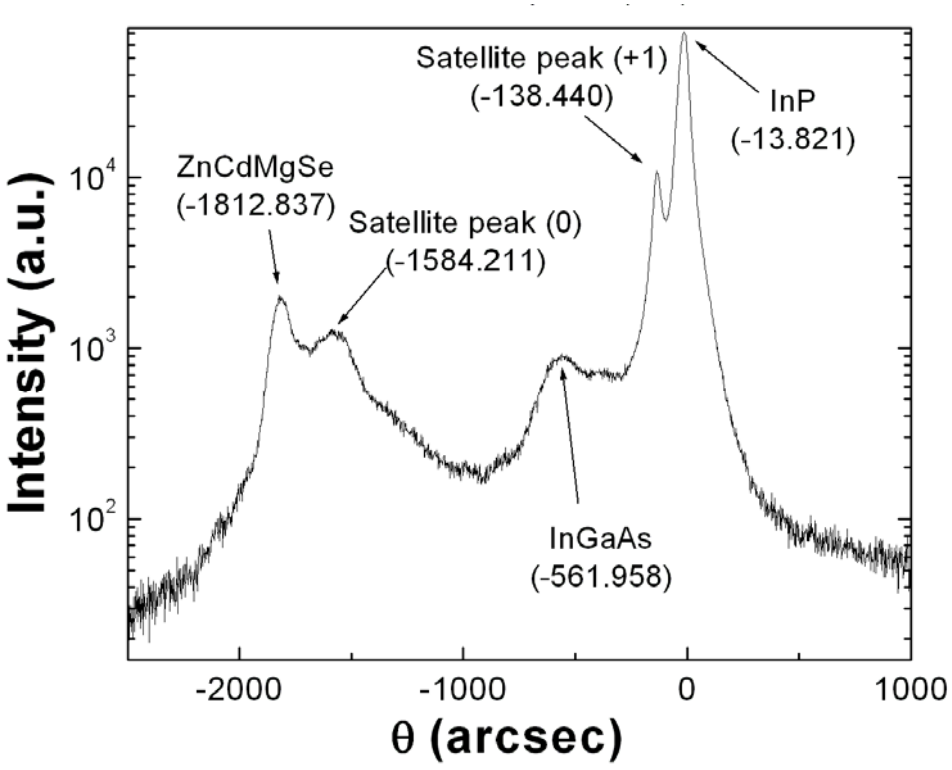

Figure 5.9. (511)]b DCXRD spectrum of the ZnSe/$Zn_xCd_yMg_{1-x-y}Se$ superlattice with a bandgap of 3.065 eV.

5.3.2.2. Engineering the exciton wave function: coupling of QDs

To study the coupling effect in CdSe MQDs grown on $Zn_xCd_yMg_{1-x-y}Se$ barriers, two sets of samples were grown: in the first set, samples contain a $Zn_xCd_yMg_{1-x-y}Se$ barrier with 59 % of MgSe, corresponding to a quaternary band gap energy of 3.065 eV, while, in the second set, the percentage was 35 % with a band gap of 2.737 eV.

The Fig. 5.10, *part a*, illustrates the normalized 77 K PL spectra of five samples belonging to the first set of samples with a MgSe content of 59% and $Zn_xCd_yMg_{1-x-y}Se$ spacer growth times (t_{SL}) equal to 5, 6, 7, 8, 9 sec, which corresponds, respectively, to spacer layer thicknesses (μ_{SL}) of 14.0, 16.7, 19.5, 22.3, 25.1 Å. In the Fig.5.10, *part b*, the normalized PL spectra at 77 K for the second set of samples with MgSe content of 35% are represented. The samples t_{SL} are equal to 6, 8, 10, 12 sec, corresponding, respectively, to 15.0, 20.0, 25.0, 30.0 Å. Each t_{SL} is indicated besides the PL spectrum of the corresponding sample. The PL spectra of two SQDs samples grown under the same conditions as the MQDs structures are represented as references, in black dashed-lines, for both cases.

As shown in figures, by appropriate choice of the $Zn_xCd_yMg_{1-x-y}Se$ t_{SL}, a strong QD coupling situation can be obtained at 6 sec, for the samples with a 59% of Mg (*part a*) and at 8 sec, for the samples with 35% of MgSe content (*part b*). It should also be noticed than in the *part a*, a weak coupling effect is observed for the

case of 7 sec. In this case, some QDs are also uncoupled, which is demonstrated by PL power dependence studies that will be shown afterward.

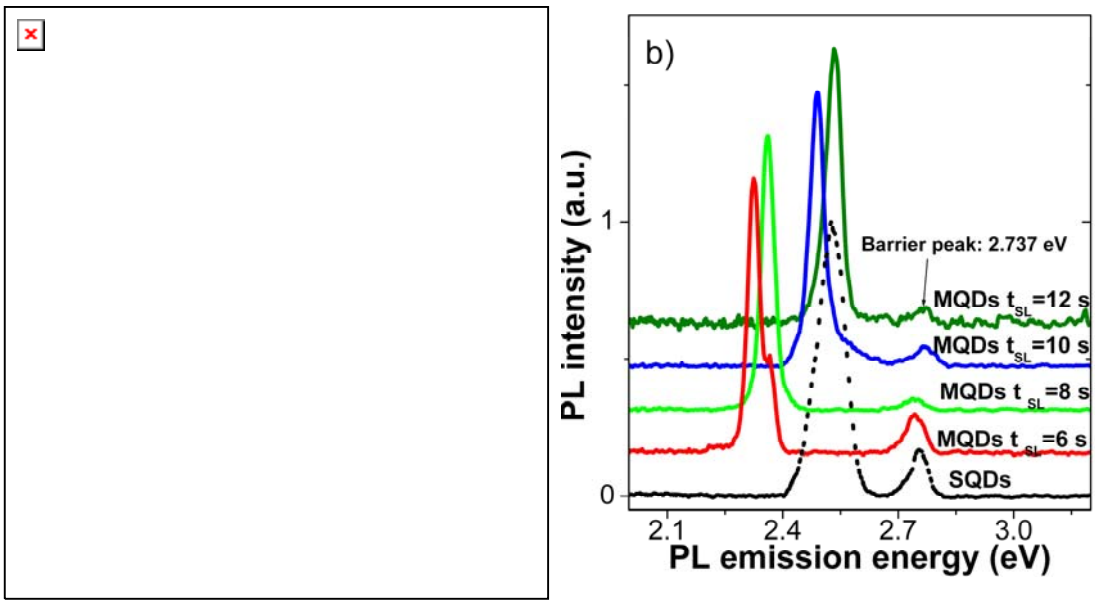

Figure 5.10. Photoluminescence spectra of the two sets of 30-MQDs samples grown with the same CdSe nominal thickness of 2MLs and different t_{SL}.
a. Five samples grown with a Mg content of 59% in the $Zn_xCd_yMg_{1-x-y}Se$ barrier.
b. Four samples grown with a Mg content of 35% in the $Zn_xCd_yMg_{1-x-y}Se$ barrier.
The t_{SL} is indicated besides the PL spectrum of the corresponding sample. PL spectra of SQDs samples grown under the same conditions as the MQDs structures are represented in dashed-line for both cases.

It can be inferred from the figures that the QD coupling effect depends on the MgSe content of the $Zn_xCd_yMg_{1-x-y}Se$ spacer. For higher content of MgSe, QD coupling happened with thinner spacers (16.7 Å) while for smaller content of MgSe, the effect appeared with thicker spacers (20.0 Å). Therefore, a reduction up to the 17 % in the thickness of the spacer is necessary to have a strong coupling effect for 59% MgSe

content. This result can be explained taking into account the influence of MgSe content in the size of the QDs. With smaller MgSe content on the $Zn_xCd_yMg_{1-x-y}Se$ barrier, the QDs will be larger and therefore the QD coupling will happen at bigger spacers. By the contrast, for smaller QDs, the electron/hole wavefunctions will be confined in small space so the influence (or perturbation) of the vicinal QD wavefunctions (on the top and the bottom layer) will occur at smaller spacers.

In addition to this result, an equivalent Mg effect as in the SQDs layers can be observed comparing both sets of samples. For higher concentration of MgSe, the QD peak position of both SQD reference and MQD layers is blue-shifted because of the influence of the Mg on the QD size.

Thus, as summary of this section, the magnesium provides ways to affect the electronic properties of the QDs, through the direct influence in the PL peak position of QDs and/or by means of the control of the coupling effect.

5.3.2.3. Linearly polarized PL experiments

To analyze the nature of the light emitted or absorbed by the QDs, polarized linearly PL experiments on edge and on surface configurations were performed. The Fig. 5.10 represents the linearly polarized PL spectra of the three samples: strong coupling, weak coupling (still presence of some uncoupled QDs) and uncoupled cases. Spectra with transversal electric (TE) polarized light are always represented by solid lines, while spectra with transversal magnetic (TM) polarization are shown by dashed lines. For the edge configuration, the difference between the Fig. 5.11, *part a* (strongly coupled QDs) and the Fig. 5.11, *part b* (uncoupled QDs) can be explained

as the following. In the case of a thick $Zn_xCd_yMg_{1-x-y}Se$ spacer (*part b*), CdSe QDs from adjacent layers are electronically uncoupled and the wave functions are localized in separated QDs. In this case, QDs behave as independently 0-dimensional potential wells in which the respective wave functions do not interact (no perturbation between wave functions of different wells). Due to the high base/ height ratio of the CdSe QDs (lens shape), it is expected that the hole wave function will be very much confined in the base (strongly flattened) and almost or not confined in the vertical direction, such as the case of lens shape InAs QDs wave functions. Therefore, both absorption and emission of light will be polarized in the (001) plane, transversal electrical (TE) polarized mode.

In contrast, in the case of a thin $Zn_xCd_yMg_{1-x-y}Se$ spacer (*part a*), a CdSe QD layer feels the influence of the closest vicinal layers (the wave functions of a QD in a given layer interact with the wave functions of the QDs in the top and bottom layers). Electron and hole wave functions of a QD are coupled vertically (growth direction) between neighboring layers and furthermore, this electronic coupling (delocalization) can be extended over the entire QD structure, forming columns of coupled QDs (wire-like structure rather that dot-like structure in the vertical direction). PL emission of this type of structure will be fundamentally polarized in transversal magnetic (TM) mode since the probability of recombination of the excitons will be higher in this direction due to the one dimensional delocalization. The Fig. 5.12 gives a visual schematic of the coupled and uncoupled MQD layer structures.

For the surface configuration, the emitted PL light is expected to be predominantly TE polarized for both cases (as expected due to the QDs shape

anisotropy). However, PL emission was slightly TE polarized for the coupled QDs while it is slightly TM polarized for the uncoupled case, suggesting a kind of surface organization. To study this effect, AFM images of MQDs structures without the top cap layer were performed.

The Fig. 5.13 shows an AFM image of an uncapped MQD structure grown in the same conditions as the uncoupled case described previously. It can be inferred from the image than the QDs formed connected structures, probably due to a change in the strain energy caused by the bottom QD layers. This result is consistent with the polarization of the light emitted by uncoupled QDs in surface configuration. No surface organization was found for an uncapped sample grown under the same conditions than the coupled case.

The *part c* in Figure 5.13, represents an intermediate situation (weakly coupled QDs) between a strongly coupled QDs and the uncoupled ones. The presence of coupled and uncoupled QDs in the same sample is verified by the power dependence studies (see next section). In the edge configuration, light is fundamentally TM polarized due to some coupling of the bigger QDs, while in the surface configuration, the emitted light is almost symmetrically polarized (50/50), indicating a situation intermediate between *part a* and *part b* (possibly an initial stage in the formation of a surface organization).

In summary, the transition from TE polarized to TM polarized PL can be driven by varying the spacer thickness. Linearly polarized PL in edge and surface configurations can provide a useful way to identify if a kind of organization (vertical or lateral) is taking place.

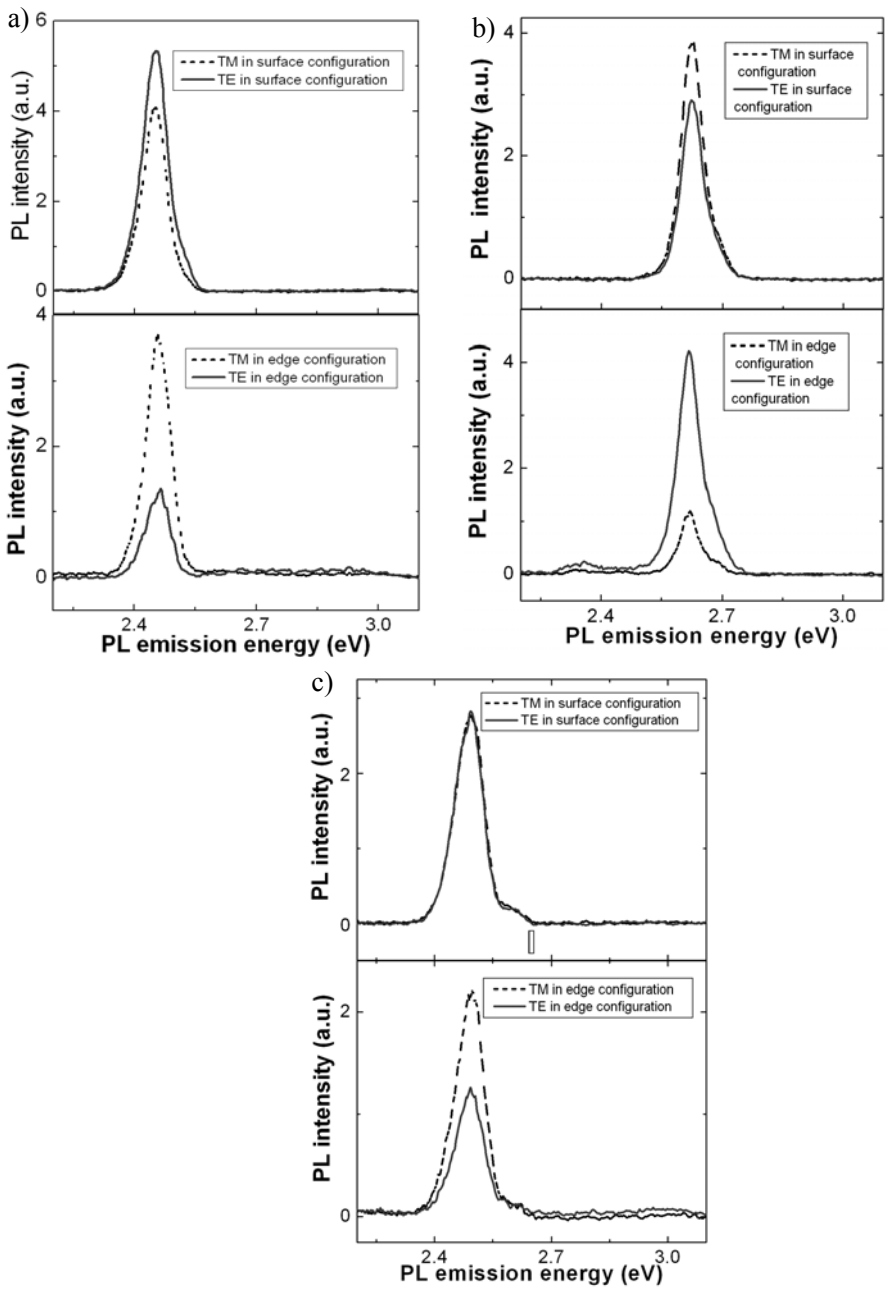

Figure 5.11. Linearly polarized spectra for three representative samples in the two configurations: edge and surface. MQDs samples have a spacer deposition time of a) 5 sec (coupled), part b) 8 sec (uncoupled) and part c) t_{SL} =7 sec (weak coupled). TE polarized light is always represented by dashed lines while TM is represented by solid lines.

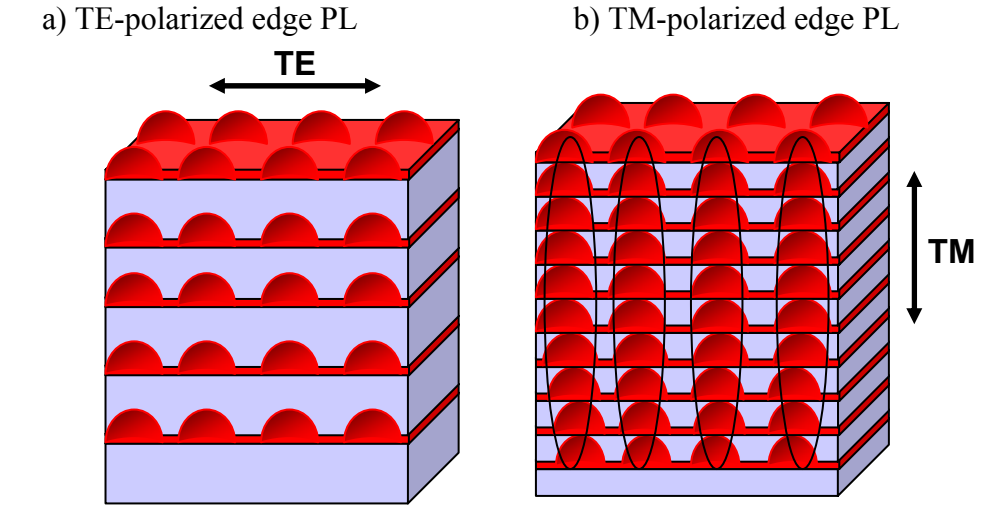

Figure 5.12. Schematic of structures to engineer the PL polarization in stacking layers of CdSe QDs separated by $Zn_xCd_yMg_{1-x-y}Se$ barriers.

a) QDs structure where CdSe QDs are separated by thick $Zn_xCd_yMg_{1-x-y}Se$ spacers, no coupling between QDs wave functions is observed. PL emission is fundamentally TE polarized.

b) QDs structure where CdSe QDs are separated by thin spacers, electronic coupling of wave functions in the vertical direction (growth direction) is observed. PL emission is meanly TM polarized.

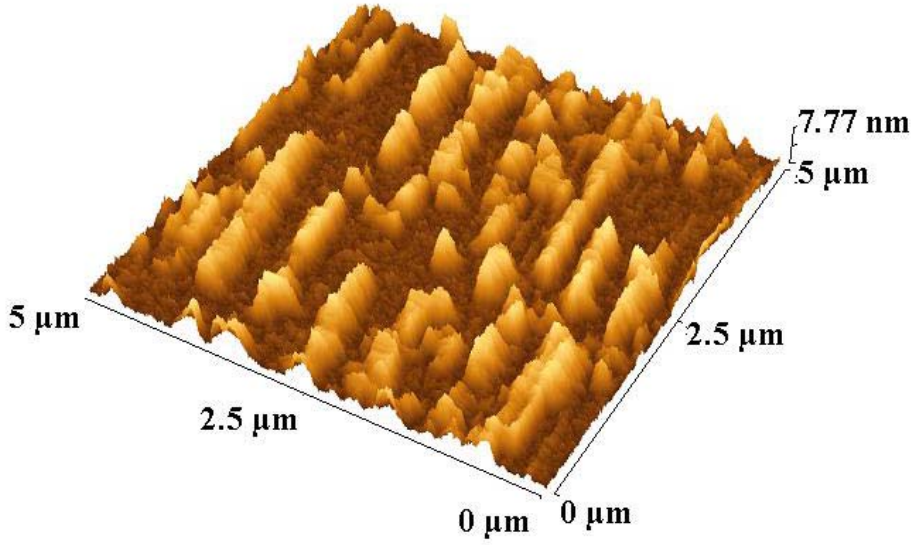

Figure 5.13. Three dimensional AFM image of uncapped MQD structure. The sample was grown with the same spacer thickness as an uncoupled case.

5.3.2.4. Power dependence PL measurements

To further investigate the formation of the coupled QD structure in the vertical direction (i.e. growth direction), power dependence studies were performed on these three samples (Fig. 5.14). *Part a* and *part b* of Figure 5.14 represent the spectra of the strong coupled sample (t_{SL}=5 sec) and the case of an uncoupled sample (t_{SL}=8 sec). It can be noted a shift of the PL peak position to blue with an increase of the laser excitation density for the strong coupled case while the PL peak of the uncoupled ones remains invariable. In the case of a weakly coupled, sample of t_{SL}=7 sec in the Fig. 5.14 (*part c*) and (d), both effects are observed. As the figures of *part c* and *part d* show, the peak corresponding to the wavelength of the coupled QDs is shifted to the blue with the increase of the excitation power while the small high energy shoulder assigned to the uncoupled QDs stays in the same place. The same spectrum than *part c* is represented in *part d* but without "y axis" offset to show more clear the effect of the excitation density in the coupled QD peak.

The blue shift of the coupled QD peak with the increase of the excitation density demonstrates the formation of a coupled QD superlattice (SL) in the growth direction. As the barrier width decreases the neighboring quantum dots interact with each other and the MQD structure becomes a SL and its discrete energy levels broaden into bands known as minibands.[140] Increasing the excitation density, higher energy levels of the miniband formed by the coupled QDs will be populated so the emission energy resultant of the recombination of the electrons and holes will also appear to higher energies.

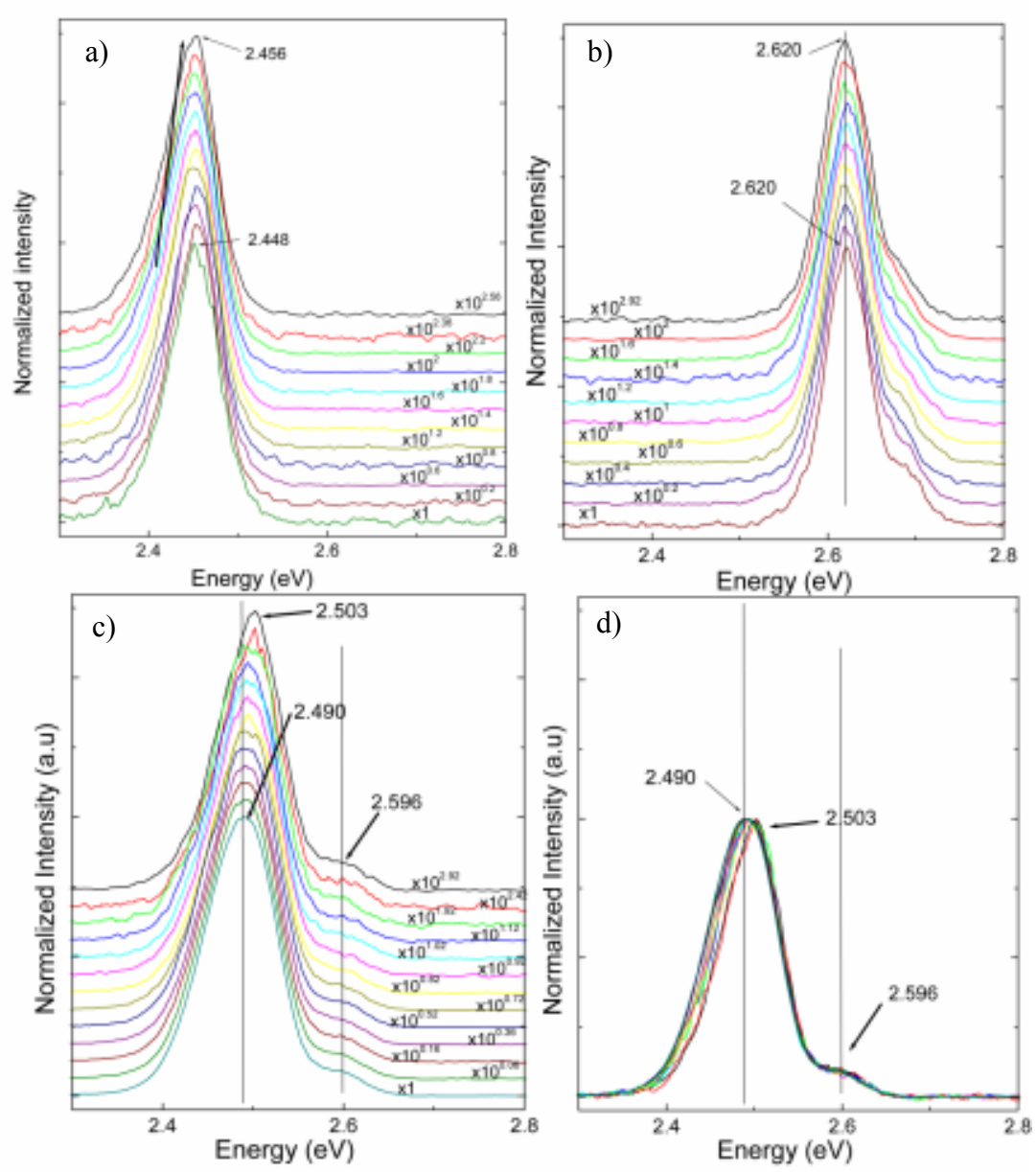

Figure 5.14. Power dependence studies of three MQDs samples. The Figures represent: a) strong coupling of QDs layers, b) uncoupled MQD structure; and c) and d) weak coupling between QDs layers. The same spectrum than *part c* is represented in *part d* but without "y axis" offset to show more clear the effect of the excitation density.

5.3.2.5. Contactless Electroreflectance of MQDs

The CER measurements were performed in some MQDs to study the effect that created by the coupling in the QDs transitions. To avoid the difficult interpretation of the spectrum derived from the signal originating from the ZnCdSe layers, a thick cap of CdSe was grown instead of the ZnCdSe cap. Even though the effect of this layer was reduced in the spectrum, there is still the presence of ZnCdSe-LT layer that must be kept for the growth of high-quality $Zn_xCd_yMg_{1-x-y}Se$ layers. In this section, the CER spectrum of a coupled MQD structure with thirty QD layers is presented. The t_{SL} was equal to 14.0 Å and the Mg content in the $Zn_xCd_yMg_{1-x-y}Se$ barrier layer was 59%.

The Fig. 5.15 shows the RT-CER spectrum and the experimental fitting of this coupled MQD sample. Solid line represents the RT-CER spectrum while the dashed line represents the Gaussian fitting. The assignment of the bandgap of the quaternary layer, E_0 ($Zn_xCd_yMg_{1-x-y}Se$), and the lowest energy level of the MQDs (coupled QDs) were straightforward when compared with the PL data. A higher energy level is assigned to the coupled QD layers at 2.559 eV. The LT-ZnCdSe-related peaks appeared at 2.231 eV and at 2.328 eV, which were assigned to transitions from light hole and heavy hole, respectively. These assignments were corroborated by the envelope calculations represented in Fig. 3.25. Based on these calculations and considering that the percentage of Zn content in the ZnCdSe layers for the $Zn_xCd_yMg_{1-x-y}Se$ reference layer represented in the Fig. 5.15 was about 76%, we can estimate the transitions for the low temperature layer of the MQD structure as 2.236 and 2.325 eV for the heavy and the light hole. Therefore, there is a good agreement

between experimental and theoretical data. The signal at about 1.69 eV corresponds to the CdSe cap layer. This layer also exhibits a region with higher energy transitions, which is indicated in the figure by a dashed line. The last transition at 2.593 eV is assigned to the MQDs layers. We propose this transition may be originating from some QDs that are not coupled, even though this peak does not appear in the PL. This result is supported by a comparison between this experimental fitting value (2.593 eV) with the PL value of other sample (uncoupled) for which the spacer is larger (22.3 Å). We consider that this assignment is plausible since the CER measurement is based on absorption of the light. If there are uncoupled QDs, a stronger signal is expected for this type of QDs in the CER spectrum than the signal of PL spectrum.

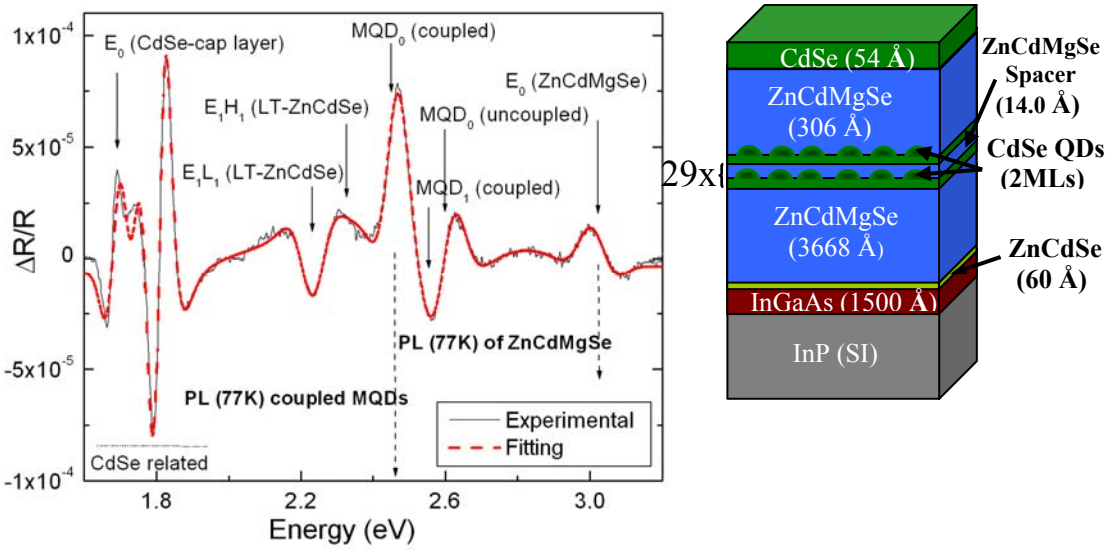

Figure 5.15. The RT-CER spectrum of a structure with thirty MQD layers of CdSe separated by 14.0 Å-$Zn_xCd_yMg_{1-x-y}Se$ spacers. A schematic of sample layer structure is represented on the right side of the CER spectrum.

The reason is that the carriers in the coupled QDs are more delocalized and their lifetime is expected to be larger than the uncoupled ones so the PL intensity of the coupled QDs peak should be also considerably enhanced in comparison with the PL intensity of the uncoupled QDs peak.

Transition	**Experiment (eV) (± 0.005)**	**Theory (eV)**	**PL (eV) (±0.002)**
MQD_0 (coupled)	2.457		2.458 (at 77K)
MQD_1 (coupled)	2.559		
MQD_0 (uncoupled)	2.593		Footnote[4]
E_1L_1 (ZnCdSe)	2.231	2.236	
E_1H_1 (ZnCdSe)	2.328	2.325	
E_0 ($Zn_xCd_yMg_{1-x-y}Se$)	3.023		3.065 (at 77K)
E_0 (CdSe)	1.688		1.692 (ref [141])

Table 5.2. Experimental and calculated interband transition energies for a structure with thirty-MQD layers of CdSe separated by 14.0 Å- $Zn_xCd_yMg_{1-x-y}Se$ spacers.

As summary, CER measurements permit on one hand, to analyze the coupling of the QDs and on the other hand, to study the higher energy transitions not shown by PL.

[4] The QD PL value for a sample grown under the same conditions but with a thicker spacer (22.3 Å) was 2.604 eV. Several studies demonstrated that the QDs of this reference sample were uncoupled.

Chapter 6. Raman Spectroscopy

6.1 Introduction to Raman phenomenon

Raman scattering is a light scattering effect that was initially discovered by the Sir. C.V Raman, who received the Novel Prize in Physics in 1930 for this discovering. Raman scattering in semiconductor is a process related with the scattering of the light by phonons or plasmons. The theory for Raman scattering in semiconductors is really complex, but from a simple classical point of view could be defined as a non-linear interaction between the radiation and the semiconductor lattice, involving a change in photon frequency of the incident radiation.

The incoming radiation that interacts with electrons, phonons and impurities in the surface of a semiconductor can be considered as a wave whose electric field oscillates at a certain point in the space (Eq. 6.1).

$$E = E_0 \cos \omega t \qquad (6.1)$$

where E_0 is the maximum value of the field, ω is the frequency, and t is the time.

The majority of the light does not change its photon frequency having a first-order elastic interaction (reflectance, transmittance, absorbance and Rayleigh scattering) but there is a small part, called Raman scattering, which shifts its initial values, interacting inelastically with phonon modes (or plasmon modes). The photons

gain (anti-Stokes shifted) or lose energy (Stokes shifted), according to the energy (Eq. 6.2) and momentum conservation rules (Eq. 6.3).

$$\omega_s = \omega_i + \Omega \qquad (6.2)$$

$$q_s = q_i \pm K \qquad (6.3)$$

where ω_i and ω_s are the incoming and scattered photon frequencies respectively, q_i and q_s are the incoming and scattered photons wavevectors respectively, and Ω and **K** are the phonon frequency and wavevector respectively.

The Raman scattering depends on the polarizability (**P**) of the lattice since the interaction with the arriving radiation is caused by the change of the electric susceptibility (χ) of the lattice. In fact, the polarizability (or electric dipole per unit volume) is related to the electric susceptibility by the approximated linear equation:

$$P = \chi \varepsilon_0 E \qquad (6.4)$$

where E is the electric field and ε_0 is the permittivity of free space (8.85×10^{-12} C^2 N^{-1} m^{-2}).

On the other hand, Polarizability can be also associated to the electric field by:

$$P = \varepsilon E \qquad (6.4)$$

where ε is the dielectric function that varies slightly with lattice spacing which can be expanded by a Taylor series:

$$\varepsilon(\omega, u) = \varepsilon(\omega) + \left(\frac{d\varepsilon}{du} \right) u + \frac{1}{2} \left(\frac{d^2\varepsilon}{du^2} \right) u^2 + \ldots . \qquad (6.5)$$

where u represents a coordinate to describe the phonon modes. The phonon coordinate for a mode with a frequency has the form:

$$u = u_0 \cos \Omega t \qquad (6.6)$$

Hence, considering equation 6.4 and 6.5, the dipole moment induced in the lattice by the radiation electric field is:

$$P = \varepsilon(\omega)E + \left(\frac{d\varepsilon}{du} \right) u E + \frac{1}{2} \left(\frac{d^2\varepsilon}{du^2} \right) u^2 E + \ldots . \qquad (6.7)$$

The second, the third and successive terms create the weak Raman side-bands. Considering the values of E and u represented, respectively, by the equations 6.1 and 6.6, the induced dipole moment contains terms $(\cos \Omega t)^n \cos \omega t$, where *n = 1, 2, 3*...

Using trigonometric relationships as:

$$\cos\theta \cos\phi = \tfrac{1}{2}\left[\cos(\theta + \phi) + \cos(\theta - \phi)\right] \qquad (6.8)$$

$(\cos \Omega t)^n \cos \omega t$ can be stated as $\cos(\omega \pm n\Omega)t$ being n=1, 2, 3… so that the outgoing light has the components $\omega \pm n\Omega$. For n=1 (single phonon bands), the strongest and first-order Raman scattering lines are represented, being $\omega + \Omega$ and $\omega - \Omega$ the corresponding frequencies for anti-Stokes and Stokes lines. In these processes, a phonon, with frequency Ω and wavevector *K*, is either being created (Stokes Raman scattering) or annihilated (anti-Stokes Raman scattering). The rest of terms, *n=2, 3, ...* are weaker terms which denote the interaction of the photon with multiple phonons.

The scattering process comes from an interaction of the electric field vector and the polarization vector (equation 6.7), thus the direction of electric field relative to crystal geometry defines the strength of Raman signal. The Raman intensity is:

$$I \alpha \left| e_i \, \mathrm{R} \, e_s \right|^2 \qquad (6.9)$$

where e_i and e_s are unit vectors giving the directions of the incident and scattered electric field respectively, and *R* is the Raman tensor, which carries the geometric information about the crystal. This determines which phonon modes are allowed and forbidden for different orientations[142].

6.2. Raman Spectroscopy in Capped Samples

In this section, we present the preliminary Raman results obtained on capped CdSe SQDs with $Zn_xCd_yMg_{1-x-y}Se$ barriers. The samples described in this section were grown using the same conditions specified in the section 3.3.3.1. A set of four QD samples with nominal thicknesses 0, 1.2, 3.6 and 5.8 MLs of CdSe were studied.

The Raman measurements were performed at ambient temperature using a triple spectrometer. The excitation energy was provided by a 514 nm line of an Ar+ laser. The spectra were not analyzed for polarization.

Figure 6.1 shows Raman spectra from 200 cm^{-1} to 1000 cm^{-1} for the samples with nominal thicknesses of 0ML, 1.2ML and 5.8ML. The sample with 0ML is measured as a reference to compare with the samples with QDs. A similar spectrum is obtained for the three of them, so only the 5.8ML sample was analyzed. Two peaks at 237 cm^{-1} and 272 cm^{-1} were observed and attributed to the InGaAs buffer layer and to the $Zn_xCd_yMg_{1-x-y}Se$ barrier layers. InGaAs layers that show two peaks at 270 cm^{-1}

and 238 cm^{-1}, named, GaAs-like and InAs-like, respectively, have been previously reported[143]. A main contribution from the $Zn_xCd_yMg_{1-x-y}Se$ layers is also expected to appear in this region. Previous works of the pure ternary $Zn_{0.51}Cd_{0.49}Se$ without Mg exhibited a peak at 239.5 cm^{-1}. Therefore, the peak at 238 cm^{-1} can be explained as a combination of two contributions: a main contribution deriving from the $Zn_xCd_yMg_{1-x-y}Se$ as well as a contribution originating from the InAs-like of the InGaAs buffer layer. The second (474 cm^{-1}), third (711 cm^{-1}) and even fourth (948 cm^{-1}) order of the 237 cm^{-1} principal peak have been observed. Since the intensity of the GaAs-like peak at 272 cm^{-1} should have double the intensity of the InAs-like peak at 238 cm^{-1}, it is probable that the signal observed at 273 cm^{-1} arises almost exclusively from the quaternary $Zn_xCd_yMg_{1-x-y}Se$ barriers. Another important point to note is that there does not seem to appear in the Fig. 6.1 any contribution from the CdSe QDs. It should be taken into account that the QDs represent a relatively small volume into the material.

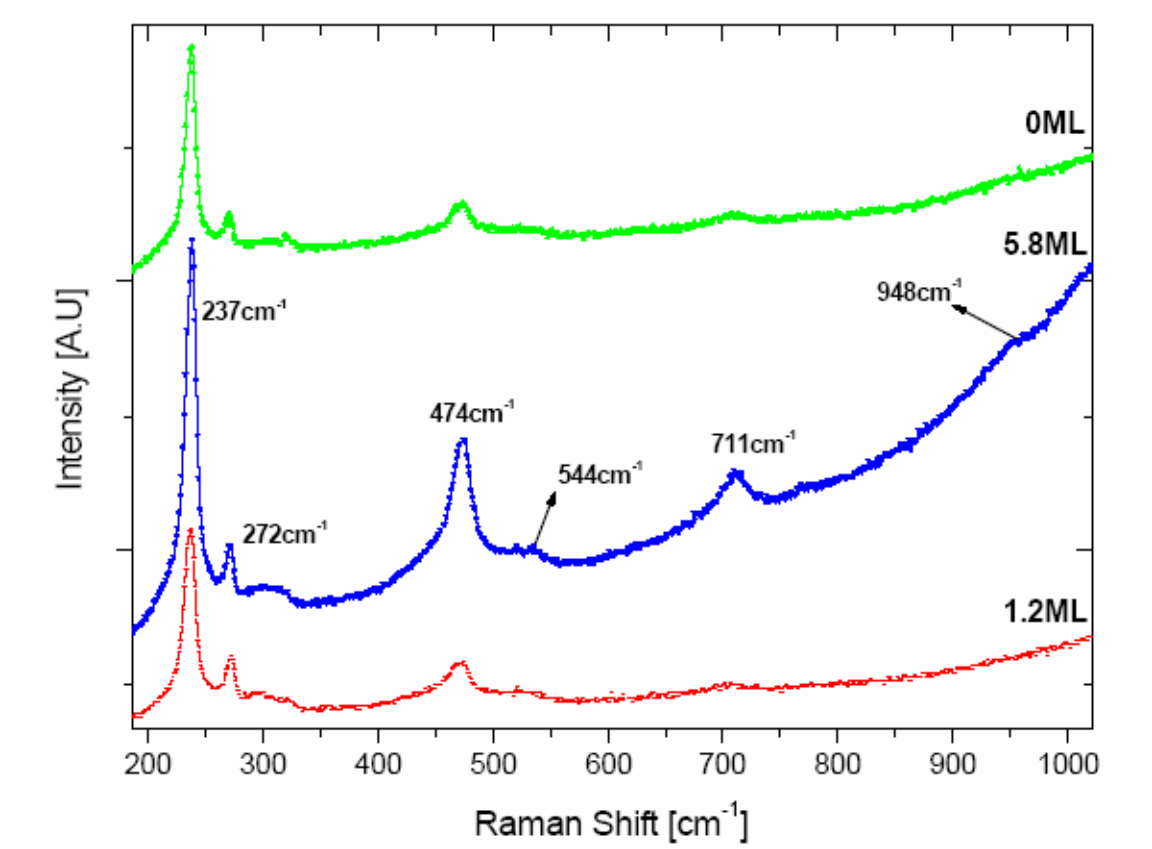

Figure 6.1. Raman spectra of three samples of CdSe SQDs layers on $Zn_xCd_yMg_{1-x-y}Se$ barriers. Nominal thicknesses of CdSe were 0, 1.2 and 5.8 MLs. These measurements were not performed under resonant Raman conditions of the CdSe QDs on $Zn_xCd_yMg_{1-x-y}Se$ barrier.

Therefore, the most favorable condition is to investigate the QDs is to study them in resonant conditions, which mean exciting the sample with a frequency close to real electronic transitions of the QDs, for instance which corresponds to the band gap of the QDs. In this way, the probability of Raman scattering is expected to be enhanced.

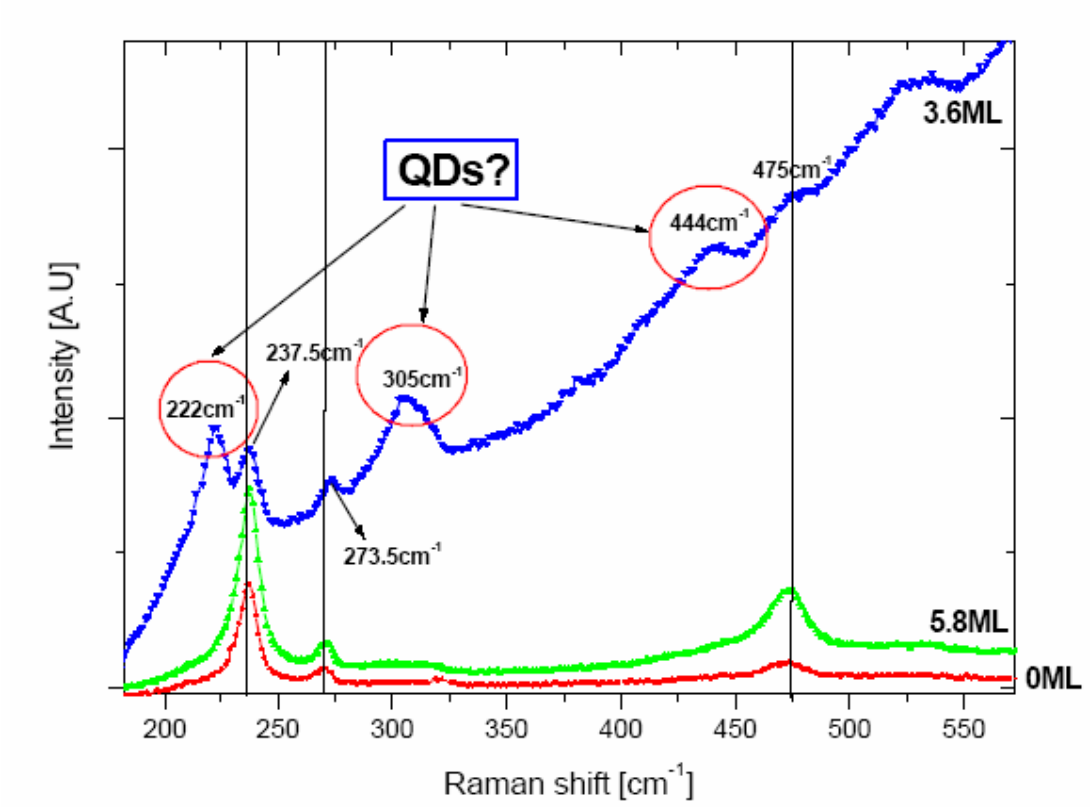

Figure 6.2. Resonant Raman spectra for a CdSe SQD of 3.6ML-nominal thickness grown of $Zn_xCd_yMg_{1-x-y}Se$ barrier. Raman spectra for SQDs layers with 0MLs and 5.8MLs are represented as comparison.

The Fig. 6.2 shows a case close to resonance for the sample with 3.6 ML-CdSe nominal thickness. Samples with 5.8 ML and 0 ML are included for comparison. Different Raman contributions were observed in the 3.6 ML sample with respect to the samples that were studied without the resonance condition. Notice that those features, enhanced in resonance with electronic transitions belonging to the QDs, correspond to excitations, which spatially overlap with them. A first interesting peak appeared at 222 cm^{-1} with its second order peak at 444 cm^{-1}. H. Rho et al.[144] obtained similar results in CdSe QDs with ZnSe cap layer. They attribute this phonon

to an interface phonon (IF) between the QD and the cap layer. They found that this phonon is located at the interface of the QD with the cap layer. A peak at 305 cm^{-1} is observed. This peak is tentatively associated with a local mode of the Mg atoms. Huang et al.[145] found previously a similar frequency for a local mode of Mg in ZnSe. We suggest two possible scenarios: the Mg could be segregated inside the QD and so the local mode is enhanced in resonant conditions, or that the strong interface effects enhance the local mode within the $Zn_xCd_yMg_{1-x-y}Se$ matrix. This result is very interesting when compared with the results coming from the magnesium effect in the formation of the QDs. As described in the section 3.3.5, magnesium atoms (or clusters) enhance the formation of the QDs either by affecting the surface energy of the ZnCdMgSe (altering the wetting layer condition) or by formation of the more atomic steps, which could act as nucleation center sites for the formation of the QDs. Therefore, the QD growth could be favored in areas with more density of magnesium atoms or clusters. We propose that this vicinal interaction between magnesium and the QDs could result in the enhancement of a local mode associated with the magnesium.

In summary, resonance condition is necessary in order to observe the QDs effects. From the results obtained and from the previous literature work, the lines observed in the 3.6 ML sample are assigned to interface phonons. However, more work needs to be done to confirm this hypothesis. For example, polarized measurements in order to study the selection rules are necessary. Resonant Raman spectra should be performed in the other samples in order to determine definitely the assignment of the QD peaks. A possible local mode of magnesium is observed in the

resonant case, which means that this mode is spatially related to the QDs, possibly at the interface or within the QDs. Interface effects are also demonstrated by other studies, which support this assumption.

6.2. Surface Enhanced Raman Spectroscopy of Uncapped QDs Samples

6.2.1. Introduction

Monodisperse nanostructures are of special interest in the field of semiconductors, where nanocrystals often display discrete, atom-like valence (hole) and conduction (electron) levels due to quantum confinement effects[146]. The QD assemblies are regarded as likely building blocks for novel electronic as well as photonic devices. Both a single-electron transistors[147] and LEDs[148] have been constructed from arrays of CdSe QDs. The QDs have also found application in the field of biosensors[149, 150]. In order to assess the characteristics of QD surfaces and their value in the field of sensing, we must develop techniques for observation of the details of the molecule-surface interaction. A high resolution, non-destructive probe is needed. Absorption and emission spectroscopy are of limited resolution, due to the rather broad line-widths obtained. A preferable technique is that of Raman spectroscopy, which has proven invaluable for detection and identification of biologically important molecules.

Normally Raman scattering from molecules adsorbed on surfaces is too weak to be detectable. In order to overcome these problems, surface enhanced Raman scattering (SERS) has been found to be of value in surface and interface Raman studies in metals. The SERS effect is characterized by an enormous increase in the Raman intensity by many orders of magnitude for species adsorbed on rough metal surfaces compared to that obtained from the same number of molecules in solution or the gas phase[151, 152, 153, 154]. Additionally fluorescence, which often obscures Raman spectra is suppressed on a surface. Typical enhancement factors obtained on a roughened Ag surface are on the order of 10^6-10^7. Although the enhancement process is not yet understood in full detail, it is now generally accepted that several mechanisms contribute to the overall enhancement of the Raman signal. Electromagnetic theories predict that the electric field at the metal surface becomes very large when excitation takes place within surface plasmon resonances of the roughened features. The chemical enhancement mechanism is generally mentioned as a charge-transfer process. In this case, the enhancement occurs when the excitation frequency is in resonance with a charge-transfer transition of a specific adsorbate-metal complex. Both electromagnetic and chemical SERS theories predict that the SERS enhancement requires surface roughness.

The SERS technique displays a number of important advantages: sensitivity, selectivity, non-destructive detection, and feasibility for *in-situ* studies. It often provides detailed information as to the nature and orientation of the adsorbed molecule, not to mention effects of adsorption on the molecular force field. Remarkable work has been carried out recently on rhodamine 6G (R6G)[155, 156] by

observing giant Raman enhancements (estimated at 10^{14}) on small, single Ag nanoparticles and nanowires[157]. Until now, SERS experiments have been essentially restricted to adsorbates on rough metallic surfaces, especially noble and alkali metals. Relatively few reports describing SERS experiments on non-coinage metal surfaces are available[158, 159, 160].

A recent work[161] reported a successful application of the SERS to surface characterization of semiconductor materials by using two different methods. The first consists of coating the semiconductor surface with a silver island film. The second method is based on the use of a chemical etching process. With both SERS-activation procedures, the surface roughness plays a crucial role in obtaining very large enhancement of the Raman signal.

More recently, SERS was observed from III-V (InAs/GaAs) semiconductor QDs[162]. This suggests a technique for sensitive, high-resolution study of the interaction of adsorbate molecules with QD surfaces. Pyridine (C_5H_5N) was chosen as probe molecule for these SERS studies because its Raman spectrum is sensitive to the environment. An enhancement factor of approximately 10^3 was obtained. The reason this enhancement factor is so much lower than that of Ag is most likely due to the fact that the surface plasmon excitation frequency for III-V semiconductors is in the infrared, quite far from the laser excitation. These considerations lead us to examine whether we can obtain higher degrees of surface enhancement due to II-VI QD, since in these systems the interband excitation frequency is closer to that of our laser excitation. In this section, the observation of surface enhancement of a Raman signal from molecules adsorbed on a CdSe SAQDs grown by MBE is shown. We have

examined several molecules of biological interest, namely adenine, tryptophan and tyrosine in order to ascertain whether the method might be of use in the growing field of biosensors. Using laser excitation at 488 nm, we have found that a much larger enhancement factor can be obtained in II-VI semiconductors than in III-V systems, and by detailed analysis of the observed Raman spectra, we can obtain information as to the orientation of the molecule with respect to the surface. Furthermore, the high degree of spectral selectivity, coupled with the high sensitivity afforded by the rather large enhancement factors, makes such systems good candidates for possible use in detecting and identifying biological molecules.

6.2.2. Experimental details

The QD assemblies were grown by MBE on InP (001) substrates in an UHV-Riber system that has two Riber 2300 growth chambers, one dedicated to III-V materials and another for II-VI materials. The InP deoxidation, the growth of the 150 nm-InGaAs buffer layer and the growth of the ZnCdMgSe barrier were performed in the same way than the one described in the section 3.3.3.1. The total thickness of the quaternary barrier is 400 nm, the RHEED showed a streaky Se-terminated (2 x 1) surface reconstruction indicating a good quality epilayer formation[20]. To initiate the CdSe deposition, the Zn and Mg shutters were closed. The CdSe QDs were formed on the $Zn_xCd_yMg_{1-x-y}Se$ barrier by 10 sec-CdSe deposition time followed by a growth interruption time of 30 sec with only the Se shutter open. The nominal thickness corresponding to this deposition time is 2.0 ML. The RHEED shows a 2 x 1 streaky pattern indicating a 2D-growth during CdSe deposition that can be associated with

wetting layer formation. When the growth is interrupted, the RHEED pattern becomes diffuse, but not completely spotty, indicating the formation of QDs on top of the wetting layer (possibly, a Stranski-Krastanow mode). Growth finished decreasing the temperature to 225 ºC under Se flux rich conditions. Samples were removed from the chamber immediately following the QD formation. The AFM images were carried out in contact mode using the same parameters and instrument than the one described in the section

Raman Spectroscopy

After the samples were removed from the MBE growth chamber, they were cut into smaller rectangles (approximately 3 mm). Then, they were stored immediately in liquid nitrogen to prevent possible ripening or oxide formation. Samples were kept in this condition until the moment performing the surface topography or Raman spectra.

A stock solution of adenine was prepared at 1mM concentration in deionized-distilled water, while tyrosine and trytophan were prepared at 0.01 M also in deionized-distilled water. One of the cut QD samples would then be removed, allowed to reach room temperature and then be immersed in a small portion (10 ml) of the liquid sample for 20 minutes. After this, the sample was sonicated for 5 minutes to remove the excess liquid and then, mounted near the entrance slit of a SPEX (1 meter) model 1401 double monochromator. Light from a Spectra Physics Model 2560 argon ion laser was filtered to remove interference from plasma lines and focused on to the sample. All spectra reported below were taken at 488 nm, unless noted. Typical power levels at the sample were measured to be approximately 30

mW. Scattered light was focused onto the slit of the spectrometer and the slit widths were set at 150 μm, providing a resolution of about 3 cm^{-1}.

6.2.3. Results

Figure 3.16 showed a representative AFM image of uncapped QD sample. The surface QD density is $7x10^{8}$ cm^{-2}. The height distribution shows an approximately Gaussian lineshape[136] with 4.5 ± 0.5 nm being the most abundant value. The average radius of the QDs base is 47 ± 10 nm.

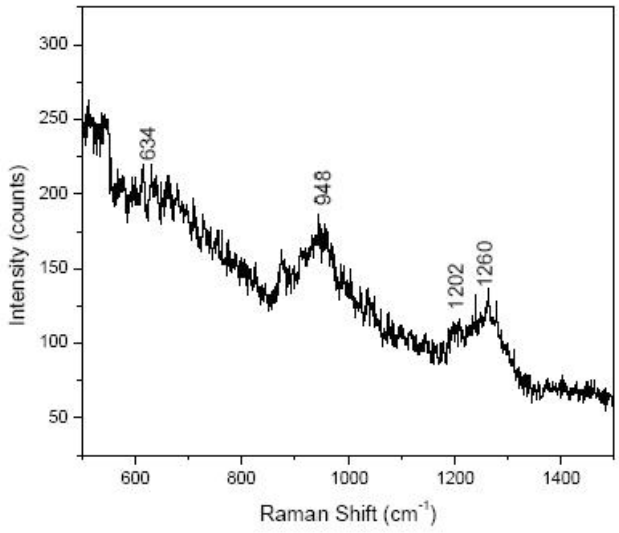

Figure 6.3. The Raman spectrum of the QD sample before coating with a molecule excited at 488 nm.

The Fig 6.3 shows the Raman spectrum of the QD sample before coating with a molecule excited at 488 nm. Note several broad but weak features, which appear to be overtones of the phonon modes of the QDs. They are not observed if we examine the substrate without the CdSe dots deposited. No bands are observed at higher

wavenumbers. When molecules are deposited on these samples, in addition to the Raman lines discussed below, we observe the appearance of several sharp and intense photo-emission bands. Some of these appear to coincide closely with the weak broad bands from the bare quantum dots (about 650, 950, and 1260 cm^{-1}). That these are due to emission, rather than Raman shifts is confirmed by observation of spectra excited at 514.5 nm, in which these lines appear at the same absolute frequency. However, any Raman intensity, which may appear excited at this wavelength is too weak to measure. Neither Raman lines nor luminescence were observed using the Krypton ion laser line at 647 nm. The emission lines observed on excitation at 488 nm appear on closer examination to be composed of closely spaced (~10 cm^{-1}) multiplets, which resemble the sequence structure of molecular spectra. Most of the lines are in the same region as Raman intensity, and are therefore somewhat congested.

The Fig 6.4, 6.5 and 6.6 show the Raman spectra of CdSe QDs assemblies coated with adenine, tryptophan, and tyrosine, respectively. Since the Raman spectra arise from surface coating of at most, monolayer coverage, it is clear that the molecular spectral lines are considerably enhanced by proximity to the QDs. When the same experiment was carried out on the substrate without QDs deposited, no spectra of these molecules could be observed. The lower frequency regions (<400 cm^{-1}) of these spectra are dominated by intense semiconductor phonon modes, obscuring any possible molecular lines, and are not shown here. However, it should be noted that application of the molecules to the surface severely perturbs the phonon modes, and these observations will be reported in a future article. The adenine spectrum in

the region 500-1800 cm^{-1} is shown in Fig 6.4, with measured frequencies listed in table 6.1. Lines attributed to emission are indicated by the annotation (*f*). Numerous lines characteristic of adenine appear, as can be seen by comparison to the normal Raman (NR) spectrum of the solid and the surface enhanced Raman spectrum (SERS) of adenine on Ag taken at 632 nm.

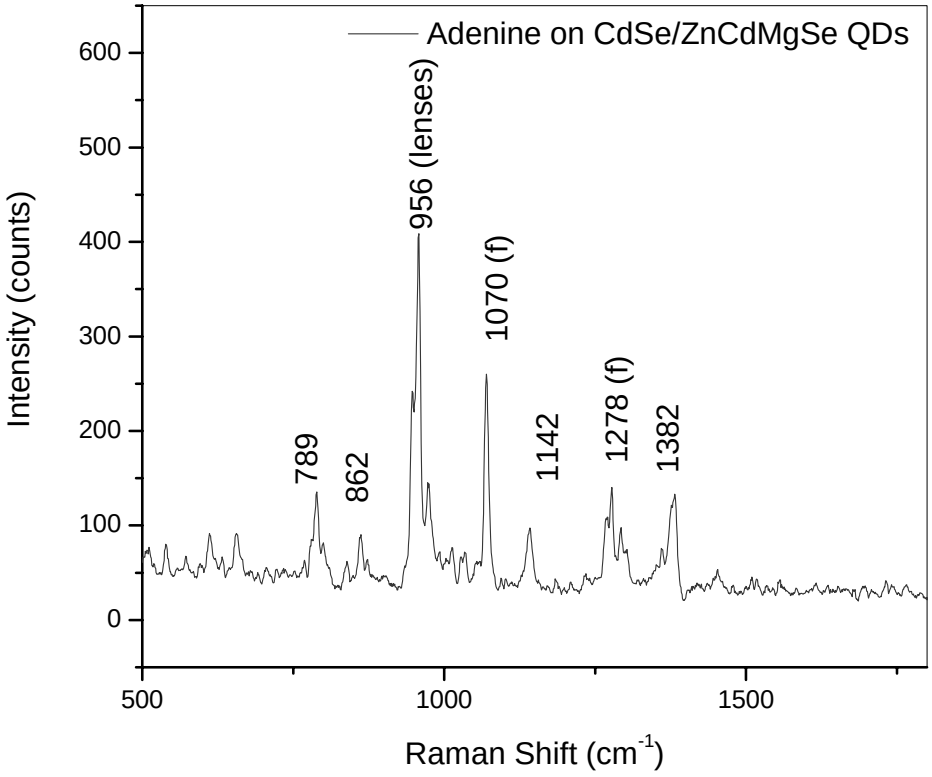

Figure 6.4. The Raman spectrum of adenine molecules adsorbed on CdSe SAQDs on ZnCdMgSe barriers in the region 500-1800 cm^{-1}.

A brief description of the normal modes assignments is included[163]. With the exception of a line at 862 cm^{-1}, and the abovementioned emission peaks, all the lines correspond to lines previously observed either in the solid or on a Ag surface. Note

the absence of the ring breathing mode ν_{21} at 731 cm^{-1}, as well as lack of most of the bands attributed to $-NH_2$ motions. Only the ν_{12} $-NH_2$ rocking mode appears in this spectrum at 1235 cm^{-1}. However, prominent in the spectra are numerous other lines (ν_{27}, ν_{20}, ν_{19} and ν_{16}) at 539, 789, 839, and 973 cm^{-1}. These have in common the fact that they represent out-of-plane vibrations. In surface enhanced Raman spectroscopy, this, along with the absence of the ring-breathing mode, is usually indicative of a molecule in which the plane lies parallel to the surface, and this is our interpretation. It is possible that in this configuration, the $-NH_2$ lies sufficiently close to surface atoms to have the modes associated with this part of the molecule either strongly shifted or decreased in intensity.

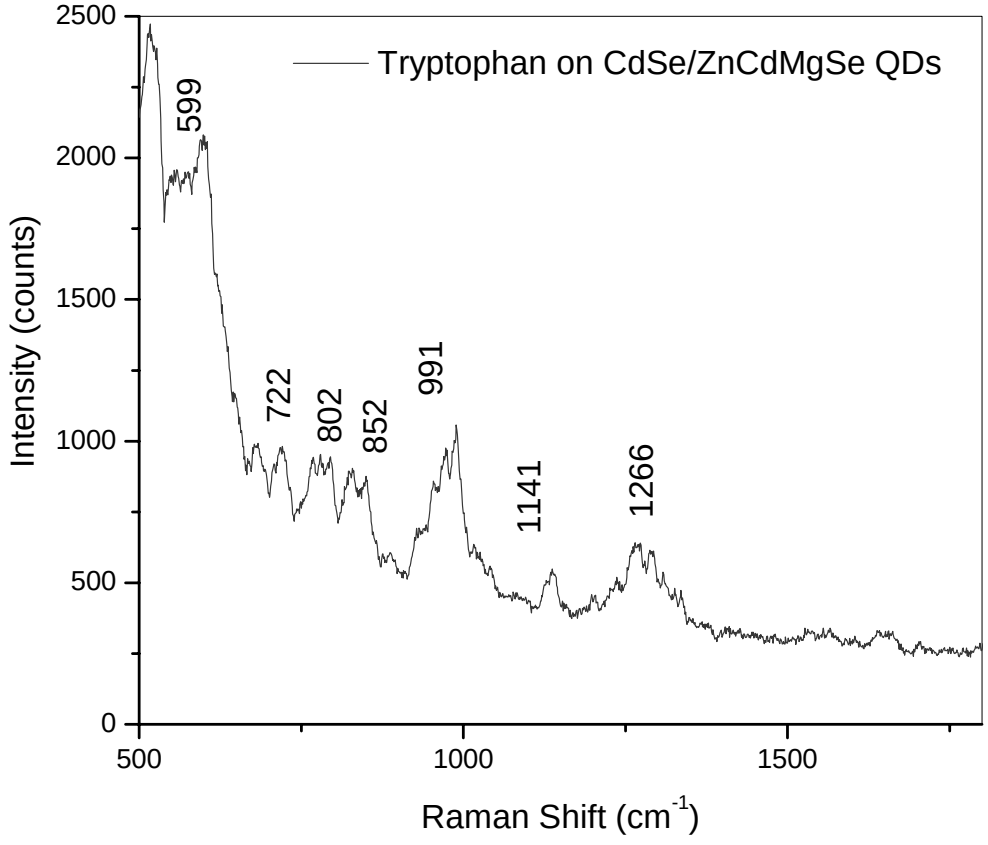

Figure 6.5. The Raman spectrum of tryptophan molecules adsorbed on CdSe/ZnCdMgSe SAQDs in the region 500-1800 cm^{-1}.

The tryptophan spectrum in the region 500-1800 cm^{-1} is shown in Fig. 6.5, with measured frequencies listed in Table 6.2. The table 6.2 lists the lines obtained for the resonance Raman spectrum of liquid tryptophan taken at 200 nm[164], a normal Raman spectrum of the solid at 488 nm, taken as part of this work, as well as the IR spectrum of the liquid zwitterion[165]. Once again, it can be seen that almost all of the lines observed in the CdSe QD spectrum correspond to either Raman or IR lines observed. In some cases possible Raman lines coincide with emission lines, resulting in some ambiguity. Since both ring breathing modes at 766 and 1011 cm^{-1} appear on the QD samples, it is likely that the molecule is oriented edge-on. Furthermore, since several prominent bands associated with either the β-NH_3^+ or the β-CO_2^- (in the zwitterionic form) are also observed relatively unshifted, it is unlikely that these species are the mode of attachment to the surface. Although there is no direct evidence, the only remaining site for adsorption to the surface is that of the nitrogen lone pair in the five-member ring.

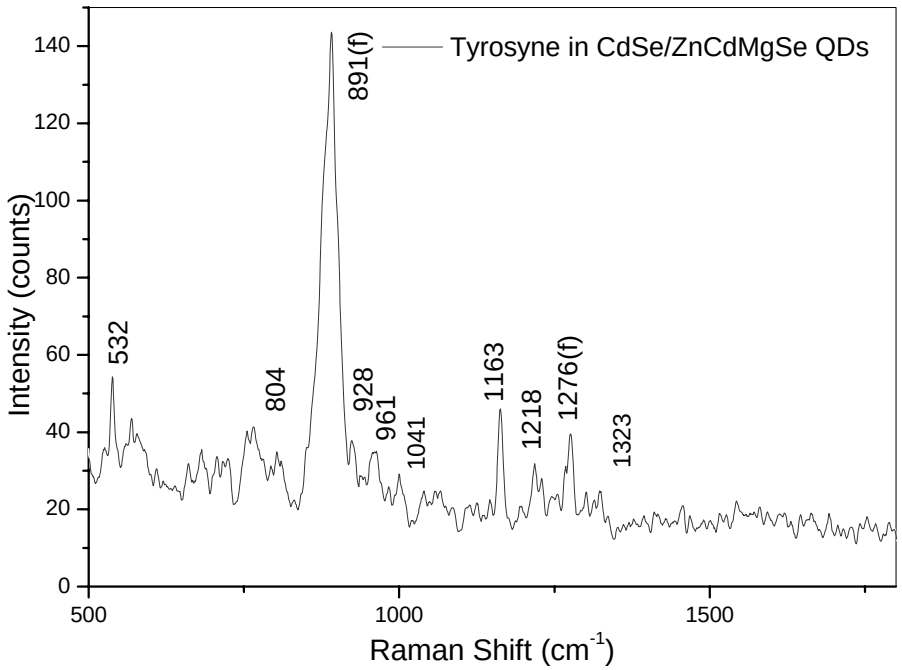

Figure 6.6. The Raman spectrum of tyrosine molecules adsorbed on CdSe/ZnCdMgSe SAQDs in the region 500-1800 cm^{-1}.

The tyrosine spectrum in the region 500-1800 cm^{-1} is shown in Fig 6.6, with measured frequencies listed in table 6.3. Also listed are the observed resonance Raman frequencies[164] obtained from the liquid at 200 nm at pH-7, as well as the results of a recent Raman spectrum[166] of the solid at 532 nm, which is listed just before the CdSe results. It can be seen that there is a strong correspondence between the QD spectrum and the solid and liquid Raman spectra. The resonance Raman spectrum is relatively sparse, due to the fact that it is sensitive only to totally symmetric vibrations. Prominent in the Raman liquid spectrum is the well-known doublet at 834 and 857 cm^{-1}. This is due to the coincidence of the ν_1 ring-breathing mode with the first overtone of an out-of-plane bending motion of the ring ν_{16a}, and the relative intensities and frequencies may be attributed to a Fermi resonance[167]. This doublet is not observed in the QD spectrum. Despite the fact that the –OH bend at

1251 is not observed, we do see the p-substituent stretch (C-O) ν_{7a} at 1218 cm^{-1}. The ν_{9a} ring stretch is observed considerably downshifted at 1163 cm^{-1}, while the C-N stretch is up-shifted to 1068 cm^{-1}. With these exceptions, all other bands observed in the QD spectrum and assigned to out-of-plane vibrations. These include the ν_{16b}, at 532 cm^{-1}, the ν_4, at 716 cm^{-1}, the ν_5, at 928 cm^{-1}, and the ν_{17a} at 961 cm^{-1}. The prominence of the usually unobserved (in SERS) out-of-plane vibrations is indicative of a molecular orientation with plane parallel to the QD surface.

NR-solid	Mode #	Description	SERS-632nm	CdSe-488nm
536	27,28	NH wag-oop	536	539
560	25	CH wag	553	556
623	24	Ring def	621	611
			690	
723	21	Ring breath	731	
797	20	Ring def-oop	788	789
839	19	CH wag-oop		839
				862
899	18	NCN def		903
942	17	NCN def	958	956
974(calc)	16	CH wag-oop		973
1025	15	rock $-NH_2$	1029	
				1070(*f*)
1126	14	CN str	1117	1142
1162	13	CH bend		
1234	12	rock $-NH_2$	1245	
1248	11	CH bend		1251
			1270	1278(*f*)
1308	10	CN str		1303
1333	8,9	CH bend	1326	
1372	7	CH bend	1372	1382
1419	6	CN str	1399	
1463	5	sciss $-NH_2$	1460	
1483	4	sciss $-NH_2$		
1597	3	sciss $-NH_2$		
1613	2	CN str		
1674	1	sciss $-NH_2$		

Table 6.1. Raman spectrum of Adenine on CdSe quantum dots excited at 488 nm. Normal Raman (NR) of solid, Mode assignments and SERS at 632 nm from: B. Giese, D. McNaughton, *J. Phys. Chem. B* **106**, 101-112 (2002).

Raman-liq 200 nm	Raman-Solid 488 nm	Description	IR-liq Zwitterion	Description	CdSe QD 488nm
	562		555	β-NH(r)	554
	580		581	β-NH(r)	
	608		613	β-CH	599
	716		725	def,r,R	722
762	764	ring-brth	763	β-CO_2^-	766
	786		794	β-CO_2^-	802
	830		821	def,r,R	828
	856		843	β-H,R	852
880	883	skel+NH	875	β-NH_3^+	895
	938			β-CH_2	
	970		955 calc		957 (lenses)
	990		990 calc		991
1016	1017	ring-brth	1007	ν_{CN},β-NH_3^+	1011
	1060		1045	β-NH_3^+	
1127	1127	9b	1111	β-H,R	
1148	1143	15 or δNH	1153	ν_{CC}	1141
1238	1234	3	1226	β-CH,νR	
1256	1262	νR	1273	νR	1266
		νR	1283	νR	1270(f)
1305	1302	5π	1316	β-CH_2	
1342	1340	14			1331
1361	1362	14π			
1434	1438	6π	1432	β-CH,νR	
1462	1465	19b	1457	β-NH_3^+	
1496	1496	19a	1489	νR	
	1540	νT			
1555	1558	ring-str	1569	β-NH_3^+	
1578	1584	8b	1578	νR	
1622	1626	8a	1625	ν_{as}-CO_2^-	

Table 6.2. Raman spectra of Tryptophan on CdSe quantum dots excited at 488 nm. Raman Spectrum at 200 nm from: R.P. Rava, T. G. Spiro, *J. Phys. Chem*. 89, 1856-1861 (1985). Solid Spectrum at 488 nm: this work. IR spectrum of Zwitterion from: X. Cao, G. Fischer, *J. Phys. Chem . A* **103**, 9995-10003 (1999). R-benzene ring, r-pyrrole ring, ν-stretch, β-bend.

Raman-liq pH-7 200 nm	Assmt	Raman-solid 532 nm	Assmt	CdSe 488 nm
		535	16b (oop)	532
		641	6b	
		714	4 (oop)	716
		739(IR)	12	
		797	-NH_2 wag	804
831	2X16a(oop)	828	1 (ring br)	
853	1 (ring br)	845	2X16a(oop)	
				891(f)
		939 (IR)	5 (oop)	928
		971	17a (oop)	961
		982	CH_2 rock	
		989	CH_2 rock	
		1046	C-N str	1041
1180	9a	1179	9a (ring str)	1163
		1200		
1210	p-subst-str	1213	7a	1218
		1251	-OH bend	
1263	7a	1263	14	
				1276(f)
		1329	13	1323
		1370	CH bend	
1443	19b	1437	19b	
1519	19a	1513 (IR)	19a	
1601	8b	1598	8b	
1617	8a	1616	8a	

Table 6.3. Raman spectrum of Tyrosine on CdSe quantum dots excited at 488 nm. Liquid Raman Spectrum from: R. P. Rava, T. G. Spiro, *J. Phys. Chem*. **89**, 1856-1861 (1985). Raman solid 532 nm from: L. Grace, R.Cohen, T. Dunn, D. M. Lubman, A. S. de Vries, *J. Molec. Spectry*. **215**, 204-219 (2002).

6.2.4. Discussion

6.2.4.1. The Nature of the Quantum Dot Surface

QD hemi-ellipsoidal shape rather than spherical or hemispherical was assumed for the calculations based on the previous results[46]. Contactless electroreflectance (CER) studies on CdSe/ZnSe or CdSe/ZnBeSe[46] provide evidence for a wetting layer. For the calculation of the enhanced factor, a similar thickness of wetting layer is assumed. Since the total amount of deposited CdSe is nominally 2.0 ML, the relative size of the wetting layer reduces the amount of material available for production of QDs. We may make an alternative estimate of the radius if we consider the total volume of CdSe deposited, subtract an assumed wetting layer of 1.5 ML and use the accurate values for the dot density and height. The QD is often described as a meniscus or lens-shaped. We may approximate it as a hemi-ellipsoid, with height *h* and radius *r*. Then the volume of a hemi-ellipsoid is $V = 2/3\pi hr^2$. We obtain for *r* a result of 68 nm, in reasonable agreement with the AFM measurement.

We must further consider the likelihood that the surface has been oxidized on removal from the molecular beam. On a clean, smooth CdSe {001} surface[42] electron-energy loss and Auger-electron spectroscopic studies indicate that initially oxygen adsorbs only on Se atoms, and then with breaking of back bonds, both selenium and cadmium oxides are formed. Part of the selenium oxide sublimes away (presumably in the form of gaseous SeO_2), leaving the surface rich in Cd=O. Bowen Katari, Colvin and Alivisatos[168] have examined this problem for QD surfaces using X-ray photoelectron spectroscopy (XPS). Both the XPS data and thermodynamic

considerations lead to the conclusion that $CdSeO_3$ is formed on the surface, although some Cd=O might also be present. In our case since the last layer is rich in Se, we expect that our QDs initially are capped with a layer of selenite, although it is possible that over time, as in the clean surface, SeO_2 sublimes leaving a surface richer in Cd=O. All the spectra shown here were obtained immediately after removal of our QD samples from liquid nitrogen. If the spectra were repeated daily afterwards, we observed a deterioration of the Raman intensities as well as some spectral shifts. It is not clear whether this is due to changes in the surface oxidation state, or merely evaporation of adsorbed molecules from the QD surfaces. AFM images of uncoated samples did not seem to change much over time after removal from liquid nitrogen. In any case, it is clear that to the extent that the molecules are adsorbed onto the CdSe surfaces, it is quite possible that they are adsorbed by means of the oxygenated species.

6.2.4.2. Calculation of the Enhancement Factor

It is now worthwhile to estimate the enhancement factor. As mentioned previously, typical enhancement factors for roughened Ag are on the order of 10^6-10^7, but under some circumstances have been observed to be as large as 10^{14}. On roughened transition metal surfaces the enhancements are more like 10^3, and this value is similar to that observed on GaAs QDs.

The enhancement factor (E_F) is the ratio of Raman intensity per adsorbed molecule divided by that of the free (or solid phase) molecule. It may be determined by the relationship:

$$E_F = I_{surf}N_{sol}/I_{sol}N_{surf}$$

Where I and N are the intensities and number of molecules on the surface and in the solid. We assume the surface is composed of two parts, one a wetting layer of roughly 0.47 nm thickness (1.5 ML), covered by a layer of hemi-ellipsoidal QDs. The dots have a height of 4.5 nm and a radius of 47 nm. It is not clear at this time whether the observed Raman enhancement is caused by molecules only adsorbed on the dots, or instead also those adsorbed between the dots on the wetting layer. We shall calculate the enhancement factor for both possibilities.

We take for our intensity measurements the 1382 cm^{-1} line of adenine. This line was chosen because it is moderately intense and isolated from other spectral lines. After subtraction of the background intensity, the intensity in the normal Raman spectrum of this line is about 200 counts, while from the surface enhanced QD spectrum, we obtain about 75 counts. In both spectra, the laser intensity was kept constant. The intensity ratio (I_{surf}/I_{sol}) is therefore approximately 0.4. We assume a laser diameter of 10 μm and that about 0.1 cm of the path in the sample is focused into the slit of the spectrometer. This leads to a volume of about 10^{-5} cm^3, and therefore $N_{sol} = 7.5 \times 10^{14}$ molecules scattering within this volume. On the surface, there are several possibilities, depending on the distribution of molecules, and their contributions to the enhancement. The two most likely situations are that only molecules adsorbed on the hemi-ellipsoidal dots contribute to the enhancement, or that molecules adsorbed between the dots in the wetting layer contribute as well, due to their proximity to the dots. In the latter case, the calculation is similar to that of a normal SERS surface. Assuming in a monolayer there are 10^{15} molecules/cm^2 in an

area of 100 μm^2, we obtain $N_{surf} = 10^9$ molecules. This results in an enhancement factor of 3×10^5. On the other hand if we assume only molecules adsorbed on the hemi-ellipsoidal quantum dots (h = 4.5 nm, r = 47 nm) contribute to the enhancement, we then find that each dot has a total area per dot of 1.3×10^4 nm^2. Multiplying by the dot density ($7x10^8$ dots/cm^2) the laser spot size (10^{-6} cm^2) and the number of molecules per unit area, we obtain $N_{surf}= 9.1x10^7$ molecules interrogated by the laser. This results in an enhancement factor of approximately $3x10^6$. The factor of approximately 10 between the two calculations merely reflects the difference in surface area presented by the dots alone, as opposed to the total surface. Even considering the more conservative value of 3×10^5 the enhancement for the II-VI CdSe QDs observed here is considerably greater than that obtained for the III-V GaAs quantum dot system, and is comparable to those observed for roughened silver surfaces.

6.2.4.3. The Enhancement Mechanism

The calculated enhancement factor for CdSe quantum dots grown by MBE is quite large, and comparable to the enhancements obtained in noble metals. However, it is difficult to invoke the enhancement mechanism usually given for metals, namely the increased electric field near the metal surface caused by plasmon resonance excited by the laser light. Typical plasmon frequencies for semi-conductors lie too far in the infrared to be the cause of the effect seen here. Another contributing factor to metallic Raman enhancement has been identified as a charge transfer between molecule and metal. This is mediated by an interaction of the molecular electronic

states with those of the metal conduction band[169]. This mechanism is usually regarded as only a minor contributor to the SERS enhancement, usually contributing at most a factor of 10-100 in the enhancement factor. It is possible, however, that for systems, which are subject to quantum confinement effects, such as quantum dots, the charge-transfer mechanism may be of more importance. The rather low contribution in metals was attributed to the broad linewidths (>200 meV) usually associated with conduction band resonances. The enhancement due to the charge-transfer mechanism was shown to be inversely proportional to the resonance linewidth. However, in semi-conductor quantum dots, both the valence band and the conduction band are considerably narrowed by quantum confinement. Furthermore, bare quantum dot assemblies grown by MBE do not display much photoluminescence. In order to observe photoluminescence in such systems it is necessary to cap the dots, usually with a deposit of a higher bandgap semiconductor material. This has the effect of filling the trap states, which usually are produced by surface defects. These trap states tend to suppress photoluminescence by providing a fast, non-radiative pathway for de-excitation. It is likely that either the oxide coat, or our added molecules provide a capping layer sufficient to produce the observed luminescence. CdO has a band gap of 2.28 eV (compared to CdSe which is 1.751 eV), and is therefore a reasonable candidate for efficient capping. However, we only observed the narrow photoluminescence when a molecule is added. It might be better to consider the CdSe/CdO structures as core/shell dots, with a molecular capping layer. The much narrower interband resonances observed here (around 1 meV as opposed to >200 meV in metals) could easily explain the increased enhancement assuming a charge-

transfer mechanism. Definitive evidence for such a mechanism can be obtained by careful excitation profile measurements, which is still under study.

Chapter 7. Conclusions

7.1. Summary of the Thesis

The thesis began in Chapter 1 with a background introduction of the preceding achievements in the growth of the ZnCdMgSe system (high quality ZnCdMgSe lattice matched to the InP substrate offering the possibility of an ample selection of band gaps, from 2.1 eV to ~3.6 eV, low-defect density as low as $5x10^4$ cm^{-2}, narrow X-ray linewidths, and efficient luminescence even at room temperature) and its promising device applications in the visible range, as well as, an outline of key problems involved in the deployment, in general, of the II-VI materials to device applications (device degradation caused by the propagation of dark line defects and low device lifetime). A proposed solution, substituting the QW active layer by a QD active layer, was formulated to solve the degradation problems of these II-VI devices, as well as to lead to an improvement in the performance of the optical and electronic devices due to the three-dimensional confinement on the carriers. In addition, the chapter argued that today photonic technologies are lacking a QD system that can be morphologically controllable to use in the entire range of the visible spectrum and for white-light source applications.

Chapter 2 presented, first, an overview of fundamental MBE principles and the main components of the MBE system used for the work of this dissertation. Then, the general procedure for the growth a II-VI material on a III-V substrate is described. Finally, the most important characterization techniques utilized to determine, either *in*

situ or *ex situ,* the morphological, electronic and optical properties of the grown materials and device structures were described.

The first part of the Chapter 3 introduced the historical development of the QDs and a synopsis of the state-of-art of the QD applications and devices. Next, the physics background of the QDs was presented to understand the quantum physics governing the physical properties of these nanostructures and then, to be able to obtain the maximum profit from their quantum characteristics. Following by this, a description of the established growth modes by MBE was illustrated, focusing, specially, on the traditional growth mode for the three-dimensional QDs, the well-known Stranski-Krastanov growth mode. The next main part of this chapter was centered on the development and characterization of a new "QD/barrier system", CdSe SAQDs on a new barrier material, ZnCdMgSe lattice-matched to InP. Initial studies of variation of QD growth temperature, QD material deposition and growth interruption serve to identify the right growth conditions giving clues about how to control the formation and the properties of the dots. In addition, the AFM images demonstrated the formation of uncapped CdSe QDs on ZnCdMgSe. Then, systematic studies of the variation of the CdSe deposition time were illustrated. These studies showed that the size, and consequently PL emission energy, of the QDs could be precisely tuned and reproduced by the CdSe deposition time. As expected, higher emission peak energy was observed for smaller QDs due to the quantum confinement effect. The CdSe QD emission, covering the entire visible range, followed a simple near linear relationship with the deposition time. Then, a comparison of our results with those obtained in the related system, ZnSe/CdSe, was shown. This comparison

indicates that the chemical composition of the barrier material is an important factor in determining the growth behavior of the SAQDs.

The following section of the Chapter 3 illustrated the initial studies about how the chemical composition and in particular, the magnesium content, on the ZnCdMgSe barrier layer affected the size, density and uniformity of the CdSe SAQDs. A reduction of the QD size, as well as, a blue shift of the QD PL peak position by increasing Mg concentration in the $Zn_{1-x}Cd_xMg_{1-x-y}$ Se barrier has been demonstrated by changing the Mg temperature. In addition, a more uniform and denser layer has been found with an increase of the percentage of MgSe in the $Zn_{1-x}Cd_xMg_{1-x-y}$ Se barrier layer, which was observed by the topographic AFM images of the surface of uncapped QDs. Results pointed to Mg as chemical factor that induced QD formation, either by increasing the atomic steps or/and by changing the energy of the $Zn_xCd_yMg_{1-x-y}Se$ surface. Finally, contactless electroreflectance from single quantum dot layers structures was utilized to recognize transitions coming from different integrating parts of the QD structure, as well as, to identify higher energy transitions originating from the QDs.

The Chapter 4 presented the growth of first stacked structures of CdSe SAQDs on ZnCdMgSe barriers for the achievement of white light emission. Stacked QD structures consisting of three or more QD layers emitting in the red, green and blue (R-G-B) regions of the spectrum were grown and characterized. Photoluminescence measurements of some specific samples exhibited bright white emission that could be observed by eye, at 77K or at room temperature, as a result of the right mixing of the three color lines. The behavior of the PL emission energy and

the FWHM with respect to the CdSe deposition time followed the same trend that the one obtained for the single QD layers, demonstrating that there is not any disruption in the properties of the QDs due to influence of other QD layers within the same structure. Finally, at the end of this chapter, preliminary designs of two LED structures are presented for the accomplishment white light emission by current injection. Good diode characteristics were obtained but no light emission was observed at this point. Improvements in the device structure design, as increase the number of the QD layers and/or a change of the p-type contact, are proposed to increase the likelihood of efficient emission. In summary, all these results indicate that this material may be an attractive alternative for optical applications in the R-G-B range and may be useful for the fabrication of white light sources.

The Chapter 5 began by introducing the significance of growing staked or multi-QDs structures for intersubband device applications as quantum cascade lasers and quantum dot infrared photodetectors, highlighting the advantages provided by the CdSe QDs on ZnCdMgSe barriers for the new near-infrared applications, such as ultra fast optical communications lasers operating in the 1.55 μm or quantum dot infrared photodetectors operating in this IR range. Then, the growth and characterization of initial MQD structures were introduced. A detailed and comprehensive understanding of the electronic and optical properties of these materials were addressed by these early studies using optical transmission and reflectivity from the UV to the IR, room and liquid-nitrogen temperature CW photoluminescence experiments from 400 nm to 700 nm, and time-resolved photoluminescence experiments. From the time-resolved studies, all samples exhibit a

fast and a slow photoluminescence decay components. The capture time of the photo-excited carriers from barriers into the QDs and recombination times inside the dots was evaluated for the first time for CdSe QDs with $Zn_xCd_yMg_{1-x-y}Se$ barriers. The existence of two exponential decays was consistent with observing two independent but energetically overlapping decays. The substantially faster relaxation in the samples with smaller QDs was attributed to the larger perturbing influence that the surface of the QDs has on the electronic states of the QDs. The strong PL emission throughout the visible range and the rather long 7.5 ns QD interband relaxation shows that the CdSe QDs with $Zn_xCd_yMg_{1-x-y}Se$ barriers are suitable for optoelectronic devices such as QD lasers and QD visible and IR photodetectors.

In the third main part of the Chapter 5, MQDs structures were grown to investigate the vertical correlation (ordering in the vertical direction) and the electronic coupling between different stacked QD layers. Due to the importance of the calibration of the thickness of the ZnCdMgSe spacer layers of the MQDs and method based on X-ray diffraction was developed. This method consists of the growth of a superlattice with a barrier with the same composition than the layer spacer that is required to be calibrated. Therefore, the achievement of a well-defined satellite superlattice of ZnSe with ZnCdMgSe barrier layers that appeared in both single and double-crystal X-ray diffraction spectra were used to calculate the superlattice period and then, the thickness and the growth rate of the ZnCdMgSe barrier. In addition, this chapter showed that the electronic properties of the samples (PL peak position and polarizability of the emitted light) as well as, nanostructural properties of the QDs could be tuned by the variation of MgSe content in the

ZnCdMgSe barrier and/or by the ZnCdMgSe spacer thickness. Control of the QD coupling was achieved adjusting these two parameters. Samples with properties intermediate between those of totally coupled MQDs and uncoupled ones were also grown. Power dependence studies demonstrated that the PL peak position associated with coupled QDs depends on the excitation power of the laser while the PL peak of the uncoupled ones remains invariable. The blue shift of the PL peak position of the peak assigned to the coupled QDs demonstrated the formation of a short-period superlattice in the vertical direction and consequently, the formation of a miniband. Linearly polarized PL studies were carried out to analyze the luminescence originating from the QDs. Results show that for the edge emission, polarization is mostly TM for the case of coupled QDs, indicating excitonic delocalization along the growth axis and TE polarized for the uncoupled QDs, consistent with the anisotropy of the QD shape. For the surface configuration, it is expected that the PL emission will be predominantly TE polarized for both cases (due to the QDs shape anisotropy). However, for the uncoupled sample, the PL emission was slightly TM polarized, which pointed out to the presence of some kind of organization on the surface. AFM images of an uncapped sample grown under the same conditions as the capped one were consistent with the polarized PL since the formation of connected structures (wire-like rather than dot-like) on the surface was observed. No surface organization was obtained for the coupled case. The last part of this chapter shows, for the first time, the contactless electroreflectance study of a coupled MQD sample. This study demonstrated the significance of this measurement because on one hand, permits the

analysis of the strength of the electronic coupling of the QDs and on the other hand, the study the higher energy transitions not shown by PL.

Finally, the Chapter 6 starts introducing the Raman phenomenon in semiconductors. Then, the Raman measurements of capped QDs grown under the same conditions but with different deposition times are presented. The importance of measuring the capped samples under resonance conditions in order to be able to observe the QD effects is demonstrated. From the results obtained and from the previous literature work, a peak is assigned to interface phonons. However, more work needs to be done to confirm this hypothesis. A possible local mode of magnesium is observed in the resonant case, which means that this mode is spatially related to the QDs, possibly at the interface or within the QDs.

The last part of this chapter presents the surface enhanced Raman spectroscopy measurements performed on uncapped QD samples. These results demonstrated that CdSe self-assembled quantum dots grown on ZnCdMgSe barriers can provide efficient enhancement of a Raman signal from molecules adsorbed on the surface. This surface enhancement is estimated to be in the range of 10^5 to 10^6, comparable to that of noble metals. The analyses of the Raman spectra of several molecule of biological interest and their possible mode of adsorption to the surface have been explained. In addition, sharp, narrow photoluminescence bands, which are attributed to the quantum dots, but are only observed by addition of the molecular layer, were reported. These results indicate that CdSe quantum dot system enable a high degree of molecular specificity and large Raman enhancement factor. This suggests a possible technique for sensitive detection and identification of biological

molecules. Large Raman enhancements (>10^5) were demonstrated for molecules adsorbed on a II-VI semiconductor CdSe sample of self-assembled quantum dots produced by molecular beam epitaxy. The observed enhancement is much larger than that previously obtained in III-V semiconductor quantum dots. The samples were grown on InP substrates with $Zn_xCd_yMg_{1-x-y}Se$ barriers. A hemi-ellipsoidal shape CdSe SAQDs formed above a thin wetting layer were assumed for the calculations of the enhancement factor. Excitation at 488 nm produces intense Raman spectra of adenine, tryptophan and tyrosine, when adsorbed on these structures. Sharp, intense luminescence bands are also observed. Examination of individual Raman frequencies provides information as to the mode of attachment of the molecules to the CdSe surface. These results demonstrate that the CdSe quantum dot system provides a high degree of molecular specificity and large Raman enhancement factor, enabling sensitive detection and identification of biological molecules.

7.2. Thesis Contribution

The main scientific work's contribution is the development and control of a new QD/barrier system, CdSe SAQDs grown by MBE on ZnCdMgSe barrier. The control in the optical, electronic and morphological properties of quantum dot layers was achieved monitoring, carefully, several growth parameters: growth temperature of the CdSe QDs, selenium/cadmium flux, growth interruption, CdSe deposition time and chemical composition of the barrier. Studies affecting directly the formation of the CdSe SAQDs grown on ZnCdMgSe by changing the CdSe deposition time, showed PL emission energy can be tuned from the blue to the red without any

reduction of optical and structural quality of the material. On the other hand, CdSe SAQD formation and morphological properties (such as, density, size and uniformity) could also be affected indirectly from the change of the MgSe content. Higher MgSe content resulted in a higher density, more uniformity and smaller size of QDs, which is desirable for optical applications.

The second main contribution of this work is the achievement of the white light emission, first, at 77K and later, at RT, from combinations of three stacked QD layers with emission in different range of the visible spectrum (red, green and blue). The preliminary light-emitting diodes structures were also designed based on the structure with white emission at RT and tested. Good current-voltage characteristics show a promising starting point for the design of white light sources based on QDs, even though improvements in the design structure are required.

The third main contribution of this dissertation is the achievement of the correlation or ordering in the growth direction of the MQD structures, reflected in a narrower PL linewidth than the one belonging to the single quantum dot layers, which is interpreted as the result of a greater uniformity in the QD size by the organization in the vertical direction.

Other important contribution related with the MQD structures is the studying of the electronic coupling by variation of the spacer or by variation of the chemical composition of the ZnCdMgSe barrier, MgSe content. For the first time, electronic QD coupling was affected by another parameter (concentration of a chemical element, i.e, Mg) aside from the spacer thickness or the number of the layers. This

result gives the opportunity to tune the electronic coupling of the QDs without changing the amount of material deposited for the formation of QDs.

An important contribution from this work is that the polarizability of the light emitted by the MQDs can be controlled by the spacer thickness, which plays a significant role for some devices applications such as surface-emitting, edge-emitting lasers and single-photon based devices.

Another remarkable biochemical contribution is that the SERS results demonstrate that the CdSe/ZnCdMgSe quantum dot system provides a high degree of molecular specificity and large Raman enhancement factor (compared to the noble metals), enabling sensitive detection and identification of biological molecules.

Finally, two important observations were obtained about the ZnCdMgSe surface. Higher magnesium concentration in the layer seems to change the surface energy, decreasing the migration of the atoms, which results in an increase of the density of the atomic steps, where the QDs will nucleate. This QD nucleation of the edges of the atomic steps is similar to the effect that initiates the formation of QD in vicinal substrates. This observation is the first study of the QD ordering in the surface by formation of the natural multi-atomic steps on the barrier material. Thus far, it is not known whether even in the traditional II-VI barrier, ZnSe surfaces, the step bunching can be achieved to obtain the alignment of the CdSe QDs.[20] The other observation was the formation of a wire-like structure rather than a dot-like on the uncapped uncoupled multi-quantum dot structures, which can be explained by the combination of two effects: the formation of the atomic steps on the ZnCdMgSe and the strain energy coming from the deeper QD layers. All these observations show the

widespread possibilities of organization of the CdSe SAQDs on ZnCdMgSe barriers, opening doors for new electronic and optoelectronic applications.

7.3. Future Work

From the applications point of view, the CdSe SAQDs on ZnCdMgSe barriers exhibit attractive optical properties that show extensive potential for optical devices applications. It is suggested to keep on investigating the R-G-B and white light visible applications of these materials, as light emitting diodes and laser diodes covering the entire visible range. In the infrared range, the application of these material system to intersubband device applications, such quantum dot infrared photodetectors and quantum cascade lasers, can improve their performance characteristics and their range of the technological applications. To illustrate, the anticipated large CdSe/$Zn_xCd_yMg_{1-x-y}Se$ conduction-band offsets highlights the potential applications to obtain QDIPs with functionality extended into near-IR, and even up to the visible region; and inter-subband quantum cascade lasers (QCLs) with emission wavelength significantly shorter, (i.e.1.55 μm at RT) than what is currently available in such devices. In addition, a less temperature influence in the device response is expected for these intersubband devices based on QDs instead of QWs, which will facilitate, first, for the case of the QCLs the operation in CW mode at RT and second, for the case of the QDIPs will decrease the influence of the detection sensibility to the temperature. In addition to these applications, specific applications of the correlated CdSe MQDs with ZnCdMgSe spacers derived from the QD coupling could be surface-emitting, edge-emitting lasers and single-photon based devices.

From the growth point of view, the investigation of the development of natural bunching atomic steps of the ZnCdMgSe and its control is a recommended direction of new investigation. The possibility of further exploiting their formation either by using different crystallographic orientations of the substrate or by the utilization of mesas is also proposed.

Finally, since some device applications require high-density QD layers (sometimes substituted by the use of MQD layers), we suggest the exploration of the seeding of QDs for this material system. Usually, traditional III-V systems as InAs /GaAs have QD densities higher, up to 10^{11} cm^{-3}, than the II-VI QDs. Considering that the MBE system in the City College of New York consists of two chambers, one for III-V materials and another for II-VI materials connected in UHV, we could grow different type of QD layers (III-V and II-VI) integrated in the same structure. Therefore, the growth of a seeding layer of high QD density in the III-V and later, the growth of the CdSe SAQDs on ZnCdMgSe barriers could modify dramatically the density of the II-VI QDs to obtain the desired applications.

Bibliography

Chapter 1

[1] S.H. Xin, P.D. Wang, A. Yin, C. Kim, M. Dobrowolska, J.L. Merz, and J.K. Furdyna, *Appl. Phys. Lett.* **69**, 3884 (1996).

[2] M. Sohel, M. Muñoz, and M. C. Tamargo, *Appl. Phys. Lett.* 85, 2794 (2004).

[3] L. Zeng, S. P. Guo, Y. Y. Luo, W. Lin, M. C. Tamargo, H. Xing and G. S. Cargill III, *J. Vac. Sci. Technol.* B **17**, 1255 (1999).

[4] L. Zeng, B. X. Yang, A. Cavus, W. Lin, Y. Y. Guo, M. C. Tamargo, Y. Guo, and Y. C. Chen, *Appl. Phys. Lett*. **68**, 3446 (1996).

[5] M. C. Tamargo, W. Lin, S. P. Guo, Y. Luo, Y. Guo, and Y. C. Chen, *J. Cryst. Growth* **214/215**, 1058 (2000).

[6] W. Faschinger and Nürnberger, *Appl. Phys. Lett.* **77**, 187 (2000).

[7] S. P. Guo, L. Zeng, and M. C. Tamargo, *Appl. Phys. Lett.* **78**, 1 (2001).

[8] Th. Schmidt, T. Clausen, J. Falta, G. Alexe, T. Passow, D. Hommel, and S. Bernstorff, *Appl. Phys. Lett.* **84**, 4367 (2004).

[9] S. P. Guo, X. Zhou, O. Maksimov, M.C. Tamargo, C. Chi, A. Couzis, C. Maldarelli, Igor L. Kuskovsky, and G. F. Neumark, *J. Vac. Sci. Technol. B* **19**, 1635 (2001).

[10] Zh. I. Alferov, A. Yu. Egorov, A. E. Zhukov, S. V. Ivanov, P. S. Kop'ev, N. N. Ledentsov, B. Ya. Mel'tser, V. M. Ustinov, *Sov. Phys. Semicond*. **26**, 959 (1992).

[11] L. Goldstein, F. Glas, J. Y. Marzin, M. N. Charasse, G. Le Roux. Appl. Phys. Lett. 47, 1099 (1985).

[12] I. L. Krestnikov, M. Straβburg, M. Caesar, A. Hoffmann, U. W. Pohl, D. Bimberg, N. N. Ledentsov, P.S.Kop'ev, Zh. I. Alferov, D. Litvinov, A. Rosenauer, D. Gerthsen, *Phys. Rev. B* **60**, 8696 (1999).

[13] M. Asada, M. Miyamoto, Y. Suematsu, IEEE *J. Quantum Electron*. **22**, 1915 (1986).

[14] Zh. I. Alferov, R. F. Kazarinov: Double Heterostructure Laser, Authors Certificate No 27448, Application No 950840 (1963).

[15] Zh. I. Alferov, V. M. Andreev, E.L. Portnoi, M.K. Trukan, *Sov. Phys. Semicond.* **3**, 1107 (1970).

[16] R. D. Dupuis, P.D. Dapkus, N. Holonyak Jr., E. A. Rezek, R. Chin. Appl. Phys. Lett. **32**, 295 (1978).

[17] W. T. Tsang, Appl. Phys. Lett. **39**, 786 (1981).

[18] R. Dingle, C. H. Henry: Quantum Effects in Heterostructure lasers, U. S. Patent No. 3982207 (1976).

[19] M. Strassburg, V. Kutzer, U. W. Pohl, A. Hoffmann, I. Broser, N. N. Broser, N.N. Ledentsov, D. Bimberg, A. Rosenauer, U. Fischer, D. Gerthsen, I. L. Krestnikov, M. V. Maximov, P. S. Kop'ev, and Zh. I. Alferov, *Appl. Phys. Lett*., **72**, 942 (1998)

[20] "II-VI Semiconductor materials and their applications", edited by Maria Tamargo, (Taylor & Francis, New York, 2002), Vol. 12.

[21] M. A. Haase, J. Qiu, J. M. De Puydt and H. Cheng, *Appl. Phys. Lett.* **59**, 1272 (1991).

Chapter 2

[22] R. B. Schoolar and J. N. Zemel, *J. Appl. Phys*. **35**, 1848 (1964).

[23] M.A. Herman and H. Sitter, "Molecular Beam Epitaxy", New York, Springer, pp. 233 (1996).

[24] A. Y. Cho, "Growth of III-V Semiconductors by Molecular Beam Epitaxy and their Properties", *Thin Solid Films* **100**, 291 (1983).

[25] J. Singh, "Semiconductor Optoelectronics", New York, McGraw-Hill, pp. 18-31 (1995).

[26] S. Taniguchi, T.Hino, S. Itoh, K. Nakano, N. Nakayama, A. Ishibashi and M. Ikeda, *Electrón. Lett.* **32**, 552 (1996).

[27] D. Li and M. D. Pashley, *J. Vac. Sci. Technol.* B **12**, 2547 (1994).

[28] H. H. Farrell, M. C. Tamargo, J. H. de Miguel, F. S. Turco, D. M. Hwang, and R. E. Nahory, *J. Appl. Phys*. **69**, 7021 (1991).

[29] S. Guha, H. Munekata, and L.L Chang, *J. Appl. Phys*. **73**, 2294 (1993).

[30] J. M. Gaines, J. Petruzzello, and B. Greenberg, *J. Appl. Phys.* **73**, 2835 (1993).

[31] L. Zeng, A. Cavus, B. X. Xang, M. C. Tamargo, N. Bambha, A. Gray, and F. Semendy, *J. Crys. Growth* **175/176**, 541 (1997).

[32] E. Bauer, "Techniques of Metals Research", Chap. 15, Vol. 2, ed. R. F. Bunshah, Wiley-Interscience, New York (1969).

[33] P. J. Dobson, B. A. Joyce, J. H. Neave and J. Zhang, *J. Cryst. Growth* **81**, 1 (1987).

[34] A. Y. Cho and J. R. Arthur, *Prog. Solid State Chem.* **10**, 157 (1975).

[35] J. I. Pankove, "Optical Process in Semiconductors", Dover Publications Inc, New York., (1975).

[36] D. K. Bowen and B. K. Tanner, "High Resolution X-ray Diffractometry and Topography", Taylor & Francis, Bristol, Pennsylvania, (1998).

[37] L. Vegard, *Z. Phys.*, **5**, 17 (1921).

[38] M. C. Tamargo, M. S. P. Brasil, R. E. Nahory, R. J. Martin, A. L. Weaver, and H. L. Gilchrist, *Semicond. Sci. Technol.* **6**, A8 (1991).

[39] L. Zeng,"Molecular Beam Epitaxy Growth and Characterization of $Zn_xCd_yMg_{1-x-y}Se$ Materials for Visible Semiconductor Lasers", PhD dissertation, City University of NewYork, (1998).

[40] C. G. Van de Valle, *Phys. Rev. B*, **39**, 1871 (1989).

[41] J. S. Vilarrubia*, J. Res. Natl. Inst, Stand. Technol*. **102**, 425 (1997).

[42] Ebina, A.; Asano, K.; Takahashi, T.*, Phys. Rev. B.,* **22**, 1980, 1980.

[43] R Leon, J. Wellman, X. Z. Liao, J. Zuo, D. J. H. Cokayne, *Appl. Phys. Lett.* **76**, 1558 (2000).

[44] V. A. Shchukin, N. N. Ledentsov, V. M. Ustinov, Yu. G. Musikhin, V. B. Volovik, A. Schliwa, O. Stier, R. Heitz, and D. Bimberg, "In Morphological and Compositional Evolution of Heteroepitaxial Semiconductor Thin Films", ed. By A. L. Barabasi, E. Jones, and J Mirecki Millunchick, *Mat. Res Soc. Symp . Proc*. **618**, 79 (2000).

[45] N. N. Ledentsov, V. A. Shchukin, D. Bimberg, V. M. Ustinov, N. A. Cherkashin, Yu. G. Musikhin, V. B. Volovik, G. E. Cirlin, Zh. I Alferov, *Semicond. Sci. and Technol*. **16**, 502 (2001).

[46] M. Muñoz, S. Guo, X. Zhou, M. C. Tamargo, Y. S. Huang, C. Trallero-Giner, and A. H. Rodríguez, *Appl. Phys. Lett*. **83**, 4399 (2003)

[47] F. H. Pollak and H. Shen, *Mater. Sci. Eng*. **R10**, 275 (1993).

[48] O. J. Glembocki and B. V. Shanabrook, "Semiconductors and Semimetals", vol. 36, ed. D. G. Seiler and C. L. Littler, (New York, Academic Press, 1992) p. 221.

[49] F. H. Pollak, "Handbook on Semiconductors", vol. **2**, ed. M. Balkanski, Amsterdam, North-Holland, p. 527 (1994).

[50] W. Krystek, M. Leibovitch, F. H. Pollak, M. L. Gray, and W. S. Hobson*, IEEE J. Selected Topics Quantum Electron.* **1**, 1002 (1995).

[51] H. Shen and M. Dutta, *J. Appl. Phys.* **78**, 2151 (1995).

[52] F. H. Pollak, "Photonic Probes of Surfaces", ed. P. Halevi, New York, North-Holland, p. 175 (1995)

[53] A. K. Ramdas and S. Rodriguez, "Semiconductors and Semimetals", vol. 36, ed. D. G. Seiler and C. L. Littler, New York, Academic Press, p. 137, (1992)

[54] D. E. Aspnes, *Mat. Res. Soc. Symp. Proc.* **324**, 3 (1994); also Proc. Society of Photo-optical Instrumentation Engineers 1361, 551 (SPIE, Bellingham, 1990).

[55] O. Acher, S. M. Koch, F. Omnes, M. Defour, M. Razeghi, and B. Drévillon, *J. Appl. Phys.* **68**, 3564 (1990); W. Richter, and Phil. Trans, *R. Soc. London A* **344**, 453 (1993).

[56] S. M. Sze, " Physics of Semiconductor Devices", 2nd Edition, John Wiley & Sons, New York (1981).

[57] D. K. Schroder, "Semiconductor Material and Device Characterization", John Wiley & Sons, New York (1990); L. J. van der Pauw, *Phil. Res. Rep* **13**, 1 (1958); L. J. van der Pauw, *Phil. Tech. Rev.* **20**, 220 (1958).

[58] Wei Cheng Lin, "Development of Wide Bandgap II-VI Materials for Visible Lasers and Light Emitting Diodes", pHD dissertation, The City University of New York, (2000).

[59] T. Marshall and D. A. Cammack. *J Appl Phys.* **69**, 4149 (1991);P. M. Mensz, S. Herko, K. W. Haberern, J. Gaines and C. Ponzoni, *Appl Phys. Lett.* **63**, 2800 (1993).

[60] J. S. Blakemore, "Semiconductor Statistics", Dover Publications, New York (1987).

Chapter 3

[61] Matthew Pelton, "An Efficient Source of Single Photons: A Single Quantum Dot in a Micropost Microcavity", pHD dissertation, Stanford University, January 2002.

[62] Zh. I. Alferov, A. Yu. Egorov, A. E. Zhukov, S. V. Ivanov, P. S. Kop'ev, N. N. Ledentsov, B. Ya. Mel'tser, and V. M. Ustinov, *Sov. Phys. Semicond*. **26**, 959 (1992).

[63] L. Goldstein, F. Glas, J. Y. Marzin, M. N. Charasse, and G. Le Roux. *Appl. Phys. Lett.* **47**, 1099 (1985).

[64] I. L. Krestnikov, M. Straβburg, M. Caesar, A. Hoffmann, U. W. Pohl, D. Bimberg, N. N. Ledentsov, P.S.Kop'ev, Zh. I. Alferov, D. Litvinov, A. Rosenauer, D. Gerthsen, *Phys. Rev. B* **60**, 8696 (1999).

[65] M. Asada, M. Miyamoto and Y. Suematsu, IEEE *J. Quantum Electron*. **22**, 1915 (1986).

[66] Zh. I. Alferov, V. M. Andreev, E.L. Portnoi, M.K. Trukan, *Sov. Phys. Semicond.* **3**, 1107 (1970).

[67] P. M. Petroff, A. C. Gossard, R. A. Logan, and W. Wiegman, *Appl. Phys. Lett.* **41**, 635 (1982).

[68] E. Kapon, M. C. Tamargo and D. M. Hwang, *Appl. Phys. Lett.* **50**, 347 (1987).

[69] Y. Arakawa and H. Sakaki, *Appl. Phys. Lett.* **40**, 939 (1982).

[70] A. I. Ekimov and A.A. Onushchenko, *JETP Lett.* 34, 345 (1981).

[71] R. Rossetti, S. Nakahara, and L. E. Brus, *J. Chem. Phys.* **79**, 1086 (1983).

[72] A. P. Alivisatos, A. L. Harris, N. J. Levinos, M. L. Steigerwald, and L. E. Brus, *J. Chem. Phys.* **89**, 4001 (1988).

[73] E. Karreich, *Nature* **413**, 450 (2001).

[74] T. Fukui, S. Ando, Y. Tokura, and T. Toriyama, *Appl. Phys. Lett.* **58**, 2018, 1991.

[75] Zh. I. Alferov, A. Yu. Egorov, A.e. Zhokov, S. V. Ivanov, P. S. Kop'ev, N. N. Ledentsov, B. Ya. Mel'tser, V. M. Ustinov, *Fiz. Tekh. Poluprovodn.* **26**, 1715 (1992) [*Sov. Phys. Semicond.* **26**, 959 (1992)].

[76] V.A. Shchukin, N. N. Ledentsov, D. Bimberg, *Epitaxy of Nanostructures*, Chap 5, pag 315-333, (Springer, New York, 2004).

[77] N. N. Ledentsov, *J. Select. Topics Quantum Electron.* **8**, 1015 (2002)

[78] D. Bimberg, N.N. Ledentsov, and J.A. Lott. *MRS Bulletin* **27**, 531 (2002).

[79] Zh. I. Alferov, V. M. Andreev, E. L. Portnoi, and M. K. Trukan, *Fiz. Tekn. Poluprovodn*. **3**, 1328 (1969), submitted December 30, 1968 [*Sov. Phys. Semicond.* **3**, 1107 (1970)]

[80] Zh. I. Alferov, V. M. Andreev, D.Z. Garbuzov, Yu. V. Zhilyaev, E. P. Morozov, E. L. Portnoi, and V. G. Trofim, *Fiz. Tekn. Poluprovodn*. **4**, 1826 (1970), submitted May 6, 1970 [*Sov. Phys. Semicond.* **4**, 1573 (1970)].

[81] Ihayashi, M. B. Panish, P. W. Foy, S. Sumski, *Appl. Phys. Lett.* **17**, 109 (1970), submitted June 8, 1970

[82] R. C. Miller, R. Dingle, A. C. Gossard, R. A. Logan, W. A. Nordland Jr., and W. Wiegmann, *J. Appl. Phys.* **47**, 4509 (1976).

[83] W. T. Tsang, *Appl. Phys. Lett.* **40**, 217 (1982)

[84] Zh. I Alferov, A. M. Vasiliev, S. V. Ivanov, P. S. Kop'ev, N. N. Ledentsov, B. Ya. Meltsev, and V. M Ustinov, *Pis'ma Zh. Tekn. Fiz.* **14**, 1803 (1988) [*Sov. Phys. Techn. Phys. Lett.***14**, 782 (1988)].

[85] Zh. I Alferov, S. V. Ivanov, P. S. Kop'ev, N. N. Ledentsov, M. E. Lutsenko, M. I Nemenov, B. Ya Meltser, V. M Ustinov, and S. V. Shaposhnikov, *Fiz, Tekn. Poluprovodn.* **24**, 152 (1990) [*Sov. Phys. Semicond*. **24**, 92 (1990)].

[86] N. Chand, E. E. Becker, J. P. van der Ziel, S. N. Gu. Chu, and N. K. Dutta, *Appl. Phys. Lett.* **58**, 1704 (1991).

[87] G. T. Liu, A Stintz, H. Li, K. J. Malloy, L. F. Lester, Electron. Lett. 35, 1163 (1999).

[88] N.N. Ledentsov, V. M Ustinov, A. Yu. Egorov, A. E. Zhukov, M. V. Maximov, I. G. Tabatadze, and P. S: Kop'ev. *Fiz. Tekh. Poluprovodn*. **28**, 1484 (1994) submitted December 29, 1993 [*Semiconductors* **28**, 832 (1994)].

[89] N. Kirstaedter, N. N. Ledentsov, M.. Grundmann, D. Bimberg, V. M. Ustinov, S.S. Ruvimov, M.V. Masimov, Ps. S. Kop'ev, Zh. I Alferov, U Richter, P. Werner, U Gösele, and J. Heydenreich, *Electron. Lett.* **30**, 1416 (1994).

[90] R. Sellin, Ch. Ribbat, M. Grundmann, D. Bimberg, Appl. Phys. Lett. 78, 1207 (2001).

[91] N. N. Ledentsov, D. Bimberg, V. M. Ustinov, M. V. Maximov, Zh. I. Alferov, V. P. Kalosha, and J. A. Lott. *Semiconductor Science and Technology* **13**, 99 (1999).

[92] K. Tachibana, T. Someya, Y. Arakawa, R. Werner, and A. Forchel. *Appl. Phys. Lett*. 75, 2605 (1999).

[93] R. Nötzel, N. N. Ledentsov, L. Däweritz, M. Hohenstein, and K. Ploog, *Phys. Rev. B.* **45**, 3507 (1992).

[94] Joel I Gersten and Frederick W. Smith, "The Physics and Chemistry of Materials", New York: John Wiley & Sons, Inc, pp. 382-387, 2001.

[95] E. Bauer, *Z. Krist* **110**, 372 (1958).

[96] F. C. Frank and J. H. van der Merwe, *Proc. Roy. Soc. London A* **198**, 205 (1949).

[97] M. Volmer and A. Weber, *Z. Physik. Chem.* **119**, 277 (1926).

[98] I. N. Stranski and L. Krastanow, *Sitzungsberichte der Akademie der Wissenschaften in Wien, Mathematisch-Naturwissenschaftliche Klasse* **146**, 797 (1937)

[99] C. Herring, *Phys. Rev*. **82**, 87 (1951).

[100] V. I. Marchenko, Sov. Phys. JEPT 54, 605 (1981).

[101] R. J. Phanauf and E. D. Williams, Phys. Rev. Lett. 58, 2563 (1987)

[102] V. A. Shchukin, N. N. Ledentsov, P. S. Kop'ev and D. Bimberg, *Phys. Rev. Lett*, **75**, 2968, (1995).

[103] István Daruka and Albert-László Barabási, *Phys. Rev. Lett*. **79**, 3708 (1997).

[104] J. M. Rickman and D. J. Srolovitz, Surf. Sci. **284**, 211 (1993).

[105] I. V. Markov, "Crystal Growth for Beginners", World Scientific, Singapore, (1995).

[106] C. B. Murray, D. J. Norris, and M. G. Bawendi*, J. Am Chem. Soc*. **115**, 8706 (1993)

[107] Yong-Hoon Cho, B. J. Kwon, J. Barjon, J. Brault, B. Daudin, H. Mariette, and Le Si Dang, *Appl. Phys. Lett.* **81**, 4934 (2002)

[108] T. Tawara, S. Tanaka, H. Kumano, and I. Suemune. *Appl. Phys. Lett.* **75**, 235 (1999)

[109] N.N. Ledentsov, J. Böhrer, M. Beer, F. Heinrichsdorff, M. Grundmann, D. Bimberg, S.V. Ivanov, B. Ya. Meltser, I.N. Yassievich, N. N. Faleev, P.S. Kop'ev, Zh. I. Alferov, *Phys. Rev. B* 52, 14058 (1995)

[110] P. Schittenhelm, M. Gail, J. Brunner, J. F. Nützel, G. Abstreiter. *Appl. Phys. Lett.* **67**, 1292 (1995)

[111] L. Goldstein, F. Glas, J.Y. Marzin, M. N. Charasse, and G. L. Roux, *Appl. Phys. Lett.*, **47**, 1099 (1985)

[112] V. M. Ustinov, E. R. Weber, S. Ruvimov, Z. Liliental-Weber, A. E. Zhukov, A. Yu. Egorov, A. R. Kovsh, A. F. Tsatsul'nikov and P. S. Kop'ev, *Appl. Phys. Lett.* **72**, 362 (1998)

[113] F. Hatami, N. N. Ledentsov, M. Grudmann, J. Böhrer, F. Heinrichsdorff, M. Beer, D. Bimberg, S.S. Ruvimov, P. Werner, U. Gösele, J. Heydenreich, S. V. Ivanov, B. Ya. Meltser, P. S. Kop'ev, Zh. I. Alferov. *Appl. Phys. Lett*. **67**, 656 (1995)

[114] F. Flack, V. Nikitin, P. A. Crowell, J. Shi, J. Levy, N. Samarth, and D.D. Awschalom, *Phys. Rev.* **B54**, R17312 (1996)

[115] X. Zhou, M.C. Tamargo, S.P. Guo, and Y. C. Chen, *J. Electron. Mater.* , **32**, 733 (2003)

[116] X. Zhou, M. Muñoz, Shiping Guo, M. C. Tamargo, Y. Gu, I. L. Kuskovsky, R. Robinson, I. P. Herman, and G. F. Neumark, *J. Vac. Sci. Technol. B* **22**, 1518 (2004).

[117] K. Arai, A. Ohtake, T. Hanada, S. Miwa, T. Yasuda and T. Yao, *Thin Solid films* **357**, 1 (1999)

[118] V.S. Bagaev, V.V. Zaitsev, E.E. Onishchenko and Yu. G. Sadofyev, *J. Cryst. Growth* **214/215**, 250 (2000)

[119] T. Yao, M. Fujimoto, S. K Chang and H. Tanino, *J. Cryst. Growth*, 111, **823** (1991)

[120] S.H. Xin, P.D. Wang, A. Yin, C. Kim, M. Dobrowolska, J.L. Merz and J.K. Furdyna, *Appl. Phys. Lett.* **69**, 3884 (1996).

[121]"Nano-Optolectronics, Concepts, Physics and Devices", ed. Marius Grundmann, Springer, New York, (2002).

[122] Ch. Heyn. *Phys. Rev. B* **66**, 075307 (2002).

[123] Ch. Heyn. *Phys. Rev. B* **64**, 165306 (2001).

[124] S.V. Ivanov, A.A. Toporov, S.V. Sorokin, T. V. Shubina, I. V. Sedova, A.A. Sitnikova, P. S. Kop'ev, Zh. I. Alferov. H. J. Lugauer, G. Reuscher, M. Keim, F. Fischer, A. Waag, and G. Landwehr, *Appl. Phys. Lett.* **74**, 498, (1999)

[125] S. V. Ivanov, A. A. Toporov, T. V. Shubina, S. V. Sorokin, A. V. Lebedev, I. V. Sedova, P. S. Kop'ev, G. R. Pozina, J. P. Bergman, and B. Monevar, *J. Appl. Phys.* **83**, 3168 (1998).

[126] S. K Park, J. Tatebayashi and Y. Arakawa, *Physica E*, **21**, 279 (2004).

[127] S. Ishida and Y. Arakawa, *Physica E,* **2,** 15 (1998).

[128] J. Tersoff, Y. H. Phang, Zh. Zhang, M. G. Lagally. Phys. Rev. Lett. 75, 2730 (1995).

[129] M. Kitamura, M. Nishioka, J. Oshinowo, and Y. Arakawa, *Appl. Phys. Lett*. **66**, 3663 (1995).

[130] G. Bastard and J. A. Brum, IEEE J. Quantum Electron. **QE-22**, 1625 (1986).

[131] O. Madelung, "Semiconductors-Basic Data", ed. O. Madelung, Springer, Berlin, 1996).

[132] M. Muñoz, H. Lu, X. Zhou, M. C. Tamargo, F. H. Pollak, Appl. Phys. Lett. **83**, 1995 (2003).

Chapter 4

[133] Y. Luo, S. P. Guo, O. Maksimov, M.C. Tamargo, V. Asnin, F.H. Pollak and Y.C. Chen, *Appl. Phys. Lett.* **77**, 4259 (2000).

[134] S. O. Ferreira, H. Sitter, W. Faschinger, R. Krump and G. Brunthaler, J. Cryst. Growth 146, 418 (1995).

Chapter 5

[135] L. Goldstein, F. Glas, J. Y. Marzin, M. N. Charasse, and G. Le Roux, Appl. Phys. Lett**.. 47**, 1099 (1985)

[136] M. N. Perez-Paz, X. Zhou, M. Muñoz, H. Lu, M. Sohel, M. C. Tamargo, F. Jean-Mary, and D. L. Akins, *Appl. Phys. Lett.* **85**, 6395 (2004).

[137] N. N. Ledentsov, V. A. Shchukin, M. Grundmann, N. Kirstaedter, J. Böhrer, O. Schmidt, D. Bimberg, V. M. Ustinov, A. Yu. Egorov, A. E. Zhukov, P.S. Kop'ev, S.

V. Zaitsev, N. Yu. Gordeev, Zh. I. Alferov, A. I. Borovkov, A. O. Kosogov, S.S. Ruvimov, P. Werner, U. Gösele, and J. Heydenreich, Phys. Rev. B **54**, 8743 (1996).

[138] J.R. Lothian, J.M. Kuo, F. Ren, S.J. Pearton, J. Elec. Mat. **21-4**, L100 (1992)

[139] A Javier, D. Magana, T. Jenings, G.F. Strouse, *Appl. Phys. Lett.* **83**, 1423 (2003).

[140] "Fundamentals of Semiconductors", P.Y. Yu and M. Cardona, Springer, New York, pp. 474 (1996).

[141] R. E. Nahory, M. J. S. P. Brasil, and M. C. Tamargo, "Semiconductor Interfaces and Microstructures", ed. Zeng, world Scientific, Singapore, p. 238, (1992).

Chapter 6

[142] S. Perkowitz, "Optical Characterization of Semiconductors: Infrared, Raman and Photoluminescence Spectroscopy", Academic Press, San Diego (1994).

[143] Takahiro Mori, Takashi Hanada, Toshiharu Morimura, Keesam Shin, Hisao Makino, and Takafumi Yao, *Appl. Surf. Sci.* **237**, 230-234 (2004).

[144]H. Rho, H. E. Jackson, S. Lee, M. Dobrowolska, and J. K. Furdyna, *Physical Review B* **61**, 15641 (2000).

[145] D. Huang, C. Jin, D. Wang, X. Liu, J. Wang and X. Wang, *Appl. Phys. Lett.* **67**, 3611, (1995).

[146]A.P Alivisatos, *J.Phys.Chem*. **100**, 13226 (1996).

[147] D.L. Klein, R. Roth, A. K. L. Lim, A. P. Alivisatos, P. L. McEuen, *Nature* **389**, 699 (1997).

[148] V. L. Colvin, M. C. Schlamp, A. P. Alivisatos, *Nature* **370**, 354 (1994).

[149] C. Cao, R. Jin, C. A. Mirkin, *Science* **297**, 1536-1762 (2002).

[150]H. Du, M. D. Disney, B. L. Miller, T. D. Krauss, *J.Am.Chem.Soc*.**125**, 4012-4013 (2003).

[151] R. K. Chang, T. E. Furtak, "Surface Enhanced Raman Scattering", Plenum, New York, (1982).

[152] R.P. Van Duyne, "*Surface Enhanced Raman Scattering"* in "Chemical and Biochemical Applications of Lasers", ed. by C. B. Moore, Academic Press, New York, (1979), Vol. 4, p.101.

[153] *M.* Moskovits, *Rev. Mod. Phys***. 1985**, 57**,** 783.

[154] R. L. Birke, J. R. Lombardi, "*Surface Enhanced Raman Scattering*" in "Spectroelectrochemistry: Theory and Practice", ed. R.J. Gale, Plenum, (1988).

[155]S. R. Emory, M. Han, W. Doering, S. Nie, *"Blinking Surface-Enhanced Raman Scattering Observed in Single Colloidal Nanocrystals"* in "Progress in Surface Raman Spectroscopy"; "Theory, Techniques and Applications", Ed. Z.Q. Tian, and B.Ren, Xiamen University Press, Xiamen, China, (2000).

[156]A. Michaels and L.Brus, "Electromagnetic Field Enhancement and the Raman Spectra of Single R6G Dye Molecules", in Progress in Surface Raman Spectroscopy; "Theory, Techniques and Applications", Ed. Z.Q. Tian, and B.Ren, Xiamen, University Press, Xiamen, China, (2000).

[157]J.P. Kottmann, J. F. Martin, D. R. Smith, and S. Schultz, *Phys. Rev. B*, **64**, 1 (2001).

[158] J. Uehara, H. Nishihara, and K. Aramaki, *J. Electrochem. Soc*. 137, 2677 **(1990)**.

[159]Q.J. Huang, X.Q.Li, J.L.Yao, B. Ren, W.B. Cai, J.S. Gao, B.W. Mao, Z.Q. Tian, , *Surface Science* **427**, 162 (1999).

[160] P.G. Cao, J. L.Yao, B. Ren, B. W. Mao, R. A. Gu, and Z. Q. Tian, *Chem. Phys. Lett*., **316**, 1 (2000).

[161] L. G. Quagliano, *"Surface Enhanced Raman Scattering (SERS) effect on semiconductor materials"* in the book: "Recent Research Developments in Raman Spectroscopy", vol. 1 (2002), edited by Transworld Research Network (Trivandrum).

[162] L. Quagliano, , *J.Am.Chem.Soc*., **126**, 7393-7398 (2004).

[163] B. Giese and D. McNaughton, *J. Phys. Chem. B*, **106**, 101 (2002).

[164] R. P. Rava, and T. G. Spiro, *J. Phys. Chem*., **89**, 1856-1861 (1985).

[165] X. Cao, G.Fischer, *J. Phys. Chem. A*, **103**, 9995-10003 (1999).

[166] L. Grace, R. Cohen, T. Dunn, D.M. Lubman, A.S. de Vries, , *J. Molec. Spectry*., **215**, 204-219 (2002).

[167] M.N. Siamwiza, R.C. Lord, M.C. Chen, T. Takamatsu, I. Harada, Matsuura, H.; Shimanouchi, T., *Biochemistry*, 1975, 14, 4870.

[168] J.E. Bowen Katari, V.L. Colvin, A.P. Alivisatos, *J. Phys. Chem*. **98**, 4109-4117 (1994).

[169] J.R. Lombardi, R.L. Birke, T. Lu, J. Xu,, *J. Chem. Phys*., **84**, 4174 (1986).

List of Publications

Journals

a. Published and submitted journals

1. "Formation and Optical Properties Stacked CdSe Self-Assembled Quantum Dots on $Zn_xCd_yMg_{(1-x-y)}Se$ Barriers", M. Noemi Perez-Paz, Hong Lu, Aidong Shen and Maria C. Tamargo, *J. Vac. Sci. Tech. B.* to be published in 2006 (submitted for revision).

2. H. Lu, M. N. Perez-Paz, M. Sohel, A. Shen, X. Zhou, M. C. Tamargo, S. K. Zhang and R. R. Alfano, P*hys. Stat. Sol. c* to be published in 2006 (submitted for revision).

3. "Surface Enhanced Raman Spectroscopy in CdSe Quantum Dots Grown by Molecular Beam Epitaxy" L. G. Quagliano, R. Livingstone, M. N. Perez-Paz, F. Jean-Mary, D. L. Akins, M. C. Tamargo, and J. R. Lombardi, *J. Am. Chem. Soc* (submitted for revision).

4. "Spectroscopy and Carrier Dynamics in CdSe Self-Assembled Quantum Dots Embedded in ZnCdMgSe" G. Comanescu, W. Wang, S. Gundry, B. Das, R.R. Alfano, M. N. Perez-Paz, M. C. Tamargo, M. Muñoz, I. Popov and L. L. Isaacs, *Appl. Phys. Lett.* **86**, 253113 (2005).

5. "Single Layer and Stacked CdSe Self-Assembled Quantum Dots with ZnCdMgSe Barriers for Visible and White Light Applications" M. N. Perez-Paz, X. Zhou, M. Muñoz, M. Sohel, H. Lu, F. Fernandez, M. C. Tamargo, F. Jean-Mary, and D. L. Akins, *J. Vac. Sci. Tech. B.* **23**, 1236 (2005) and selected journal in an issue of *Virtual Journal of Nanoscale Science & Technology*, June 20 (2005).

6. “Optical Characterization and Evaluation of the Conduction Band Offset for ZnCdSe/ZnMgSe Quantum Wells Grown on InP(001) by MBE” M. Sohel, X. Zhou, H. Lu, M. N. Perez-Paz, M. C. Tamargo, and M. Muñoz , *J. Vac. Sci. Tech. B.* **23**, 1209 (2005).

7. “CdSe Self-Assembled Quantum Dots with ZnCdMgSe Barriers Emitting throughout the Visible Spectrum”, M. N. Perez-Paz, X. Zhou, M. Muñoz, H. Lu, M. Sohel, M. C. Tamargo, F. Jean-Mary and D. L. Akins, *Appl. Phys. Lett.* **85**, 6395 (2004) and selected journal in an issue of *Virtual Journal of Nanoscale Science & Technology*, January 10 (2005).

b. Journals in preparation

8. “Growth and Control of Vertical Correlation of CdSe Stacked Quantum Dots with ZnCdMgSe barriers varying spacer thickness and magnesium content” M. N. Perez-Paz, H. Lu, A. Shen, and M. C. Tamargo.

9. “Contactless electroreflectance measurements of Single CdSe quantum dots multi-quantum dots with ZnCdMgSe barriers” M. N. Perez-Paz, M. Muñoz, H. Lu, A. Shen and M. C. Tamargo.

10. “Raman and Elipsometry Measurements of Capped Self-Assembled CdSe Quantum Dots with ZnCdMgSe Barriers” J. S. Reparaz, A. R. Goñi, M. N. Perez-Paz, M. C. Tamargo.

Conferences

1. “CdSe Quantum Dots with ZnCdMgSe Barriers Emitting throughout the Visible Spectrum”, J. S. Reparez, M. I. Alonso, A. R. Goñi, M. N. Perez-Paz, M. C. Tamargo , 14th International Workshop on Heterostructure Technology, October 2sd – 5th, Bratislava, Slovakia, 2005, (invited talk). J. S Raparez, M. I. Alonso, A. R. Goñi, M. N. Perez-Paz, M. C. Tamargo.

2. “Single and Stacked CdSe Self-Assembled Quantum Dots on ZnCdMgSe Barriers: Formation and Optical Properties” M. N. Perez-Paz, H.Lu, M. Sohel, A. Shen, M. C. Tamargo, 23nd North American Conference on Molecular Beam Epitaxy, September 11th-14th , 2005, Santa Barbara, California, USA.

3. “Study of Intersubband Transitions in ZnCdSe/ZnCdMgSe Quantum Well structures prepared by Molecular Beam Epitaxy” H. Lu, M. N. Perez-Paz, A. Shen, M. Sohel, S. K. Zhang, R. R. Alfano, M. C. Tamargo and M. Muñoz, 23nd North American Conference on Molecular Beam Epitaxy, September 11th-14th , 2005, Santa Barbara, California, USA.

4. “SERS as sensing method for bio-molecules”, R. Livingstone L. G. Quagliano, N. Perez, F. Jean-Mary, M. C. Tamargo, and J. R. Lombardi, (oral presentation), SPIE Optics East Conference, October 23th-26th, Boston, Massachusetts, USA. (Invited talk).

5. “Detection of Biomolecules from MBE-Grown II-VI Quantum Dots by means of SERS Spectroscopy”, L. G. Quagliano, R. Livingstone, N. Perez, M. Munoz, M. C. Tamargo, and J. R. Lombardi, (oral presentation), Materials Research Society Spring Meeting,, March 28th –April 1st, 2005, San Francisco, California, USA.

6. “Study of ZnCdSe/ZnCdMgSe Multi-Quantum Well structures prepared by Molecular Beam Epitaxy” H. Lu, M. N. Perez-Paz, M. Sohel, A. Shen, X. Zhou, M. C. Tamargo, S. K. Zhang and R. R. Alfano (oral presentation), 12th International Conference on II-VI Compounds, September 12 - 16, 2005, Warsaw, Poland.

7. “Growth And Vertical Correlation Of CdSe Stacked Quantum Dots On ZnCdMgSe Barriers Varying Spacer Thickness And Mg Content” M. N. Perez-Paz, H. Lu, X. Zhou, M. Sohel, A. Shen and M. C. Tamargo (poster presentation), 12th International Conference on II-VI Compounds, September 12 - 16, 2005, Warsaw, Poland.

8. “Wide Bandgap ZnMgSe alloys and ZnCdSe/ZnMgSe Quantum Wells for Intersubband Devices” M. Sohel, M. N. Perez-Paz, H. Lu, X. Zhou, M. Munoz and M. C. Tamargo (poster presentation), 12th International Conference on II-VI Compounds, September 12 - 16, 2005, Warsaw, Poland.

9. “Wideband Gap ZnMgSe Alloys and ZnCdSe/ZnMgSe Quantum Wells for Application in Quantum Cascade Lasers for Ultra Fast Optical Communications” M. Sohel, H. Lu, N. Perez- Paz, X. Zhou, M. Muñoz and M. C. Tamargo, (poster presentation), Einsteins in the City, April 10th -11th , New York, USA.

10. “Growth and Characterization of ZnCdSe/ZnCdMgSe Multi-Quantum Wells for Infra-Red Opto-electronic Applications” H. Lu, O. Othman, A. Shen, M. N. Perez-Paz, M. Sohel, X. Zhou and M. C. Tamargo (poster presentation), Einsteins in the City, April 10th -11th , New York, USA.

11. “Single- and Multi-Layers of CdSe Self-Assembled Quantum Dots with ZnCdMgSe Barriers: Formation Control and Optical Applications” M. N. Perez-Paz,

X. Zhou, H. Lu, M. Sohel, and M. C. Tamargo (poster presentation), Einsteins in the City, April 10^{th} -11^{th} , New York, New York, USA.

12. "Mg Influence in the Formation of CdSe Self-Assembled Quantum Dots with ZnCdMgSe Barriers" M. N. Perez-Paz, H.Lu, M. Sohel, X. Zhou, and M. C. Tamargo, Annual 2005 March meeting of American Physical Society, March 21–25, Los Angeles, California, USA.

13. "CdSe Self-Assembled Quantum Dots with ZnCdMgSe Barriers Emitting throughout the Visible Spectrum", M. N. Perez-Paz, X. Zhou, M. Muñoz, F. Fernandez, and M. C. Tamargo, (oral presentation), 22nd North American Conference on Molecular Beam Epitaxy, October 10^{th}-14^{th}, 2004, Banff, Alberta, Canada.

14. "Optical Characterization and Evaluation of the Conduction Band Offset for ZnCdSe/ZnMgSe Quantum Wells Grown on InP (001) by MBE" M. Sohel, X. Zhou, H. Lu, M. N. Perez-Paz, M. C. Tamargo, and M. Muñoz (oral presentation), 22nd North American Conference on Molecular Beam Epitaxy, October 10^{th}-14^{th}, 2004, Banff, Alberta, Canada.